

Université du Québec
Institut national de la recherche scientifique
Énergie Matériaux Télécommunications

Designing Dynamic Resource Allocation Mechanisms for Wireless Powered Communication Networks

By

Ali Bayat

A dissertation submitted in partial fulfillment of the requirements for the degree of
Doctor of Philosophy (Ph.D.) in Telecommunications

External examiner:	Prof. Yousef Shayan Concordia University
External examiner:	Prof. Wessam Ajib Université du Québec
Internal examiner:	Prof. Douglas O'Shaughnessy INRS University
Research director	Prof. Sonia Aïssa INRS University

October 21, 2020

© Copyright by Ali Bayat, 2020

Abstract

In this dissertation, we focus on designing resource allocation algorithms and scheduling schemes for wireless information and power transfer systems. In contrast to wireless information transfer (WIT) systems, the end-to-end channel from the wireless power transmitter to the energy harvesting output in wireless power (WPT) systems is *non-linear*. This non-linearity should be taken into account while designing optimal transmit signals and scheduling schemes in WPT systems. As the first milestone in this PhD dissertation, novel closed-form formulas relating the output DC current of a rectifier to the shape of transmit signals in WPT systems is derived. Then, using these formulas, two scheduling schemes, i.e. time sharing and spatial multiplexing, are studied, revealing by the end, the importance of considering the nonlinearity effect in designing such schemes. As the second milestone of the thesis, we focus on designing resource allocation mechanisms for WPT, WIT, and simultaneous wireless and information transfer (SWIPT) systems through applying auction theory. In particular, for WIT and SWIPT systems, we design deep learning-based auction mechanisms to solve the NP-hard resource allocation problems for real-time applications in 5G and beyond.

The first part of this four-part thesis, is about finding a tractable formula for energy harvesting devices which can be applied by researchers for designing transmit signals for WPT systems. Recently, multi-tone transmit signals are shown to be more efficient for WPT systems. However, there is a lack of a tractable mathematical representation of the output harvested energy to the transmit signal while considering the nonlinearity of the rectifiers. The proposed formula avoids most of the tractability issues already in the literature.

As in multi-user WIT systems, the harvesting devices far from the power transmitter in multi-user WPT systems require much more wireless power shares compared with the near devices—known as the near-far problem—when fairness is the objective of the system. One main fairness metric

is the min-max criterion. One interesting challenge is how the nonlinearity effect of the energy receivers in WPT systems could affect choosing the optimal scheduling schemes considering the max-min fairness. In part II, using the Bessel-based formulas derived in part I, we mathematically prove that the time sharing scheduling scheme outperforms the spatial multiplexing scheme under the max-min criterion. The results of this part are novel and highlight the importance of considering the nonlinearity effect while designing scheduling schemes for WPT systems.

In the next generations of the wireless communications, the economical behavior of devices is going to be considered so that the users have the option to choose between different service providers while considering their own monetary budgets. Auctions provide a proper competition framework for the devices who behave selfishly in order to maximize their own payoff. Game theory is the appropriate tool for analyzing the auctions and finding the equilibrium points of the game. Consisting part III of the thesis, chapters 6 and 7 present distributed algorithms which converge efficiently to the Nash equilibrium points of the game, played by the energy harvesting devices in a WPT system. The problem of finding the optimal allocation strategy considering bidding behavior of the energy harvesting devices, where the bids are dynamically generated by the users, is tackled in this part. A joint game theory and queuing theory analysis approach is applied which illustrates how these two theories can contribute the solution.

While in Part III, the allocation algorithms are analyzed with game theory for a WPT system, in the last part, i.e. Part IV, of this dissertation, we are in pursuit of designing optimal auction mechanisms for the task of resource allocation for simultaneous information and power transfer systems. In this part, we face a complex NP-hard resource allocation problem which has exponential time complexity and cannot be solved applying conventional iterative beamforming algorithms. One big challenge with the emergence of 5G and its service heterogeneity is the complexity of resource allocation in such complex systems. Recently, machine learning has successfully entered the wireless domain. One promising practical solution to carry out such complex resource allocation tasks in real-time is through applying deep learning.

Acknowledgment

Here, I would like to express my sincere gratitude to my supervisor, Prof. *Sonia Aiïssa* for her support and mentorship in this research journey. She has helped me develop my character and be persistent in achieving my goals. It is also a great honor for me to have prominent figures like Prof. *Yousef Shayan* from Concordia University, Prof. *Wessam Ajib* from Quebec University, and Prof. *Douglas O'Shaughnessy* from INRS as my jury composition.

I am always thankful to my beloved parents for their ever-lasting support and kindness and all their efforts to help me become a better human. I am so grateful to my beloved wife, *Shabnam*, whose permanent love, support, and patience can not be thanked in words. My special thanks goes to my little son, *Ayeen*, who kindly allowed me to finish my research journey!

Once Einstein said, "There are only two ways to live your life. One is as though nothing is a miracle. The other is as though everything is a miracle."

Contents

Abstract	iii
Acknowledgment	v
List of figures	xv
List of tables	xix
Abbreviations	xxi
1 Introduction and Objectives	1
1.1 Introduction to Wireless Powered Communications	1
1.1.1 WPT—Applications and Challenges	2
1.1.2 WIPT—Applications and Challenges	4
1.1.3 Resource Allocation for WIPT Networks	5
1.2 The Research Problems	7
1.3 Research Objectives	8
1.3.1 Part I: Nonlinear Analysis of Rectifiers in ERs	8
1.3.2 Part II: Performance Analysis of Scheduling Schemes for WPT Systems	9
1.3.3 Part III: Auction-Driven Resource Allocation Algorithm Design and Analysis for WPT Systems	9
1.3.4 Part IV: Auction Mechanism Design with Deep Learning for SWIPT Systems	9
1.4 Methodology	10
1.4.1 Nonlinear Analysis of ER Rectifiers	10
1.4.2 Performance Analysis of Scheduling Schemes for WPT Systems	12

1.4.3	Auction-Driven Resource Allocation Algorithm Design and Analysis for WPT Systems	12
1.4.4	Auction Mechanism Design with Deep Learning for SWIPT Systems	13
I	Waveform Design Leveraging Nonlinearity of Energy Harvesters	15
2	Energy Harvesting Formula	19
2.1	Literature Review	19
2.2	Problem Statement	20
2.3	Rectenna Output DC Current	22
2.4	Comparative Results and Discussion	27
2.5	Summary	28
3	Energy Beamforming to Multiple-Antenna Energy Harvesters	29
3.1	Wireless Power Transfer System and Devices	31
3.1.1	The Rectifier Circuit	31
3.1.2	The MIMO WPT System	31
3.2	Energy Beamforming using Fixed-Coefficient and Bessel-based Formulas	33
3.2.1	Fixed-Coefficient Based Design	33
3.2.2	Bessel-Based Formula Design	36
3.3	Numerical Results and Discussion	37
3.4	Summary	40
II	Optimal Scheduling Schemes: Time Sharing vs. Spatial Multiplexing	41
4	Optimal Fair Energy Beamforming in Multi-User MISO Systems	45
4.1	Developing the Wireless Power Transfer Model	46
4.2	Homogeneous Network: Time-Sharing versus Spatial-Multiplexing	48
4.3	Heterogeneous Network: Time-Sharing versus Spatial-Multiplexing	50
4.4	Summary	53

5	Fair Scheduling and Energy Beamforming in Multi-Band WPT Systems	55
5.1	The Wireless Power Transfer Network Models	56
5.1.1	The Wireless Power Transfer Model	56
5.2	Homogeneous Network:	
	Time-Sharing versus Spatial-Multiplexing	59
5.2.1	Homogeneous Network	59
5.3	Heterogeneous Network:	
	Time-Sharing versus Spatial-Multiplexing	61
5.4	Summary	64
III	Auction-Based Wireless Power Transfer	65
6	Auction-Based Wireless Power Charging—Queuing Theory Approach	69
6.1	The Wireless Power Charging Network	70
6.2	Finding the Nash Equilibrium	71
6.3	User Admission and Power Allocation	73
6.4	Numerical Results and Evaluation	75
6.5	Summary	78
7	Auction-Based Wireless Power Charging with Reneging Devices	79
7.1	The Wireless Power Charging Network	80
7.2	Non-Reneging and Reneging Games: Analysis	82
7.2.1	Non-Reneging Game with no Critical User	82
7.2.2	Non-Reneging Game with a Critical User	82
7.2.3	Reneging Game with no Critical User	83
7.2.4	Reneging Game with a Critical User	84
7.3	Social Welfare and Price of Anarchy	85
7.4	Comparative Results	86
7.5	Summary	89
IV	Deep Learning-Based Auction-Driven Beamforming	91
8	Auction-Driven Multiuser Information Beamforming with Deep Learning	95

8.1	Literature Review	95
8.2	The System Modeling	97
8.2.1	Bidding Modeling	98
8.2.2	Auction Framework	99
8.2.3	Utility Functions	100
8.3	Social-Welfare Maximizing Mechanism	101
8.3.1	The Optimal Allocation Rule	101
8.3.2	The Optimal Payment Rule	104
8.4	Deep Learning Based Allocation Rule	104
8.4.1	The Proposed Deep Neural Network Architecture	105
8.5	Performance Evaluation and Discussion	106
8.5.1	Computational Complexity	108
8.6	Summary	109
9	Learning-Based Auction-Driven Beamforming for SWIPT	111
9.1	Literature Review	111
9.1.1	Related Works	112
9.1.2	The Contribution of Our Work	114
9.2	The Network Modeling	116
9.2.1	Physical Modeling	116
9.2.2	Bidding Modeling	118
9.2.3	Auction Framework	119
9.2.4	Utility Functions	120
9.3	The Problem Formulation	121
9.4	Finding the Feasible Allocation Set \mathcal{A}_F	121
9.4.1	Wireless Information Transfer Network	123
9.4.2	Wireless Power Transfer Network	126
9.4.3	SWIPT Network	127
9.5	Revenue-Maximizing Mechanism	127
9.5.1	Social-Welfare Maximization—VCG Auction	128
9.5.2	Revenue Maximization Mechanism—Mayerson Mechanism	129
9.6	Iterative Algorithms for Finding the Allocation Rule	131

9.6.1	Branch-and-Bound Algorithm	131
9.6.2	Heuristic Sub-Optimal Iterative Solutions	131
9.7	Deep Learning Based Allocation Rule	133
9.7.1	The Proposed Deep Neural Network Architecture	134
9.7.2	Computational Complexity	135
9.8	Performance Evaluation and Discussion	136
9.9	Summary	140
10	Summary	141
10.1	Part I	141
10.2	Part II	141
10.3	Part III	142
10.4	Part IV	142
A	Proofs	143
A.1	Proof of Eq. (2.10)	143
A.2	Proof of Theorem 1	144
A.3	Proof of Theorem 2	150
A.4	Helpful Plots	152
References		143
B	Publications	153
B.1	Journal Papers	153
B.2	Conference Papers	154
V	Résumé Français	155
C	Introduction et Objectifs	157
C.1	Communications Alimenté sans Fil	157
C.2	Les Problèmes de Recherche	158
C.3	Objectifs de Recherches	159
C.3.1	Analyse non Linéaire des Redresseurs dans les ER	160
C.3.2	Analyse des Performances des Schémas de Planification Pour les Systèmes WPT160	160

C.3.3	Conception et Analyse d'Algorithmes d'Allocation de Ressources Basés sur les Enchères pour les Systèmes WPT	160
C.3.4	Conception de Mécanismes d'Enchères avec Apprentissage en Profondeur pour les Systèmes SWIPT	161
C.4	Methodologie	161
C.4.1	Analyse non Linéaire des Redresseurs dans les ER	162
C.4.2	Analyse des Performances des Schémas de Planification pour les Systèmes WPT	163
C.4.3	Conception et Analyse d'Algorithmes d'Allocation de Ressources Basés sur les Enchères pour les Systèmes WPT	163
C.4.4	Conception de Mécanismes d'Enchères avec Apprentissage en Profondeur pour les Systèmes SWIPT	164
D	Dérivation de Formules Tractables pour les Récolteuses d'Énergie	167
D.1	Le Modèle du Système	168
D.2	Nos Nouvelles Formules	169
E	Planification Équitable et Formation de Faisceaux d'Énergie dans les Systèmes WPT Multi-Bandes	171
E.1	Réseau Homogène:	
	Partage de Temps versus Multiplexage Spatial	172
E.1.1	Signal de Transmission Mono-Ton	173
E.1.2	Signal de Transmission Multi-Tons	175
E.2	Réseau Hétérogène:	
	Partage de Temps versus Multiplexage Spatial	176
F	Charge d'Alimentation sans Fil Basée sur les Enchères	177
F.1	La Chaîne de Markov en Temps Continu	178
F.2	Trouver l'Équilibre de Nash	179
F.3	Admission des Utilisateurs et Allocation de Puissance	180
G	Formation de Faisceaux Axée sur les Enchères Basée sur l'Apprentissage Profond pour SWIPT	183
G.1	La Modélisation de Réseau	184
G.1.1	Modélisation Physique	184

G.1.2	Modélisation des Enchères	185
G.1.3	Cadre d'Enchères	186
G.2	La Formulation du Problème	187
G.3	Trouver l'Ensemble d'Allocation Réalisable \mathcal{A}_F	187
G.4	Mécanisme de Maximisation des Revenus	187
G.4.1	Maximisation du Bien-Être Social — Vente aux Enchères VCG	188
G.4.2	Mécanisme de Maximisation des Revenus — Mécanisme de Mayerson	189
G.5	L'Architecture de Réseau Neuronal Profond Proposée	189
G.6	Conclusion	191

List of figures

1.1	End-to-end WPT conversion efficiency.	4
1.2	WIPT architectures: solid and dotted arrows show the direction of energy transfer and information transfer, respectively. ER, IR, and IT stand for energy receiver, information receiver, and information transmitter.	6
1.3	Research objectives.	8
1.4	Objectives and methodologies.	11
2.1	Simplified block diagram of the rectifier.	21
2.2	Comparison of different formulas for i_{out} for (a) the single-tone scenario ($R_L = 1 \text{ k}\Omega$); and for the multi-tone scenario ($R_L = 10 \text{ k}\Omega$) with (b) $N = 4$ and (c) $N = 8$. Plots labeled ‘Exact expression’, ‘Lower bound’, ‘Bessel’, and ‘Taylor’ are related to Eqs. (2.3), (2.15), (2.20), and (2.4), respectively.	27
3.1	Typical energy harvesting circuit.	31
3.2	(a) Steady-state waveform shapes of $i_d(t)$ and (b) its corresponding spectrum for $P_{\text{in}} = -30 \text{ dBm}$ (dotted red curve) and $P_{\text{in}} = -10 \text{ dBm}$ (solid blue curve). The right Y-axis in (a) corresponds to the dotted red curve.	34
3.3	The simulation circuit related to Fig. 3.2.	35
3.4	The lower bounds on the ER’s output DC current when applying the BL and FC formulas for several numbers of transmit antennas (M_t) and fixed number of receive antennas ($M_r = 2$).	39
3.5	The lower bounds on the ER’s output DC current when applying the BL and FC formulas for several numbers of receive antennas (M_r) and fixed number of transmit antennas ($M_t = 4$).	39
4.1	Illustration of (a) UDP and (b) UDT schemes for $K = 4$ devices.	48

4.2	The harvested energy per ER during the transmission block \mathcal{T} for (a) $M = 4$ and (b) $M = 50$	50
4.3	The minimum amount of harvested energy per ER for the TS and SM schemes: (a) $M = 4$ and (b) $M = 10$	52
5.1	The harvested energy per ER during the transmission block \mathcal{T} for $N = 4$ sub-bands: (a) $M = 4$ and (b) $M = 50$	60
5.2	The minimum amount of harvested energy per ER for the TS and SM schemes with $N = 2$ sub-bands: (a) $M = 4$ and (b) $M = 10$	64
6.1	The continuous-time Markov chain.	71
6.2	(a) The allocated power and (b) the limiting probability in each state, when the users' utilities are considered (constrained case) and when not considered (unconstrained case).	76
6.3	(a) Feasible capacity of the power charger, (b) average allocated power ratio, (c) average utility of the power charger, (d) average utility of the user, (e) average number of admitted users in the network, and (f) ratio of the average waiting time over the mean requested charging time.	77
7.1	Comparison of the four games for two values of β : (a) Number of active users over the total number of users M ; (b) Average utility of the CU.	87
7.2	(a) Average utility of the PB; (b) Average social welfare of the users.	88
7.3	(a) Average price of anarchy of the users; (b) Average number of iterations for convergence to the NEP.	88
8.1	Breakout of each auction round.	99
8.2	The DNN used for finding the allocation vector.	105
8.3	(a) The binary cross-entropy metric versus each epoch of training the DNN; (b) the accuracy metric versus each epoch of training the DNN.	107
8.4	The normalized confusion matrix of the trained DNN.	108
9.1	Breakout of each auction round.	119
9.2	The flow diagram of finding the optimal revenue maximization mechanism.	131
9.3	The DNN used for finding the allocation vector.	134

9.4	(a) The binary cross-entropy metric versus each epoch of training the DNN; (b) The accuracy metric versus each epoch of training the DNN.	137
9.5	Comparison of the DNN-based and λ -based methods: (a) The mean square error (MSE), (b) The exact accuracy.	138
9.6	Comparison of the DNN-based and μ -based methods: (a) The mean square error (MSE), (b) The exact accuracy.	138
9.7	The normalized confusion matrix of the trained DNN.	139
A.1	Illustration for checking validity of (A.23).	148
A.2	152
D.1	Schéma fonctionnel simplifié du redresseur.	168
E.1	Illustration des schémas (a) UDP et (b) UDT pour les appareils $K = 4$	173
E.2	L'énergie récoltée par ER pendant le bloc de transmission \mathcal{T} pour (a) $M = 4$ et (b) $M = 50$	174
E.3	L'énergie récoltée par ER pendant le bloc de transmission \mathcal{T} pour $N = 4$ sous-bandes: (a) $M = 4$ et (b) $M = 50$	176
F.1	La chaîne de Markov en temps continu.	178
F.2	(a) La puissance allouée et (b) la probabilité limite dans chaque état, lorsque les utilités des utilisateurs sont prises en compte (cas contraint) et lorsqu'elles ne sont pas prises en compte (cas sans contrainte).	182
G.1	Répartition de chaque tour d'enchères.	186
G.2	L'organigramme de recherche du mécanisme optimal de maximisation des revenus.	190
G.3	Le DNN utilisé pour trouver le vecteur d'allocation.	190

List of tables

1.1	Comparison of Main Technologies for WPT	3
3.1	Simulations Setting	38
8.1	Layout of the proposed DNN architecture (# trainable parameters: 10,362, # non-trainable parameters: 292)	107
8.2	Comparison of the Computational Complexity	108
9.1	Comparison of the Computational Complexity	136
9.2	Layout of the proposed DNN architecture (# trainable parameters: 201,454; # non-trainable parameters: 1,376)	136
9.3	Accuracy of the DNN-Based Method for Different System Models	140

Abbreviations

5G	Fifth Generation of Telecommunication
AI	Artificial Intelligence
AP	Access Point
AWGN	Additive White Gaussian Noise
BER	Bit Error Rate
BL	Bessel-Based
BnB	Branch-and-Bound
CNN	Convolutional Neural Network
CSCG	Circularly-Symmetric Complex Gaussian
CSI	Channel Side Information
CTMC	Continuous-Time Markov Chain
CU	Critical User
DC	Direct Current
DL	Deep Learning
DNN	Deep Neural Network
DSIC	Dominated-Strategy Incentive-Compatible
EH	Energy Harvesting

EIP	Edge Infrastructure Provider
ER	Energy Receiver
ET	Energy Transmitter
FC	Fixed Coefficient
FcNN	Fully-Connected Neural Network
HAP	Hybrid Access Point
IoT	Internet of Things
IR	Information Receiver
LC	Inductance-Capacitance
LoS	Line-of-Sight
MIMO	Multiple-Input Multiple-Output
MISO	Multiple-Input Single-Output
ML	Machine Learning
MSE	Mean Square Error
NEP	Nash Equilibrium Point
NLoS	Non-Line-of-Sight
PB	Power Beacon
PoA	Price of Anarchy
QCQP	Quadratically-Constraint Quadratic Problem
ResNet	Residual Neural Network
RF	Radio Frequency
SDMA	Space-Division Multiple Access
SDR	Semidefinite Programming Relaxation

SINR	Signal-to-Interference-Plus-Noise Ratio
SM	Spatial Multiplexing
SNR	Signal-to-Noise Ratio
SOCP	Second-order Cone Program
SP	Service Provider
SW	Social Welfare
SWIPT	Simultaneous Information and Power Transfer
TDMA	Time-Division Multiple Access
TS	Time Sharing
UDD	Uplink-Downlink Duality
UDP	Uniform Distribution of Power
UDT	Uniform Distribution of Time
UE	User Equipment
ULA	Uniform Linear Array
VCG	Vickrey-Clarke-Groves
WET	Wireless Energy Transfer
WIPT	Information and Power Transfer
WIT	Wireless Information Transfer
WPBC	Wireless-Powered Back-Scatter Communication
WPC	Wireless Power Charger
WPC	Wireless Powered Communications
WPCN	Wireless Powered Communication Network
WPT	Wireless Power Transfer

Chapter 1

Introduction and Objectives

1.1 Introduction to Wireless Powered Communications

Every new paradigm comes true after both the demand and the available technology allow it to. Wireless powered communication¹ is a paradigm for current and future wireless communication systems (5G and beyond), which enables the wireless devices to communicate while obtaining their needed operation energy in a wireless way.

Wireless powered communications refers to communication networks in which both wireless information and power transfer (WIPT)² coexist—in contrast to conventional wireless networks wherein only wireless information transfer (WIT) exists. In the following, we first introduce the wireless power transfer (WPT)³ technology along with its applications and challenges; and then narrow our attention toward WIPT technologies and challenges. Afterwards, by narrowing further, we focus on the challenges in joint resource (power and radio bandwidth) allocation in a dynamic WIPT network, which is the subject of this thesis.

¹Also called *wirelessly* powered communications

²WIPT and WPC point to the same meaning.

³Also called wireless energy transfer (WET) in the literature.

1.1.1 WPT—Applications and Challenges

Limited device battery life is a key concern in the design of modern wireless technologies. Frequent recharging or replacement of the batteries is often costly due to the large number of wireless devices in use, and even infeasible in many critical applications such as sensors embedded in structures, installed in harsh environments, or implanted medical devices. Charging devices wirelessly is not something new and goes back to 1899 when Tesla conducted the first experiment on WPT [1, 2]. The wireless transfer of electromagnetic (EM) wave energy can be broken down to four classes: *inductive coupling*, *magnetic resonant coupling*, *laser power beaming*, and *radio-frequency wireless power transfer* (RF-WPT). Table 1.1 compares these four WPT technologies from different aspects. Since our research focus is on RF-WPT only, henceforth we simply call it WPT for convenience.

WPT provides an attractive solution by powering devices with continuous and stable energy over the air. By leveraging the far-field radiative properties of EM waves, wireless receivers can harvest energy remotely from RF signals radiated by an energy transmitter (ET)⁴. WPT enjoys many practical advantages due to being stable, fully controllable in its transmit power, waveforms, and occupied time/frequency dimensions to power energy receivers (ERs)—in contrast to intermittent and uncontrollable energy resources like solar, wind, or ambient EM radiations. Hence, WPT is a very good candidate for applications requiring deployment of low-power devices as in wireless sensor networks (WSNs), wireless body area networks (WBANs), and the Internet of things (IoT). The typical operation range for WPT systems is from several meters to hundreds of kilometers [3]. WPT has advantages like long-range operation, small receiver form factor, deployment flexibility, power multicasting, and not necessarily requiring a line-of-sight (LoS) link; whereas having low end-to-end power transfer efficiency and safety issues are among the main bottlenecks of applying this technology[4].

Improving the end-to-end WPT efficiency $\eta = P_{DC}^r/P_{DC}^t = \eta_1\eta_2\eta_3$ (cf. Fig. 1.1) is of paramount importance and one of the most challenging design aspects. An effective WPT system is expected to achieve an overall efficiency from a few tenth of a percent to a few percent, depending on the distance. This requires efficient DC to RF power conversion at the transmitter (η_1), highly directive RF transmission or energy beamforming (EB) (η_2), as well as highly efficient RF to DC conversion at the ER (η_3) (cf. Fig. 1.1). For instance, using two antennas for both the ET and ER, we

⁴When speaking of WPT, which is performed on the energy transmitter side, energy harvesting (EH) would be carried out on the receiver side, where an energy receiver (ER) is located.

Table 1.1: Comparison of Main Technologies for WPT.

Technology	Inductive Coupling	Magnetic Resonant Coupling	RF-WPT	Laser Power Beaming
Main Devices	Wire coils	Tuned wire coils, lumped element resonators	Dish antenna, antenna arrays, rectenna	Laser emitter, photovoltaic receiver
Typical Range	Millimeter to centimeters	Few meters	Several meters to hundreds of kilometers	Up to kilometers
Typical Frequency	Hz to MHz	kHz to MHz	MHz to dozens of GHz	THz
Main Advantages and Limitations	High efficiency, requirement for transmitter/receiver coil alignment, very short range, single receiver only	High efficiency, safe, middle range, large transmitter/receiver size	Long range, small Rx form factor, flexibility in deployment and mobility, power multicasting, applicable in SWIPT, massive MIMO, and mmWave, operating in both LoS and NLoS, low efficiency, safety and health issues	Compact size, high energy concentration, no interference to other communication systems, hazardous laser radiation, LoS requirement and exact targeting, vulnerable to atmospheric absorption and scattering
Current and Potential Applications	Electric tooth brush and razor battery charging, electrical vehicle charging, cell-phone charging, factory automation	Charging consumer electronics e.g. cell-phones and laptops, charging biomedical implants, electrical vehicles, RFIDs	Charging wireless sensors, IoT, RFID, consumer electronics, wireless-powered UAVs, solar power satellite	Laser-powered UAVs, laser-based solar power satellite
Representative Companies	Powermat, Delphi, GetPower-Pad, WildCharge, Primove	PowerbiProxi, WiTricity, WiPower, Intel (Wireless resonant energy link)	Intel (WISP), Energous(Wattup), Powercast, Ossia (Cota)	LaserMotive

could achieve a beamforming gain to increase the harvested energy by about four times (6 dB) compared to the case with single antennas. This could be more cost effective in practice than the alternative approach of improving the energy conversion efficiency, say from 25% to 99%, with more complicated rectifying circuits at the ER [4]. Thus, leveraging the EB technique is crucial for WPT

networks to alleviate the problem of low energy transfer efficiency. In general, the larger the number

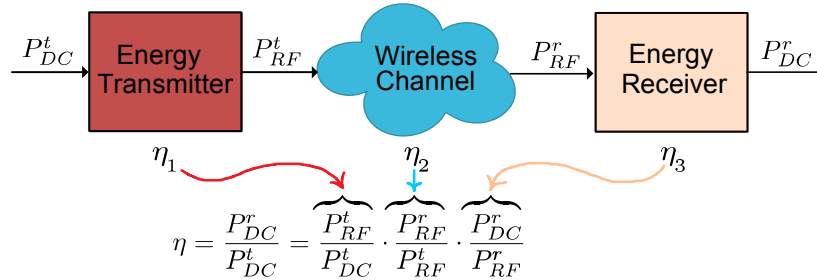


Figure 1.1: End-to-end WPT conversion efficiency.

of antennas at the ET, the sharper the energy beam would be in a particular spatial direction. With only one ER, the transmitter could steer a single sharp beam to maximize the harvested energy. When there are multiple ERs, generating a single beam may result in severe unfairness among ERs, also known as the *energy near-far problem*, where devices near the ET harvest much more energy than far devices. In this case, the transmitter may need to generate multiple energy beams in different directions to balance the energy harvesting (EH) performance among the ERs [5].

Another technique to improve the end-to-end power conversion efficiency η (cf. Fig. 1.1) is to design optimal transmit waveforms [6]. In fact, due to non-linearity of the rectifying circuit, the end-to-end energy transfer link is non-linear. Thus, the output DC energy in the ER does not only depend on the power of the input signal but also on the shape of it. Therefore, designing optimal transmit waveforms can help increase the net power conversion efficiency [7].

1.1.2 WIPT—Applications and Challenges

In contrast to the conventional wireless communication where the wireless channel is aimed to carry information between nodes, in WIPT network architectures, wireless power (or energy) is also transferred through the media to charge the ERs and enable them to carry out their communications. In this way, WIPT can be viewed as an application of WPT in the wireless communication domain. By WIPT, devices use the harvested RF energy to transmit/decode information to/from other devices. Without being interrupted by energy depletion due to communication usage, WIPT is expected to improve user experience and convenience, with higher and more sustainable throughput performance than conventional battery-powered communication [4].

There are three operation modes for WIPT: *wirelessly powered communications network* (WPCN), *simultaneous wireless power and information transfer* (SWIPT), and *wirelessly powered backscatter communication* (WPBC) [8, 9, 10, 11, 12] (cf. Fig. 1.2).

In WPCN, energy is transferred in the downlink (DL) and information is transferred in the uplink (UL). The receiver is a low-power device that harvests energy in DL and uses it to send data on the UL.

In SWIPT, energy and information are simultaneously transferred on the DL from one or multiple access points (APs) to one or multiple receivers. ERs and information receivers (IRs) can be co-located or separated. In SWIPT with separated receivers, ERs and IRs are different devices, the former being low-power devices being charged, the latter being devices receiving data. In SWIPT with co-located receivers, each receiver is a single low-power device that is simultaneously being charged and receiving data. In SWIPT, data and energy are transmitted in the same frequency band at the same time. Therefore, it is more spectral efficient compared to WPCN with orthogonal temporal or spectral energy and data transfer. However, in SWIPT, a careful joint energy and information beamforming is required to avoid the interference from energy signal on the IRs. Also, an efficient SWIPT scheme involves a rate-energy trade-off to balance between the information decoding rate and the amount of harvested energy. It is worth pointing out that since IRs and ERs operate with rather different power sensitivities (e.g., -10 dBm for ERs vs. -60 dBm for IRs) [4], ERs should in general be closer to the transmitter than IRs for effective energy reception.

In WPBC—just like WPCN—energy is transferred on the DL, and information is transferred on the UL. However, backscatter modulation at a tag is used to reflect and modulate the incoming RF signal for communication with a reader. Since tags do not require oscillators to generate carrier signals, backscatter communications benefit from orders-of-magnitude lower power consumption than conventional radio communications.

1.1.3 Resource Allocation for WIPT Networks

Irrespective of the WIPT network model, designing optimal algorithms and mechanisms to allocate resources of wireless energy and bandwidth to the heterogeneous devices in the network while satisfying the devices' quality of service (QoS) is challenging. Maximizing energy efficiency and

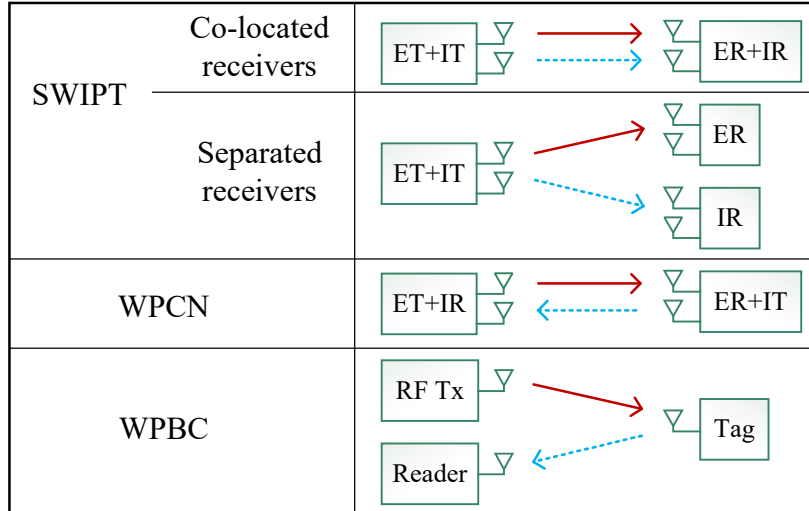


Figure 1.2: WIPT architectures: solid and dotted arrows show the direction of energy transfer and information transfer, respectively. ER, IR, and IT stand for energy receiver, information receiver, and information transmitter.

sum throughput of WIPT networks are among the most explored criteria in the literature [9, 13, 14, 15, 16, 17]. As a different criteria, the authors in [18] considered the physical-layer security of resource allocation among users with the help of transmitting some artificial noise towards the probable eavesdroppers in a WIPT network. In this kind of network models, the ERs and IRs are subscribed to the network service providers, i.e. (hybrid) APs and/or power beacons (PBs). In this regard, the service providers are the entities that do the resource allocation for their registered and subscribed devices and users.

Another network setting is in applications where the service providers and the devices are all independent entities, every one of which can behave selfishly to maximize its own pay-off. In this type of network, the devices are regarded as smart entities with monetary budgets who can participate in an auction game to get their required service. Designing optimal resource allocation mechanisms for such heterogeneous networks by combining pricing and marketing in the MAC-PHY cross-layer design is an interesting research avenue [19]. In this area, while a huge amount of research is based on assuming a static and homogeneous scenario, almost no research has been conducted on dynamic and heterogeneous WIPT network setting, which is what happens in practice.

1.2 The Research Problems

Knowing that WPT is regarded as a promising candidate for future communications [4], one big challenge is the near-far problem in scheduling fairly the wireless power to the ERs. The end-to-end channel in a WPT system is nonlinear and most of the research in the literature assumes a linear model in their analysis and design of scheduling schemes and energy beamforming [9, 20, 21]. Recent researches [6, 7] show the importance of considering the nonlinearity of the ERs in modeling the device and designing more efficient multi-tone transmit signals. A problem not investigated in this research path is design and analysis of power scheduling and beamforming algorithms while considering the nonlinearity effect of the ERs. So, it is first needed that a tractable formula relating the amount of harvested energy in an ER output node to the input signal waveform be derived.

Another relevant research problem, which can be viewed as a continuation of the already mentioned problem, is designing allocation algorithms to beamform information and/or power using an auction framework. The next generation of communication networks is going to be mainly based on user-centric online service provisioning schemes, which will give the user more degrees of freedom to choose among different service providers to get its QoS requirement fulfilled with the minimum cost. Thus, marketing and pricing tasks are no more going to be statically settled at different layers. Instead, we face a cross-layer resource allocation/planning problem [22, 23, 24, 25]. Independent of which type of WIPT technology is deployed, the number of information and power transmitters (which can be co-located or separate) is limited, and service providers need to serve multiple users at the same time. In many applications, wireless devices are independent entities with limited monetary budget requesting a service with a certain level of quality from a provider, which is independently trying to maximize its own revenue. In such networks, where all entities behave selfishly, auctions and designing optimal auction-based resource allocation mechanisms can make every entity happy and maximize the social welfare. Although not many, there are research works on applying auctions and game-theory techniques for resource allocation in WPT networks [26, 27, 28]; and only few on WIPT. To the best of our knowledge, designing optimal auction-based mechanisms applicable to WIPT networks has not been (well) explored yet and this problem is what is studied in this dissertation. One big challenge in designing auction mechanisms for the WIPT channels is the increased amount of complexity that arises particularly while the number of devices,

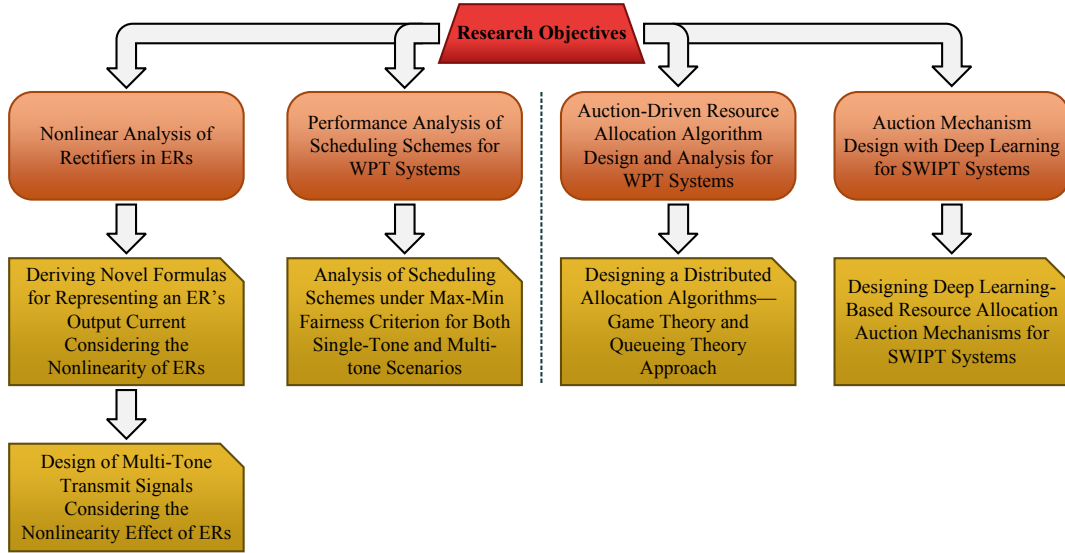


Figure 1.3: Research objectives.

i.e. IRs and ERs, in the network increases. With this level of complexity, conventional iterative algorithms are time-greedy and thus not applicable any more for real-time applications.

1.3 Research Objectives

Having discussed the main research problems in the previous subsections, this subsection describes the objectives of this dissertation in four parts. The objectives are shown in a diagram in Fig. 1.3. In the following, these objectives are explained. As shown in this diagram, the research objectives are broken into four parts.

1.3.1 Part I: Nonlinear Analysis of Rectifiers in ERs

The first part of this dissertation proposes tractable formulas describing, with enough accuracy, the output DC current of a typical rectifier based on the characteristics of the input waveform. This formula can be applied for accurate analysis of ERs' output DC to input RF power conversion efficiency (cf. η_3 in Fig. 1.1), efficient shaping of the ET transmit signal in WPT systems; and designing power scheduling and energy beamforming in WPT systems.

1.3.2 Part II: Performance Analysis of Scheduling Schemes for WPT Systems

Considering the nonlinear effect of the ERs, which in turn makes the end-to-end channel nonlinear, this second part of the research analyzes the fairness-provisioning scheduling schemes in a WPT system. Using the formulas derived in the previous part, the objective here is to analyze power scheduling schemes, namely time sharing and spatial multiplexing, and evaluate their performance in satisfying the max-min fairness among ERs. Such analyses will emphasize the importance of considering the nonlinearity of the end-to-end channels in designing power scheduling algorithms.

1.3.3 Part III: Auction-Driven Resource Allocation Algorithm Design and Analysis for WPT Systems

The third part of the dissertation welcomes auctions, as the proper competition framework for selfish-behavior agents, to the problem of resource allocation in WPT systems. The objective is seeking an efficient distributed resource allocation algorithm run by the agents playing repeated auctions. Then, the algorithm is analyzed for the existence of the Nash equilibrium points and the efficiency of these points as well as the convergence rate of the algorithm. In this part, the acting agents are the ERs, rather than the ET—the latter is what is studied in Part IV. Most of related algorithms in the literature are designed for static networks where there is a fixed number of operating users and/or the users behave in a non-adaptive way to other users' bids. Therefore, they are not optimal for dynamic networks where there is *traffic* of devices with different bid request arrival rates and /or the devices have ability to adapt their bidding strategies with regard to other users' bidding behavior.

1.3.4 Part IV: Auction Mechanism Design with Deep Learning for SWIPT Systems

This part explores tractable algorithms for real-time resource allocation in SWIPT systems in an auction framework. The objective of this last part of the dissertation is seeking real-time solutions to tackle the time-greediness issues with regard to solving real-time resource allocation problems, in particular, joint information and power beamforming SWIPT systems, with social-welfare or revenue as the objectives of the design. To tackle this issue, one solution is making use of machine

learning, and in particular, deep learning. Recently, artificial intelligence (AI) has started to attract significant interest in the research domain of mobile and wireless communication networks [29]. After its clear success in computer vision, natural language processing, speech and image recognition, AI is now touching other domains such as wireless communications and mobile networking. Such AI-related research soaring in the wireless domain is indeed due to the growing diversity and complexity of mobile network architectures, which has made the processing, monitoring, and managing in such networks intractable. Thus, one candidate solution to tackle the problem of complexity in designing auction-based real-time allocation for SWIPT networks is application of AI in the design process.

1.4 Methodology

In this section, we describe how the objectives explained in the previous chapter are met by the methodologies shown in Fig. 1.4. The related contributions are also listed at the end of each section. Figure 1.4 illustrates the relation between the objectives and the required methodologies.

1.4.1 Nonlinear Analysis of ER Rectifiers

Circuit theory is applied for modeling the rectifying elements, diodes, in the ER circuits. The ADS system design platform from KeySight is applied for drawing the ER circuits and running simulations to calculate the output DC current. Manufacturer's SPICE models are used for modeling the diodes used in the simulations. *Transient* and *Harmonic Balance* simulation engines are applied to solve the related circuits and to obtain the simulation results. Matching LC filters for the input of the ERs are designed and optimized in ADS.

The residue theorem of complex analysis is applied to solve the complicated integral that appears during mathematical formulation of the output DC current of ERs. The Maple platform is used to check the validity of the results. Matlab is used for writing all the formulas and for plotting purposes. The simulation data from ADS is exported to CSV format and then is imported in Matlab for comparison purposes.

Stochastic processes, as an inseparable component in wireless communications, here for this objective, is simply used for modeling the wireless channels throughout the dissertation. In general,

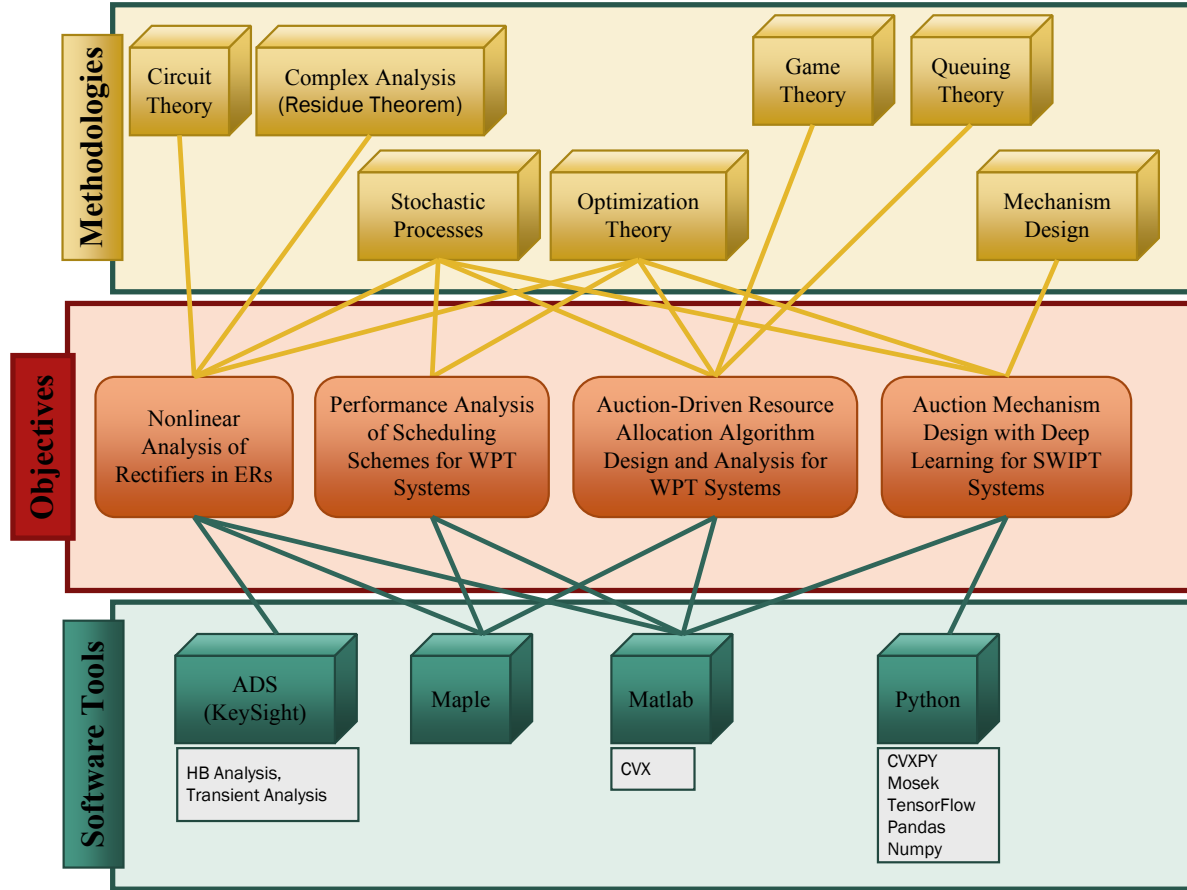


Figure 1.4: Objectives and methodologies.

Optimization Theory is used widely throughout the dissertation for solving different forms of optimization problems. In particular, the CVX package and the built-in nonlinear solution interior-point algorithms in Matlab are used for solving the problem of energy beamforming to multiple-antenna energy harvesters.

Contributions

- An exact novel closed-form formula for representing the output current of ERs in terms of the spectral content of the incident waveform is derived.
- A tractable lower-bound formula, which still can be applied to a large range of input power of ERs, is also derived.
- Based on the lower-bound formula energy-beamforming vectors for a point-to-point multiple-input multiple-output (MIMO)-WPT system are obtained. Then, the importance of consid-

ering nonlinear models instead of linear models is emphasized through comparisons of their accuracy in describing the output DC current of the ERs in WPT systems.

1.4.2 Performance Analysis of Scheduling Schemes for WPT Systems

Stochastic processes are used for modeling the wireless channels. The optimization algorithms along with some heuristic algorithms in Matlab to find the beamforming vectors are applied. The platform Maple is used for checking the validity of the proposed theorems. The network is modeled as a multi-user multiple-input single-output (MU-MISO) WPT system.

Contributions

- Using complex Lambert-Bessel inequalities, mean-value theorem, monotonicity theorem, and a few more, we solidly prove the superiority of a time sharing scheduling scheme over a spatial multiplexing under a max-min fairness criterion while the nonlinearity of the ERs is taken into account. The proof is first carried out for single-tone signals, and then is extended to multi-tone signals.
- The performance analysis is carried out for single-tone and multi-tone transmit signal types.

1.4.3 Auction-Driven Resource Allocation Algorithm Design and Analysis for WPT Systems

Game theory is the necessary tool for analyzing auctions. We apply game theory to analyze distributed-run algorithms to see whether it converges to the Nash equilibrium points (NEPs). We use two metrics of social welfare and price of anarchy (PoA) to evaluate the efficiency of the algorithms. In order for the ET to perform power control and admission control of the ERs, the generation process of the bid requests is modeled by continuous-time Markov chains (CTMC), and analyzed by stochastic processes. The corresponding $M/M/N/N$ queue, which is the same as Erlang's loss system, is analyzed using queuing theory.

To make the bidding behavior of the ERs adaptive to the ET strategy as well as to other ERs bidding behavior, we use learning theory to reinforce the ERs to adapt their behaviors so as to

maximize their payoff. We come up with a self-stabilizing bidding strategy that results in higher payoff for users and an increase in the social welfare and a decrease in the price of anarchy. The interior-point algorithm in Matlab is applied to compute these metrics and compare the static bidding strategy with the dynamic one.

Contributions

- Designing a distributed algorithm considering the dynamics and bidding behavior of the ERs.
- Applying game theory and queuing theory for analyzing the algorithm which is a novel approach.
- Devising a learning-based adaptive playing strategy for ERs which pushes them to a better NEP compared to the one when the ERs play simultaneously without learning from past game play history.

1.4.4 Auction Mechanism Design with Deep Learning for SWIPT Systems

This last research objective has three key elements. Auction mechanism design, deep learning, and beamforming. For the mechanism design part, Myerson's lemma and Vickrey-Clarke-Groves (VCG) mechanisms in economics are suitable candidates for designing methods. For the deep learning part, the Python programming language with its huge collection of machine-learning libraries is undoubtedly the right platform. The proposed deep neural network (DNN) is trained using the well-known TensorFlow application program interface (API). Thanks to ComputeCanada for providing remote computing resources, which hugely accelerated the training process and the generating process of the large amount of training samples. The training data is manipulated using the Pandas library. For the last part, i.e. beamforming, semidefinite relaxation (SDR) techniques to solve second-order quadratic cone problems is applied. The Python library CVXPY, similar to its Matlab counterpart CVX, is applied to take advantage of formulating the standard forms of optimization problems in an abstract way in Python. Particularly the Mosek solver for solving semi-definite programming is used as the solving method in CVXPY.

Contributions

- Proposing a DNN-based approach to solve the revenue-maximization problem, which conventionally has exponential time complexity. This approach has linear time complexity in terms of the number of UEs in the network and the number of ET antennas. This approach highlights that how deep learning can be applied in complex problems of resource allocation as a promising solution.
- Proposing a heuristic iterative algorithm with polynomial time complexity for solving the complex resource allocation problem.
- Proposing an efficient Branch-and-Bound (BnB) algorithm.

Part I

**Waveform Design Leveraging
Nonlinearity of Energy Harvesters**

This first part of the thesis encompasses two chapters. In Chapter 2, we study the effect of nonlinearity of rectifiers in harvesting devices to obtain a closed-form formula relating the output DC current of an ER to its input waveform. The obtained formula is later applied in Chapter 3 for designing optimal transmit waveforms resulting in the maximum harvested energy by multiple antenna ERs.

Chapter 2

Energy Harvesting Formula¹

In this chapter, we present a closed-form formula relating the harvested energy, or equivalently, the output DC current, of a harvesting node in terms of the Fourier coefficients of the input waveform. We also present a more tractable lower-bound formula, which will be later applied in designing the optimal beamforming vectors.

2.1 Literature Review

RF-WPT technology can bring about reliable and customizable wireless energy to harvesting devices.

In RF-WPT, the low end-to-end energy conversion efficiency can be tackled in multiple ways, particularly by i) increasing the power amplifier efficiency at the ET, ii) exploiting multiple antennas to beamform the energy towards the ERs [3], iii) shaping the transmit signal according to the non-linearity of ERs [7], and iv) improving the rectenna circuits by employing multiple antennas and high-performance rectifiers [30, 31, 32].

Due to non-linearity of the rectifying circuit, the end-to-end RF-WPT channel is no more linear. Hence, the output DC power would depend on the shape of the incident waveform and its power. While most of the works on RF-WPT consider a linear model relating the output DC current of

¹A. Bayat and S. Aissa, "When Bessel Meets Fourier in the Power Representation of Energy Harvesting Rectennas," in IEEE Communications Letters, vol. 24, no. 1, pp. 67-70, Jan. 2020.

the ER circuit to the received power at its antenna(s) [4, 20], few have taken into account the nonlinearity of the rectifiers (cf. [6, 7] and references therein). In [6], by writing the ER's diode current in Taylor series expansion form, the authors analyzed a rectifier circuit and shed light on the fact that using signals with high peak-to-average power ratio, like orthogonal frequency division multiplexing signals, can increase the end-to-end conversion efficiency. In this vein of light, [7] proposed a multi-sine transmit waveform design that leverages the non-linearity to maximize the DC current of harvesting devices.

In this chapter, leveraging the residue theorem, we propose a closed-form formula which relates the output DC current of a typical rectifier circuit to the magnitude of the Fourier-series coefficients of its multi-tone input signal. Based on that, another easily tractable formula is also proposed, referred to as lower-bound formula hereafter.

Comparisons based on analysis and circuit simulations show that both formulas are good approximates for the square-law operation region, i.e. for received signal power less than -20 dBm [33]. Also, while both formulas become the same as the exact expression in the case of single-tone input signal, they are shown to keep their validity for larger input signal power levels, say 0 dBm.

To shed a light on how the proposed formulas can be exploited in shaping the transmit signal, their derivation in Section 2.3 is carried out for a multiple-input single-output (MISO) system as defined in Section 2.2. In Section 2.4, the formulas are compared with the one based on Taylor-series and also with the exact expression. Finally, Section 2.5 concludes the part.

2.2 Problem Statement

Consider point-to-point RF-WPT between an ET equipped with M antennas and a single-antenna ER. At the ET, a bandwidth B of N equal-width channels is used to send weighted sinusoidal tones. The received signal at the ER is given by

$$y(t) = \sum_{n=1}^N y_n(t) = \sum_{n=1}^N \Re \left\{ \mathbf{w}_n^T \mathbf{h}_n e^{j2\pi f_n t} \right\}, \quad (2.1)$$

where superscript T denotes transpose, $\mathbf{h}_n = (h_{n,1}, \dots, h_{n,M})^T$ is the channel vector, and $\mathbf{w}_n = (w_{n,1}, \dots, w_{n,M})^T$ is the beamforming vector corresponding to the n^{th} channel with center frequency

$f_n = f_1 + (n - 1)\Delta f$ wherein $\Delta f = B/N$. Note that $\sum_{n=1}^N \|\mathbf{w}_n\|^2 \leq 2P$, where $\|\cdot\|$ stands for Euclidean norm and P is the transmit power of the ET.

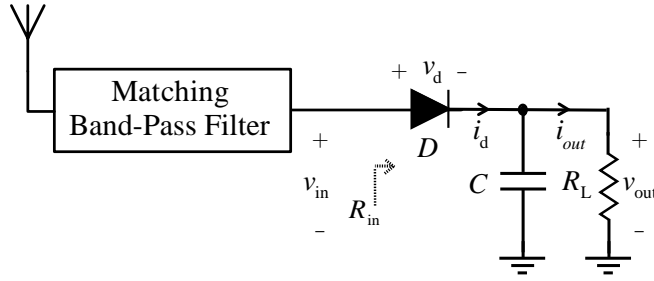


Figure 2.1: Simplified block diagram of the rectifier.

Considering the typical harvesting circuit shown in Fig. 2.1 for the ER, the diode current can be written as

$$i_d(t) = I_s \left(e^{\frac{v_d(t)}{\eta v_T}} - 1 \right), \quad (2.2)$$

where $v_d(t)$ is the voltage drop over the diode, η and I_s are the dimensionless ideality factor and the saturation current of the diode, respectively, and where $v_T = kT/q$ is the thermal voltage with k , q , and T being the Boltzmann's constant, the charge of an electron, and the diode junction temperature in Kelvin, respectively.

We assume that the matching band-pass filter matches the multi-tone received signal to the input of the diode with impedance ratio λ .² That is, $R_{in} = \lambda R_{ant}$ for the whole frequency band B , where R_{ant} is the antenna resistance. As such, $\mathbb{E}\{|y(t)|^2\} = \mathbb{E}\left\{\frac{|v_{in}(t)|^2}{\lambda R_{ant}}\right\}$, where $\mathbb{E}\{\cdot\}$ is the averaging operator. Noting that $v_d(t) = v_{in}(t) - v_{out}$, with $v_{out} = i_{out}R_L$ being the output DC voltage, the output DC current is

$$\begin{aligned} i_{out} &= \mathbb{E}\{i_d(t)\} = \mathbb{E}\left\{I_s e^{\sum_{n=1}^N \alpha_n \cos(2\pi f_n t + \theta_n) - v_{out}}\right\} - I_s \\ &= \frac{I_s e^{-\frac{v_{out}}{\eta v_T}}}{T_0} \int_0^{T_0} e^{\sum_{n=1}^N \alpha_n \cos(2\pi f_n t + \theta_n)} dt - I_s \\ &= \frac{I_s e^{-\frac{i_{out} R_L}{\eta v_T}}}{2\pi} \int_0^{2\pi} e^{\sum_{n=1}^N \alpha_n \cos(L_n \vartheta + \theta_n)} d\vartheta - I_s, \end{aligned} \quad (2.3)$$

where $\theta_n = \angle \mathbf{h}_n^T \mathbf{w}_n$ is the phase of $\mathbf{h}_n^T \mathbf{w}_n$, $a_n = |\mathbf{h}_n^T \mathbf{w}_n|$, $\alpha_n = \frac{a_n \sqrt{\lambda R_{ant}}}{\eta v_T}$, and $L_n = N_0 + n - 1$ by assuming the first channel frequency f_1 to be an integer multiple of Δf , i.e. $f_1 = N_0 \Delta f$; hence

²The band-pass filter also suppresses the harmonics of the incident signal produced by the rectifier from reradiation. Note that λ may vary depending on the input power level.

$T_0 = \frac{1}{\Delta f}$ is the period of the input signal $i_d(t)$. The last integral in (2.3) is obtained by variable substitution of $\vartheta = \frac{2\pi}{T_0}t$. Equation (2.3) is the exact expression for the output DC current and involves calculation of one integral. One approach to find an approximation for i_{out} is to write the Taylor series expansion of $i_d(t)$ in (2.2) around v_{out} and apply the averaging operation $\mathbb{E}\{\cdot\}$. In this way, the average output DC current passing through the load R_L is approximately equal to [7]:

$$i_{\text{out}} \approx k_0 + \sum_{\substack{\hat{N} \\ r \text{ even}, r \geq 2}} k_r (\lambda R_{\text{ant}})^{r/2} \mathbb{E}\{y(t)^r\}, \quad (2.4)$$

where \hat{N} is the truncation number, $k_0 = I_s(e^{\frac{-v_{\text{out}}}{\eta v_T}} - 1)$, and $k_r = \frac{I_s}{(\eta v_T)^{r/2}} e^{\frac{-v_{\text{out}}}{\eta v_T}}$ for $r \geq 2$. In [7], $\hat{N} = 4$ was assumed in the simulations. $\mathbb{E}\{y(t)^r\}$ becomes more computationally complicated with increasing r . This also motivates us to take a different approach and look for a more illustrative formula for the output DC current, which can be exploited in designing and analyzing efficient energy harvesters and transmit waveforms.

2.3 Rectenna Output DC Current

Next, a mathematically tractable formula for i_{out} is presented. Based on that, a lower-bound will be presented as well.

To solve the last integral in (2.3), we apply the Euler formula to get $\cos(L_n \vartheta + \theta_n) = \frac{1}{2}(e^{i(L_n \vartheta + \theta_n)} + e^{-i(L_n \vartheta + \theta_n)})$, and by variable substitution of $z = e^{i\vartheta}$ we cast the real integral into a complex one over a unity contour. Thus, we have

$$\int_0^{2\pi} e^{\sum_{n=1}^N \alpha_n \cos(L_n \vartheta + \theta_n)} d\vartheta = \oint_{|z|=1} \frac{e^{\sum_{n=1}^N \frac{\alpha_n}{2} (z^{L_n} e^{i\theta_n} + z^{-L_n} e^{-i\theta_n})}}{iz} dz = \oint_{|z|=1} f(z) dz. \quad (2.5)$$

A careful look at (2.5) reveals that the only pole of $f(z)$ is $z = 0$. Thus, by applying the *residue theorem*, which states that $\oint_c f(z) dz = 2\pi i \sum_{k=1}^K \text{Res}\{f(z)\}_{|z=p_k}$ —where p_k 's are the poles of $f(z)$ in the contour of c —we can conclude for our case that $\oint_{|z|=1} f(z) dz = 2\pi i c_1$, where $c_1 = \text{Res}\{f(z)\}_{|z=0}$. Let $g(z)$ denote the numerator of $f(z)$. We can write $g(z)$ in its Laurent expansion form around its critical point $z = 0$ as $g(z) = \sum_{k=-\infty}^{\infty} A_k z^k$, where the A_k 's are complex-valued coefficients. Noting that $f(z) = \frac{g(z)}{iz}$, one can easily find out that $c_1 = A_0/i$. Thus, we conclude that $\oint_{|z|=1} f(z) dz = 2\pi A_0$. To find A_0 , we apply the following identity [34], which implies that $e^{\frac{x}{2}(z+z^{-1})}$ is the generating

function of the first-kind n^{th} -order modified Bessel function $I_n(x)$, i.e.,

$$e^{\frac{x}{2}(z+z^{-1})} = \sum_{n=-\infty}^{\infty} I_n(x)z^n. \quad (2.6)$$

Applying (2.6), the function $g(z)$ can be rewritten as

$$\begin{aligned} g(z) &= e^{\sum_{n=1}^N \frac{\alpha_n}{2} \left((z^{L_n} e^{i\theta_n}) + (z^{L_n} e^{i\theta_n})^{-1} \right)} \\ &= \prod_{n=1}^N \left(\sum_{m_n=-\infty}^{\infty} I_{m_n}(\alpha_n) \left(z^{L_n} e^{i\theta_n} \right)^{m_n} \right) \\ &= \sum_{m_1=-\infty}^{\infty} \dots \sum_{m_N=-\infty}^{\infty} I_{m_1}(\alpha_1) \dots I_{m_N}(\alpha_N) z^{m_1 L_1 + \dots + m_N L_N} e^{i(m_1 \theta_1 + \dots + m_N \theta_N)}. \end{aligned} \quad (2.7)$$

Examining (2.7), we see that A_0 can be obtained by choosing those indexes m_n 's that produce $m_1 L_1 + \dots + m_N L_N = 0$ which, upon substitution of $L_n = N_0 + n - 1$, leads to

$$N_0 \sum_{n=1}^N m_n + \sum_{n=2}^N (n-1)m_n = 0. \quad (2.8)$$

Let \mathbb{M} be the set of all N -dimensional integer vectors whose components satisfy the condition in (2.8). That is, $\mathbb{M} = \{\mathbf{m} \in \mathbb{Z}^N \mid N_0 \|\mathbf{m}\|_1 + \mathbf{d}^\top \mathbf{m} = 0\}$, where $\mathbf{m} = (m_1, m_2, \dots, m_N)^\top$, $\mathbf{d} = (0, 1, 2, \dots, N-1)^\top$, and $\|\cdot\|_1$ indicates the 1-norm. Therefore, the exact value of A_0 is

$$A_0 = \sum_{\forall \mathbf{m} \in \mathbb{M}} \left(\prod_{n=1}^N I_{m_n}(\alpha_n) \right) e^{i \mathbf{m}^\top \boldsymbol{\theta}}, \quad (2.9)$$

where the summation is multi-fold and $\boldsymbol{\theta} = (\theta_1, \dots, \theta_N)^\top$.

Now, by substituting $\oint_{|z|=1} f(z) dz = 2\pi A_0$ in (2.5) and making use of Appendix A.1, we can write i_{out} in (2.3) as

$$i_{\text{out}} = -I_s + \frac{1}{\alpha} W_0 \left(A_0 \alpha I_s e^{\alpha I_s} \right), \quad (2.10)$$

where $W_0(\cdot)$ is the principal branch Lambert function, $\alpha = \frac{R_L}{\eta v_T}$, and A_0 is as shown in (2.9). It is important to note that (2.10) is the exact solution of (2.3) that relates the output DC current i_{out} of the rectifier to the exponential Fourier-series coefficients of the periodic input signal. To compute i_{out} for any arbitrary periodic input waveform, we first find the (dominant) Fourier-series coefficients $\alpha_n e^{i\theta_n}$ of the input signal, and then use (2.10).

To maximize i_{out} in (2.10), A_0 needs to be maximized because $W_0(\cdot)$ is a monotonically increasing function. Maximizing A_0 requires $\mathbf{m}^\top \boldsymbol{\theta} = 2k\pi$, $k \in \mathbb{Z}$, $\mathbf{m} \in \mathbb{M}$, where $k = 0$ causes what we look for, i.e. $\mathbf{m}^\top \boldsymbol{\theta} = 0$, for which $\boldsymbol{\theta} = \mathbf{0}$ is a quick solution, i.e. the complex weight vectors \mathbf{w}_n 's are such that $\theta_n = 0 \forall n \in \{1, 2, \dots, N\}$. Thus, (2.9) simplifies to

$$A_0 = \sum_{\forall \mathbf{m} \in \mathbb{M}} I_{m_1}(\alpha_1) I_{m_2}(\alpha_2) \dots I_{m_N}(\alpha_N). \quad (2.11)$$

Furthermore, one can assume $\angle w_{n,m} = -\angle h_{n,m}$ for all n and m to satisfy the condition of $\theta_n = 0$, $n \in \{1, 2, \dots, N\}$. Note that in this case, the α_n 's reduce to $\bar{\alpha}_n = \frac{\sqrt{\lambda R_{\text{ant}}}}{\eta v_T} \bar{\mathbf{h}}_n^\top \bar{\mathbf{w}}_n$, where $\bar{h}_{n,m} = |h_{n,m}|$ and $\bar{w}_{n,m} = |w_{n,m}|$. Thus, to maximize i_{out} , assuming perfect CSI available at the ET, \mathbf{w}_n 's should be chosen such that $\angle w_{n,m} = -\angle h_{n,m}$ for all n and m ; and the $\bar{w}_{n,m}$'s are found by solving the maximization problem

$$\max_{\bar{w}_{n,m}} \bar{A}_0 = \sum_{\forall \mathbf{m} \in \mathbb{M}} \prod_{n=1}^N I_{m_n}(\bar{\alpha}_n) \quad \text{s.t.} \quad \sum_{n=1}^N \sum_{m=1}^M \bar{w}_{n,m}^2 \leq 2P. \quad (2.12)$$

For the particular case of single-tone transmit signal, i.e. when $N = 1$, checking the condition in (2.8) we notice that $\mathbb{M} = \{0\}$. Thus, $A_0 = I_0(\alpha_1)$.³ Next, we aim to obtain a much simpler, but accurate, approximation for A_0 in (2.9). Since the starting-tone frequency f_1 is much higher than the inter-tone spacing Δf , then $N_0 = \frac{f_1}{\Delta f} \gg 1$. In the following, we first calculate A_0 for two more values of N , namely, $N = 2, 3$, knowing that $N_0 \gg 1$. Then, we find A_0 for any $N > 3$.

$N = 2$:

In this case, the condition in (2.8) becomes

$$N_0(m_1 + m_2) + m_2 = 0 \Rightarrow m_1 = -\frac{m_2}{N_0} - m_2. \quad (2.13)$$

In order for m_1 to be an integer, m_2 must be an integer multiple of N_0 . $m_2 = 0$ results in $m_1 = 0$. However, $m_2 \neq 0$ results in a large number for both m_1 and m_2 , e.g., $m_2 = N_0$ gives $m_1 = -N_0 - 1$,

³In [35], a similar Bessel function for describing the DC output current of a rectifier for sinusoidal input signal is derived.

and $m_2 = 2N_0$ gives $m_1 = -2N_0 - 2$. Noting that $I_{-n}(x) = I_n(x)$, (2.9) can be written as follows:

$$A_0 = I_0(\alpha_1)I_0(\alpha_2) + 2 \sum_{m=1}^{\infty} I_{m(N_0+1)}(\alpha_1)I_{mN_0}(\alpha_2). \quad (2.14)$$

Noting that the order numbers of the Bessel functions in the summation terms in (2.14) are much greater than their arguments α_n 's in practice,⁴ the summation terms can be easily neglected. Hence, A_0 boils down to $A_0 = I_0(\alpha_1)I_0(\alpha_2)$. In the latter, A_0 does not depend on the θ_n 's.

In general, for any N , as $\alpha_n \rightarrow 0 \forall n \in \{1, 2, \dots, N\}$, (2.9) and (2.11) converge to

$$A_0 = I_0(\alpha_1)I_0(\alpha_2) \dots I_0(\alpha_N). \quad (2.15)$$

Expression (2.15) is a lower-bound on A_0 , which upon substitution into (2.10) yields a lower-bound on i_{out} which can tractably be exploited in the analysis and design of RF-WPT systems.

$N = 3$:

This time, the condition in (2.8) simplifies to

$$N_0(m_1 + m_2 + m_3) + m_2 + 2m_3 = 0 \Rightarrow m_1 = -\frac{m_2 + 2m_3}{N_0} - (m_2 + m_3). \quad (2.16)$$

Arguing similarly to the previous special case, we can say that since N_0 is a very large number, we only care about those m_n 's in (2.16) that are not that large. Therefore, to write the approximation of A_0 , we rewrite (2.16) as follows:

$$m_1 + m_2 + m_3 = 0, m_2 + 2m_3 = 0 \Rightarrow m_1 = m_3, m_2 = -2m_1.$$

Thus, (2.9) can be very accurately approximated as follows:

$$A_0 = \sum_{m=-\infty}^{\infty} I_m(\alpha_1)I_{2m}(\alpha_2)I_m(\alpha_3)e^{i(\theta_1 - 2\theta_2 + \theta_3)}. \quad (2.17)$$

⁴For maximum α_n , we assume large voltage $v_{\text{in}} = \sqrt{\lambda R_{\text{ant}} \mathbb{E}\{y(t)^2\}} = 230$ mV in the square-law region. With the typical values $\eta = 1.05$ and $v_T = 26$ mV [36], a maximum value can be found as $\hat{\alpha}_n = \frac{v_{\text{in}}}{\eta v_T} = 8.5$. Assuming $f_1 = 1$ GHz and $\Delta f = 100$ kHz, which yields $N_0 = 10^4$, we get $I_{10000}(8.5) = 2.7 \times 10^{-29376}$. For large n , $I_n(x) \simeq \frac{x^n}{2^n n!}$ can be used.

To maximize A_0 , we should have $\theta_1 + \theta_3 = 2\theta_2$. As discussed earlier, one easy choice for the θ_n 's is to set them all zero, as we did in obtaining (2.11). Note that the summation in (2.17) can be truncated to a certain value of m , say \mathcal{M} . Let $\epsilon_{\mathcal{M}}$ denote the relative error due to truncation to \mathcal{M} . For example, for $\alpha_n = 8.5/\sqrt{3}$ and $\mathcal{M} = 2$, the relative error $\epsilon_{\mathcal{M}}$ is

$$\epsilon_{\mathcal{M}=2} = \frac{\left| \sum_{m=-2}^2 (I_m(x))^2 I_{2m}(x) - \sum_{m=-\infty}^{\infty} (I_m(x))^2 I_{2m}(x) \right|}{\sum_{m=-\infty}^{\infty} (I_m(x))^2 I_{2m}(x)} = 0.01, \quad (2.18)$$

which shows that $\mathcal{M} = 2$ is sufficient.

$N \geq 3$:

Condition (2.8) is approximated to

$$\sum_{n=1}^N m_n = 0, \quad \sum_{n=2}^N (n-1)m_n = 0 \Rightarrow m_1 = \sum_{n=3}^N (n-2)m_n, \quad m_2 = -\sum_{n=3}^N (n-1)m_n. \quad (2.19)$$

Therefore, when using (2.11), the generic formula for A_0 as a function of $\boldsymbol{\alpha} = (\alpha_1, \dots, \alpha_N)^\top$ can be expressed as

$$A_0(\boldsymbol{\alpha}) = \sum_{\substack{\mathbb{R}^N \rightarrow \mathbb{R} \\ m_3=-\infty, m_4=-\infty, \dots, m_N=-\infty}}^{\infty} \sum_{m_3=-\infty}^{\infty} \dots \sum_{m_N=-\infty}^{\infty} I_{\sum_{n=3}^N (n-2)m_n}(\alpha_1) I_{\sum_{n=3}^N (n-1)m_n}(\alpha_2) I_{m_3}(\alpha_3) I_{m_4}(\alpha_4) \dots I_{m_N}(\alpha_N). \quad (2.20)$$

We can form $\tilde{A}_0(\boldsymbol{\alpha})$ by truncating each summation in (2.20) from the lower limit of $-\mathcal{M}$ to the upper limit of \mathcal{M} .

It is noteworthy that (2.20) is an elegant simplified formula which reveals that the output DC current is summation of products of some modified Bessel functions of the first kind, with different orders carrying the magnitudes of the exponential Fourier-series coefficients as their arguments. For $N = 1, 2$, (2.20) and (2.15) become the same.

2.4 Comparative Results and Discussion

Simulation results are provided to validate the formulation and analysis. Unless otherwise stated, we assume $\eta = 1.05$, $I_s = 5 \mu\text{A}$, and $v_T = 26 \text{ mV}$, as per typical diode parameters [36]. Also, $f_1 = 1 \text{ GHz}$, $B = 10 \text{ MHz}$, and $R_{\text{ant}} = 50 \Omega$. We evaluate the accuracy of the proposed formulas for the single-tone and multi-tone scenarios, separately. Indeed, the single-tone formula is valid for the square-law region as well as a good portion of the large-signal operation region of the rectifier, whereas the multi-tone formulas are valid for the square-law region only. Without loss of generality, the a_n 's are chosen equally, taking into account the received power constraint. For both scenarios, circuit simulations in ADS platform (Keysight Technologies) are also provided.

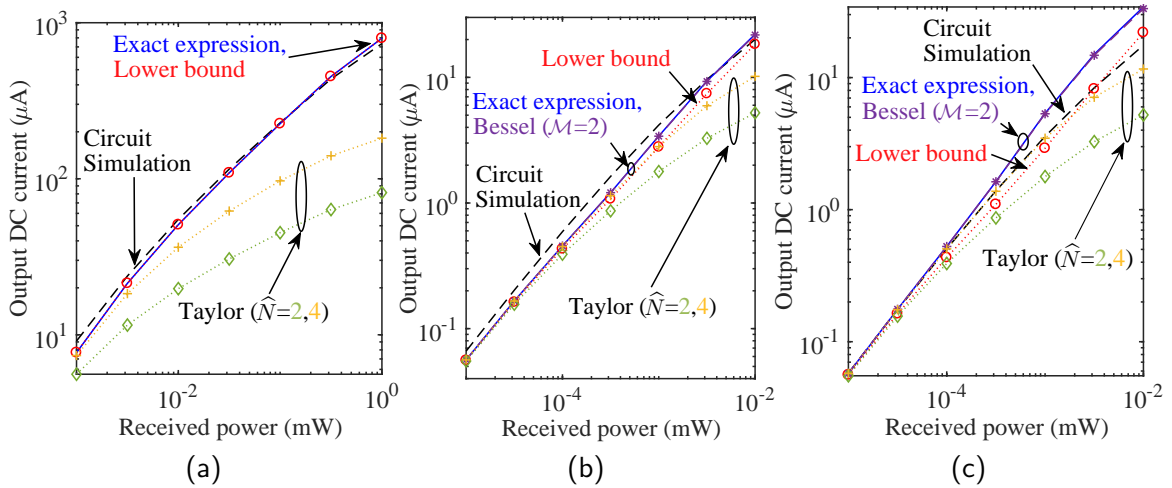


Figure 2.2: Comparison of different formulas for i_{out} for (a) the single-tone scenario ($R_L = 1 \text{ k}\Omega$); and for the multi-tone scenario ($R_L = 10 \text{ k}\Omega$) with (b) $N = 4$ and (c) $N = 8$. Plots labeled ‘Exact expression’, ‘Lower bound’, ‘Bessel’, and ‘Taylor’ are related to Eqs. (2.3), (2.15), (2.20), and (2.4), respectively.

Single-tone Scenario: We evaluate (2.10) with $A_0 = I_0(\alpha_1)$ for incident power ranging from -30 dBm to 0 dBm . To have a ripple-free output, $R_L = 1 \text{ k}\Omega$ and $C = 100 \text{ pF}$ are chosen (cf. Fig. 2.1). As confirmed from Fig. 2.2a, the analysis and simulation curves are in close match even in the large-signal region, which is due to the fact that there are no intermodulation products and that the harmonics of the input signal are fairly filtered. As aforementioned, for $N = 1$ the lower-bound is the same as the exact expression.

Multi-tone Scenario: We evaluate (2.10) with A_0 as per (2.20) and (2.15), respectively, for $N \in \{4, 8\}$ and for incident power in the range $[-50, -20] \text{ dBm}$. The multi-tone scenario requires

decreasing the cutting frequency of the output RC filter for ripple-free output. Thus, we choose $R_L = 10\text{ k}\Omega$ and $C = 1\text{ nF}$ (cf. Fig. 2.1). As Fig. 2.2b and Fig. 2.2c demonstrate, the approximate formula shown in (2.20) with $\mathcal{M} = 2$ tracks the exact expression (2.3) very closely, confirming the truncation number $\mathcal{M} = 2$ to be sufficient for both values of $N = 4$ and $N = 8$. The lower-bound formula (2.15) loses its accuracy as the number of tones increases. Interesting to note is that while the truncation number $\hat{N} = 4$ in the Taylor formula (2.4) is not sufficient for the case of $N = 1$ in the large-signal region (Fig. 2.2a), it brings a good alignment in the multi-tone scenario, especially for $N = 8$ in comparison to $N = 4$. Indeed, for the diode model used, and highly likely for others with similar parameters, the amount of dissipated power on the intermodulation products is almost equal to the higher-order Taylor terms ignored. Of notice is that the Taylor-based curves gradually converge to the results from the exact expression (2.3) as \hat{N} becomes larger. As seen in Fig. 2.2b and Fig. 2.2c, when the incident power and/or the number of tones increase, due to the emergence of more in-band intermodulation products in the multi-tone scenario, the accuracy of the proposed formulas loosens and the square-law region ends up with incident powers smaller than the -20 dBm threshold.

2.5 Summary

Using the residue theorem, a novel formula for the output DC current of a typical energy harvesting circuit, as well as an applicable mathematically tractable lower-bound, was proposed. The result relates the output current to the Fourier coefficients of the incident waveform using modified Bessel functions. It was shown that in the case of multi-tone input signal, the formula is mainly applicable in the square-law region, although its accuracy loosens with increasing the incident power and/or the number of tones. For single-tone signals, the formula remains valid even in the large-signal operation region of the rectifier.

Chapter 3

Energy Beamforming to Multiple-Antenna Energy Harvesters¹

In this chapter, applying the formulas obtained in the previous chapter, we design the optimal beamforming vector which maximizes the amount of harvested energy by the ER. A point-to-point MIMO WPT is considered. The optimization problem is formulated and the optimal solutions are found through applying optimization algorithms and tools such as CVX [37].

While most of the works in the context of energy harvesting and WPT consider a fixed-coefficient formula relating the output DC current of the energy-harvesting device to the received power at its antenna(s) [20, 4], [32], few works have taken into account the nonlinearity of the rectifiers [6, 7, 38, 39, 40].

In [6], by expressing the diode current in the form of Taylor series expansion, the authors analyzed a rectifier circuit to shed light on the fact that using high peak-to-average power ratio signals like orthogonal frequency division multiplexing signals, can increase the end-to-end conversion efficiency of a WPT system. In the same vein, the authors in [7] applied the idea of Taylor expansion to design optimal multi-sine transmit signals in terms of achieving higher levels of micro-amperes at the output of a single ER in a MISO-WPT setting. In stark contrast to [6] and [7], the work in [38] made use of the residue theorem to present a novel compact formula relating the output DC current

¹A. Bayat and S. Aissa, "Shaping Energy Beamforming to the Nonlinearity of Energy Harvesting Devices : (Invited Paper)," 2020 International Conference on Computing, Networking and Communications (ICNC), Kona, HI, USA, 2020, pp. 746-750, doi: 10.1109/ICNC47757.2020.9049478.

of the ER to the Fourier series coefficients of its input waveform by using modified Bessel functions. Therein, a practical lower-bound formula on the output DC current is provided as well. Taking into account the nonlinearity of energy harvesters through the aforementioned Bessel-based exact formula for the single-tone WPT scenario, the superiority of time-sharing access over space-division access in single-band WPT to multiple ERs under max-min fairness criterion is proven in [39]. On the other hand, [40] proposed a method to design waveforms for wireless information and power transfer (WIPT), and characterized the rate-energy region of a point-to-point MISO WIPT system while accounting for the nonlinearity of the energy harvesters.

Of importance in designing WPT systems and analyzing their performance is the use of accurate-enough formulas and metrics that can be relied upon. In this chapter, taking the lower-bound Bessel-based formula presented in [38] as a starting point, which is denoted by BL hereafter, our goal is to demonstrate the importance of considering the non-linear relation between the output current of an ER and its received input waveform. A MIMO WPT system is considered. The problem of finding the optimal beamforming vectors for all sub-bands is formulated and solved once using the BL formula, and once using the conventional fixed coefficient (FC) formula. The latter is extensively used in the related literature when the rectifier is deployed in its square-law region. Although the FC formula provides a fairly good lower-bound approximation for low-power input signals, say less than -20 dBm [33], the bound becomes too loose when the rectifier operates beyond the square-law region. On the other hand, the BL formula is a better approximation for the square-law region, and still provides a fairly good lower-bound at the head of the large-scale region. In particular, when the two techniques of energy beamforming and multi-sine waveform design [3] are employed together, the ER input power level may become so high that it exceeds the square-law region, which necessitates the utilization of more accurate formulas such as the BL formula. Using both the FC and the BL formulas, we formulate and solve non-convex optimization problems to find their corresponding optimal beamforming vectors for all sub-channels. Notably, while [38] and [39] have investigated a MISO WPT channel, this work considers the more general MIMO case.

The organization of the chapter is as follows. The system model is detailed in Section 3.1. Then, in Section 3.2, the energy beamforming optimization problem is formulated for the FC and BL cases. Through extensive simulations in Section 3.3, the two cases are compared in terms of the output DC current of the ER. Finally, Section 3.4 summarizes the chapter.

3.1 Wireless Power Transfer System and Devices

3.1.1 The Rectifier Circuit

Consider a typical harvesting circuit for the ER as depicted in Fig. 3.1. Accordingly, the diode current is given by

$$i_d(t) = I_s \left(e^{\frac{v_d(t)}{n v_T}} - 1 \right). \quad (3.1)$$

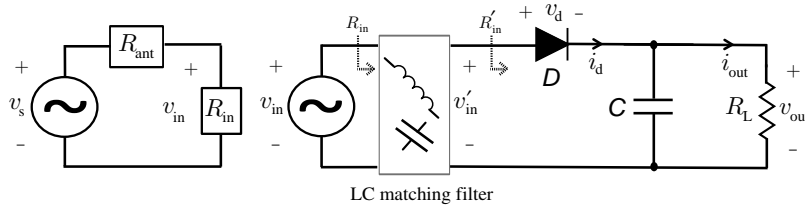


Figure 3.1: Typical energy harvesting circuit.

It is assumed that the LC impedance matching network in Fig. 3.1 matches the received antenna signal to the input of the diode for the whole frequency bandwidth B , with zero insertion loss. Usually, the matching network is a bandpass filter which, beside performing the matching, suppresses the unwanted high-frequency contents produced by the rectifier current from being re-radiated through the ER antenna.² Thus, $R_{in} = R_{ant}$, and $\mathbb{E}\{|y(t)|^2\} = \mathbb{E}\left\{\frac{|v_{in}(t)|^2}{R_{ant}}\right\}$, where $\mathbb{E}\{\cdot\}$ is the averaging operator.³ Also, $v_d(t) = v_{in}(t) - v_{out}$, where $v_{out} = i_{out}R_L$ is the output DC voltage and $i_{out} = \mathbb{E}\{i_d(t)\}$ is the output DC current.

3.1.2 The MIMO WPT System

A multi-channel point-to-point WPT system is considered. The ET and ER are equipped with M_t and M_r antennas, respectively. Ignoring the additive Gaussian noise at the ER,⁴ the received signal is given by $y(t) = \sum_{m=1}^{M_r} y_m(t)$, where $y_m(t)$ is the signal of all N sinusoidal tones on the m^{th}

²Re-radiation of out-of-band spurs and harmonics should not violate the spectrum mask forced by the radio regulatory organizations like the ITU.

³The matching filter has an impedance ratio λ , i.e. $R'_{in} = \lambda R_{in}$. Without loss of generality, we assume $\lambda = 1$ and, as such, $R'_{in} = R_{in} = R_{ant}$ and $v'_{in}(t) = v_{in}(t)$.

⁴Practically speaking, the received signal power in WPT systems is much higher than the noise floor.

antenna of the ER and is given by

$$y_m(t) = \sum_{n=1}^N r_{n,m}(t) = \sum_{n=1}^N \Re \left\{ \mathbf{w}_n^H \mathbf{h}_{n,m} e^{j2\pi f_n t} \right\}, \quad (3.2)$$

where the superscript H stands for conjugate transpose operation, $\mathbf{r}_m(t) = (r_{1,m}(t), \dots, r_{N,m}(t))^T$ denotes the receive signal vector of all tones on the m^{th} antenna of the ER, $\mathbf{h}_{n,m} = (h_{n,m,1}, \dots, h_{n,m,M_t})^T$ denotes the channel coefficient vector between the ET and the m^{th} antenna of the ER related to the n^{th} sub-band, and $\mathbf{w}_n = (w_{n,1}, \dots, w_{n,M_t})^T$ is the complex beamforming vector of the n^{th} sub-band. The latter is such that $\sum_{n=1}^N \|\mathbf{w}_n\|^2 \leq 2P$, where P is the transmit power of the ET and $\|\cdot\|$ denotes the Euclidean norm. The center frequency of sub-band n is $f_n = f_1 + (n-1)\Delta f$, where $\Delta f = B/N$ and B is the total available bandwidth.

A quasi-static flat-fading channel model and block-based WPT is assumed. As such, the wireless channels remain constant during each transmission block of length \mathcal{T} . It is also assumed that the channel-state information is available at the ET at the beginning of each WPT block. The MIMO channel random matrix $\mathbf{H}_n = (\mathbf{h}_{n,1}, \dots, \mathbf{h}_{n,M_r})^T \in \mathbb{C}^{M_r \times M_t}$ for sub-band n can be written $\mathbf{H}_n = \sqrt{G} \tilde{\mathbf{H}}_n$, where G denotes the (local average) large-scale gain, which encompasses the distance-dependent decay, the shadowing effect, and the gains of the antennas, and where $\tilde{\mathbf{H}}_n$ is the normalized channel matrix between ET and ER for sub-band n , written as in [41]:

$$\tilde{\mathbf{H}}_n = \sqrt{\frac{K}{K+1}} \tilde{\mathbf{H}}^{\text{LoS}} + \sqrt{\frac{1}{K+1}} \tilde{\mathbf{H}}_n^{\text{NLoS}}, \quad (3.3)$$

where K is the Rice factor, $\tilde{\mathbf{H}}^{\text{LoS}} = \mathbf{e}_r(\phi_r) \mathbf{e}_t(\phi_t)^H$, with $\mathbf{e}_t(\phi_t)$ and $\mathbf{e}_r(\phi_r)$ being the spatial signatures in the departure direction of LoS (determined by ϕ_t) and in the arrival direction of LoS (determined by ϕ_r) related to the transmit and receive antenna arrays, respectively.⁵ Considering uniform linear arrays at ET and ER, we have

$$\mathbf{e}_x(\phi_x) = \begin{bmatrix} 1 \\ \exp(j2\pi\Delta_x \cos(\phi_x)) \\ \vdots \\ \exp(j2\pi(M_x - 1)\Delta_x \cos(\phi_x)) \end{bmatrix}, \quad x \in \{\text{t}, \text{r}\}, \quad (3.4)$$

⁵Without loss of generality, $\tilde{\mathbf{H}}^{\text{LoS}}$ is assumed to be fixed for all sub-bands.

where Δ_x is the antenna spacing in wavelengths related to $x \in \{t, r\}$ antenna array. For each sub-band $n \in \{1, \dots, N\}$, the elements of the non-LoS (NLoS) component $\tilde{\mathbf{H}}_n^{\text{NLoS}}$ are statistically independent zero-mean unit-variance complex Gaussian random variables.

3.2 Energy Beamforming using Fixed-Coefficient and Bessel-based Formulas

In this section, the two lower-bound formulas will be presented and their corresponding optimization problems will be defined. By solving these problems, the beamforming vectors for optimizing the FC- and BL- modeled ERs will be found.

3.2.1 Fixed-Coefficient Based Design

The received power at the ER can be written as

$$\begin{aligned}
 P_{\text{in}} &= \sum_{m=1}^{M_r} \mathbb{E}\{y_m(t)^2\} \\
 &\stackrel{(a)}{=} \sum_{m=1}^{M_r} \mathbb{E} \left\{ \left(\Re \left\{ \sum_{n=1}^N \mathbf{w}_n^H \mathbf{h}_{n,m} e^{j2\pi f_n t} \right\} \right)^2 \right\} \\
 &\stackrel{(b)}{=} \frac{1}{2} \sum_{m=1}^{M_r} \sum_{n=1}^N |\mathbf{w}_n^H \mathbf{h}_{n,m}|^2 \\
 &= \frac{1}{2} \sum_{n=1}^N \|\mathbf{H}_n^* \mathbf{w}_n\|^2 = \frac{1}{2} \sum_{n=1}^N \text{tr} \left(\mathbf{H}_n^T \mathbf{H}_n^* \mathbf{w}_n \mathbf{w}_n^H \right),
 \end{aligned} \tag{3.5}$$

where (a) leads to (b) by noting that $\Re\{z\} = \frac{1}{2}(z + z^*)$ and by time averaging the resulting terms after raising to the power of 2. In general, the Schottky diode in a rectifier circuit may work in two regions: square-law region, a.k.a. small-signal region, and large-signal region. Over a wide range of input power level P_{in} , the output current i_{out} follows the formula [33]

$$i_{\text{out}} = \kappa \left(\sqrt{P_{\text{in}}} \right)^\delta. \tag{3.6}$$

For low levels of input power at the harvesting device, say below -20 dBm, we have $\delta = 2$. This leads to

$$i_{\text{out}} = \kappa P_{\text{in}}, \quad (3.7)$$

which, in fact, describes the square-law region. In this region, as (3.7) shows, the output current (voltage) is linearly proportional to the input power.⁶ Equivalently, the output DC power is proportional to the square of the input AC power, i.e. $P_{\text{out}} = R_{\text{L}} i_{\text{out}}^2 = R_{\text{L}} \kappa^2 P_{\text{in}}^2$.

In the large-signal region, a significant amount of harmonics and inter-modulation components will appear in the diode current. In this region, the linear small-signal solving methods are not accurate anymore. Non-linear methods like harmonic balance should be applied [42].

In Fig. 3.2, the operational behavior of the rectifier in the two aforementioned regions is illustrated by running simulation of the circuit shown in Fig. 3.3 while using the harmonic balance simulation engine in ADS platform of Keysight Technologies [42]. The input is a single-tone 1 GHz signal, with small and medium power levels of -30 dBm and -10 dBm chosen to account for the square-law and large-signal regions, respectively. As observed in the square-law region, the diode current keeps the sinusoidal shape of the input signal, whereas in the large-signal region the diode current is no more sinusoidal and, thus, produces a good amount of harmonics.

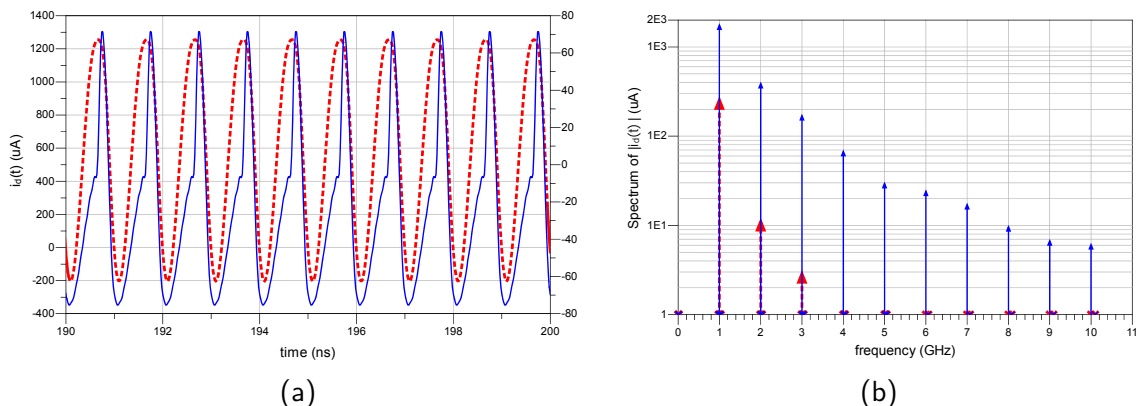


Figure 3.2: (a) Steady-state waveform shapes of $i_d(t)$ and (b) its corresponding spectrum for $P_{\text{in}} = -30$ dBm (dotted red curve) and $P_{\text{in}} = -10$ dBm (solid blue curve). The right Y-axis in (a) corresponds to the dotted red curve.

In order to find the fixed coefficient κ in (3.7), one approach consists of expanding $i_d(t)$ shown in (3.1) into the form of Taylor series expansion around the output DC voltage v_{out} , and then applying

⁶In the open literature, e.g. [7], the FC rectifier modeling is also called linear rectifier model.

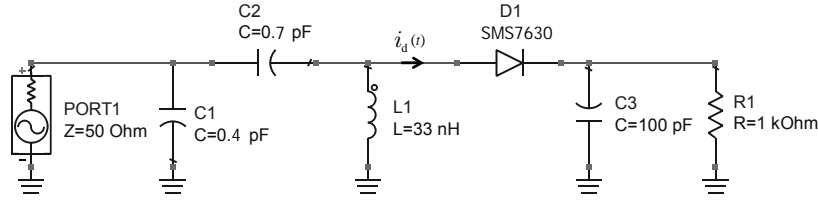


Figure 3.3: The simulation circuit related to Fig. 3.2.

the averaging operator $\mathbb{E}\{\cdot\}$ to obtain the approximated i_{out} [7], as follows:

$$i_{\text{out}} \approx k_0 + \sum_{\substack{\widehat{N}_r \\ r \text{ even}, r \geq 2}} k_r R_{\text{ant}}^{r/2} \mathbb{E}\{y(t)^r\}, \quad (3.8)$$

where \widehat{N}_r is the truncation number, $k_0 = I_s(e^{\frac{-v_{\text{out}}}{\eta v_T}} - 1)$, and $k_r = I_s \frac{e^{\frac{-v_{\text{out}}}{\eta v_T}}}{(\eta v_T)^{r r!}}$ for $r \geq 2$. In the square-law region, which results in voltage levels below the voltage threshold of the diode, i.e. the knee of the characteristic current-voltage (I-V) curve, by ignoring the higher terms ($r > 2$) and solving for i_{out} , we get

$$i_{\text{out}} = \frac{\eta v_T I_s R_{\text{ant}} P_{\text{in}}}{2\eta^2 v_T^2 (\eta v_T + I_s R_L) + I_s R_L R_{\text{ant}} P_{\text{in}}}, \quad (3.9)$$

which, under the condition of

$$P_{\text{in}} \ll \frac{2\eta^2 v_T^2 (\eta v_T + I_s R_L)}{I_s R_L R_{\text{ant}}}, \quad (3.10)$$

leads to the approximation of (3.9) given by

$$i_{\text{out}}^{\text{FC}} = \frac{R_{\text{ant}} I_s}{2\eta v_T (\eta v_T + I_s R_L)} P_{\text{in}} = \kappa P_{\text{in}}, \quad (3.11)$$

where $\kappa = \frac{R_{\text{ant}} I_s}{2\eta v_T (\eta v_T + I_s R_L)}$, and P_{in} is as shown in (3.5). For instance, assuming $\eta = 1.05$, $I_s = 5 \mu\text{A}$, and $v_T = 26 \text{ mV}$, as per the parameters of a typical diode [36], the square-law condition in (3.10) becomes $P_{\text{in}} \ll 190 \mu\text{W}$. Thus, it validates the previously mentioned square-law condition $P_{\text{in}} \leq -20 \text{ dBm}$ ($= 10 \mu\text{W}$). For this typical diode, $i_{\text{out}}^{\text{FC}} = \kappa P_{\text{in}} = 0.14 P_{\text{in}}$.

The resulting output harvested energy during the WPT block time $\mathcal{T} = 1$ is given by

$$Q^{\text{FC}} = R_L \left(i_{\text{out}}^{\text{FC}}\right)^2 = R_L \kappa^2 P_{\text{in}}^2. \quad (3.12)$$

Equation (3.12) suggests that in order to maximize the ER's harvested energy Q^{FC} , one should maximize P_{in} given in (3.5) by solving the following optimization problem:

$$\begin{aligned} \max_{\{\mathbf{w}_n | n \in \{1, \dots, N\}\}} \quad & P_{\text{in}} = \frac{1}{2} \sum_{n=1}^N \|\mathbf{H}_n^* \mathbf{w}_n\|^2 \\ \text{s.t.} \quad & \sum_{n=1}^N \|\mathbf{w}_n\|^2 \leq 2P, \\ & \|\mathbf{w}_n\|^2 \leq 2P_s, \quad n \in \{1, \dots, N\}, \end{aligned} \quad (3.13)$$

where P_s is the per-sub-band power limit. It is reasonably assumed that $P_s \leq P \leq NP_s$, and also that $P = N'P_s$ wherein N' is an integer number ranging from 1 to N .

3.2.2 Bessel-Based Formula Design

Inspired by the formula in [38], which relates the output DC current to the exponential Fourier coefficients of the input waveform at the ER, we have the following lower-bound for the output current:

$$i_{\text{out}}^{\text{BL}} \geq -I_s + \frac{\eta v_{\text{T}}}{R_{\text{L}}} W_0 \left(A_0 \frac{I_s R_{\text{L}}}{\eta v_{\text{T}}} e^{\frac{I_s R_{\text{L}}}{\eta v_{\text{T}}}} \right), \quad (3.14)$$

where $W_0(\cdot)$ is the principal-branch Lambert function and A_0 is given by the following relation:

$$A_0 = \prod_{n=1}^N I_0 \left(\frac{\sqrt{R_{\text{ant}}}}{\eta v_{\text{T}}} |\mathbf{w}_n^H \mathbf{h}_n| \right), \quad (3.15)$$

where $I_0(\cdot)$ is the first-kind zero-order modified Bessel function and $\mathbf{h}_n = \sum_{m=1}^{M_{\text{r}}} \mathbf{h}_{n,m}$ with $\mathbf{h}_{n,m}$ being the channel vector from the M_{t} transmit antennas to the m^{th} receive antenna and on the n^{th} sub-band as defined earlier. Thus, the BL formula is obtained by substituting (3.15) into (3.14).

That is,

$$i_{\text{out}}^{\text{BL}} = -I_s + \frac{\eta v_{\text{T}}}{R_{\text{L}}} W_0 \left(\frac{I_s R_{\text{L}}}{\eta v_{\text{T}}} e^{\frac{I_s R_{\text{L}}}{\eta v_{\text{T}}}} \prod_{n=1}^N I_0 \left(\frac{\sqrt{R_{\text{ant}}}}{\eta v_{\text{T}}} |\mathbf{w}_n^H \mathbf{h}_n| \right) \right). \quad (3.16)$$

Applying (3.16), energy harvested by the ER can be expressed as

$$Q^{\text{BL}} = R_{\text{L}} \left(i_{\text{out}}^{\text{BL}} \right)^2. \quad (3.17)$$

Comparing (3.16) and (3.11), one can quickly spot the difference between them, namely, that the output current in the BL-based formulation depends on the resultant signal level $|\mathbf{w}_n^H \mathbf{h}_n|$ rather than the total received power $\frac{1}{2} \sum_{n=1}^N \|\mathbf{H}_n^* \mathbf{w}_n\|^2$. Once again, to maximize the harvested energy Q^{BL} at the ER, the output current $i_{\text{out}}^{\text{BL}}$ needs to be maximized. Thus, we have the following optimization problem to solve:

$$\begin{aligned} & \max_{\{\mathbf{w}_n | n \in \{1, \dots, N\}\}} i_{\text{out}}^{\text{BL}} \\ & \text{s.t.} \quad \sum_{n=1}^N \|\mathbf{w}_n\|^2 \leq 2P, \\ & \quad \|\mathbf{w}_n\|^2 \leq 2P_s, \quad n \in \{1, \dots, N\}. \end{aligned} \quad (3.18)$$

Since the Lambert function W_0 is a monotonically increasing function, the optimization problem in (3.18) boils down to

$$\begin{aligned} & \max_{\{\mathbf{w}_n | n \in \{1, \dots, N\}\}} \prod_{n=1}^N I_0 \left(\frac{\sqrt{R_{\text{ant}}}}{\eta v_T} |\mathbf{w}_n^H \mathbf{h}_n| \right) \\ & \text{s.t.} \quad \sum_{n=1}^N \|\mathbf{w}_n\|^2 \leq 2P, \\ & \quad \|\mathbf{w}_n\|^2 \leq 2P_s, \quad n \in \{1, \dots, N\}. \end{aligned} \quad (3.19)$$

Both optimization problems, (3.13) and (3.19), are non-convex. We solve the problems by running extensive interior-point algorithms with many randomly chosen initial values, and choosing the maximum value of the entire set.

3.3 Numerical Results and Discussion

A multi-band MIMO WPT system is simulated while applying the FC and the BL formulas shown in (3.11) and (3.16), and solving their respective optimization problems shown in (3.13) and (3.19). The accuracy of the two formulas is compared for different system settings. The plots are the averaged result of 1000 simulation runs. The main simulation parameters are presented in Table 3.1.

First, Fig. 3.4 compares the accuracy of the FC and BL formulas against each other in representing the amount of output DC current, as a function of the number of tones for several values of the number of ET antennas. The number of ER antennas is fixed to $M_r = 2$. In both design

Table 3.1: Simulations Setting

Parameter	Value	Description
P	30 dBm	ET transmit power
P_s	20 dBm	Max. transmit power per sub-band
R_L	1 k Ω	ER load resistance
R_{ant}	50 Ω	ER antenna resistance
I_s	5 μ A	ER diode saturation current
v_T	26 mV	Thermal voltage of the ER diode at room temperature
η	1.05	ER diode ideality factor
K	1	Rice factor
N	{1, 2, 4, 8, 16}	Number of sub-bands (tones)
M_t	{4, 8, 16}	Number of ET antennas
M_r	{1, 2, 4}	Number of ER antennas
ϕ_t	$\pi/2$	Direction-of-Departure of the ET signal
ϕ_r	$\pi/2$	Direction-of-Arrival of the ER signal
Δ_t	1/2	Transmit antenna spacing in wavelength
Δ_r	1/2	Receive antenna spacing in wavelength
G	-60 dB	Average power gain of each channel link

scenarios, FC and BL, the output current increases when the number of tones increases. In the FC plots, there is a mere difference between them in terms of the number of transmit antennas. In the BL curves, on the other hand, the output current increases tremendously with the number of transmit antennas. Also, comparing the results, one can easily conclude that the BL formula is more suitable to be applied in the analysis and design since it leads to higher values of output DC currents, which means that it provides a much tighter lower bound on the output DC current. In fact, the difference between the BL and FC designs becomes much more noticeable as the number of tones and/or the number of transmit antennas increases.

Figure 3.5 provides comparisons in terms of the number of tones and the number of ER antennas. The number of antennas at the ET is fixed to $M_t = 4$. As observed, the output current increases when increasing the number of tones in both design cases, which validates the fact that using multi-tone waveforms has the potential to increase the end-to-end efficiency of the WPT. Plots pertaining to both the FC design and the BL design increase monotonically in terms of the number of tones and the number of antennas at the harvesting device.

The comparative results shown in Fig. 3.4 and Fig. 3.5 confirm that the BL formula is a much better approximation to be applied in the analysis and design of WPT systems, thanks to the fact that it provides a tighter lower-bound on the output DC current compared to the FC formula.

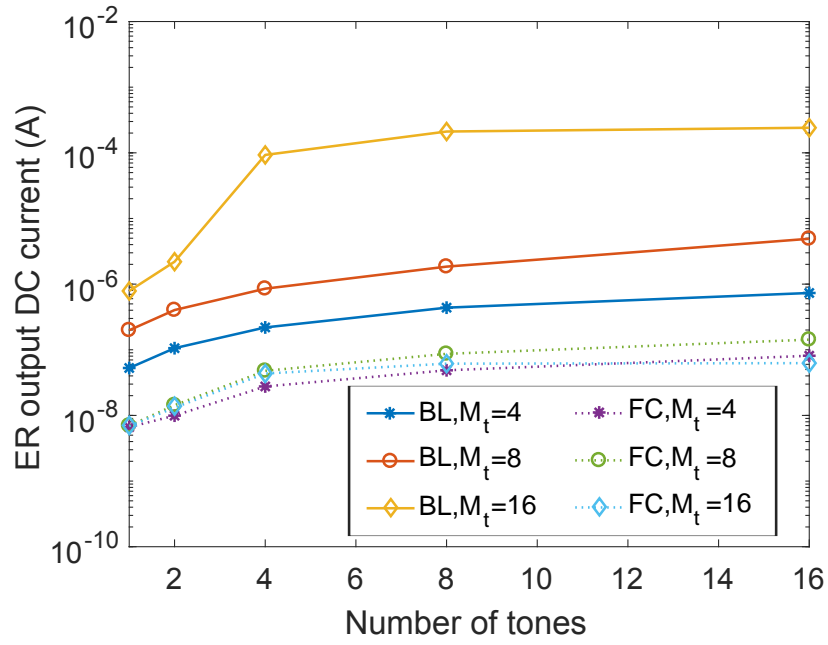


Figure 3.4: The lower bounds on the ER's output DC current when applying the BL and FC formulas for several numbers of transmit antennas (M_t) and fixed number of receive antennas ($M_r = 2$).

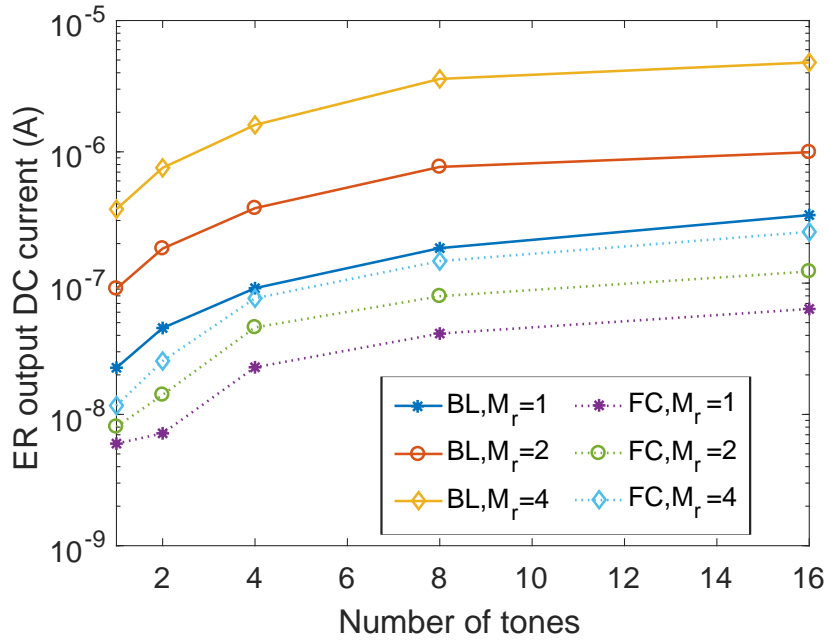


Figure 3.5: The lower bounds on the ER's output DC current when applying the BL and FC formulas for several numbers of receive antennas (M_r) and fixed number of transmit antennas ($M_t = 4$).

3.4 Summary

Considering a multi-channel MIMO wireless power transfer system, we compared the conventional fixed-coefficient rectifier formula (FC), which relates the output DC current of an energy harvester linearly to the incident power, with a more accurate recently proposed Bessel-based lower-bound formula (BL). To design the optimal multi-tone transmit signal, we formulated and solved the optimization problems corresponding to the FC-based and BL-based designs, and showcased the superiority of the latter in providing a tighter lower-bound on the output DC current, and the ensuing harvested power.

Part II

Optimal Scheduling Schemes: Time Sharing vs. Spatial Multiplexing

In this part, we study the time sharing and spatial multiplexing scheduling schemes in satisfying the fairness among ERs in a WPT system. Here, we apply the non-linear model and the formulas obtained in Chapter 2. We apply inequalities related to Lambert and Bessel functions in order to compare analytically these two scheduling techniques. Chapter 4 deals with single-tone transmit signals while Chapter 5 generalizes the concept to the multi-tone transmit signals. Since Chapter 5 is an extension of Chapter 4, some materials of both chapters may overlap.

Chapter 4

Optimal Fair Energy Beamforming in Multi-User MISO Systems¹

In a multi-user WPT context, an important design issue is achieving target fairness in the wireless energy service the devices receive from the corresponding ET. By assuming a fixed power conversion efficiency, regardless of the ER input power levels, the time sharing (TS) and spatial multiplexing (SM) scheduling methods may perform similarly in terms of fairness among users [21]. In practice, however, the efficiency has a non-linear relation with the incident power on ER antennas, which raises the question on how these two scheduling schemes would perform in terms of satisfying fairness among ERs.

Taking the above question as a starting point, and unlike most of the works in which a fixed linear conversion coefficient is assumed for relating the output DC power of an ER to its input power [20, 21], in this chapter, a nonlinear relation is considered and the superiority of TS over SM for block-based WPT over flat-fading channels is demonstrated. The TS and SM scheduling schemes are investigated considering two network operation scenarios: *homogeneous* and *heterogeneous*. Being a particular case of the latter, the former can be viewed as a worst-case scenario for comparing the TS and SM schemes in terms of providing max-min fairness among ERs. In the homogeneous scenario, the optimal SM and TS schemes are the *uniform distribution of power* (UDP) and the

¹A. Bayat and S. Aissa, "Wireless Power Transfer Scheduling: Comparative Study of TDMA and SDMA under Harvesters Nonlinearity," 2019 IEEE Global Communications Conference (GLOBECOM), Waikoloa, HI, USA, 2019, pp. 1-6, doi: 10.1109/GLOBECOM38437.2019.9013202.

uniform distribution of time (UDT), respectively. Considering the non-linear power conversion model, it is proven that transferring the available power at the ET to the ERs in a round-robin TS fashion, i.e. UDT, outperforms sharing the available power through simultaneous equal-gain beams to the ERs in such SM fashion, i.e. UDP. To detail these findings, the following content of the chapter is structured as follows. The multi-user WPT model is described in Section 4.1. The homogeneous and heterogeneous network scenarios and their corresponding power allocation schemes are introduced and analyzed in Section 4.2 and Section 4.3, respectively. Finally, Section 4.4 summarizes the chapter.

4.1 Developing the Wireless Power Transfer Model

The WPT network consists of K single-antenna ERs within the coverage of an ET equipped with M antennas. A block-based wireless energy transmission model over quasi-static flat-fading channels is assumed, where the wireless channels remain constant during each WPT block of length \mathcal{T} . Each channel coefficient vector between ET and ER $_k$ ($k \in \{1, 2, \dots, K\}$) can be written as $\mathbf{h}_k = \sqrt{G_k} \tilde{\mathbf{h}}_k$, where G_k denotes the (local average) large-scale path gain encompassing distance-dependent decay, shadowing effect, and the gains of the individual antennas; and where $\tilde{\mathbf{h}}_k = (\tilde{h}_{k,1}, \tilde{h}_{k,2}, \dots, \tilde{h}_{k,M})^\top$ is the normalized channel fading vector, with the superscript \top denoting transpose operation. Considering a Ricean fading model [41],² the normalized channel vector $\tilde{\mathbf{h}}_k$ can be written as

$$\tilde{\mathbf{h}}_k = \sqrt{\frac{\kappa_k}{\kappa_k + 1}} \tilde{\mathbf{h}}_k^{\text{LoS}} + \sqrt{\frac{1}{\kappa_k + 1}} \tilde{\mathbf{h}}_k^{\text{NLoS}}, \quad (4.1)$$

where κ_k denotes the Rice factor related to ER $_k$, $\tilde{\mathbf{h}}_k^{\text{LoS}} = \mathbf{e}(\phi_k)$ with $\mathbf{e}(\phi_k)$ being the LoS array response from the ET to the k^{th} ER, and ϕ_k is the angle of departure of the LoS component. The array response from the M -element uniform linear array (ULA) of the ET to ER $_k$ is given by $\mathbf{e}(\phi_k) = (1, \exp(j2\pi\Delta \cos(\phi_k)), \dots, \exp(j2\pi\Delta(M-1) \cos(\phi_k)))^\top$, where Δ is the ET antenna spacing in wavelengths. The non-LoS term $\tilde{\mathbf{h}}_k^{\text{NLoS}}$ is an $M \times 1$ vector, the elements of which are circularly symmetric complex Gaussian (CSCG) random variables with unit variance. It is noted that $\kappa_k = 0$ results in a Rayleigh fading channel model between the ET and ER $_k$.

²WPT is more practical in environments with a line-of-sight (LoS) between the ET and the ERs.

Ignoring the additive Gaussian noise at the receiver,³ and assuming transmission of an unmodulated signal, the received signal of the k^{th} ER is given by

$$y_k(t) = \Re \left\{ \mathbf{w}^T \mathbf{h}_k e^{j2\pi ft} \right\}, \quad (4.2)$$

where $\mathbf{w} = (w_1, \dots, w_M)^T$ is the complex beamforming vector with $\|\mathbf{w}\|^2 \leq 2P$ wherein P is the ET transmit power and $\|\cdot\|$ denotes the Euclidean norm, and where f is the frequency of the transmit tone.

Consider the typical harvesting circuit shown in Fig. 2.1 where the ER's diode current is given by (2.2). $v_T \approx 26$ mV in (2.2) is approximately 26 mV at room temperature. Unless otherwise stated, in the numerical examples that will be provided we assume $\eta = 1.05$, $I_s = 5 \mu\text{A}$, and $v_T = 26$ mV as per a typical diode parameters [36].

The ER antenna is assumed lossless and modeled as a voltage source $v_s(t)$ in series with a pure resistive impedance $R_{\text{ant}} = 50 \Omega$ as illustrated in Fig. 3.1. Again, we assume that the LC matching network in Fig. 3.1 matches *losslessly* the receive antenna signal to the input of the diode, i.e. $R_{\text{in}} = R_{\text{ant}}$ and that $\lambda = 1$. In order to have a meaningful comparison between the TS and SM allocation policies, it is assumed that all the ER devices are of the same structure. Therefore, for a typical ER $_k$ with incident signal $v_{\text{in}}(t)$, the average received power is $\mathbb{E}\{|y_k(t)|^2\} = \mathbb{E}\left\{\frac{|v_{\text{in}}(t)|^2}{R_{\text{ant}}}\right\}$, where $\mathbb{E}\{\cdot\}$ denotes the averaging operator. Thus, noting that $v_d(t) = v_{\text{in}}(t) - v_{\text{out}}$ where $v_{\text{out}} = i_{\text{out}}R_L$ is the output DC voltage, we can write the output DC current of ER $_k$ as follows:

$$\begin{aligned} i_{\text{out},k} &= \mathbb{E}\{i_d(t)\} = \mathbb{E}\left\{I_s \left(e^{\frac{a_k \sqrt{R_{\text{ant}}} \cos(2\pi ft + \theta_k) - v_{\text{out}}}{\eta v_T}} - 1 \right)\right\} \\ &= \frac{I_s e^{-\frac{v_{\text{out}}}{\eta v_T}}}{2\pi} \int_0^{2\pi} e^{\frac{a_k \sqrt{R_{\text{ant}}}}{\eta v_T} \cos(2\pi ft + \theta_k)} d(2\pi ft + \theta_k) - I_s \\ &= I_s e^{-\frac{i_{\text{out}} R_L}{\eta v_T}} I_0 \left(\frac{a_k \sqrt{R_{\text{ant}}}}{\eta v_T} \right) - I_s, \end{aligned} \quad (4.3)$$

where θ_k is the angle of $\mathbf{h}_k^T \mathbf{w}$, $a_k = |\mathbf{h}_k^T \mathbf{w}|$, and $I_0(x) = \frac{1}{\pi} \int_0^\pi e^{\pm x \cos(\theta)} d\theta$ is the zero-order modified Bessel function of the first kind. Interesting to note from (4.3) is that the output current of each ER $_k$ is independent of θ_k .

³Practically, the received signal power in WPT systems is much greater than the noise floor.

4.2 Homogeneous Network: Time-Sharing versus Spatial-Multiplexing

In this section, the allocation schemes UDT and UDP are compared for the homogeneous network scenario. In this case, the channel power gains of all ERs, which are assumed to be distributed sparsely and far-apart from each other with regard to the beamwidth of the ET antenna array, are assumed the same. The homogeneous network setup can be seen as a worst-case scenario for the heterogeneous network. Hence, the homogeneous scenario is first tackled to compare the TS and SM allocation schemes. Notably, it will be proved that TS performs better than SM when considering the max-min fairness criterion. In fact, under such criterion, the harvested energy by each ER during each WPT block duration \mathcal{T} , for both the TS and SM schemes, will reach its maximum if the channel gains of ERs are all equal to the largest channel power gain in the network, i.e. $\|\mathbf{h}_k\|^2 = \|\mathbf{h}_v\|^2$ for $k, v \in \{1, 2, \dots, K\}$.

In the UDT scheme, all the transmit power P is directed by the ET to the desired ER for a duration of \mathcal{T}/K . For the UDP scheme, it is assumed that the ET uniformly distributes its transmit power P in its equal-width beams so that each ER receives the same amount of energy all the time. For both allocation schemes, the ER devices are assumed to be distributed much farther than the beam-width of the ET antenna array (cf. Fig. 4.1).

Shortly, it will be proved in Theorem 1 that when the non-linearity of rectifiers is taken into account, then under the max-min fairness criterion, the UDT scheme is superior to the UDP scheme.

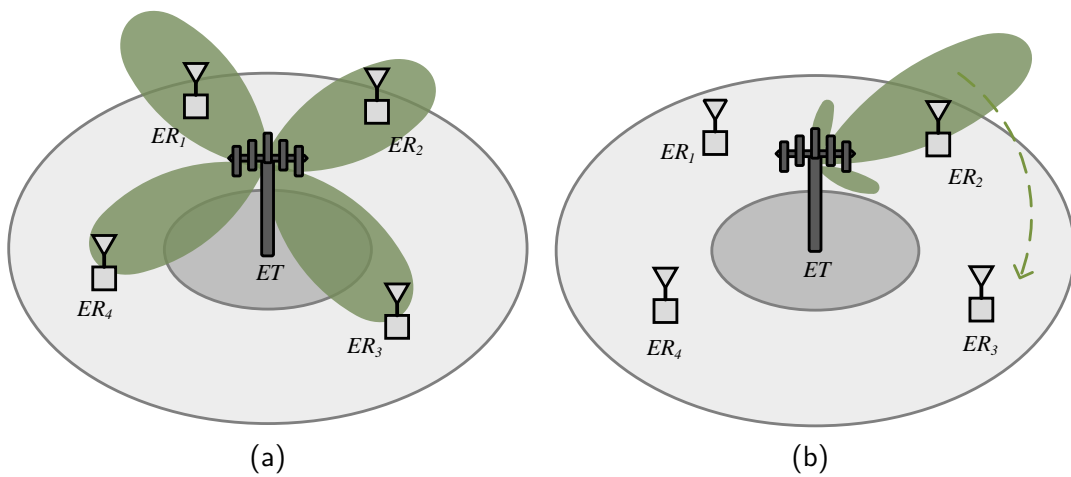


Figure 4.1: Illustration of (a) UDP and (b) UDT schemes for $K = 4$ devices.

Let us look back at the expression of the output DC current shown in (4.3). Since the Bessel function $I_0(x)$ is an increasing function for $x \geq 0$, i_{out} is maximized if and only if $a = |\mathbf{h}^\top \mathbf{w}|$ is maximized.⁴ This means that the optimal beamforming vector for the UDT and UDP schemes are $\mathbf{w}_{\text{UDT}}^* = \sqrt{2P}\mathbf{h}^*/\|\mathbf{h}\|$ and $\mathbf{w}_{\text{UDP}}^* = \sqrt{2P/K}\mathbf{h}^*/\|\mathbf{h}\|$, respectively. Therefore, i_{out} can be written as,⁵

$$i_{\text{out}}^{\text{UDT}} = \frac{1}{\sqrt{K}} \mathcal{Z}_0 \left(I_s e^{-\frac{i_x R_L}{\eta v_T}} I_0 \left(\frac{\|\mathbf{h}\| \sqrt{2P R_{\text{ant}}}}{\eta v_T} \right) - I_s - i_x \right), \quad (4.4a)$$

$$i_{\text{out}}^{\text{UDP}} = \mathcal{Z}_0 \left(I_s e^{-\frac{i_x R_L}{\eta v_T}} I_0 \left(\frac{\|\mathbf{h}\| \sqrt{2P R_{\text{ant}}/K}}{\eta v_T} \right) - I_s - i_x \right), \quad (4.4b)$$

for the UDT and UDP schemes, respectively, where the operator $\mathcal{Z}_0(\cdot)$ outputs the root of its argument function in terms of i_x . By solving the equations in (4.4), we obtain

$$i_{\text{out}}^{\text{UDT}} = \frac{1}{\alpha \sqrt{K}} W_0 \left(\alpha I_s I_0(\beta) e^{\alpha I_s} \right) - \frac{I_s}{\sqrt{K}}, \quad (4.5a)$$

$$i_{\text{out}}^{\text{UDP}} = \frac{1}{\alpha} W_0 \left(\alpha I_s I_0(\beta/\sqrt{K}) e^{\alpha I_s} \right) - I_s, \quad (4.5b)$$

where $\alpha = \frac{R_L}{\eta v_T}$, $\beta = \frac{\sqrt{2P R_{\text{ant}}}}{\eta v_T} \|\mathbf{h}\|$, and $W_0(\cdot)$ is the principal branch of the Lambert function [43]. The details are provided in Appendix A.1.

Theorem 1. According to (4.5), $i_{\text{out}}^{\text{UDT}} > i_{\text{out}}^{\text{UDP}}$ for any $K > 1$, $\alpha > 0$, $\beta > 0$, and $I_s > 0$.

Proof. The proof is provided in Appendix A.2. ■

Figure 4.2a compares the harvested energy when using the UDT and UDP techniques for the following typical setup: $R_L = 1 \text{ k}\Omega$, $R_{\text{ant}} = 50 \text{ }\Omega$, the Rice factor $\kappa = \infty$, $G = -50 \text{ dB}$, and $M = 4$. The figure reveals the superiority of UDT over UDP. As observed, the performance gap between these two allocation schemes stands out as the ET transmit power P increases while the number of ERs in the system is fixed; and also as the number of ERs increases while the transmit power remains the same.

⁴The subscript ‘ k ’ is dropped since channels are assumed to undergo equal coefficients in the homogeneous setting.

⁵Without loss of generality, it is assumed that $\mathcal{T} = 1$. Thus, the words ‘power’ and ‘energy’ pertain to the same value for a transmission block.

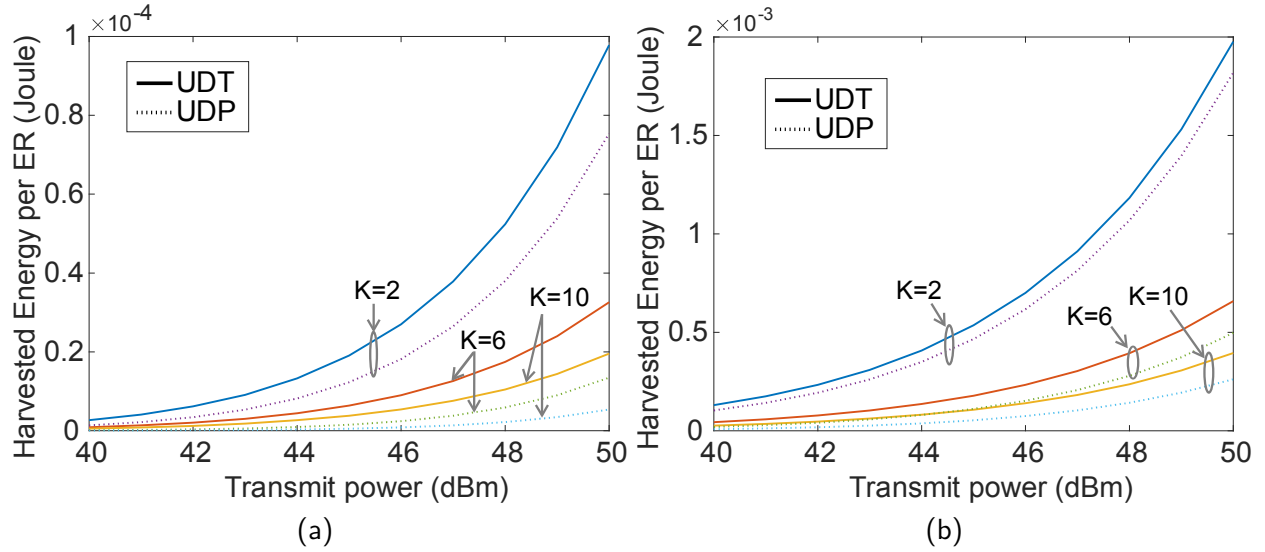


Figure 4.2: The harvested energy per ER during the transmission block \mathcal{T} for (a) $M = 4$ and (b) $M = 50$.

Figure 4.2b is generated using the same setting as that in Fig. 4.2a except for the number of antennas which has increased largely from $M = 4$ to $M = 50$. In this case, the ET has a massive number of antennas. Compared to Fig. 4.2a, the harvested energy has tremendously increased due to the larger diversity gain as a result of employing massive antenna arrays at the ET. Also, it is seen that as M increases the performance gap between UDT and UDP becomes smaller.

4.3 Heterogeneous Network:

Time-Sharing versus Spatial-Multiplexing

After proving that the UDT scheme is superior to the UDP under the max-min fairness criterion for the homogeneous network, in this section, the more general heterogeneous scenario is considered. Here, extensive Monte Carlo simulations for different network operation settings and parameters will be run to check the validity of Theorem 1. The heterogeneous network is, in fact, a practical network scenario in which the assumption of equal channel gains for the ERs does not necessarily hold, and the ERs can be distributed freely in the network. Thus, several ERs may undergo the same beam of the ET antenna array.

Energy harvested by ER_k in the network, $k \in \{1, \dots, K\}$, during each WPT block, can be written as

$$Q_k^{\text{TS}} = \tau_k R_L \left(i_{\text{out},k}^{\text{TS}} \right)^2 + R_L \sum_{\substack{v=1 \\ v \neq k}}^K \tau_v \left(i_{\text{out},v}^{\text{TS}} \right)^2, \quad (4.6a)$$

$$Q_k^{\text{SM}} = R_L \left(i_{\text{out},k}^{\text{SM}} \right)^2, \quad (4.6b)$$

for the TS and SM schemes, respectively, where $\boldsymbol{\tau} = (\tau_1, \dots, \tau_K)^\top$ is the time sharing vector with $\sum_{k=1}^K \tau_k = 1$ and τ_k being the portion of the transmission block dedicated for the WPT to ER_k. The summation term in (4.6a) is the amount of energy that ER_k collects while the ET is serving other ERs; it is in fact the *beneficial interference* in energy harvesting systems. Similar to (4.5a), $i_{\text{out},k}^{\text{TS}}$ and $i_{\text{out},v}^{\text{TS}}$ in (4.6a) can be written as follows:

$$i_{\text{out},k}^{\text{TS}} = \frac{1}{\alpha} W_0 \left(\alpha I_s I_0 \left(\frac{\|\mathbf{h}_k\| \sqrt{2PR_{\text{ant}}}}{\eta v_T} \right) e^{\alpha I_s} \right) - \frac{I_s}{\alpha}, \quad (4.7a)$$

$$i_{\text{out},v}^{\text{TS}} = \frac{1}{\alpha} W_0 \left(\alpha I_s I_0 \left(\frac{|\mathbf{h}_k^H \mathbf{h}_v| \sqrt{2PR_{\text{ant}}}}{\|\mathbf{h}_k\| \eta v_T} \right) e^{\alpha I_s} \right) - \frac{I_s}{\alpha}, \quad (4.7b)$$

where the superscript H denotes the conjugate transpose. Also, the current $i_{\text{out},k}^{\text{SM}}$ in (4.6b) can be expressed as

$$i_{\text{out},k}^{\text{SM}} = \frac{1}{\alpha} W_0 \left(\alpha I_s I_0 \left(\frac{|\mathbf{w}^H \mathbf{h}_k| \sqrt{R_{\text{ant}}}}{\eta v_T} \right) e^{\alpha I_s} \right) - I_s. \quad (4.8)$$

In order to find the optimal time sharing vector $\boldsymbol{\tau}^*$ for the TS scheduling and the optimal beamforming vector \mathbf{w}^* for the SM method under the max-min fairness criterion, the following optimization problems should be solved. The optimization problem for the TS scheme is

$$\begin{aligned} & \max_{\boldsymbol{\tau}} \min_{k \in \{1, \dots, K\}} Q_k^{\text{TS}} \\ \text{s.t.} \quad & 0 \leq \tau_k, & k \in \{1, \dots, K\}, \\ & \sum_{k=1}^K \tau_k = 1, & k \in \{1, \dots, K\}, \end{aligned} \quad (4.9)$$

and the one for the SM scheme is

$$\begin{aligned} & \max_{\mathbf{w}} \min_{k \in \{1, \dots, K\}} Q_k^{\text{SM}} \\ \text{s.t.} \quad & \|\mathbf{w}\|^2 \leq 2P. \end{aligned} \quad (4.10)$$

The optimization problem in (4.9) is a convex problem and can be solved by standard convex optimization techniques such as CVX [37]. The problem in (4.10) is a non-convex problem which can be solved using an exhaustive search algorithm by trying a large number of random initial points and retaining the optimal value in each iteration. However, a better start point \mathbf{w}_0 can be heuristically found by solving the following disciplined convex optimization problem:

$$\begin{aligned} & \max_{\mathbf{w}_0} \min_{k \in \{1, \dots, K\}} \Re(\mathbf{w}_0^H \mathbf{h}_k) \\ \text{s.t.} \quad & \|\mathbf{w}_0\|^2 \leq 2P, \end{aligned} \quad (4.11)$$

which can be solved by the same CVX tool [37]. In (4.11), $\Re(\mathbf{w}_0^H \mathbf{h}_k)$ is used instead of $|\mathbf{w}_0^H \mathbf{h}_k|^2$ which is the received power on the ER_k antenna, to make the problem convex. By using the optimal \mathbf{w}_0^* as the initial guess for \mathbf{w} in (4.10) and applying the interior-point method, the optimal beamforming vector \mathbf{w}^* can be obtained. The validity of the above heuristic method was checked through extensive simulations.

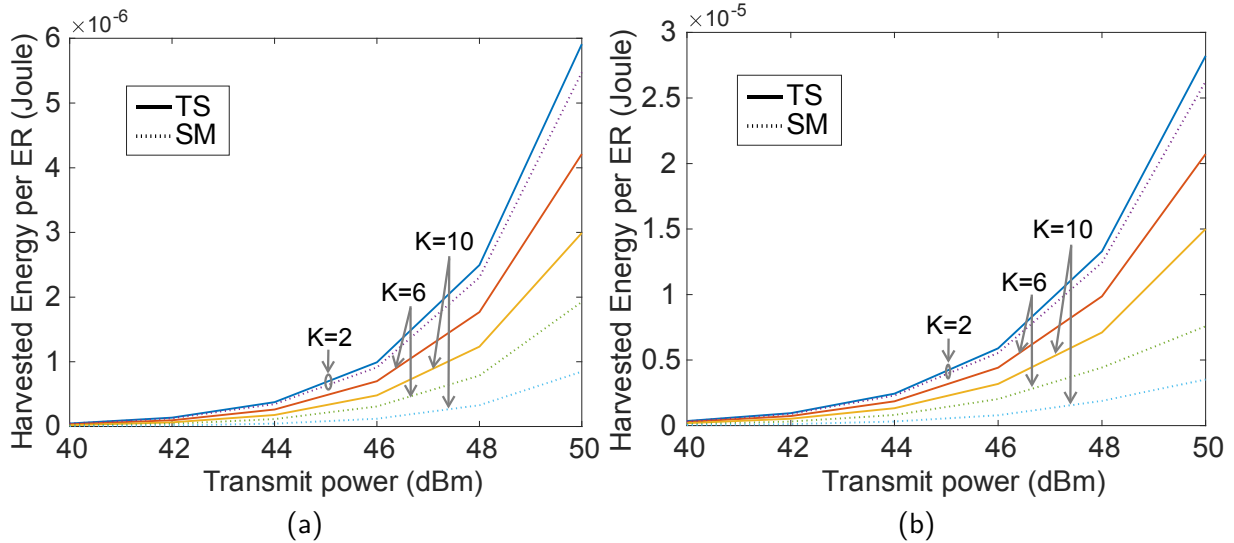


Figure 4.3: The minimum amount of harvested energy per ER for the TS and SM schemes: (a) $M = 4$ and (b) $M = 10$.

The superiority of UDT over UDP in the homogeneous network was already shown through Fig. 4.2a and Fig. 4.2b in Section 4.2. Now, using Monte Carlo simulations, we compare the performance of the TS and SM schemes for the heterogeneous network scenario. The results are demonstrated in Fig. 4.3. All the simulations are averaged over 1000 runs with the following settings. For $k \in \{1, \dots, K\}$, G_k (in dB) and ϕ_k (in radians) are randomly chosen from uniform distributions $\mathcal{U}(-60, -40)$ and $\mathcal{U}(0, 2\pi)$, respectively. The Rice factor $K_k = 1$ for all ERs, $R_L = 1 \text{ k}\Omega$, and $R_{\text{ant}} = 50 \Omega$. A ULA with half-wavelength antenna spacing is assumed for the ET.

Comparing the TS and SM schemes in Fig. 4.3, the minimum harvested energy by each ER is plotted in terms of the transmit power P (in dBm) and different numbers of ERs. Fig. 4.3a and Fig. 4.3b are for the cases of $M = 4$ and $M = 10$, respectively. As it is seen, when the number of antennas increases, thanks to an increase in the diversity (power) gain, the harvested energy increases—in this case, from a few μW to a few tens of μW . It is observed that for $P = 40 \text{ dBm}$, all curves fall almost on top of each other. However, as P increases, the TS and SM curves separate from each other. In general, as the number of devices in the network increases, although the minimum amount of harvested energy by each ER decreases, the superiority of TS over SM becomes grosser. For instance, for $P = 50 \text{ dBm}$, i.e. 100 W , and $K = 10$, Fig. 4.3a reveals that the amount of minimum harvested energy by each ER for the SM scheme is about $0.9 \mu\text{W}$ whereas for the TS scheme it is about $3 \mu\text{W}$, i.e. over three times more. As Fig. 4.3b shows, for the larger number of antennas the harvested energy through the SM scheme is about $4 \mu\text{W}$ whereas with the TS scheme it is about $15 \mu\text{W}$, which is around 4 times better. Therefore, the superiority of the TS scheme over the SM scheme under the max-min fairness criterion for multi-user MISO WPT was demonstrated.

4.4 Summary

When the nonlinearity of the energy harvesters circuit is taken into account, time sharing scheduling, i.e., time-division multiple access (TDMA), was proven to perform better than spatial multiplexing, i.e., space-division multiple access (SDMA), in provisioning max-min fairness among devices which are harvesting wireless energy from the serving multiple-antenna energy transmitter in the WPT network.

Chapter 5

Fair Scheduling and Energy Beamforming in Multi-Band WPT Systems¹

Following Chapter 4, here in this chapter, we look for optimal scheduling scheme satisfying max-min fairness criterion for *multi-tone* transmit signals. We will show the superiority of TS over SM for block-based WPT over flat-fading channels for multi-tone scenarios. Again, the TS and SM scheduling schemes are investigated considering two network conditions, *homogeneous* and *heterogeneous*. The particular case of the homogeneous network can be viewed as a worst-case scenario for comparing the two scheduling schemes in terms of providing max-min fairness among ERs. In the homogeneous scenario, the optimal SM and TS schemes are shown to be the *uniform distribution of power* (UDP) and the *uniform distribution of time* (UDT), respectively. Considering the non-linear power conversion model, it is proven that transferring the available power at the ET to the ERs in a round-robin TS fashion, i.e. UDT, outperforms sharing the available power through simultaneous equal-gain beams to the ERs in such SM fashion, i.e. UDP. While that is proven analytically for the homogeneous case, extensive simulations are conducted to confirm the said superiority for the homogeneous scenarios as well. As such, the main contributions of this work are twofold: First, for the abstract network setting, i.e. homogeneous scenario, we analytically prove that when the non-

¹A. Bayat and S. Aïssa, "Fair Scheduling of Wireless Energy to Nonlinear Energy Harvesters," IEEE Transactions on Green Communications and Networking—submitted, 2020

linearity model of rectifiers in the harvesting circuits is taken into account, then the TS scheduling outperforms SM under the max-min fairness criteria for multi-tone transmit signal. The proofs are first provided for the homogeneous scenario, then, inspired by the analytical way of reasoning carried out in the homogeneous scenario, we validate the claim for the heterogeneous scenario through extensive runs of simulations for different network settings. Collectively, the results here provide important guidelines for the design of fairness-provisioning scheduling schemes in WPT systems.

To detail these findings, the following content of the chapter is structured as follows. The multi-user multi-tone WPT model is described in Section 5.1. The homogeneous and heterogeneous network scenarios and their corresponding power allocation schemes are introduced and analyzed in Section 5.2 and Section 5.3, respectively. Finally, Section 5.4 summarizes the chapter.

5.1 The Wireless Power Transfer Network Models

The wireless power network consists of K single-antenna ERs within the coverage of an ET equipped with M antennas and having access to B Hz of bandwidth which is divided into N equi-bandwidth sub-bands such that $B = N\Delta f$. The goal of the ET is to maximize the harvested energy of the ER with the least level of harvested energy during each power transmission period \mathcal{T} by finding the optimal beamforming vectors based on the acquired channel side information (CSI) from the ERs.²

5.1.1 The Wireless Power Transfer Model

Block-based wireless energy transmission over quasi-static flat-fading channels is assumed, where the radio channels remain constant during each WPT block of length \mathcal{T} . Each channel coefficient vector between the ET and ER $_k$ ($k \in \{1, 2, \dots, K\}$) can be formulated as $\mathbf{h}_{n,k} = \sqrt{G_k} \tilde{\mathbf{h}}_{n,k}$, where G_k denotes the (local average) large-scale path gain encompassing the distance-dependent decay, the shadowing effect, and the gains of the individual antennas which are assumed the same all over the entire bandwidth B ; and where $\tilde{\mathbf{h}}_{n,k} = (\tilde{h}_{n,k,1}, \tilde{h}_{n,k,2}, \dots, \tilde{h}_{n,k,M})^\top$ is the normalized channel fading

²To estimate the CSI, one can consider either one-way training by assuming channel reciprocity, or two-way training which requires each receiver to perform channel estimation followed by feedback to the ET, which in turn would consume additional energy. In practice, there exists a design tradeoff especially for the ERs: higher accuracy for both the estimation and the feedback reporting may lead to higher harvested energy due to the transmit beamforming gain, but also induces higher energy consumption that can even offset the harvested energy gain [44]. For simplicity, this work assumes that such energy consumption at ERs is negligible compared to their harvested energy, and that the training time is negligible compared to the WPT period.

vector, with the superscript \top denoting transpose operation. Considering Ricean fading [41],³ the normalized channel vector $\tilde{\mathbf{h}}_{n,k}$ for sub-band n can be written as

$$\tilde{\mathbf{h}}_{n,k} = \sqrt{\frac{\kappa_k}{\kappa_k + 1}} \tilde{\mathbf{h}}_{n,k}^{\text{LoS}} + \sqrt{\frac{1}{\kappa_k + 1}} \tilde{\mathbf{h}}_n^{\text{NLoS}}, \quad (5.1)$$

where κ_k denotes the Rice factor related to ER_k and assumed to be fixed for all sub-bands, $\tilde{\mathbf{h}}_{n,k}^{\text{LoS}} = \mathbf{e}(\phi_k)$ in which $\mathbf{e}(\phi_k)$ denotes the LoS array response from the ET to the k^{th} ER, and ϕ_k is the angle of departure of the LoS component.⁴ The array response from the M -element uniform linear array (ULA) of the ET to ER_k is given by $\mathbf{e}(\phi_k) = (1, \exp(j2\pi\Delta \cos \phi_k), \dots, \exp(j2\pi\Delta(M-1) \cos \phi_k))^\top$, where Δ is the ET antenna spacing in wavelengths. The non-LoS term $\tilde{\mathbf{h}}_n^{\text{NLoS}}$ shown in (5.1) is an $M \times 1$ vector for each sub-band n , the elements of which are circularly symmetric complex Gaussian (CSCG) random variables with unit variance. It is noted that $\kappa_k = 0$ results in a Rayleigh fading channel model between the ET and each ER_k .

Ignoring the additive Gaussian noise at the receiver,⁵ and assuming transmission of an unmodulated signal, the received signal of the k^{th} ER can be expressed as

$$y_k(t) = \sum_{n=1}^N \Re \left\{ \mathbf{w}_n^\top \tilde{\mathbf{h}}_{n,k} e^{j2\pi f_n t} \right\}, \quad (5.2)$$

where $\mathbf{w}_n = (w_{n,1}, \dots, w_{n,M})^\top$ is the complex beamforming vector for sub-band n and we have $\sum_{n=1}^N \|\mathbf{w}_n\|^2 \leq 2P$ wherein P is the ET transmit power and $\|\cdot\|$ denotes the Euclidean norm, and where f_n is the frequency of the n^{th} sub-band.

Consider the typical harvesting circuit shown in Fig. 2.1 and the ER's diode current given by (2.2). Unless otherwise stated, typical diode parameters will be considered later in the numerical examples, namely, $\eta = 1.05$, $I_s = 5 \mu\text{A}$, and $v_T = 26 \text{ mV}$ [36].

The ER antenna is assumed lossless and modeled as a voltage source $v_s(t)$ in series with a pure resistive impedance $R_{\text{ant}} = 50 \Omega$ as illustrated in Fig. 2.1. The LC matching network in Fig. 2.1 is assumed to match *losslessly* the received antenna signal to the input of the diode, i.e., $R_{\text{in}} = R_{\text{ant}}$ and $\lambda = 1$. Again, in order to have a meaningful comparison between the TS and SM allocation policies, it is assumed that all the ER devices are of the same structure. Therefore, for a typical ER_k

³WPT is generally more practical in environments with line-of-sight (LoS) between the ET and the ERs.

⁴Without loss of generality, it is assumed that the LoS component is the same for all sub-bands.

⁵Practically, the received signal power in WPT systems is much greater than the noise floor.

with incident signal $v_{\text{in},k}(t)$, the average received power is $\mathbb{E}\{|y_k(t)|^2\} = \mathbb{E}\left\{\frac{|v_{\text{in},k}(t)|^2}{R_{\text{ant}}}\right\}$, where $\mathbb{E}\{\cdot\}$ denotes the averaging operator. Thus, noting that $v_{\text{d},k}(t) = v_{\text{in},k}(t) - v_{\text{out},k}$, for any $k \in \{1, \dots, K\}$, where $v_{\text{out},k} = i_{\text{out},k}R_{\text{L}}$ is the output DC voltage, we can write the output DC current of ER_k as follows:

$$\begin{aligned} i_{\text{out},k} &= \mathbb{E}\{i_{\text{d},k}(t)\} \\ &= \mathbb{E}\left\{I_{\text{S}} e^{\sum_{n=1}^N \alpha_{n,k} \cos(2\pi f_n t + \theta_{n,k}) - v_{\text{out},k}}\right\} - I_{\text{S}} \\ &= \frac{I_{\text{S}} e^{-\frac{v_{\text{out},k}}{\eta v_{\text{T}}}}}{T_0} \int_0^{T_0} e^{\sum_{n=1}^N \alpha_{n,k} \cos(2\pi f_n t + \theta_{n,k})} dt - I_{\text{S}} \\ &= \frac{I_{\text{S}} e^{-\frac{i_{\text{out},k} R_{\text{L}}}{\eta v_{\text{T}}}}}{2\pi} \int_0^{2\pi} e^{\sum_{n=1}^N \alpha_{n,k} \cos(L_n \vartheta + \theta_{n,k})} d\vartheta - I_{\text{S}}, \end{aligned} \quad (5.3)$$

where $\theta_{n,k} = \angle \mathbf{w}_n^{\text{T}} \mathbf{h}_{n,k}$ is the phase of $\angle \mathbf{w}_n^{\text{T}} \mathbf{h}_{n,k}$; $\alpha_{n,k} = a_{n,k} \frac{\sqrt{\lambda R_{\text{ant}}}}{\eta v_{\text{T}}}$ where $a_{n,k} = |\mathbf{w}_n^{\text{T}} \mathbf{h}_{n,k}|$; and $L_n = N_0 + n - 1$ by assuming the first channel frequency f_1 to be an integer multiple of Δf , i.e. $f_1 = N_0 \Delta f$; hence, $T_0 = \frac{1}{\Delta f}$ is the period of the input signal.

Starting from (5.3), a closed-form lower-bound expression for the DC output current can be obtained [38]. The output DC current for ER_k can then be formulated as

$$i_{\text{out},k} = I_{\text{S}} e^{-\frac{i_{\text{out},k} R_{\text{L}}}{\eta v_{\text{T}}}} A_0(\boldsymbol{\alpha}_k) - I_{\text{S}}, \quad (5.4)$$

where $\boldsymbol{\alpha}_k = (\alpha_{1,k}, \dots, \alpha_{N,k})^{\text{T}}$, and we have

$$A_0(\boldsymbol{\alpha}_k) = \prod_{n=1}^N I_0(\alpha_{n,k}). \quad (5.5)$$

Using Lambert functions as shown in Appendix A.1, the output current in (5.4) can be obtained as follows

$$i_{\text{out},k} = -I_{\text{S}} + \frac{1}{\mu} W_0\left(A_0(\boldsymbol{\alpha}_k) \mu I_{\text{S}} e^{\mu I_{\text{S}}}\right), \quad (5.6)$$

where $\mu = \frac{R_{\text{L}}}{\eta v_{\text{T}}}$ and $W_0(\cdot)$ is the principal branch of the Lambert function [43].

5.2 Homogeneous Network: Time-Sharing versus Spatial-Multiplexing

In this section, the allocation schemes UDT and UDP are compared for the homogeneous network scenario. In this case, the channel power gains of all ERs, which are assumed to be distributed sparsely and far-apart from each other with regard to the beamwidth of the ET antenna array, are assumed the same in all the N sub-bands. The homogeneous network setup can be seen as a worst-case scenario for the heterogeneous network. Hence, the homogeneous scenario is first tackled to compare the TS and SM allocation schemes. Notably, it will be proven that TS performs better than SM when considering the max-min fairness criterion. In fact, under such criterion, the harvested energy by each ER during each WPT block duration \mathcal{T} , for both the TS and SM schemes, will reach its maximum if the channel gains of ERs are all equal to the largest channel power gain in the network, i.e. $\|\mathbf{h}_{n,k}\|^2 = \|\mathbf{h}_{n,k}\|^2$ for $u, v \in \{1, 2, \dots, K\}$ and $n \in \{1, \dots, N\}$.

In the UDT scheme, all the ET power budget P is directed to the desired ER for a duration of \mathcal{T}/K . For the UDP scheme, the ET uniformly distributes its transmit power P in its equal-width beams so that each ER receives the same amount of energy all the time. For both power allocation schemes, the harvesting devices are assumed to be distributed much farther than the beam-width of the ET antenna array.

5.2.1 Homogeneous Network

For the homogeneous case, since all ERs experience the same channel coefficient, although well apart from each other, the optimal beamforming weights for all ERs are the same. In this case, the output DC currents for the UDT and UDP schemes become:

$$i_{\text{out}}^{\text{UDT}} = \frac{1}{\mu\sqrt{K}} W_0 \left(\mu I_s A_0(\boldsymbol{\alpha}) e^{\mu I_s} \right) - \frac{I_s}{\sqrt{K}}, \quad (5.7a)$$

$$i_{\text{out}}^{\text{UDP}} = \frac{1}{\mu} W_0 \left(\mu I_s A_0(\boldsymbol{\alpha}/\sqrt{K}) e^{\mu I_s} \right) - I_s. \quad (5.7b)$$

Again, since we are in the homogeneous case, the subscript k is dropped from $i_{\text{out},k}^{\text{UDT}}$, $i_{\text{out},k}^{\text{UDP}}$, and $\boldsymbol{\alpha}_k$.

Generalization of the result of Theorem 1 stated in Chapter 4 for the multi-tone scenario homogeneous scenario here is stated in the following theorem.

Theorem 2. According to (5.7), $i_{\text{out}}^{\text{UDT}} > i_{\text{out}}^{\text{UDP}}$ for any $K > 1$, $\mu > 0$, $I_s > 0$, and $\alpha_n > 0$, $n \in \{1, \dots, N\}$.

Proof. The proof is provided in Appendix A.3. ■

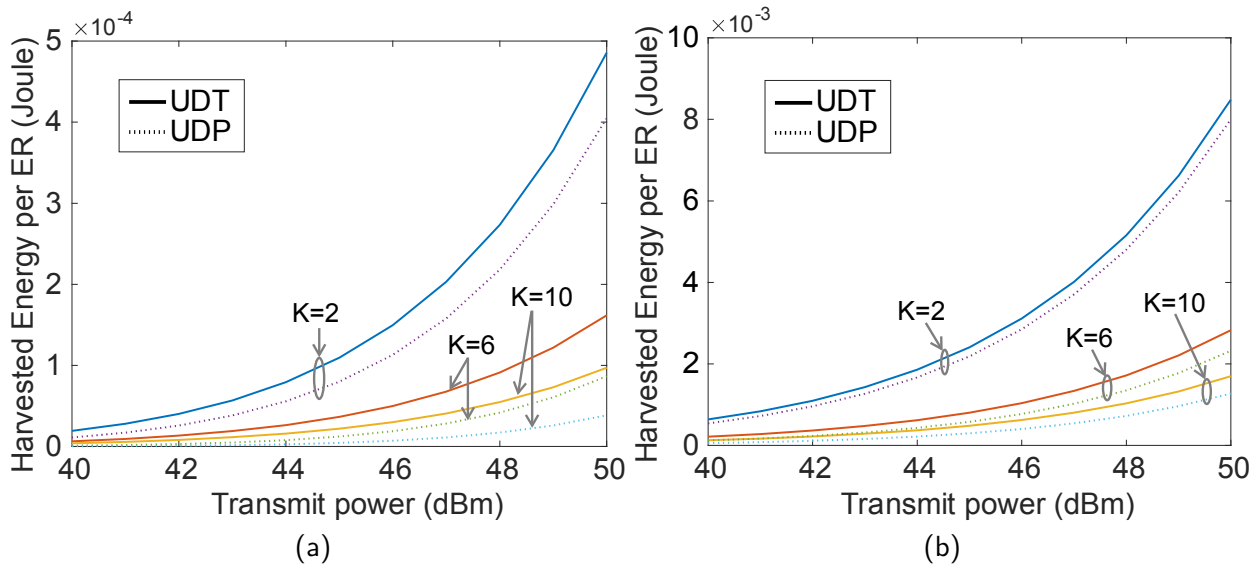


Figure 5.1: The harvested energy per ER during the transmission block \mathcal{T} for $N = 4$ sub-bands: (a) $M = 4$ and (b) $M = 50$.

As we provided validations for Theorem 1 in Fig. 4.2, similarly here we illustratively show the validity of Theorem 2 through Fig. 5.1. The system setup here is the same as the one used in plotting Fig. 4.2 except the number of tones, N , which in Fig. 5.1 is 2 for the multi-tone homogeneous scenario. Fig. 5.1 compares the harvested energy when using the UDT and UDP techniques. As a sample validation of Theorem 2, it is seen that Fig. 5.1a and Fig. 5.1b reveal the superiority of UDT over UDP for $M = 4$ and $M = 50$, respectively. As observed, the performance gap between these two allocation schemes stands out as the ET transmit power P and/or the number of ERs, K , increases. Here, the weights are assumed $\mathbf{w}_n = \sqrt{2P/N} \mathbf{h}_n^* / \|\mathbf{h}_n\|$ for $n \in \{1, \dots, N\}$.

Another interesting observation is when comparing Fig 5.1 related to multi-tone, with Fig. 4.2 related to single-tone. Since the former takes advantage of frequency diversity from using multiple frequencies besides the spacial diversity from using multiple antennas, and importantly, taking

advantage of the nonlinear feature of the rectifiers in ERs in a more effective way, the amount of harvested energy is a few times more than that in the single-tone case.

5.3 Heterogeneous Network: Time-Sharing versus Spatial-Multiplexing

After proving that the UDT scheme is superior to the UDP under the max-min fairness criterion, we tackle the more general heterogeneous scenario. Here, extensive simulations for different network operation settings and parameters will be run to check the validity of Theorem 2. The heterogeneous network is, in fact, a practical network scenario in which the assumption of equal channel gains for the ERs does not necessarily hold, and the ERs can be distributed freely in the network. Thus, several ERs may undergo the same beam of the ET antenna array.

Energy harvested by ER_k in the network, $k \in \{1, \dots, K\}$, during each WPT block, can be written as

$$Q_k^{\text{TS}} = \tau_k R_L \left(i_{\text{out},k}^{\text{TS}} \right)^2 + R_L \sum_{\substack{v=1 \\ v \neq k}}^K \tau_v \left(i_{\text{out},v}^{\text{TS}} \right)^2, \quad (5.8a)$$

$$Q_k^{\text{SM}} = R_L \left(i_{\text{out},k}^{\text{SM}} \right)^2, \quad (5.8b)$$

for the TS and SM schemes, respectively, where $\boldsymbol{\tau} = (\tau_1, \dots, \tau_K)^\top$ is the time sharing vector, with $\sum_{k=1}^K \tau_k = 1$ and τ_k being the portion of the transmission block dedicated for the WPT to ER_k. The summation term in (5.8a) indicates the amount of energy that ER_k collects while the ET is serving other ERs; it is in fact the *beneficial interference* in energy harvesting systems.

In this part, we formulate and solve the optimization problems related to the time-sharing strategy and the simultaneous spatial energy multiplexing. The beamforming vectors should be found for each scenario.

In the case of SM, the ET should find N optimal beamforming vectors corresponding to each sub-band $n \in \{1, \dots, N\}$. In this case, the output current of each ER_k, denoted by $i_{\text{out},k}^{\text{SM}}$, is given by

$$i_{\text{out},k}^{\text{SM}} = \frac{1}{\mu} W_0 \left(\mu I_s \prod_{n=0}^N I_0 \left(\left| \mathbf{w}_n^\top \mathbf{h}_n^{(k)} \right| \frac{\sqrt{2PR_{\text{ant}}}}{\eta v_T} \right) e^{\mu I_s} \right) - I_s. \quad (5.9)$$

The optimal beamforming vectors can be found by solving the following optimization problem

$$\begin{aligned} \tilde{Q}^{\text{SM}} &= \max_{\mathbf{w}_n, n \in \{1, \dots, N\}} \min_{k \in \{1, \dots, K\}} Q_k^{\text{SM}} \\ \text{s.t.} \quad &\sum_{n=1}^N \|\mathbf{w}_n\|^2 \leq 2P, \end{aligned} \quad (5.10)$$

where $Q_k^{\text{SM}} = R_L \left(i_{\text{out},k}^{\text{SM}} \right)^2$, with $i_{\text{out},k}^{\text{SM}}$ defined in (5.9).

In the TS scheduling, if we were to maximize the received power on the targeted ER instead of its output DC current, the optimal beamforming vector for ER_k during each time sharing interval τ_k for any $k \in \{1, \dots, K\}$ would be

$$\mathbf{w}_{n,k}^* = \begin{cases} \sqrt{2P} \mathbf{h}_{n,k}^* / \|\mathbf{h}_{n,k}\|, & n = \bar{n}_k \\ \mathbf{0}, & n \neq \bar{n}_k \end{cases} \quad (5.11)$$

where $\bar{n}_k = \arg \max_n \|\mathbf{h}_{n,k}\|^2$ for $k \in \{1, \dots, K\}$. However, considering the nonlinear modeling, the optimal weights $\mathbf{w}_{n,k}^*$'s and the optimal time sharing vector $\boldsymbol{\tau}$ for the TS scheduling can be found by solving the following optimization problem

$$\begin{aligned} &\max_{\tau_k, \mathbf{w}_{n,k}, k \in \{1, \dots, K\}} \min_{k \in \{1, \dots, K\}} Q_k^{\text{TS}} \\ \text{s.t.} \quad &0 \leq \tau_k, & k \in \{1, \dots, K\}, \\ &\sum_{u=1}^K \tau_u = 1, & k \in \{1, \dots, K\}, \\ &\sum_{n=1}^N \|\mathbf{w}_{n,k}\|^2 \leq 2P, & k \in \{1, \dots, K\}, \end{aligned} \quad (5.12)$$

where Q_k^{TS} is as defined in (5.8a).

Assuming that the channel coefficients do not vary during each scheduling, the optimization problem in (5.12) breaks into two separable problems: first finding the optimal beamforming vectors $\mathbf{w}_{n,k}$'s that maximize the output DC current of each ER_k during the time sharing duration τ_k and, then, finding the optimal time sharing vector $\boldsymbol{\tau}$ which satisfies the max-min fairness criteria, while applying the already obtained optimal beamforming vectors. Thus, we first solve the following

optimization problems for each ER_k to find the corresponding optimal beamforming vector:

$$\begin{aligned} & \max_{\mathbf{w}_{n,k}, n \in \{1, \dots, N\}} Q_k^{\text{SM}} \\ \text{s.t.} \quad & \sum_{n=1}^N \|\mathbf{w}_{n,k}\|^2 \leq 2P. \end{aligned} \quad (5.13)$$

Note that in the first separated problem for the TS scheme we have used Q_k^{SM} . Then, after finding all the maximal beamforming vectors for each time sharing interval τ_k , we seek the fairness-maximizing time sharing intervals solving the next optimization part, i.e.,

$$\begin{aligned} & \max_{\boldsymbol{\tau}} \min_{k \in \{1, \dots, K\}} Q_k^{\text{TS}} \\ \text{s.t.} \quad & 0 \leq \tau_k, \quad k \in \{1, \dots, K\}, \\ & \sum_{k=1}^K \tau_k = 1, \quad k \in \{1, \dots, K\}. \end{aligned} \quad (5.14)$$

The problem in (5.13) is a non-convex problem which can be solved using an exhaustive search algorithm by trying a large number of random initial points and retaining the optimal value in each iteration. However, better starting points $\mathbf{w}_{0,n,k}$ for each ER_k are heuristically found to be the one along with the maximum eigen-vector of the corresponding sub-band as defined in (5.11). Then the well-known *interior point method* can be applied to find the optimal weights. Again, the validity of the above heuristic method has been checked through extensive simulation runs.

Next, the optimal time sharing vector $\boldsymbol{\tau}$ in (5.14) can be obtained via CVX [37].

Assuming the same network setup used in plotting Fig. 4.3 in the previous chapter, except for the number of tones which is assumed to be $N = 2$ here, we compare the two schemes TS and SM, under the max-min criterion in harvesting energy. As seen in Fig. 5.2, the TS scheme is compared with the SM scheme for multi-tone heterogeneous network setting. As it can be seen just following almost the same trend as the heterogeneous single-tone, the TS scheme outperforms the SM scheme while by increasing the number of ERs and/or the ET transmit power the performance gap becomes grosser.

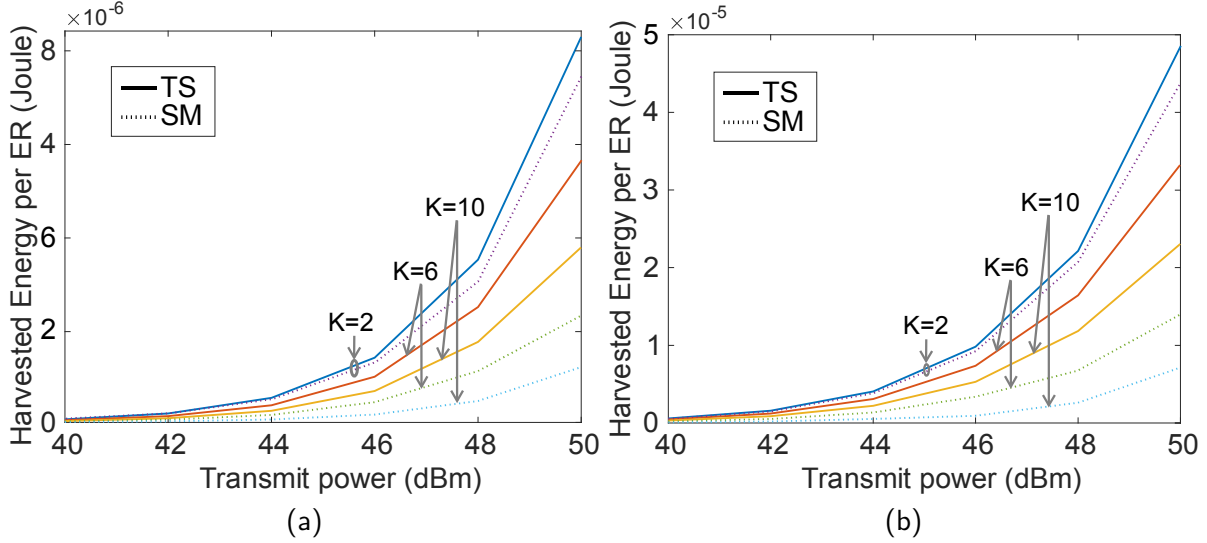


Figure 5.2: The minimum amount of harvested energy per ER for the TS and SM schemes with $N = 2$ sub-bands: (a) $M = 4$ and (b) $M = 10$.

5.4 Summary

Taken into account the inherent nonlinearity of energy harvesting devices in a multi-user MISO wireless power transfer system, the performance of two scheduling schemes, time sharing and spatial multiplexing are compared. The performance metric is the max-min fairness. Two network settings of homogeneous and heterogeneous for multi-tone transmit signals are considered. It is analytically proved for the homogeneous network setting, that the time sharing scheduling scheme outperforms the spatial multiplexing schemes. Through running extensive simulations for the heterogeneous scenarios, that superiority is verified to hold true.

Part III

Auction-Based Wireless Power Transfer

In this part, and also the next part, we study auction-based resource allocation for WPT systems. In this part, we present distributed resource allocation schemes in an auction premise and then analyze its efficiency in terms of "social welfare" and "price of anarchy" by means of game theory.

Chapter 6

Auction-Based Wireless Power Charging—Queuing Theory Approach¹

In this chapter, we analyze a WPT system where ERs send their request following a Poisson process having specific bid values and service demand. Applying both queuing theory and game theory we analyze the proposed distributed algorithm.

The number of energy transmitters (ETs) is usually limited and each wireless power charger (WPC) needs to serve multiple users at the same time. In [28] and [27], the authors studied a power beacon-assisted WPCN using a Stackelberg game. Both games are two-player games and there is no competition between users. In [26], a WPCN is considered where the users send their bids to an access point for receiving energy from it. Under an auction mechanism and using Markov modeling, the authors analyze the convergence of the users' strategy toward the Nash Equilibrium of the game. However, the users' dynamics, in terms of arrival and traffic for instance, and the utility of the WPC have not been considered. In fact, how to control the admission of users by the WPC and allocate the power resource optimally to different users remains a fundamental problem of major importance and requires particular attention.

¹A. Bayat and S. Aissa, "Admission control and power allocation in wireless power charging networks," 2017 IEEE 28th Annual International Symposium on Personal, Indoor, and Mobile Radio Communications (PIMRC), Montreal, QC, 2017, pp. 1-5, doi: 10.1109/PIMRC.2017.8292579.

In this chapter, considering a WPCN, we take into account the arrival rate of the users in the WPC coverage zone, and propose an admission and power allocation scheme which maximizes the WPC utility while keeping the users' utilities up to their satisfaction level. On one hand, the more the users in the WPCN, the higher the payoff of the WPC will be. Therefore, to increase its profit rate, the WPC would tend to delay the service to users by not allocating its maximum power so as to let them accumulate toward its full-accommodation capacity, which in turn may cause a tremendous decrease in the users' utilities. On the other hand, if the WPC allocates its maximum power independently of the number of users, its network will be empty most of the time when the users' arrival rate is low. In this case, users will be the more satisfied. This dilemma necessitates to look for an efficient admission control and power allocation scheme in which both the users and the WPC utilities are considered.

In our proposal, the wireless power charger maintains its service rate by leveraging its power. From the viewpoint of an arriving (external) user, there is an $M/M/N/N$ queue—the same as Erlang's loss system [45]—which we model by a continuous-time Markov chain. From the viewpoint of an admitted (internal) user, there is a game in which the users compete with each other for receiving power from the power charger. We properly formulate the problem as a non-linear constrained optimization, and solve it using an iterative algorithm designed on the basis of the interior-point technique [46].²

6.1 The Wireless Power Charging Network

First off, we use the term 'user' and 'user equipment' (UE) interchangeably, and assume that each user who arrives at the wireless power charging network, or simply say network, sends immediately a charging request to the WPC to get admission. Therefore, 'arrival of a user' and 'sending an admission request' carry the same meaning.

The arrival of users to the WPCN follows a Poisson process with rate λ . Each UE i has a power request of q units that it wishes to be fulfilled by the WPC within a time duration which is exponentially distributed with rate parameter μ . The continuous-time Markov chain (CTMC)

²To the best of the author's knowledge, this is the first time that this important problem is modeled and solved with the joint game- and queuing-theoretic approach proposed in this chapter.

model of the network is shown in Fig. 6.1. Each state number of the CTMC represents the number of UEs in the network.

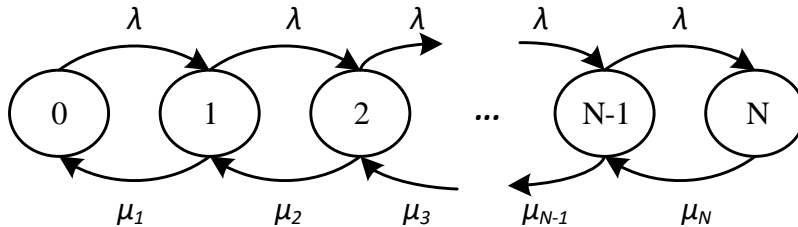


Figure 6.1: The continuous-time Markov chain.

Users admitted by the power charger broadcast their bids in a time-slot schedule which is updated along with the total allocated power whenever a new user is admitted. Therefore, after each bidding period all users compute their new best-response strategies (bids) based on the knowledge of other users' bids, and broadcast them on their dedicated time slots in the next bidding period.

At the WPC side, the maximum power capacity is P_{\max} units of power, and the maximum accommodation capacity is N UEs. The latter is determined based on P_{\max} , and on the minimum possible distance to the users and the minimum possible value for the UE harvested power. We assume that the channel power coefficients between UEs and the WPC do not differ significantly, and hence denoted by h . With fixed power charger stations and stationary devices, this is a plausible assumption.

6.2 Finding the Nash Equilibrium

Now, we formulate the non-cooperative game and find the Nash Equilibrium strategy for it. We define the utility of user $i \in \{1, 2, \dots, n\}$ in state $n \in \{1, 2, \dots, N\}$ by

$$u_{i,n}(s_{i,n}, s_{-i,n}) = \frac{y_{i,n}}{q} - \frac{\nu w_n s_{i,n}^2}{\sum_{j=1}^n s_{j,n}}, \quad (6.1)$$

where $s_{i,n}$ is the strategy (bid) of UE i which takes values in the range $[s_L, s_U]$ with s_L being a small positive value to avoid ambiguities in the analysis, $s_{-i,n}$ denotes the strategies of other $n - 1$

users, $y_{i,n}$ is the power received by UE i , all related to state n . Further, ν scales the quantitative value of the service cost ($w_n s_{i,n}^2 / \sum_{j=1}^n s_{j,n}$) to the amount of satisfaction factor ($y_{i,n}/q$) to produce a meaningful utility for the user, and w_n is the power that is allocated by the WPC to all admitted users in state n . Note that ν can also be interpreted as the users' belief about the real value of their monetary bid for the power resource. The lower the factor is, the more willing the users are for paying for the charging service. The power received by UE i in state n is written

$$y_{i,n} = \frac{hw_n s_{i,n}}{\sum_{j=1}^n s_{j,n}}. \quad (6.2)$$

The best response function of each user i to the strategy $s_{-i,n}$ of other users is defined as

$$F_{i,n}(s_{-i,n}) = \arg \max_{s_i} u_{i,n}(s_{i,n}, s_{-i,n}) = s_{i,n}^*. \quad (6.3)$$

Since $\partial^2 u_{i,n}(s_{i,n}, s_{-i,n}) / \partial s_{i,n}^2 < 0$, $i \in \{1, 2, \dots, n\}$, the utility function in (6.1) would be a concave function. Thus, the stationary point, wherein $\partial u_{i,n}(s_{i,n}, s_{-i,n}) / \partial s_{i,n} = 0$, would be the maximizing strategy of the utility function, i.e. $s_{i,n}^*$. As such, we can express the best-response function in closed-form, according to

$$F_{i,n}(s_{-i,n}) = \frac{h}{q\nu \left(1 + \sqrt{1 + \frac{h}{q\nu \sum_{j \neq i} s_j}} \right)}. \quad (6.4)$$

Equation (6.4) implies that as n increases, the best-response strategy for each user is to increase its bid price. And this is the reason why the WPC would like the network to be full most of the time, so as to gain the best pay-off. The Nash equilibrium point of the game is when each user plays its best response to other users, i.e., $s_{i,n}^* = F_{i,n}(s_{-i,n}^*)$. For better exposition and to make it analytically easier to describe, we assume that q and h do not change from one user to another, although each user has its own specific service duration request. In this regard, the best-response strategy and the utility for all users are the same. Hence, by applying (6.4), the best-response strategy for a typical user i when there are n UEs in the network is obtained as

$$\bar{s}_{i,n} = \frac{h(n-1)}{q\nu(2n-1)}, \quad n \in \{2, 3, \dots, N\}, \quad (6.5)$$

and by substituting $\bar{s}_{i,n}$ into (6.1), the corresponding average utility is obtained as

$$\bar{u}_{i,n} = \frac{hw_n}{q(2n-1)}, \quad n \in \{2, 3, \dots, N\}. \quad (6.6)$$

Since for $n = 1$ there is no opponent for the only UE in the network, we assume that $\bar{s}_{i,1} = \bar{s}_{i,2}$, i.e., as if the player is playing with himself. Hence, $\bar{u}_{i,1} = \frac{hw_1}{3q}$. As (6.6) implies, the maximum utility of the user, playing the game, depends on w_n which is determined by the WPC performing the queuing analysis and optimization.

6.3 User Admission and Power Allocation

By writing the balance equations, which say that the rate at which the process leaves a state equals the rate at which the process enters it, we can find the limiting probability P_n for each state of the CTMC. Thus, the balance equations are

$$\begin{cases} \lambda P_0 = \mu_1 P_1, & n = 0 \\ (\lambda + \mu_n) P_n = \lambda P_{n-1} + \mu_{n+1} P_{n+1}, & 0 < n < N \\ \lambda P_{N-1} = \mu_N P_N, & n = N, \end{cases} \quad (6.7)$$

and can be simplified to

$$\lambda P_n = \mu_{n+1} P_{n+1}, \quad n \in \{0, 1, 2, \dots, N-1\}, \quad (6.8)$$

where $\mu_n, n \in \{1, 2, \dots, N\}$, is the departure rate from state n (cf. Fig. 6.1) and is calculated as follows:

$$\begin{aligned} \frac{1}{\mu_n} &= \frac{q/\mu}{hw_n/n} \\ \Rightarrow \mu_n &= \frac{1}{n} \frac{hw_n}{q} \mu, \quad 1 \leq n \leq N. \end{aligned} \quad (6.9)$$

Note that the departure rate is reciprocally proportional to the number of users in the network. Equation (6.8) along with the equality $\sum_{n=0}^N P_n = 1$ can be written in the matrix form

$$\begin{bmatrix} \lambda & -\mu_1 & 0 & \dots & 0 & 0 \\ 0 & \lambda & -\mu_2 & \dots & 0 & 0 \\ \vdots & \vdots & \vdots & \ddots & \vdots & \vdots \\ 0 & 0 & 0 & \dots & \lambda & -\mu_N \\ 1 & 1 & 1 & \dots & 1 & 1 \end{bmatrix} \begin{bmatrix} P_0 \\ P_1 \\ \vdots \\ P_{N-1} \\ P_N \end{bmatrix} = \begin{bmatrix} 0 \\ 0 \\ \vdots \\ 0 \\ 1 \end{bmatrix}. \quad (6.10)$$

After solving (6.10), the limiting probabilities, P_n 's, can be found in the closed-form formula

$$P_n = \frac{n! \lambda^n (h\mu/q)^{N-n} w_N w_{N-1} \dots w_{n+1}}{\sum_{n=0}^N n! \lambda^n (h\mu/q)^{N-n} w_N w_{N-1} \dots w_{n+1}}, \quad (6.11)$$

which is valid for all $n \in \{0, 1, 2, \dots, N\}$.

The WPC tries to find the power vector $\mathbf{w} = (w_1, w_2, \dots, w_N)^T$ with which it will maximize its long-run utility. The ensuing optimization problem is given by

$$\begin{aligned} \max_{\mathbf{w}, N} \quad & \mathbb{E}[u_{\text{WPC}}] \\ \text{subject to:} \quad & \mathbb{E}[u_i] \geq 1/\nu, \quad i \in \{1, 2, \dots, N\} \\ & w_n \geq 0, \quad n \in \{1, 2, \dots, N\}, \end{aligned} \quad (6.12)$$

where $\mathbb{E}[\cdot]$ is the expectation operator, and $\mathbb{E}[u_{\text{WPC}}]$ is the average utility of the power charger. In writing the first constraint in (6.12), we sensibly considered the reciprocal effect of the scaling factor ν by which the satisfaction level of users is adapted. So, a low value of ν requires that the user's utility should be respected more tightly. The average utility of the power charger can be written as

$$\mathbb{E}[u_{\text{WPC}}] = P_1 \frac{hw_1}{q\nu} + \underbrace{\sum_{n=2}^N P_n w_n \bar{s}_{i,n}}_{\text{revenue}} - \underbrace{c \bar{w}}_{\text{cost}}, \quad (6.13)$$

where $\bar{s}_{i,n}$ is obtained from (6.5), c is the power charger cost for transmitting each unit of power, and \bar{w} is the average power transmission of the WPC given by

$$\bar{w} = \sum_{n=1}^N P_n w_n. \quad (6.14)$$

As for the average utility of the typical user, i.e., $\mathbb{E}[u_i]$ in (6.12), it is obtained as follows:

$$\begin{aligned}\mathbb{E}[u_i] &= \frac{1}{1 - P_0} \sum_{n=1}^N P_n \bar{u}_{i,n} \\ &= \frac{1}{1 - P_0} \left(P_1 \frac{hw_1}{3q} + \sum_{n=2}^N P_n \frac{hw_n}{q(2n-1)} \right).\end{aligned}\tag{6.15}$$

The optimization problem in (6.12) is in fact a mixed-integer non-linear problem. We solve the problem by iteratively decreasing N and applying the interior-point method [46]. The procedure is shown in Algorithm 0.

Algorithm 1 Calculate \mathbf{w}^* and N^*

```

initialize  $\mathbf{w}_0 = \mathbf{0}$ ;
while  $N > 0$  do
  solve (6.12) with interior-point method;
  if  $\mathbf{w}$  is feasible then
     $N^* \leftarrow N$ ;
     $\mathbf{w}^* \leftarrow \mathbf{w}$ ;
    break;
  else
     $N \leftarrow N - 1$ ;
```

The average number of users in the network equals

$$L_a = \sum_{n=1}^N P_n n,\tag{6.16}$$

and applying the famous Little's formula, the average waiting time of each user in the network is given by

$$T_a = \frac{L_a}{(1 - P_N)\lambda}.\tag{6.17}$$

6.4 Numerical Results and Evaluation

In this section, the performance of the proposed power charging scheme is evaluated. Unless otherwise stated, the network parameters are as follows: $N = 10$, $P_{\max} = 20$ W, $c = 0.01$, $h = 0.15$, $q = 0.3$ W, $\mu = 1/900$, $\lambda = 1/900$, and $\nu = 1$. Note that $\lambda = 1/900$ means that, on average, four service requests per hour are sent to the power charger.

Figure 6.2 shows the allocated power w_n and the corresponding limiting probability P_n in each state n for two optimization cases: unconstrained and constrained. The simulation parameters are the default ones, except that here $N = 5$ for better exposition. In the unconstrained case, the WPC does not care about the users' utilities and satisfaction, but rather greedily wants to maximize its own utility. As Fig. 6.2a shows, the WPC mainly allocates its power when there are more users in the system, thus the network is almost always full (cf. Fig. 6.2b). In this case, the probability of n users in the system is larger for higher states than for the lower states. Conversely does the constrained case behave. That is, the WPC cares about the users' utilities and puts a constraint on itself to keep the users satisfied up to their required level as per the scaling factor. As Fig. 6.2a shows, the WPC transmits almost in all states with its maximum power. In this way, it can serve the users more quickly and keeps the network more often empty (cf. Fig. 6.2b).

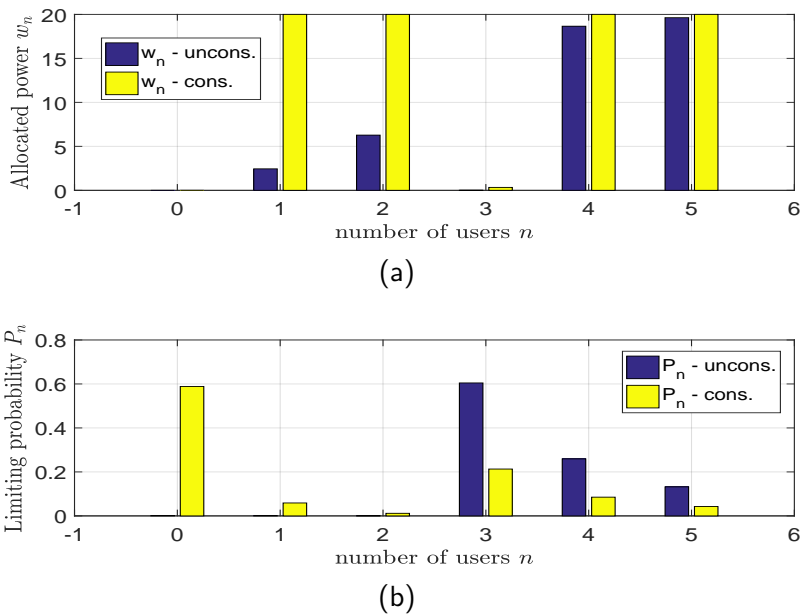


Figure 6.2: (a) The allocated power and (b) the limiting probability in each state, when the users' utilities are considered (constrained case) and when not considered (unconstrained case).

We solve the constrained non-linear optimization problem of (6.12) by the interior-point method and find the solution \mathbf{w}^* and N^* . In fact, this optimization problem is a mixed-integer non-smooth problem which we solve via Algorithm 1. In Fig. 6.3, we compare two scenarios with each other: i) the solution to (6.12), named '*Alloc. w^** ' in the figure's legend; and ii) the case the WPC allocates its maximum power, although it is still seeking the feasible N that satisfies the users' utilities, referred to by '*Alloc. P_{\max}* ' in the legend.

As Fig. 6.3a shows, the feasible capacity of the WPC decreases with the users arrival rate and increases with the scaling factor ν . If the users' ν is low, then their expectation about the service is high, while being willing to pay more generously. Note that when N^* changes, this may cause a discontinuity in other sub-figures in Fig. 6.3. Also, for the default network parameters, here both scenarios yield the same feasible N^* .

Figure 6.3b shows the average allocated power ratio w_n/P_{\max} . As observed, the WPC transmits more often in the optimum scenario, i.e. 'Alloc. w^* ', than in the scenario 'Alloc. P_{\max} '. This causes the WPC utility in the former scenario to become larger than that in the latter one. Note that under higher arrival rates, the first-scenario curves get close to the second-scenario curves as observed in Fig. 6.3b–6.3f.

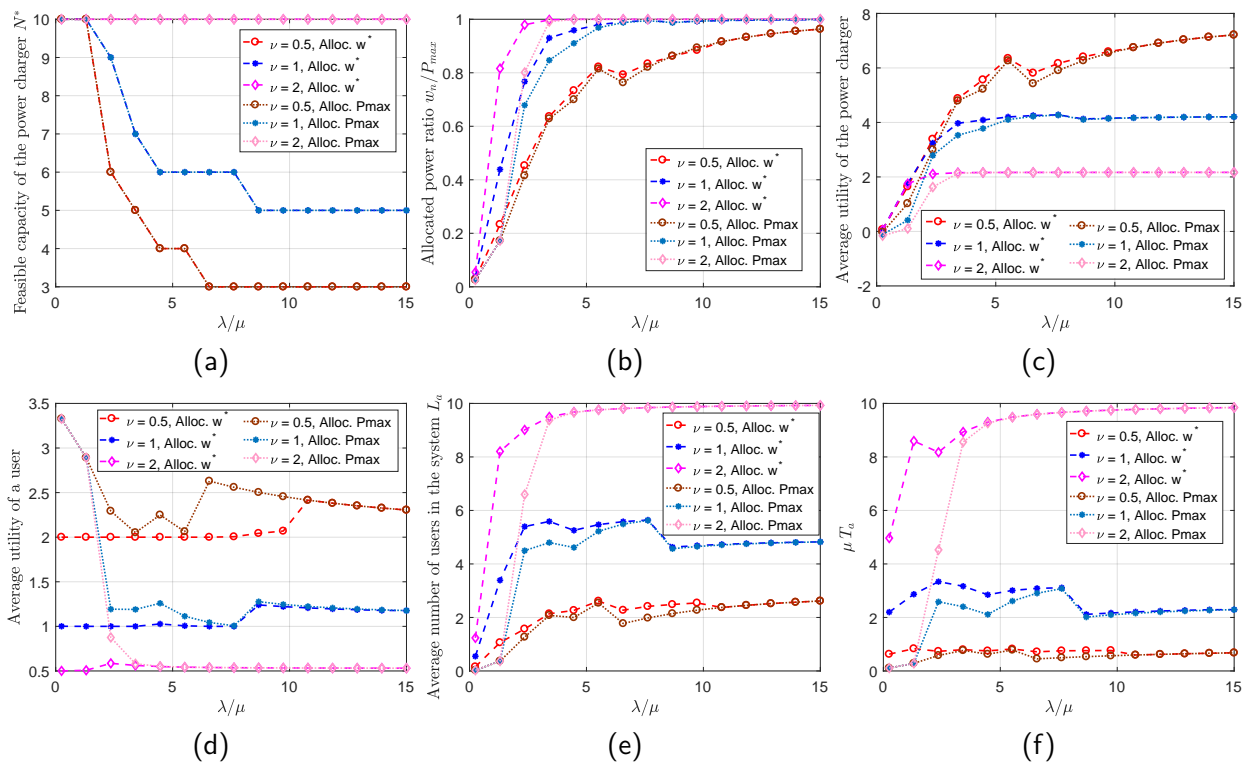


Figure 6.3: (a) Feasible capacity of the power charger, (b) average allocated power ratio, (c) average utility of the power charger, (d) average utility of the user, (e) average number of admitted users in the network, and (f) ratio of the average waiting time over the mean requested charging time.

As seen in Fig. 6.3c, the mean utility of the WPC clearly increases with λ . Users with lower scaling factor bring more profit for the WPC, although their own utility should be respected more strictly as Fig. 6.3d confirms. Note that the WPC utility of the optimum scenario outperforms scenario 2, especially for low and moderate values of λ/μ and for large values of ν .

Figure 6.3d shows the average utility of a typical user for both scenarios. In the first scenario, as the constraint function in (6.12) dictates for the \mathbf{w}^* to be feasible, we must have $\mathbb{E}[u_i] \geq 1/\nu$ as it can be easily observed from the figure. We see here that, contrary to Fig. 6.3c, it is the users that are more satisfied with the maximum power allocation. In fact, solving (6.12) gives a balanced strategy with which the utilities of both the users and the WPC are taken into account.

The average number of users admitted by the WPC is depicted in Fig. 6.3e. The said number for the optimum scenario is larger than that in scenario 2, as expected. Figure 6.3f shows the relative waiting time of a typical user compared to their expected charging time. Note that there is a reciprocal relationship between the average utility of a user and his waiting time. The higher the utility, the lower the waiting time. This is clear when comparing Fig. 6.3d and Fig. 6.3f with each other.

6.5 Summary

In this chapter, we modeled a wireless power charging network jointly with game theory and queuing theory tools. The game theory approach takes places in the short-run viewpoint, and the queuing theory approach is applied from the long-run viewpoint. We showed that depending on what value is taken for the scaling factor of the users, the wireless power charger can reach its maximum utility by solving a mixed-integer non-linear constrained optimization problem. The solution of the problem determines the amount of power that the power charger should allocate for a specific number of users in the network, and the charger's feasible capacity that meets the users' satisfaction level. In particular, it was shown that under moderate user arrivals, allocating the maximum power does not necessarily maximize the utility of the power charger.

Chapter 7

Auction-Based Wireless Power Charging with Reneging Devices¹

In this chapter, we investigate the distributed resource allocation while giving the ERs the freedom to decide whether to stay or live the game. We also consider the presence of some critical user which has critical service request. We apply game theory and analyze the Nash equilibrium point. Also, we present a reinforced learning formula to encourage the ERs to play toward a better NEP.

In the WPCN considered in the previous chapter, users compete with each other in a non-cooperative game for wireless power from the PB as per their bid prices. The PB distributes its power budget P , by beamforming its multi-antenna transmitter according to a proportional share auction. Therein, a non-reneging playing strategy is assumed in which users who enter the game are obliged to play it till the end, which is not necessarily what users desire in real WPCNs. In this chapter, we propose a *reneging* strategy under which the users are free to decide, after getting admission in the WPCN, to continue playing the game or to quit it if the service is not up to their expectation. Further, we study both strategies, reneging and non-reneging, in the presence of a *critical user* (CU) in the network. Such user is one whose service expectation is much higher than a typical user in the WPCN. We derive key performance metrics including the social welfare of users,

¹A. Bayat and S. Aissa, "Auction-Based Design and Analysis of Wireless Power Transfer Network With Critical Users," in IEEE Communications Letters, vol. 22, no. 11, pp. 2374-2377, Nov. 2018, doi: 10.1109/LCOMM.2018.2866433.

price of anarchy, utility of the CU, and utility of the PB. The reneging strategy outperforms the conventional non-reneging strategy in terms of all metrics, and service provisioning to CUs.

To provide users with the freedom to leave the game after starting to play, we modify the non-reneging strategy into the better—from the viewpoints of both the users and the PB—and more realistic reneging strategy. This flexibility is implemented by introducing sigmoid function into the users' playing strategy. We analyze the game and derive the aforementioned metrics. In fact, by investigating the conventional strategy and finding that its NEP is not an efficient point, we came to design the new reneging strategy by applying mechanism design theory to cause a better NEP. In particular, with the cost of a bit more time for converging to the NEP in the reneging strategy, the users can achieve higher social welfare at a lower price; and the PB can achieve higher utility. Further, we study the performance of the WPCN when operating in the presence of a CU, in terms of service priority. The reneging and non-reneging strategies are studied for both operation cases, *non-critical* and *critical*, and in addition to the previous metrics, the utility of the CU is derived and the effectiveness of each strategy in meeting said user's demand while maintaining the social welfare of other users at acceptable levels is analyzed.

7.1 The Wireless Power Charging Network

The WPCN consists of M users to be serviced by one PB with power budget P Watts. Each user i is assumed to need an average power of $q_i = E_i/D_i$, where E_i is the energy that the user wishes to acquire within a duration D_i . The power that the i^{th} user equipment (UE)² receives from the PB in each round of auction, denoted y_i , is given by,

$$y_i = s_i h_i P / \sum_{j=1}^M s_j, \quad (7.1)$$

where $s_i \in [s_L, \infty)$, in terms of currency unit per Joule, is the bid price proposed by user i as its playing strategy, with s_L denoting the minimum price set by the auctioneer PB. Users are assumed to have no budget limitation, i.e. there is no upper bound on s_i . h_i in (7.1) is the effective RF-DC channel power/conversion gain between UE $_i$ and the PB, i.e., without loss of generality (w.l.o.g) the harvesting efficiency of UE $_i$ is also taken into h_i . We assume free-space losses.³ Thus, h_i is

²The terms user and UE denote the playing agent.

³Non-line-of-sight fading channels endure a huge power loss.

assumed fixed during the entire charging time of the UE. The UEs are assumed to have rechargeable batteries and not to run out of power during their charging process.

Users broadcast their bids in a time-slotted schedule controlled by the PB, every $T = T_b + T_c$ units of time, where T_b is the bidding period and T_c is the charging period. Users update their bid prices at nT , $n \in \{1, 2, 3, \dots\}$. At the beginning of the bidding period, UE₁ updates its bid and broadcasts it to the PB and other users, then UE₂ does the same, and so on. Although UEs indexed with higher numbers have prior information about lower-numbered UEs in calculating their own bids, the NEP was attested to remain unique irrespective of the ordering. Having received all the bids at the end of a bidding period, the PB steers its antenna beams by tuning its weighting coefficients and starts charging UEs for the duration T_c .⁴ The utility of user i is defined as

$$u_i(s_i, \mathbf{s}_{-i}) = \frac{y_i}{q_i} - \frac{\lambda_i P s_i^2}{\sum_{j=1}^M s_j} = \frac{P \lambda_i s_i}{\sum_{j=1}^M s_j} (K_i - s_i), \quad (7.2)$$

where the latter equality is obtained after substitution of y_i (7.1), $\mathbf{s}_{-i} = (s_1, s_2, \dots, s_{i-1}, s_{i+1}, \dots, s_M)^T$ is a vector holding other $M - 1$ users' actions, factor λ_i scales the quality-type revenue y_i/q_i to the quantity-type cost $P s_i^2 / \sum_{j=1}^M s_j$ —which is the money user i pays per unit of time for its power share—to produce a meaningful utility for user i , and $K_i = \frac{h_i}{\lambda_i q_i}$ is the *goodness* factor. The lower the scaling factor is, the higher the price that the user would be willing to pay for the power service. The utility of the power beacon is defined as

$$u_{\text{PB}} = \frac{\sum_{i=1}^M s_i^2}{\sum_{j=1}^M s_j} P - c, \quad (7.3)$$

where c is the operational cost rate of the PB.⁵

⁴We assume $\min\{D_i\} \gg N_g T$, where N_g is the number of iterations needed for convergence of each game to its NEP.

⁵To guarantee a non-negative utility, the PB should propose its reserve price s_L such that $s_L \geq c/P$. Finding the optimum s_L to maximize the PB revenue is another interesting problem but not the purpose of this chapter.

7.2 Non-Reneging and Reneging Games: Analysis

7.2.1 Non-Reneging Game with no Critical User

We start with defining the game and recalling the NEP of the non-reneging case without CU. The multi-user charging problem is formalized as a non-cooperative game

$$\mathcal{G} = \langle \mathcal{V}, [s_L, \infty)^M, \{u_i(s_i, \mathbf{s}_{-i})\}_{i \in \mathcal{V}} \rangle, \quad (7.4)$$

where $\mathcal{V} = \{1, 2, \dots, M\}$ denotes the players' set, $[s_L, \infty)^M$ is the M -dimensional strategy space, and $u_i(s_i, \mathbf{s}_{-i})$ is the utility function for player i . The best-response function of each user $i \in \mathcal{V}$, denoted $F_i(\mathbf{s}_{-i})$, is found by solving:

$$\begin{aligned} \arg \max_{s_i} u_i(s_i, \mathbf{s}_{-i}) \\ \text{subject to: } s_i \geq s_L. \end{aligned} \quad (7.5)$$

By solving $\partial u_i(s_i, \mathbf{s}_{-i}) / \partial s_i = 0$ and finding the unique positive stationary point which is a maximizing point since $\partial^2 u_i(s_i, \mathbf{s}_{-i}) / \partial s_i^2 < 0$, we obtain the closed-form formula for the best-response function of UE_i as

$$F_i(\mathbf{s}_{-i}) = \max \left\{ s_L, K_i / \left(1 + \sqrt{1 + K_i / \sum_{j \in \mathcal{V}, j \neq i} s_j} \right) \right\}. \quad (7.6)$$

To find the NEP \mathbf{s}^* of the game, one should solve the system of equations $\{s_i^* = F_i(\mathbf{s}_{-i}^*), i \in \mathcal{V}\}$, which gets more complicated for large M . It is shown in [47] that the conventional non-reneging game has a unique NEP. It should be noted that (7.6) implies that the best strategy for user i if other users increase their bids integrally—i.e. $\sum_{j \in \mathcal{V}, j \neq i} s_j$ becomes greater—is to increase its bid value too. Also, if $\sum_{j \in \mathcal{V}, j \neq i} s_j \rightarrow \infty$, then $F_i(\mathbf{s}_{-i}) \rightarrow K_i/2$. Therefore, for user i playing a bid greater than $K_i/2$ is a dominated strategy.

7.2.2 Non-Reneging Game with a Critical User

The scaling factor of a CU would be much lower than that of other users due to the associated service criticality. The lower the scaling factor, the higher the payment the user is willing to make.

We assume, without loss of generality, that UE₁ is the CU in the WPCN. What is important for the CU is whether the power he gets from the PB fulfills its requirement, i.e., $y_1 \geq q_1$. In this vein, the CU calculates its bid price with the constraint of $y_1 \geq q_1$ which, by substitution of y_1 from (7.1), is equivalent to $s_1 \geq \check{s}_1$ where $\check{s}_1 = \frac{q_1}{h_1 P - q_1} \sum_{j=2}^M s_j$. Thus, we face a convex constrained optimization problem:

$$\begin{aligned} \max_{s_1} \quad & u_{\text{CU}} = \frac{P\lambda_1 s_1}{s_1 + \sum_{j=2}^M s_j} (K_1 - s_1) \\ \text{subject to:} \quad & s_1 \geq \check{s}_1; s_1 \geq s_L, \end{aligned} \quad (7.7)$$

for which the solution is easily found to be

$$s_1^* = \max\{\check{s}_1, F_1(\mathbf{s}_{-1})\}. \quad (7.8)$$

If $q_1 \geq h_1 P$, the CU will never get satisfied with playing any bid. To show the intensity of the CU's critical status quantitatively, we write $\lambda_{\text{CU}} = \zeta \lambda_{\text{avg}}$, where ζ is the criticality factor and λ_{avg} is the average of the λ_i 's pertaining to the ordinary users.⁶ Since these users are not aware of the presence of the CU, they play the same non-cooperative game.

7.2.3 Reneging Game with no Critical User

For the reneging scheme, we design a new controlled bidding where we let users decide on remaining in the game or leaving it. Here, we assume that users' expectations depend on their valuations. A user with higher valuation, i.e. lower scaling factor, expects a better service compared to users with lower valuations. In particular, we make use of the logistic (sigmoid) function $\mathcal{I}_k(x) = 1/(1 + \exp(-kx))$ with roll-off parameter k . k quantifies the intensity of decision hardness of users; as k increases the user will decide more sharply on leaving the game if its utility does not meet its expectation. The sigmoid function mimics the behavior of the non-smooth step function for large values of k in a smooth way.

In this strategy, user i wants his utility to be higher than his valuation ν_i . ν_i is defined with a reciprocal relation to λ_i as

$$\nu_i = (1 - \mathcal{I}_1(\lambda_i - 2))/(1 - \mathcal{I}_1(-1)). \quad (7.9)$$

⁶The scaling factor λ_i 's for reneging users can be defined based on the initial battery status of the UEs; and the criticality factor ζ can be an indicator of a low-battery status of the CU.

In defining ν_i (7.9), it is assumed that a user i whose scaling factor $\lambda_i = 1$ also has a valuation $\nu_i = 1$. For a user with $\lambda_i < 1$ we have $\nu_i > 1$, and $\nu_i < 1$ when $\lambda_i > 1$. Now, we define the bid of user i at the n^{th} round of auction, $n > 1$:

$$\tilde{F}_i(\mathbf{s}_{-i}^{(n)}) = F_i(\mathbf{s}_{-i}^{(n)}) \mathcal{I}_{k_n} \left(u_i(F_i(\mathbf{s}_{-i}^{(n-1)}), \mathbf{s}_{-i}^{(n-1)}) - \nu_i \right), \quad (7.10)$$

where the roll-off parameter $k_n = (n - 1)k_1$, k_1 being the initial roll-off parameter. Equation (7.10) is the distributed updating algorithm. Each UE_i updates its bid in the first round ($n = 1$) as per (7.6), and using (7.10) for $n > 1$. k_n models the gradual increase in users' strictness about their expectations, i.e., as n increases, users accept less deviation from their expectation in order to stay in the game. Parameter k_1 plays an important role in assuring the algorithm to reach the NEP. If k_1 is small enough, the algorithm always reaches the same NEP. Smaller k_1 yields longer convergence time. It is the flexible strategy in (7.10) that allows a user to decide to zero-force its bid strategy, i.e., leave the game, when the average service it received from the PB is not to its satisfaction.⁷ Through extensive simulations with arbitrary positive values for the initial bids, different values for the number of users, and different scenarios, the uniqueness of the NEP and the convergence of the updating function (7.10) were confirmed.

7.2.4 Reneging Game with a Critical User

The CU is assumed to remain in the network as long as $q_1 < h_1 P$, and updates his bid in each round according to (7.8). The main difference between this game and the non-reneging game with CU is that here the ordinary users leave the WPCN if the service they receive from the PB is not up to their expectation level ν_i , $i \in \mathcal{V} \setminus \{1\}$. Indeed, the ordinary users update their bids in each round according to (7.10).

⁷A user leaving the game may join it again and get readmitted by the PB after a service completion or a new user arrival in the WPCN.

7.3 Social Welfare and Price of Anarchy

The social welfare of the users in the NEP is defined as

$$\mathcal{W} = \sum_{i \in \mathcal{V}} u_i(s_i^*, \mathbf{s}_{-i}^*). \quad (7.11)$$

For all strategies, $u_i(s_i^*, \mathbf{s}_{-i}^*)$ is obtained from (7.2) for $i \in \mathcal{V}$. Then the price of anarchy (PoA) is defined as

$$\mathcal{P}_A = \frac{\max_{s_1, s_2, \dots, s_M} \sum_{i \in \mathcal{V}} u_i(s_i, \mathbf{s}_{-i})}{\mathcal{W}}, \quad (7.12)$$

where the maximization is a different constrained optimization problem for each of the four strategies. Note that the strategy space of the CU in the non-reneging and reneging games is $[s_L, \infty)$, since he pays as much as necessary to get the service and will leave the system only when his service demand is met. Also, the strategy space of each ordinary user in the non-reneging game is the same, $[s_L, \infty)$. In the reneging game, the strategy space of each ordinary user is $\{[s_L, \infty) \cup \{0\}\}$. For the non-reneging strategy, in the non-critical and critical cases, we have

$$\begin{aligned} & \max_{s_1, s_2, \dots, s_M} \sum_{i \in \mathcal{V}} u_i(s_i, \mathbf{s}_{-i}) \\ & \text{subject to: } s_i \geq s_L, i \in \mathcal{V}, \end{aligned} \quad (7.13)$$

$$\begin{aligned} & \max_{s_1, s_2, \dots, s_M} \sum_{i \in \mathcal{V}} u_i(s_i, \mathbf{s}_{-i}) \\ & \text{subject to: } y_1 \geq q_1; s_i \geq s_L, i \in \mathcal{V} \setminus \{1\}, \end{aligned} \quad (7.14)$$

respectively. In both cases, the objective function is quasiconcave over its convex domain set. Thus, each problem has a unique global solution that can be found using the non-linear optimization method of interior-point.

Next is the problem of non-critical reneging strategy:

$$\begin{aligned} & \max_{\mathbf{d}_m, m \in \{0, 1, \dots, 2^M - 1\}} \max_{s_i, i \sim \mathbf{d}_m} \sum_{i \sim \mathbf{d}_m} u_i(s_i, \mathbf{s}_{-i}) \\ & \text{subject to: } u_i(s_i, \mathbf{s}_{-i}) \geq \nu_i \ \& \ s_i \geq s_L, i \sim \mathbf{d}_m, \end{aligned} \quad (7.15)$$

where \mathbf{d}_m is an M -dimension binary vector which determines which of the M variables s_i should be set to zero and hence their constraints should be excluded from the problem. By $i \sim \mathbf{d}_m$, we consider

those indexes i which point to a ‘1’ in \mathbf{d}_m . There are 2^M possible permutations of $\{\mathbf{d}_0, \dots, \mathbf{d}_{2^M-1}\}$. For example, for $M = 3$, $\mathbf{d}_2 = [0, 1, 0]$ means that $s_1 = s_3 = 0$ and the constraint in (7.15) is $u_2(s_2, \mathbf{s}_{-2}) \geq \nu_2$; $s_2 \geq s_L$. Each permutation corresponds to a sub-problem with a quasi-concave objective function and convex constraints. Thus, each sub-problem either has a global solution or no solution. For the sub-problem related to \mathbf{d}_0 , the solution is the zero value.

The last problem is for the reneging strategy with CU:

$$\begin{aligned} & \max_{\mathbf{d}_m, m \in \{2^{M-1}, \dots, 2^M-1\}} \max_{s_i, i \sim \mathbf{d}_m} \sum_{i \sim \mathbf{d}_m} u_i(s_i, \mathbf{s}_{-i}) \\ & \text{subject to: } y_1 \geq q_1; u_i(s_i, \mathbf{s}_{-i}) \geq \nu_i \ \& \ s_i \geq s_L, i \sim \mathbf{d}_m, \end{aligned} \quad (7.16)$$

which has a global solution that can be found similarly to (7.15).

7.4 Comparative Results

The reneging (rng) and non-reneging (non-rng) strategies are evaluated for both cases, *with* and *without* a CU. A user’s power request q_i varies uniformly in $R = [0.2, 0.3]W$, and the corresponding h_i varies uniformly in $H = [0.11, 0.19]$ as per experimental results in [48]. The PB budget P and operation cost rate c are 20W and 0.01, respectively; thus the reserve price $s_L = 5 \times 10^{-4}$. The initial roll-off $k_1 = 1$. The scaling factor follows a two-section uniform distribution with parameter β to classify users into two groups: users with scaling factors higher than 1, and those with factors less than 1. That is, we assume $\lambda_i \in [0.1, 10]$ and partition this interval into sub-intervals $[0.1, 1)$ and $[1, 10]$, each of which has uniform distribution.⁸ Each interval is chosen with a Bernoulli distribution of parameter β , e.g., when $\beta = 0.2$, the upper interval will be selected with probability 0.2 and $\lambda_{\text{avg}} = 1.54$. The criticality factor $\zeta = 0.1$; thus the CU’s scaling factor is $\lambda_{CU} = \zeta \lambda_{\text{avg}} = 0.154$. In the plots, results are averaged over 1000 simulation runs, and the uniqueness of NEP’s and the convergence of the algorithm are confirmed for a large number of repetitions with various random initial points in $[s_L, \infty)$. As mentioned earlier, the initial roll-off parameter k_1 in (7.10) should be small enough; $k_1 = 1$ is chosen in the simulations. In Fig. 7.1b, Fig. 7.2, and Fig. 7.3, the number of active users, i.e., the ones who do not leave the game, varies according to the initial number of users in the WPCN (Fig. 7.1a).

⁸Other distributions such as log-normal can also be used.

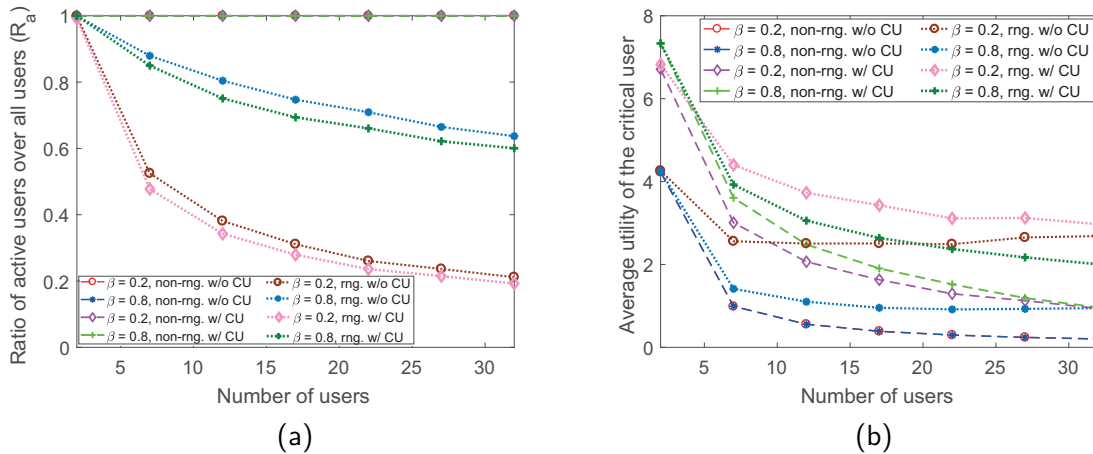


Figure 7.1: Comparison of the four games for two values of β : (a) Number of active users over the total number of users M ; (b) Average utility of the CU.

Figure 7.1a shows the ratio of the number of remaining users over M . For the non-reneging game, this ratio is unity ($R_a = 1$) because no users are allowed to leave the game. In the reneging game, the number of active users decreases as the average scaling factor decreases because users with higher valuations have higher expectations. The small gap between the same- β curves is due to the CU's utility. Fig. 7.1b shows the average utility of the CU. The average utility of a user for cases with no CU is also plotted. The CU's utility in the reneging game is considerably higher than the non-reneging case for $M \geq 7$. Indeed, the CU in the reneging game competes with less users, and as (7.6) implies the CU will bid a lower value while the PB power is also satisfactorily allocated among less users. In the non-reneging strategy, as M increases the CU should pay more, but its utility becomes less. In the reneging game, users end up paying less and their utilities increase. In Fig. 7.2, the utility of the PB and the users' social welfare are plotted. The reneging games outperform the non-reneging games. That is because the winners in the reneging game are those users with higher K_i 's while their utilities are also greater than their valuations ν_i 's. As such, the PB power will be distributed among those users who are willing to pay more per unit of power, thus increasing the revenue of the PB. Those users will also bring about more aggregate utility, i.e., social welfare. Further, because of the low scaling factor of the CU, the PB utility gets higher in the presence of CU in the WPCN.

As illustrated in Fig. 7.3a, the reneging strategy yields lower price of anarchy PoA. The freedom given to users to decide upon staying or leaving the game, which filters out users with low goodness factors, contributed to this decrease in PoA. Fig. 7.3b depicts the average number of iterations for

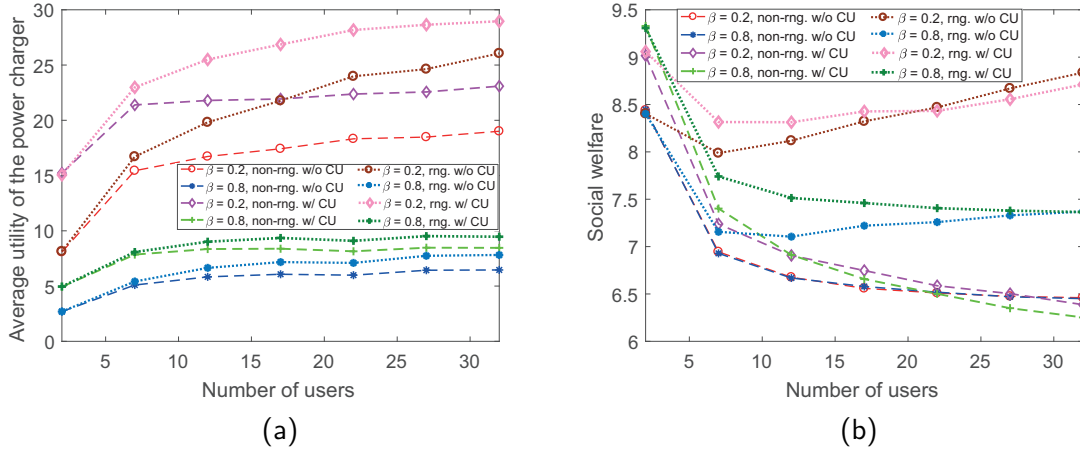


Figure 7.2: (a) Average utility of the PB; (b) Average social welfare of the users.

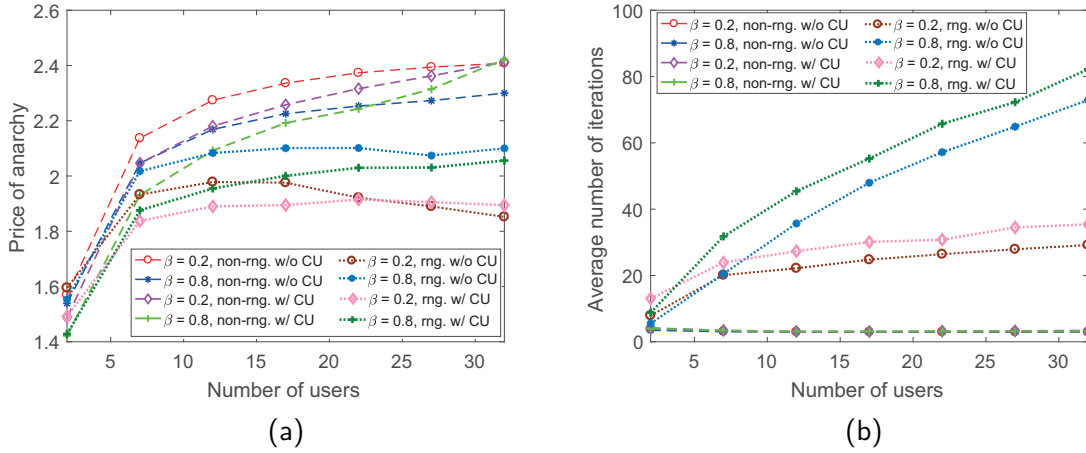


Figure 7.3: (a) Average price of anarchy of the users; (b) Average number of iterations for convergence to the NEP.

convergence of the distributed algorithm. Convergence is slower in the renegeing strategy because users therein decide about their participation. As (7.10) infers, calculation of the NEP for the non-renegeing game is an intermediate stage in the calculation pertaining to the renegeing case. The longer convergence of the renegeing case is tolerable as long as $T \ll \min\{D_i\}$ for all users, which is normally the case in practice.

7.5 Summary

A practical auction-based reneging playing strategy was devised to model a WPCN in which users compete for wireless power. In contrast to the conventional non-reneging game, users in the reneging strategy are free to decide to continue playing the game or to leave it if they judge the service to be not worth the cost. The two strategies were also analyzed for network operations in the presence of CU. By driving the game towards a better NEP, the reneging strategy outperforms the non-reneging strategy in terms of utility of the PB, social welfare of the users, and service provisioning for the CU.

Part IV

Deep Learning-Based Auction-Driven Beamforming

In this part, the resource allocation problems are formulated as mixed-integer nonlinear programming (MINLP). We apply deep learning to tackle the problem of infeasibility of the time-greedy iterative Branch-and-Bound resource allocation algorithms for real-time applications. The objective in Chapter 8 is maximizing the social welfare of IRs in a WIT system whereas that in Chapter 9 is maximizing the revenue of the hybrid access point in a SWIPT system. Since Chapter 9 is an extension of Chapter 8, some materials of both chapters may overlap.

Chapter 8

Auction-Driven Multiuser Information Beamforming with Deep Learning¹

8.1 Literature Review

The conventional approach to solve the resource management problems in wireless information transfer systems is through optimization theory techniques which are effective when the problem is amendable to a mathematically-tractable one. Most of the time, this is typically not the case in interference-limited systems, where multi-user interference puts most relevant resource allocation problems into the NP-hard class. For instance, maximizing the sum-rate through power allocation to several users in interference-limited systems is an NP-hard problem [49]. Even if one could solve NP-hard problems with an acceptable level of complexity [50], the optimal resource allocation will still depend on the system parameters, e.g., the users' positions, the number of connected users, the slow- or fast-fading channel realizations, the number of antennas, etc. Whenever one of these parameters changes, which occurs very often in mobile environments, the optimization problem needs to be solved afresh. This adds a significant amount of complexity, which limits the real-time implementation of the available optimization-theory based techniques, especially in large and complex systems like future wireless communication systems. In this context, the use of deep

¹A. Bayat and S. Aïssa, "Auction-Driven Multiuser Beamforming with Deep Learning," in Proc. IEEE Global Communications Conference (GlobeCom'20), Taipei, Taiwan, Dec. 2020.

learning techniques based on artificial neural networks can significantly reduce the burden of system design, enabling true online resource management [29].

One instance of such complexity occurs when a wireless access point tries to maximize the network social welfare when devices compete in an auction way for the resources. Evidently, as wireless systems evolve with new technologies, they tend to become more complicated in terms of architecture and resource management. Auctions, on the other hand, as a sub-field of economics, are known to provide a competitive premise for radio resource allocation, e.g., allocation of sub-channels, time slots, and transmit powers, among devices in wireless systems [19], [25]. Yet, an important aspect of future wireless communications is the on-demand inclusion of the clients in choosing their desired level of service quality as per their financial capabilities [25, 51, 52]. In other words, the devices seen as decision-making clients tend to take part in market competitions like auctions in order to choose their most desired services. In this way, while giving the clients the opportunity to dynamically participate in choosing their desired service levels, e.g., through bidding in auctions, the service seller should also be agile enough to decide upon the best strategy that maximizes its own objective such as social welfare.

An application of social welfare as the objective is when service providers (SPs) as the business entities do not have sufficient infrastructure and/or resources to satisfy the service demands of their subscribed users, in which case they can purchase infrastructure and/or resources from other entities known as edge infrastructure providers (EIPs) [24]. In this chapter, we consider a wireless information transfer system in which a multi-antenna access point as the EIP tries to beamform information streams towards several user equipments (UEs) which are subscribers of a SP. The access point, hired by the SP, aims to hold optimal auctions for selling its wireless multiplexing links to the UEs in such a way that the social welfare of the entire system is maximized. While finding the optimal linear precoder constrained by the UEs' desired signal-to-interference-plus-noise ratios (SINRs) can efficiently be found by applying uplink-downlink-duality-based algorithm (UDD) [50] or semidefinite programming relaxation (SDR) technique [53], finding the set of UEs that maximizes the social welfare needs many runs of the algorithms, which in turn can violate the real-time running necessity for this type of application. One way to overcome this problem is to use machine-learning tools for estimating the allocation set in almost no time. In this vein, after formulating the social-welfare maximization problem, we first find all the feasible allocation rules based on the SINR requests and channel state information (CSI) reports of the UEs. We then propose and train a deep

neural network (DNN) to estimate the optimal set of users for the allocation. The accuracy of the DNN-based estimator is demonstrated for different target allocation sets by obtaining the confusion matrix.

In detailing these contributions, the remainder of the chapter is organized as follows. Section 8.2 models the wireless information transfer system, both physically and economically. In Section 8.3, we find the optimal social-welfare maximizing mechanism for the proposed auction framework defined in Section 8.2, by first formulating the social-welfare maximization problem and then using two conventional solvers: UDD-based algorithm and SDR-based technique. Section 8.4 presents the proposed DNN-based solution, and discusses its architecture and training. In Section 8.5, we illustrate the loss and the accuracy metrics per epoch for the training and validation sets, and discuss the confusion matrix for a sample system setup. Finally, Section 8.6 summarizes the chapter.

Notations: The following set of notations will be adopted throughout the chapter. Vectors and matrices are shown with bold lower- and upper-case letters, respectively. Symbols $(\cdot)^T$ and $(\cdot)^H$ denote the transpose and conjugate transpose operators, respectively. The identity matrix of order m is denoted by \mathbf{I}_m , $\text{tr}(\mathbf{A})$ is the trace of square matrix A , and $\mathbf{0}$ is a zero vector with proper dimensions. The l_1 -norm and l_2 -norm (Euclidean) are denoted by $\|\cdot\|_1$ and $\|\cdot\|$, respectively, and $\mathbb{E}[\cdot]$ stands for mathematical expectation.

8.2 The System Modeling

In the multi-user system, the access point (AP) is to serve K UEs within a single band. The AP is equipped with M antennas and has a power budget of P Watts. The UEs are single-antenna devices, and assumed to be always demanding to receive data from the AP. The AP and the UEs work in half-duplex mode. Linear precoding is implemented at the AP, whereby each device is assigned one dedicated information beam. Denoting the set of UEs in the system by $\mathcal{K} = \{1, \dots, K\}$, the signal transmitted from the AP is given by

$$\mathbf{x} = \sum_{k \in \mathcal{K}} \mathbf{w}_k s_k, \quad (8.1)$$

where $\mathbf{w}_k \in \mathbb{C}^{M \times 1}$ is the beamforming vector and s_k is the information-bearing signal, for UE $_k$, $\forall k \in \mathcal{K}$. Assuming Gaussian inputs, the s_k 's are i.i.d. circularly-symmetric complex Gaussian random

variables with zero mean and unit variance, i.e., $s_k \sim \mathcal{CN}(0, 1) \forall k \in \mathcal{K}$. Given the transmit power constraint at the AP, we have $\mathbb{E}[\mathbf{x}^H \mathbf{x}] = \sum_{k \in \mathcal{K}} \|\mathbf{w}_k\|^2 \leq P$.

We assume quasi-static fading, i.e., channel coefficients are assumed to be fixed during the channel coherence time. Denote the channel vector from the AP to UE $_k$ by $\mathbf{h}_k = (h_{k,1}, \dots, h_{k,M})^T$, where $\|\mathbf{h}_k\|^2 = \sigma_k^2, \forall k \in \mathcal{K}$. Each channel vector \mathbf{h}_k is drawn independently from continuous distribution function $F_k(\mathbf{h}_k)$, where $h_{k,m}$ as the complex channel gain from the m^{th} antenna of the AP array, $m \in \{1, \dots, M\}$, to UE $_k$ is assumed to be perfectly tracked at the receiver and fed back to the transmitter via an error-free zero-delay feedback channel.

The received base-band equivalent signal at the k^{th} UE is

$$y_k = \mathbf{h}_k^T \mathbf{x} + z_k, \quad (8.2)$$

where $z_k \sim \mathcal{CN}(0, \sigma^2)$ is the i.i.d. Gaussian noise.² Therefore, the SINR of UE $_k$ can be written as

$$\Gamma_k = \frac{|\mathbf{h}_k^T \mathbf{w}_k|^2}{\sum_{i \neq k, i \in \mathcal{K}} |\mathbf{h}_k^T \mathbf{w}_i|^2 + \sigma^2} = \frac{\mathbf{w}_k^H \mathbf{R}_{\mathbf{h}_k} \mathbf{w}_k}{\sum_{i \neq k, i \in \mathcal{K}} \mathbf{w}_i^H \mathbf{R}_{\mathbf{h}_k} \mathbf{w}_i + \sigma^2}, \quad (8.3)$$

where $\mathbf{R}_{\mathbf{h}_k} = \mathbb{E}[\mathbf{h}_k \mathbf{h}_k^H]$ is the covariance matrix of \mathbf{h}_k , which for the case of perfect full CSI knowledge becomes $\mathbf{R}_{\mathbf{h}_k} = \mathbf{h}_k \mathbf{h}_k^H$. The SINR is directly related to the system performance metrics such as the bit error rate (BER) and the data rate. For example, under a fixed BER and assuming quadrature-amplitude modulation, a practical achievable rate can be computed as $R_k = \log(1 + \Gamma_k/\Upsilon)$ bps/Hz, where Υ is the signal-to-noise ratio (SNR) gap to capacity. The SNR gap is always greater than 1 (0 dB), and gives an approximate relation between the SINR and the data rate.

8.2.1 Bidding Modeling

The AP, as the service seller, plays the role of auctioneer as well. The UEs, which have different service valuations, play the roles of bidders by sending their bids in each round of auction to get served by the AP. The AP solicits the bids in a sealed fashion, i.e., UEs are not aware of each others' bids.

²Without loss of generality, noise power is assumed the same for all UEs.

It is assumed that all UEs have non-zero service requests, and play in all rounds of auction. The UEs send their service requests in the form of the minimum SINR, γ_k , required to receive D_k bits of data in the auction duration τ_a by bidding b_k . It is further assumed that the auction duration τ_a is less than the coherence time of all the channels so that during each auction the channel coefficients remain fixed. Without loss of generality, we set $\tau_a = 1$. Also, let $\boldsymbol{\gamma} = (\gamma_1, \dots, \gamma_K)^T$ and $\mathbf{b} = (b_1, \dots, b_K)^T$ denote the demand profile and the bid profile of the UEs during an auction round, respectively.

8.2.2 Auction Framework

We consider a single-parameter (or single-dimensional) auction environment, where the outcomes of the AP as the mechanism designer are (i) the allocation rule $\mathbf{a} = (a_1, \dots, a_K)^T$, with a_k being an indicator for whether UE $_k$ is served or not, i.e., $a_k \in \{0, 1\} \forall k \in \mathcal{K}$; and (ii) the payment rule $\mathbf{p} = (p_1, \dots, p_K)^T$, where p_k is the payment which should be made by UE $_k$ at the current round of auction.

As depicted in Fig. 8.1, each round of auction is composed of four parts: (i) bids-and-demands (B&D) acquisition, (ii) CSI acquisition, (iii) auction results announcing, and (iv) information beamforming.

To find the optimal precoding matrix, i.e., the beamforming vectors \mathbf{w}_k^* 's, the key step is to find the optimal allocation vector \mathbf{a}^* and the optimal payment vector \mathbf{p}^* that maximize the social welfare. Then, the AP sends to each UE $_k$ the pair (a_k^*, p_k^*) as the auction result to let each bidder know whether he won the auction or not and how much to pay if he won.³

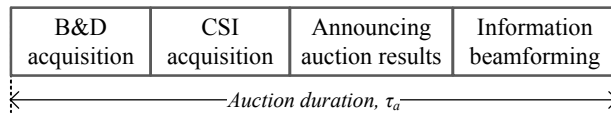


Figure 8.1: Breakout of each auction round.

At the beginning of each auction round, i.e., during the B&D-acquisition period, the AP solicits the UEs for their service level demands, i.e., the γ_k 's, and their corresponding bids, i.e., the b_k 's.

³Allocation (payment) "rule" and allocation (payment) "vector" are used interchangeably throughout this chapter.

Then, the AP acquires the CSI.⁴ Based on the acquired information, i.e., the demand profile $\boldsymbol{\gamma}$, the bid profile \mathbf{b} , and the CSI's, the AP seeks the optimal allocation vector which would maximize the social welfare. Finally, the AP performs beamforming to transfer the information to the chosen set of UEs by one-time running of the UDD algorithm.

8.2.3 Utility Functions

In designing optimal mechanisms for auctions, there are two fundamental objectives: *social welfare*, a.k.a. social surplus, and *revenue*, a.k.a. profit.

The revenue generated from the allocation-payment pair (\mathbf{a}, \mathbf{p}) is the utility of the AP. Specifically, it is the cumulative payment of the bidders minus the service cost, $c(\mathbf{a})$. That is,

$$u_{\text{AP}}(\mathbf{a}, \mathbf{p}) = \sum_{k \in \mathcal{K}} p_k - c(\mathbf{a}). \quad (8.4)$$

For each UE $_k$, $k \in \mathcal{K}$, with valuation v_k , the utility—assuming the quasi-linear model [54]—is defined as follows:

$$u_k(v_k, \mathbf{b}_{-k}) = v_k a_k(\mathbf{b}) - p_k(\mathbf{b}), \quad (8.5)$$

where \mathbf{b}_{-k} is the vector holding the bids of all devices except UE $_k$, and where the notations $a_k(\mathbf{b})$ and $p_k(\mathbf{b})$ are to emphasize that the allocation and payment rules depend on the bid profile \mathbf{b} .

The social welfare resulting from the allocation rule \mathbf{a} is the cumulative valuations of all the agents in the auction minus the service cost, i.e.,

$$S(\mathbf{v}, \mathbf{a}) = \sum_{k \in \mathcal{K}} v_k a_k - c(\mathbf{a}) = \mathbf{a}^T \mathbf{v} - c(\mathbf{a}), \quad (8.6)$$

where vector $\mathbf{v} = (v_1, \dots, v_K)^T$ indicates the valuations of the UEs. The CSI training costs may be part of the service cost. Herein, for simplicity and without affecting the main contributions of this chapter, the cost function is assumed zero. Also, note that bid b_k is the number that UE $_k$ declares to the AP to pay for its demand γ_k , whereas valuation v_k is the true belief of UE $_k$ about its demand γ_k . Truthfulness, which means that each UE bids with its true valuation, i.e., $b_k = v_k$, is fulfilled by

⁴This requires each UE to perform channel estimation followed by CSI feedback to the transmitter through a narrow-band feedback channel.

designing the payment rule—which is carried out in Section 8.3—so as to keep the UEs motivated to play truthfully. Under these conditions, $S(\mathbf{v}, \mathbf{a}) = S(\mathbf{b}, \mathbf{a}) = \mathbf{a}^T \mathbf{b}$.

8.3 Social-Welfare Maximizing Mechanism

Finding the optimal social-welfare maximizing (SWmax) mechanism is equivalent to finding the optimal allocation rule and the optimal payment rule. Since finding the latter depends on the former, we start with the allocation rule.

8.3.1 The Optimal Allocation Rule

The optimal allocation rule can be found by solving the SWmax problem

$$\underset{\mathbf{a} \in \mathcal{A}_F}{\text{maximize}} S(\mathbf{b}, \mathbf{a}) = \mathbf{a}^T \mathbf{b}, \quad (8.7)$$

where \mathcal{A}_F is the set of all feasible allocation vectors, which depends on the \mathbf{h}_k 's and on the UEs' SINR demands, i.e., the γ_k 's. The problem in (8.7) states that the optimal allocation vector \mathbf{a}^* corresponds to the feasible set of users that results in the largest sum of bids. In other words, given the bid profile \mathbf{b} , the maximum social welfare $S^*(\mathbf{b})$ which is equal to $S(\mathbf{b}, \mathbf{a}^*)$ is simply found by looking up the table of all social-welfare corresponding to each allocation vector in the feasible set \mathcal{A}_F and selecting the maximum value.

In order for the AP to find all feasible allocation vectors out of all possible realizations of allocation vectors $\mathbf{a}_l \in \{0, 1\}^K$, $l \in \{0, 1, \dots, 2^K - 1\}$, a series of non-convex optimization problems should be solved. Let us correspond a subset $A_l \subset \mathcal{K}$ to each $\mathbf{a}_l = (a_{l1}, \dots, a_{lK})^T$, $l \in \{0, 1, \dots, 2^K - 1\}$, so that $k \in A_l$ if and only if $a_{lk} = 1 \forall k \in \mathcal{K}$.⁵ In general, we face a mixed-integer non-linear program. Note that there are $2^K - 1$ optimization problems to be solved, as worst-case, to get \mathcal{A}_F . Each problem corresponding to \mathbf{a}_l is a power minimization problem, which consists of finding the minimum transmit power required by the AP to fulfill the SINR demands of the chosen UEs in

⁵Subscript l is indeed the decimal representation of the binary vector \mathbf{a}_l which will be regarded as the labels based on which the confusion matrix in Section 8.5 is obtained.

subset A_l , and is formulated as

$$\begin{aligned}
 P_{A_l}^{\min} &= \min_{\mathbf{w}_k, k \in A_l} \sum_{k \in A_l} \|\mathbf{w}_k\|^2 \\
 \text{s.t. : } &\Gamma_k \geq \gamma_k, \quad k \in A_l,
 \end{aligned} \tag{8.8}$$

where γ_k implies the SINR required for achieving a certain data rate at UE $_k$, and Γ_k is shown in (8.3). If the found $P_{A_l}^{\min}$ in (8.8) is within the AP's power budget P , then the corresponding A_l is a feasible subset of UEs and, equivalently, $\mathbf{a}_l \in \mathcal{A}_F$. Furthermore, the feasible subsets are *downward-closed*, which means that subsets of feasible sets are feasible.

Two well-known methods can be used to solve the sub-problems in (8.8): semidefinite relaxation based technique [53], and uplink-downlink duality based algorithm [50].

SDR-Based Solution

By defining $\mathbf{W}_k = \mathbf{w}_k \mathbf{w}_k^H, \forall k \in \mathcal{K}$, and relaxing the rank-1 constraint $\text{rank}(\mathbf{W}_k) = 1, \forall k \in \mathcal{K}$, we can write the second-order cone program (SOCP) in (8.8) in the semidefinite relaxed program format shown in (8.9). The resulting problem can be solved by SDR techniques and standard tools such as CVX [37].

$$\begin{aligned}
 P_{A_l}^{\min} &= \min_{\mathbf{w}_k, k \in A_l} \sum_{k \in A_l} \text{tr}(\mathbf{W}_k) \\
 \text{s.t. : } &\text{tr}(\mathbf{R}_{\mathbf{h}_k} \mathbf{W}_k) - \gamma_k \sum_{\substack{i \in A_l \\ i \neq k}} \text{tr}(\mathbf{R}_{\mathbf{h}_k} \mathbf{W}_i) \geq \gamma_k \sigma^2, \quad k \in A_l.
 \end{aligned} \tag{8.9}$$

Interestingly, it turns out that the SDR form (8.9) and the original problem (8.8) are exactly equivalent [55]. Therefore, the solution to the SDR problem outputs rank-1 matrices. However, it should be noted that, in general, an SDR problem gives a lower-bound on the optimal objective function.

UDD-Based Solution

While the SDR method yields the optimal solution for the problem in (8.9), there exists a more efficient solver which is a fast iterative algorithm based on the uplink-downlink duality [50]. The

optimization in the SDR method is performed over the M -by- M \mathbf{W}_k matrices, which have more unknowns than the original M -element beamforming vectors \mathbf{w}_k 's. Hence, the SDR solution comes at the cost of a relatively high computational complexity. To take advantage of the UDD method, we re-write the problem in (8.8) by using the normalized beamforming vectors, i.e., $\mathbf{u}_k = \mathbf{w}_k / \|\mathbf{w}_k\|$, and organizing them in matrix $\mathbf{U} = (\mathbf{u}_1, \dots, \mathbf{u}_K)$, using the notation $q_k = \|\mathbf{w}_k\|^2$. Accordingly, the problem becomes

$$\begin{aligned} P_{A_l}^{\min} &= \min_{\mathbf{U}, \mathbf{q}} \|\mathbf{q}\|_1 \\ \text{s.t. : } &\Gamma_k(\mathbf{U}, \mathbf{q}) \geq \gamma_k, \|\mathbf{u}_k\|_1 = 1, \forall k \in A_l, \end{aligned} \quad (8.10)$$

where $\mathbf{q} = (q_1, \dots, q_K)^T$, and $\Gamma_k(\mathbf{U}, \mathbf{q})$ is obtained by replacing $\mathbf{w}_k = \sqrt{q_k} \mathbf{u}_k$ in (8.3). Then, the minimum powers, q_k^* 's, and the normalized beamforming vectors, \mathbf{u}_k^* 's, can be found by applying the algorithm in [50, Table II].

Remark 1

In order for problem (8.8) to always have a solution, the rank of the channel matrix $\mathbf{H} = [\mathbf{h}_1, \dots, \mathbf{h}_K]$ should be greater than or equal to the number of UEs. For well-conditioned channels, the latter condition becomes $M \geq K$. Of course, there may be solutions for cases in which $M < K$, depending on the devices' required SINRs, i.e., the γ_k 's, and their channels, i.e., the \mathbf{h}_k 's.

With either method, SDR or UDD, the AP should solve the subproblems in (8.8) for at most $2^K - 1$ times to obtain the optimal allocation vector \mathbf{a}^* . While using the iterative algorithm in [50] is faster than solving with the SDR-based method, the exponential dependence of either of the two solution methods on the number of UEs makes them time-consuming, especially when the number of UEs is large. Sub-optimal solvers can be applied to overcome this issue. In Section 8.4, we propose a DNN-based approximate solver which outputs the allocation vector in almost no time, and is an attractive solution for complex systems where conventional iterative solvers lose their validity. Before proposing our DNN-based solution, let us find the optimal payment rule \mathbf{p}^* that encourages the UEs to play truthfully as their dominant strategy.

8.3.2 The Optimal Payment Rule

In the previous subsection, we leveraged optimization techniques for finding the optimal allocation rule. Here, our goal is to find the optimal payment rule based on the obtained optimal allocation rule. These two together constitute the optimal SWmax mechanism.

According to [54, Lemma 3.1], for each UE_k and all bid values of other UEs, i.e., \mathbf{b}_{-k} , the optimal allocation indicator a_k^* for UE_k , which is the k^{th} element of $\mathbf{a}^* = \operatorname{argmax}_{\mathbf{a} \in \mathcal{A}_F} S(\mathbf{b}, \mathbf{a})$, is a step function in terms of b_k . The critical value of this step function is $\tilde{b}_k = S^*(0, \mathbf{b}_{-k}) - S_{-k}^*(\infty, \mathbf{b}_{-k})$, where $S^*(0, \mathbf{b}_{-k})$ is the optimal social welfare from UEs other than UE_k assuming that UE_k is *not* served; and $S_{-k}^*(\infty, \mathbf{b}_{-k})$ is the optimal social welfare from UEs other than UE_k assuming that UE_k is served [54]. Consequently, the AP's SWmax mechanism, based on the bid profile \mathbf{b} from the UEs, is described by [54]

$$\mathbf{a}^* = \operatorname{argmax}_{\mathbf{a} \in \mathcal{A}_F} S(\mathbf{b}, \mathbf{a}), \quad (8.11a)$$

$$p_k^* = \begin{cases} \tilde{b}_k & \text{if } a_k = 1, \\ 0 & \text{if } a_k = 0, \end{cases} \quad (8.11b)$$

where (8.11b) is the payment rule.

The SWmax mechanism found above is dominant-strategy incentive-compatible (DSIC). DSIC auctions are those desired auctions in which the seller needs no strategy, i.e., need not know the valuation distribution of the UEs to design the auction; and each UE, independent of other agents' bidding strategies, should play truthfully to maximize its own benefit. The SWmax mechanism is often referred to as Vickrey-Clarke-Groves (VCG) mechanism in the auction literature [56].

8.4 Deep Learning Based Allocation Rule

As detailed in Section 8.3, the time-greediness feature of designing the optimal mechanism for the wireless information transfer system under consideration is due to the many runs of the optimization methods needed to find the allocation rule. In fact, once the optimal allocation rule is found, finding the optimal payment rule is straightforward by applying (8.11b). A practical solution to overcome the complexity of finding the allocation vector is via the application of DNNs.

To find $\mathbf{a}^* = \operatorname{argmax}_{\mathbf{a} \in \mathcal{A}_F} S(\mathbf{b}, \mathbf{a})$ via deep learning, we observe that it can be regarded as an unknown function mapping from the ensemble of the system parameters of interest, i.e., b_k 's, \mathbf{h}_k 's, and γ_k 's, to the corresponding optimal allocation rule \mathbf{a}^* . Note that the mapping depends on the \mathbf{h}_k 's and the γ_k 's through \mathcal{A}_F . Indeed, DNNs can be viewed as *universal approximators*: if properly trained, they are able to learn the input-output relationship between the system parameters and the desired allocation vector. This means that we can optimize a desired performance function for given parameters without explicitly having to solve any optimization problem—via SDR, UDD, or other optimization methods—but rather letting the DNN compute the allocation vector.

8.4.1 The Proposed Deep Neural Network Architecture

After trying several core architectures, such as fully-connected neural network (FcNN), convolutional neural network (CNN), and residual neural network (ResNet), the FcNN model showed the best performance in terms of accuracy.

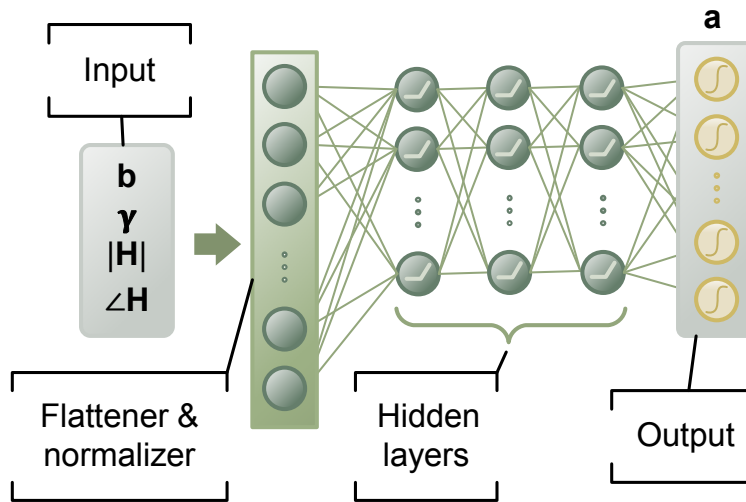


Figure 8.2: The DNN used for finding the allocation vector.

The schematic of the proposed DNN architecture is depicted in Fig. 8.2. The input to the DNN is $[\mathbf{b}, \boldsymbol{\gamma}, |\mathbf{H}|, \angle \mathbf{H}]$, where \mathbf{b} and $\boldsymbol{\gamma}$ are the bid and the demand profiles, and where $|\mathbf{H}|$ and $\angle \mathbf{H}$ are matrices holding the absolute value and angle of the complex elements of matrix \mathbf{H} . The input data is fed to a preprocessing unit composed of two operations: flattening and normalizing. With flattening, all the input data are placed in a column vector, and by the normalization operation the flattened data are bias-shifted and scaled to look like a standard normal distribution. The output

layer has K nodes, which corresponds to the dimension of the allocation vector \mathbf{a} . The output layer after being activated by the sigmoid (logistic) function will take values between 0 and 1. In fact, since our network is a multi-label multi-class classifier, the activation function of the output layer should be sigmoid function $f(x) = \frac{1}{1+\exp(-x)}$ that maps the summation node value $x \in \mathbb{R}$ to $(0, 1)$. When using the trained DNN for prediction, we round this output to only take binary values since the allocation vector is a binary vector.

To train the proposed DNN, we need to populate the training data-set and the corresponding labels. To this end, we solve the corresponding optimization problems for many network realizations using the efficient UDD-based algorithm. We used the *TensorFlow* interface [57] for building and training our DNN model. We tuned the hyper-parameters of the proposed DNN using the recently released hyper-parameter optimization framework *Keras-tuner* [58], which tries a preset number of trials looking for the best possible set of hyper-parameters with built-in search algorithms.

8.5 Performance Evaluation and Discussion

Now, we evaluate the accuracy of the proposed DNN architecture in predicting the exact allocation vectors. We instantiate our DNN from the architecture presented in Fig. 8.2 targeted for a system operation where transmissions undergo Rayleigh fading with $\mathbf{h}_k \sim \mathcal{CN}(\mathbf{0}, \sigma_k^2 \mathbf{I}_M)$. The system parameters are as follows: $P_{\max} = 3 \text{ W}$, $K = 4$, $M = 6$, $\sigma^2 = -50 \text{ dBm}$; and $b_k \sim \mathcal{U}(0.1, 1)$, $\gamma_k \sim \mathcal{U}(5, 35) \text{ dB}$, $\sigma_k^2 \sim \mathcal{U}(-80, -60) \text{ dBm}$, for $k \in \mathcal{K}$. $\mathcal{U}(a, b)$ denotes the uniform distribution in the interval (a, b) .

We first populate the training data by solving the optimization problem (8.7) offline, to find the optimal allocation vectors (as target labels) using the UDD-based algorithm for 199,000 realizations of the system model with the aforementioned parameters. The proper set of hyper-parameters found for the said system setting are shown in Table 8.1. We dedicated 20% of the data for testing purposes, and split the remaining 80% into 80% for the training and 20% for the validation. While the training and validation sets are used in plotting Fig. 8.3, the testing data is used in plotting the confusion matrix in Fig. 8.4.

As depicted in Fig. 8.2, our DNN has three hidden layers, each of which is described in Table 8.1. The regularizer used in the first hidden layer is the $l1$ -activity-regularizer with parameter $l1$ set

Table 8.1: Layout of the proposed DNN architecture (# trainable parameters: 10,362, # non-trainable parameters: 292)

Layer	Output dimension
Input (after flattening and normalizing)	56
Dense + Regularizer + ReLU	40
Dense + Batch normalization + ReLU	56
Dense + Batch normalization + ReLU	90
Dense + sigmoid	4

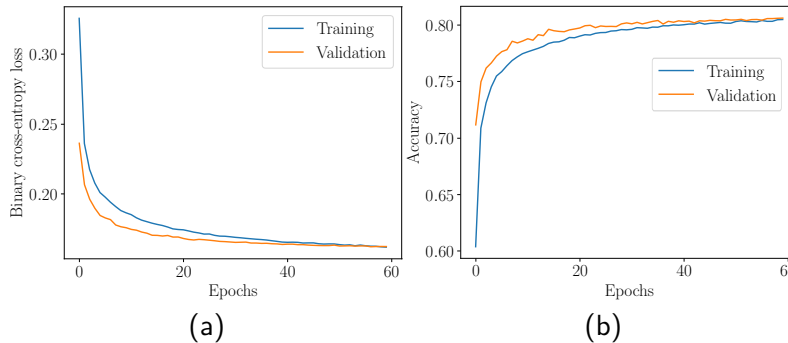


Figure 8.3: (a) The binary cross-entropy metric versus each epoch of training the DNN; (b) the accuracy metric versus each epoch of training the DNN.

to 0.0015. Activity regularizers allow us to apply penalties on layer activity during optimization. These penalties are incorporated in the binary cross-entropy loss function that the DNN tries to minimize during training. By doing this, we avoid over-fitting of our model. We used the well-known Adam optimizer [59] with initial learning rate 0.01 and a decay rate 0.0027. The batch size for training is 64. The last layer has a sigmoid activation layer as explained before.

Figure 8.3a shows the loss value of the training and validation data-sets. As observed, the curves intersect at almost the last epoch, after which over-fitting will occur. Fig. 8.3b shows the accuracy related to the training and validation data-sets. The accuracy metric used here differs from the built-in accuracy metric in the *Keras* library. It is a customized metric to measure the fraction of *exact* match between the target data and the predicted output data of the DNN. Fig. 8.3b reveals that an accuracy of 81% is reached with the proposed DNN.

To demonstrate the accuracy of the DNN for a specific target label, we rely on confusion matrices. Such matrices are usable only for multi-class single-label classifications. However, by decoding our model's binary target labels to decimal-valued target labels, we can use the confusion matrix to evaluate the accuracy of our model for different classes. In fact, such decoded target labels are the

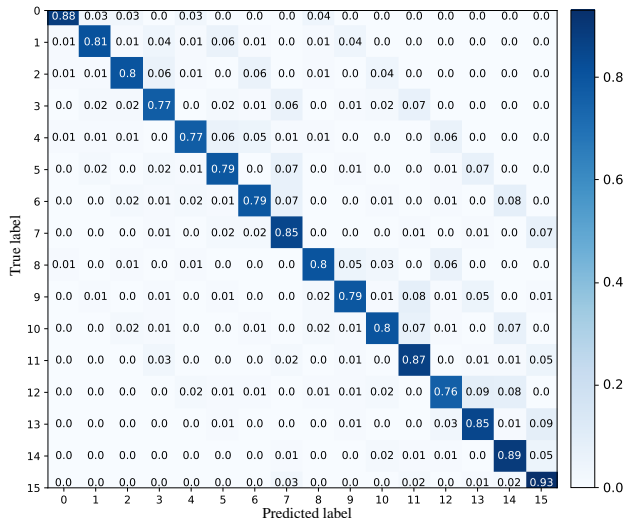


Figure 8.4: The normalized confusion matrix of the trained DNN.

Table 8.2: Comparison of the Computational Complexity

SDR	UDD	DNN
$\mathcal{O}(M^4 2^K)$	$\mathcal{O}(M^3 2^K)$	$\mathcal{O}(MK)$

same as subscript l in \mathbf{a}_l as defined in Section 8.3. Fig. 8.4 shows the normalized confusion matrix for the considered system setting with $K = 4$. Thus, the decoded (One-Hot) targets will have 16 labels. As observed from the diagonal of the confusion matrix, the normalized correct predictions range from 76% to 93%.

8.5.1 Computational Complexity

The iterative-based algorithms, SDR- and UDD-based, have exponential time complexity. In Table 8.2, the computational complexity of the proposed DNN-based method is compared to that of the SDR- and UDD-based techniques. In computing the computational complexity, it is assumed that, for the SDR-based method, the general-purpose interior-point algorithm [60] is used for each branch $k \in \{1, \dots, 2^K - 1\}$ of the well-known Branch-and-Bound (BnB) algorithm, and for the UDD-based method the iterative algorithm in [50] is used in each branch of the BnB algorithm. In terms of the number of antennas, M , either of the conventional methods has polynomial time complexity whereas the proposed DNN-based method has linear time complexity. Importantly, while the conventional algorithms both have exponential time complexity in terms of the number of UEs, K , the DNN-based method has linear complexity.

8.6 Summary

We tackled the problem of finding the optimal social-welfare maximizing (SWmax) dominant-strategy incentive-compatible mechanism, namely, the allocation and payment rules, for a wireless information transfer system wherein a multi-antenna AP sells its spatially-multiplexed radio links to SINR-constrained UEs. Having solved the SWmax problem by applying two conventional optimization techniques, namely, semidefinite relaxation and uplink-downlink duality methods, we highlighted the time greediness of such techniques for finding the optimal allocation rule, especially as the number of UEs increases. Then, we proposed and trained a deep neural network to find the allocation rule in almost real time, with an accuracy of 81%. While exploring other architectures to increase accuracy is a promising step for future work, considering partial CSI availability at the AP and then applying machine-learning techniques to jointly estimate the CSI and the optimal allocation rule is also another challenging avenue.

Chapter 9

Learning-Based Auction-Driven Beamforming for SWIPT¹

9.1 Literature Review

Recently, artificial intelligence (AI) has started to attract significant interest in the research domain of mobile and wireless communication networks [29]. After its clear success in computer vision, natural language processing, speech and image recognition, AI is now touching other domains such as wireless communications and mobile networking. Such AI-related research soaring in the wireless domain is indeed due to the growing diversity and complexity of mobile network architectures which has made the processing, monitoring, and managing in such networks intractable.

Such complexity in wireless networks arises in the allocation task of the network resources to wireless devices that are heterogeneous in different aspects, including the service demands, the device capability, the operating conditions, etc. Assuming many devices with different quality-of-service requirements in the inherently varying condition of the wireless channels, the resource allocation can simply become impractical without reaching out for learning-based techniques. Deep learning (DL), being generally considered as the key branch of machine-learning (ML) techniques, is about learning and prediction by means of training (deep) neural networks (DNNs).

¹A. Bayat and S. Aïssa, “Learning-Based Auction-Driven Beamforming for Wireless Information and Power Transfer,” IEEE Transactions on Wireless Communications, (under second round of review).

Besides AI, the application of economical models such as auctions for allocation of the available (virtual and real) resources to the clients is becoming necessary for the operation of future wireless communication networks [19]. In fact, next-generation communication networks are envisioned to be mainly based on user-centric online service provisioning schemes, where users act as economical agents that compete for their target services according to competition market models such as *auctions* [25]. Auctions are probably the best marketing model when entities tend to behave selfishly to maximize their own utility. The inclusion of the economical behavior of the agents in managing the resources grants the agents more degrees of freedom to bid for their desired service based on their demands and their monetary budgets while considering probable availability of resources from other service providers in the market. It is foreseen that marketing and pricing tasks will no more be statically settled in a different offline service-level agreement, but rather of dynamic, online, and cross-layered, design nature [22, 23, 24, 25].

9.1.1 Related Works

The subsection reviews the related works to this chapter in three sections which might have some overlap with each other in terms of their subject. The first part reviews the beamforming algorithms for wireless systems, and in particular, for information and power transfer systems. The next part reviews the application of AI in the wireless domain, in particular, related to resource allocation in wireless networks. And as the last part, a review on the recent applications of game theory, in particular auction theory, in wireless networks is presented.

Beamforming Algorithms

Probably a pioneer work for applying semidefinite programming for downlink beamforming is [53]. Therein, the authors formulate the problem of finding the optimal choice of beamformers for simultaneous transmission to several co-channel users while minimizing the total transmitted power and satisfying a certain level of quality of service for the users. The problem is then solved using a semidefinite relaxation and interior-point methods. About the same time, Rashid-Farrokhi et al in [61] derived a faster solution for the problem of transmit beamforming and power control for cellular wireless systems, devising the idea of “virtual uplink power”. The latter idea was indeed a

duality property which was introduced in [50] and reapplied for designing a more integral solution that accounts for the aspect of feasibility which was not considered in [61].

The authors in [62] applied the idea of the uplink-downlink duality in [50] and tailored the algorithm to find the optimal beamforming vectors for SWIPT systems. The objective is to maximize the weighted sum-power transferred to all energy receivers while respecting the SINR constraints of the information receivers. The complexity of the proposed algorithm in [62] is then compared with the SDR-based solution approaches revealing that their proposed algorithm is slightly more efficient than the conventional SDR-based techniques. In [63], algorithms for transmit beamforming for wireless information and power transfer are proposed for two receiver types of time-sharing and power splitting. Again the computational complexity, i.e., running time, of the proposed algorithms is compared with the SDR-based methods. Therein, a thorough complexity analysis of the beamforming algorithms is presented. Further, for some state-of-the-art multiuser beamforming algorithms for wireless information and power transfer systems one can refer to [63] and the references therein.

Application of AI in Wireless Communications

A recent comprehensive survey of DL methodologies, and their application in wireless communications networks, is provided in [49]. The survey in [29] reviews the applications of AI in mobile networking. A few of such network-level applications are related to mobility analysis, network control, and network security. There are also studies on the application of AI in the physical layer of wireless communication networks [64, 65, 66, 67, 68, 69]. The authors in [64] demonstrate the power of DL in signal compression and signal detection. In [66], the possibility of exceeding the performance of the conventional spatial diversity multiple-input multiple-output (MIMO) systems using DL techniques and autoencoders is demonstrated. DL is applied in [65] to develop an autoencoder-based CSI sensing and recovery mechanism, namely CsiNet, which learns to effectively use channel structure from training samples. CsiNet is shown to improve reconstruction quality compared with existing compressive sensing-based methods. Works [68] and [69] apply DL and reinforcement learning techniques in simultaneous wireless information and power transfer (SWIPT) systems. The authors in [70] apply deep reinforcement learning for simultaneous energy harvesting and information transmission in a MIMO full-duplex system.

Application of Auction Theory in Wireless Communications

While there is a large body of work on the application of game theory and auction theory for the design and analysis of resource allocation mechanisms in wireless communication networks [71, 19, 24, 25], works related to wireless powered communications are relatively scarce [26, 72, 27, 28, 51, 52]. In general, service providers need to simultaneously serve multiple users with different requirements. In some applications, information receivers (IRs) and energy receivers (ERs) are independent entities with limited monetary budget requesting a service with a certain level of quality from a provider which is independently trying to maximize its own revenue. In such networks, where all entities behave selfishly, auctions are undoubtedly the best market model to keep every entity happy. As an example application, consider a network of wireless-powered devices like electronic wearable devices capable of harvesting wireless energy from the environment as the wireless energy receivers (ERs) in co-existence with wireless devices like smart phones which need to download data (IRs) from the access point. Here the hybrid access point (HAP) belongs to a third-party company who wishes to maximize its own revenue through designing optimal allocation-payment rules.

9.1.2 The Contribution of Our Work

In this work, we consider a single-band heterogeneous SWIPT network, in which a multi-antenna hybrid access point (HAP) tries to maximize its revenue by beamforming the information and energy towards the single-antenna IRs and ERs, respectively. The network operates in an auction framework. Based on the bids, requested service levels, learned valuation distributions, and channel state information (CSI) of the users, the HAP, as the auctioneer and the seller, aims to find the optimal set of users and the optimal pricing which maximize its revenue while encouraging the users to bid truthfully. We formulate this mechanism problem as a mixed-integer non-linear programming one—which is NP-hard—and solve it using an efficient Branch-and-Bound algorithm while applying the semidefinite programming (SDP) technique in each branch. Since solving this problem is time-greedy, particularly when the number of devices in the network is fairly large, such conventional dynamic programming optimization techniques are no more practical due to their excessive computation delays—exponential time complexity. A promising solution to this problem consists of applying DL algorithms, particularly deep neural networks (DNN), to output the solution almost in real time. We propose a DNN-based architecture to solve the multi-label classification task and

find the desired subset of users, based on which the optimal beamforming vectors can be found by one-time running of the semidefinite relaxation (SDR) algorithm or the faster uplink-downlink duality based one [50, 62]. Such DNN-based architectures are black-boxes which need to be trained, and their performance has to be validated before they can be integrated in the system to predict the solution. In this vein, we solve the mixed-integer non-linear programming problem offline for a very large number of realizations of the input data to the HAP, save the training dataset and the obtained training labels in a database, and then use the latter to train our proposed DNN so as to estimate the allocation rule of the proposed revenue-maximizing auction mechanism. Furthermore, we propose a heuristic sub-optimal algorithm, which follows the accuracy performance of the DNN-based solution with polynomial time complexity. The criteria used in the proposed heuristic model is exploited in transforming the input data to the proposed DNN into a form that leads to faster training convergence rate and more accurate training.²

In detailing these contributions, the remainder of the chapter is organized as follows. Section 9.2 models the SWIPT network, both physically and economically. In Section 9.3, we formulate the revenue maximization problem. In Section 9.4, we find the feasible allocation set as part of the solution of the revenue-maximization problem using the SDR-based technique. We also investigate wireless information transfer (WIT) and wireless power transfer (WPT) as two particular cases of the SWIPT model. In section 9.5, the optimal revenue-maximizing mechanism is obtained. Section 9.6 presents an efficient Branch-and-Bound algorithm to obtain the optimal allocation rule along with a heuristic iterative algorithm which finds a sub-optimal solution. Section 9.7 presents the proposed DNN-based solution, and discusses its architecture and training. In section 9.8, we evaluate the performance of the proposed DNN for three network operation modes: SWIPT, WIT, and WPT. We also compare the accuracy of the proposed DNN-based and heuristic methods. Finally, Section 9.9 summarizes the chapter.

²While this work was in progress, preliminary results related to the special case where the network is comprised of information devices only and, specifically, on the application of deep learning for the data beamforming to IRs with the objective of maximizing the social welfare of the users, were submitted to IEEE Globecom 2020 [73]. Our current work has the following key differences with [73]: i) our current work is about designing revenue-maximization for a SWIPT network whereas [73] proposes a deep neural network for social welfare maximization in a WIT network, ii) in the current chapter, an efficient Branch-and-Bound algorithm to find the optimal solutions is proposed, iii) in the current chapter a heuristic goodness-based algorithm is also proposed and its performance is compared for different input active IR or ER densities.

Notations

The following set of notations will be adopted throughout the chapter. Vectors and matrices are shown with bold lower- and upper-case letters, respectively. Symbols $(.)^T$ and $(.)^H$ denote the transpose and conjugate transpose operators. The identity matrix of order m is denoted by \mathbf{I}_m , $\text{tr}(\mathbf{A})$ is the trace of square matrix A , and $\mathbf{0}$ is a zero vector with proper dimension. The l_1 -norm and l_2 -norm (Euclidean) are denoted by $\|\cdot\|_1$ and $\|\cdot\|$, respectively, and $\mathbb{E}[\cdot]$ stands for mathematical expectation.

9.2 The Network Modeling

Modeling the SWIPT network consists of the physical modeling of the network elements, the economical (bidding) behavioral modeling of the devices, and the framework of the auction.

9.2.1 Physical Modeling

The SWIPT network consists of an HAP serving multiple devices within a shared spectrum band. The HAP is equipped with M antennas, and has a power budget of P Watts. A total number of $K = I + J$ user equipments (UEs) coexist in the network, with I denoting the number of IRs, and J being the number of ERs. The set $\mathcal{I} = \{1, \dots, I\}$ contains the indices of the information devices, and $\mathcal{J} = \{1, \dots, J\}$ is the index set of the energy devices. All devices are equipped with single antennas, and work in half-duplex mode similar to the HAP. The HAP is to provide wireless energy to ERs, and to send data to IRs. Without loss of generality, we consider linear precoding at the HAP, such that each ER/IR receiver is assigned with one dedicated energy/information transmission beam.³ The signal transmitted from the HAP is given by

$$\mathbf{x} = \sum_{i \in \mathcal{I}} \mathbf{w}_i s_{\text{IR}_i} + \sum_{j \in \mathcal{J}} \mathbf{v}_j s_{\text{ER}_j}, \quad (9.1)$$

where, for any $\text{IR}_i, i \in \mathcal{I}$, $\mathbf{w}_i \in \mathbb{C}^{M \times 1}$ is the beamforming vector and s_{IR_i} is the information-bearing signal, and where, for any $\text{ER}_j, j \in \mathcal{J}$, $\mathbf{v}_j \in \mathbb{C}^{M \times 1}$ is the beamforming vector and s_{ER_j} is the energy-carrying signal.

³Later in Section 9.4, we will show that only one beamforming vector is sufficient for all ERs.

For the information signals, we assume Gaussian inputs, i.e., the s_{IR_i} 's are i.i.d. circularly-symmetric complex Gaussian (CSCG) random variables with zero mean and unit variance, denoted by $s_{\text{IR}_i} \sim \mathcal{CN}(0, 1), i \in \mathcal{I}$. For the energy signals, since $s_{\text{ER}_j}, j \in \mathcal{J}$, carries no information, it can be any arbitrary (random) signal that satisfies the radio regulations on microwave radiation [20]. Without loss of generality, we assume that the s_{ER_j} 's are independent white sequences from an arbitrary distribution with $\mathbb{E}[|s_{\text{ER}_j}|^2] = 1, j \in \mathcal{J}$. Given the limit P on the HAP's transmit power, the constraint $\mathbb{E}[\mathbf{x}^H \mathbf{x}] = \sum_{i \in \mathcal{I}} \|\mathbf{w}_i\|^2 + \sum_{j \in \mathcal{J}} \|\mathbf{v}_j\|^2 \leq P$ must hold.

The fading channels between the transmitter and the receivers are quasi-static, i.e., channel coefficients are assumed to be fixed during the channel coherence time. Denote $\mathbf{h}_i = (h_{i,1}, \dots, h_{i,M})^T$ and $\mathbf{g}_j = (g_{j,1}, \dots, g_{j,M})^T$ as the channel vectors from the HAP to IR_i and ER_j , respectively, where $\|\mathbf{h}_i\|^2 = \sigma_{\mathbf{h}_i}^2$ and $\|\mathbf{g}_j\|^2 = \sigma_{\mathbf{g}_j}^2$ for all $i \in \mathcal{I}$ and $j \in \mathcal{J}$. The channel vectors $\mathbf{h}_i, i \in \mathcal{I}$, and $\mathbf{g}_j, j \in \mathcal{J}$, are drawn independently from continuous distribution functions $F_{h_i}(\mathbf{h}_i)$ and $F_{g_j}(\mathbf{g}_j)$, with $h_{i,m}$ and $g_{j,m}$ being the complex channel gains from the m^{th} antenna of the HAP array, $m \in \{1, \dots, M\}$, to IR_i and ER_j , respectively, are assumed to be perfectly tracked at the devices and fed back to the HAP via an error-free zero-delay feedback channel.

The received base-band equivalent signal at $\text{IR}_i, i \in \mathcal{I}$, is

$$y_i = \mathbf{h}_i^T \mathbf{x} + z_i, \quad (9.2)$$

where $z_i \sim \mathcal{CN}(0, \sigma_i^2)$ is the i.i.d. Gaussian noise. Therefore, the signal-to-noise-plus-interference ratio (SINR) of information receiver $\text{IR}_i, i \in \mathcal{I}$, can be written as

$$\begin{aligned} \Gamma_i &= \frac{|\mathbf{h}_i^T \mathbf{w}_i|^2}{\sum_{k \in \mathcal{I}, k \neq i} |\mathbf{h}_i^T \mathbf{w}_k|^2 + \sum_{j \in \mathcal{J}} |\mathbf{h}_i^T \mathbf{v}_j|^2 + \sigma_i^2} \\ &= \frac{\mathbf{w}_i^H \mathbf{R}_i \mathbf{w}_i}{\sum_{k \in \mathcal{I}, k \neq i} \mathbf{w}_k^H \mathbf{R}_i \mathbf{w}_k + \sum_{j \in \mathcal{J}} \mathbf{v}_j^H \mathbf{R}_i \mathbf{v}_j + \sigma_i^2}, \end{aligned} \quad (9.3)$$

where $\mathbf{R}_i = \mathbb{E}[\mathbf{h}_i \mathbf{h}_i^H]$ is the covariance matrix, which for the case of full CSI knowledge becomes $\mathbf{R}_i = \mathbf{h}_i \mathbf{h}_i^H$.

The SINR is directly related to the device's performance indicators such as the bit error rate (BER) and the data rate. For example, under a fixed BER and assuming quadrature-amplitude modulation, a practical achievable rate can be computed as $R_i = \log(1 + \Gamma_i/\Upsilon)$ bps/Hz, in which

Υ denotes the SNR gap to capacity. The SNR gap is always greater than 1 (0 dB), and it gives an approximate relation between the SINR and the rate.

The received power at ER $_j$, $j \in \mathcal{J}$, is given by

$$\begin{aligned} Q_j &= \sum_{i \in \mathcal{I}} |\mathbf{g}_j^T \mathbf{w}_i|^2 + \sum_{k \in \mathcal{J}} |\mathbf{g}_j^T \mathbf{v}_k|^2 \\ &= \sum_{i \in \mathcal{I}} \mathbf{w}_i^H \mathbf{C}_j \mathbf{w}_i + \sum_{k \in \mathcal{J}} \mathbf{v}_k^H \mathbf{C}_j \mathbf{v}_k. \end{aligned} \tag{9.4}$$

where $\mathbf{C}_j = \mathbb{E}[\mathbf{g}_j \mathbf{g}_j^H]$ is the covariance matrix, which for the case of full CSI knowledge becomes $\mathbf{C}_j = \mathbf{g}_j \mathbf{g}_j^H$.

9.2.2 Bidding Modeling

The HAP as the service seller plays the role of the auctioneer as well. The devices play the roles of bidders which have different service valuations sending their bids in each round of auction to get served by the HAP. The HAP solicits the devices' bids in a sealed fashion, i.e., the devices are not aware of each others' bids.

It is assumed that all devices have non-zero service requests and play in all auction rounds. Each IR $_i$, $i \in \mathcal{I}$, sends its service request in the form of the minimum SINR, γ_i , required to receive D_i bits of data in the auction duration τ_a , by bidding b_{IR_i} . Similarly, each ER $_j$, $j \in \mathcal{J}$, requests q_j units of energy for the auction duration τ_a by bidding b_{ER_j} . The HAP knows in advance that IR $_i$ and ER $_j$ draw their private valuations ν_{IR_i} and ν_{ER_j} from the distributions $\mathcal{F}_{\text{IR}_i}$ and $\mathcal{F}_{\text{ER}_j}$ for each round of auction.⁴ These distributions are assumed independent, but not necessarily identical. Without loss of generality, we set $\tau_a = 1$. Also, let $\boldsymbol{\gamma} = (\gamma_1, \dots, \gamma_I)^T$ and $\mathbf{q} = (q_1, \dots, q_J)^T$ denote the demand profiles of IRs and ERs, respectively, and denote $\mathbf{b}_{\text{IR}} = (b_{\text{IR}_1}, \dots, b_{\text{IR}_I})^T$ and $\mathbf{b}_{\text{ER}} = (b_{\text{ER}_1}, \dots, b_{\text{ER}_J})^T$ as the bid profiles of IRs and ERs, respectively.

⁴By private values, it is meant that the values are unknown to the seller (HAP) and to other bidders. Valuation is the maximum willingness-to-pay of an agent for the commodity being sold. Also, the distributions $\mathcal{F}_{\text{IR}_i}$ and $\mathcal{F}_{\text{ER}_j}$ can be estimated (learned) from the UEs' bids history in the past auctions [56, 74].

9.2.3 Auction Framework

We consider a single-parameter (or single-dimensional) auction environment, where the outcomes of the HAP as the auction mechanism designer are two rules: (i) the *allocation rule* $\mathbf{a} = (\mathbf{a}_{\text{IR}}, \mathbf{a}_{\text{ER}})$, where $\mathbf{a}_{\text{IR}} = (a_{\text{IR}_1}, \dots, a_{\text{IR}_I})^T$ and $\mathbf{a}_{\text{ER}} = (a_{\text{ER}_1}, \dots, a_{\text{ER}_J})^T$, with each element of vector \mathbf{a}_{IR} (\mathbf{a}_{ER}) being an indicator for whether IR_i (ER_j) is to be served or not and, thus, $\mathbf{a}_{\text{IR}} \in \{0, 1\}^I$ ($\mathbf{a}_{\text{ER}} \in \{0, 1\}^J$); and (ii) the *payment rule* $\mathbf{p} = (\mathbf{p}_{\text{IR}}, \mathbf{p}_{\text{ER}})$, where $\mathbf{p}_{\text{IR}} = (p_{\text{IR}_1}, \dots, p_{\text{IR}_I})^T$ and $\mathbf{p}_{\text{ER}} = (p_{\text{ER}_1}, \dots, p_{\text{ER}_J})^T$, with each element of vector \mathbf{p}_{IR} (\mathbf{p}_{ER}) denoting the amount IR_i (ER_j) is required to pay the auctioneer, i.e. the HAP, during any round of auction. As depicted in Fig. 9.1, each round of

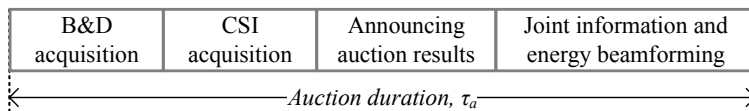


Figure 9.1: Breakout of each auction round.

auction is composed of four parts: (i) bids-and-demands (B&D) acquisition, (ii) CSI acquisition, (iii) auction results announcing, and (iv) information beamforming.

To find the optimal beamforming vectors \mathbf{w}_i^* , $i \in \mathcal{I}$, and \mathbf{v}_j^* , $j \in \mathcal{J}$, the key step is to find the optimal allocation vector \mathbf{a}^* and the optimal payment vector \mathbf{p}^* that maximize the revenue of the HAP. Then, the HAP sends to IR_i and ER_j the pairs $(a_{\text{IR}_i}^*, p_{\text{IR}_i}^*)$ and $(a_{\text{ER}_j}^*, p_{\text{ER}_j}^*)$, respectively, as the auction result to let them know whether they have won the auction and how much they should pay in case of a win.⁵

At the beginning of each auction round, the HAP solicits the UEs for their demands and their corresponding bids during the B&D-acquisition period. Then, the HAP acquires the CSI.⁶ Afterwards, the HAP solves for the optimal allocation rule and payment rule that maximize its expected revenue while keeping the devices incentivized to play truthfully, announces the allocation-payment rules to all UEs to let them know who are going to get service and how much to pay for it and, finally, performs joint beamforming to transfer the information and power to the chosen UEs.

⁵Allocation (payment) “rule” and allocation (payment) “vector” are used interchangeably throughout this chapter.

⁶To estimate the CSI, one can consider either *one-way training* by assuming existence of channel reciprocity, or *two-way training* which requires each receiver to perform channel estimation followed by channel feedback to the HAP, which in turn will consume additional energy. In practice, there exists a design tradeoff especially for the ERs: higher accuracy for both channel estimation and feedback reporting may lead to higher harvested energy due to the transmit beamforming gain, but also induces higher energy consumption that can even offset the harvested energy gain [44]. For simplicity, in this work, we assume that such energy consumption at ERs is negligible compared to their harvested energy, and that the training time is also negligible compared to the auction period.

9.2.4 Utility Functions

First off, for ease of writing, let us define $\mathcal{K} = \{1, \dots, I-1, I, I+1, \dots, I+J\}$ as the ordered set of all the UEs in the network. With this notational convention, $\text{UE}_k = \text{IR}_k$ for $k \in \mathcal{I}$ and $\text{UE}_k = \text{ER}_k$ for $k \in \{I+1, \dots, I+J\}$. We also denote the bid vector by $\mathbf{b} = \begin{pmatrix} \mathbf{b}_{\text{IR}} \\ \mathbf{b}_{\text{ER}} \end{pmatrix}$, and the demand vector with $\mathbf{d} = \begin{pmatrix} \gamma \\ \mathbf{q} \end{pmatrix}$.

In designing optimal mechanisms for auctions, there are two fundamental objectives: *social welfare*, a.k.a. social surplus, and *revenue*, a.k.a. profit.

The revenue generated from the payment rule \mathbf{p} constitutes the utility of the HAP. Specifically, it is the cumulative payment of the bidders, i.e.

$$u_{\text{HAP}} = \sum_{k \in \mathcal{K}} p_k. \quad (9.5)$$

For $\text{UE}_k, k \in \mathcal{K}$, with valuation v_k , the utility—assuming the quasi-linear model [54]—is defined as follows:⁷

$$u_k = \nu_k a_k - p_k, \quad (9.6)$$

It should be emphasized that a_k and p_k depend on the bid profile \mathbf{b} .

The social welfare, resulting from the allocation rule \mathbf{a} , is the cumulative valuations of all the agents in the auction, i.e.

$$S(\boldsymbol{\nu}, \mathbf{a}) = \sum_{k \in \mathcal{K}} \nu_k a_k = \mathbf{a}^T \boldsymbol{\nu}, \quad (9.7)$$

where vector $\boldsymbol{\nu} = \begin{pmatrix} \boldsymbol{\nu}_{\text{IR}} \\ \boldsymbol{\nu}_{\text{ER}} \end{pmatrix}$, in which $\boldsymbol{\nu}_{\text{IR}} = (\nu_{\text{IR}_1}, \dots, \nu_{\text{IR}_I})^T$ and $\boldsymbol{\nu}_{\text{ER}} = (\nu_{\text{ER}_1}, \dots, \nu_{\text{ER}_J})^T$, holds the valuations of the UEs. Thus, $u_{\text{HAP}} = \sum_{k \in \mathcal{K}} p_k = \sum_{i \in \mathcal{I}} p_{\text{IR}_i} + \sum_{j \in \mathcal{J}} p_{\text{ER}_j}$, and $S(\boldsymbol{\nu}, \mathbf{a}) = \mathbf{a}^T \boldsymbol{\nu} = \mathbf{a}_{\text{IR}}^T \boldsymbol{\nu}_{\text{IR}} + \mathbf{a}_{\text{ER}}^T \boldsymbol{\nu}_{\text{ER}}$. Bid b_k is the number that $\text{UE}_k, k \in \mathcal{K}$, declares to the HAP as payment for its demand d_k , whereas valuation v_k is the true belief of the device about its demand d_k .

⁷In a quasi-linear utility model, an agent goal is choosing his bid so as to maximize the difference between his valuation and his payment

9.3 The Problem Formulation

Finding the optimal revenue maximizing (Rmax) mechanism is equivalent to finding the optimal allocation and payment rules. These rules can be obtained by solving the following Rmax problem:

$$\max_{\mathbf{a} \in \mathcal{A}_F} \mathbb{E}_{\nu} [u_{\text{HAP}}] = \mathbb{E}_{\nu} \left[\sum_{k \in \mathcal{K}} p_k(\nu) \right], \quad (9.8)$$

where the expectation is w.r.t. the distribution $\mathcal{F}_{\mathcal{K}} = \prod_{k \in \mathcal{K}} \mathcal{F}_k = \prod_{i \in \mathcal{I}} \mathcal{F}_{\text{IR}_i} \prod_{j \in \mathcal{J}} \mathcal{F}_{\text{ER}_j}$ over the bidders' valuations $\nu_k, k \in \mathcal{K}$. In (9.8), \mathcal{A}_F is the set of all feasible allocation vectors, which depends on the CSI of the channels $\mathbf{h}_i, i \in \mathcal{I}$, and $\mathbf{g}_j, j \in \mathcal{J}$, and on the devices' demand profile \mathbf{d} . An allocation vector is deemed feasible if the minimum power required to satisfy the demand constraints of the subset of devices represented by that allocation vector is less than the power budget of the HAP.

The problem in (9.8) states that the optimal allocation vector \mathbf{a}^* corresponds to the feasible set of users that results in the largest sum of payments. However, the payment rule \mathbf{p} itself should be carefully found to keep the devices incentivized to play truthfully. In fact, there are three unknowns in (9.8): \mathbf{a}^* , \mathbf{p}^* , and \mathcal{A}_F . The latter is independent of the first two unknowns and is what is firstly obtained in Section 9.4. The revenue-maximizing mechanism which constitutes the optimal pair $(\mathbf{a}^*, \mathbf{p}^*)$ will be obtained in Section 9.5.

9.4 Finding the Feasible Allocation Set \mathcal{A}_F

In order for the HAP to find the feasible allocation vectors out of all possible realizations of allocation vectors $\mathbf{a}^{(l)} \in \{0, 1\}^K, l \in \{0, 1, \dots, 2^K - 1\}$, a series of non-convex optimization problems should be solved. Let's correspond a subset $A^{(l)} \subset \mathcal{K}$ to each $\mathbf{a}^{(l)} = (a_1^{(l)}, \dots, a_K^{(l)})^T$ for any $l \in \{0, 1, \dots, 2^K - 1\}$, so that $\text{UE}_k \in A^{(l)}$ iff $a_k^{(l)} = 1, k \in \mathcal{K}$. Superscript l is the decimal representation of the binary vector $\mathbf{a}^{(l)}$. We put the IR-type and the ER-type devices in $A^{(l)}$ into the subsets $A_{\text{IR}}^{(l)}$ and $A_{\text{ER}}^{(l)}$, respectively. Similarly, $\mathbf{a}^{(l)} = \begin{pmatrix} \mathbf{a}_{\text{IR}}^{(l)} \\ \mathbf{a}_{\text{ER}}^{(l)} \end{pmatrix}$.

In general, we face a mixed-integer non-linear program. Note that there are $2^K - 1$ optimization problems to be solved, as worst-case, to get \mathcal{A}_F . Hence, the problem has exponential time complexity.

To illustrate how $\mathbf{a}^{(l)}$ is interpreted, consider the example of $I = 3$ and $J = 1$, which results in $K = 4$ devices and the index set $\mathcal{K} = \{1, 2, 3, 4\}$. Then, $\mathbf{a}^{(0)} = (0, 0, 0, 0)^T$ corresponds to $A^{(0)} = \emptyset$, meaning that no devices are chosen for allocation; $\mathbf{a}^{(1)} = (0, 0, 0, 1)^T$ corresponds to $A^{(1)} = \{4\}$ meaning that no IR devices are chosen and the only ER device is selected for allocation; and $\mathbf{a}^{(2)} = (0, 0, 1, 0)^T$ corresponds to $A^{(2)} = \{3\}$ which means that only IR₃ is chosen for allocation.

Each problem corresponding to $\mathbf{a}^{(l)}$ is a power minimization problem, which consists of finding the minimum transmit power required by the HAP to fulfill the demands of the chosen UEs in subset $A^{(l)}$, and is formulated as follows

$$\begin{aligned}
P_{A^{(l)}}^{\min} &= \min_{\substack{\mathbf{w}_i, i \in A_{\text{IR}}^{(l)} \\ \mathbf{v}_j, j \in A_{\text{ER}}^{(l)}}} \sum_{i \in A_{\text{IR}}^{(l)}} \|\mathbf{w}_i\|^2 + \sum_{j \in A_{\text{ER}}^{(l)}} \|\mathbf{v}_j\|^2, \\
\text{s.t. : } &\Gamma_i \geq \gamma_i, i \in A_{\text{IR}}^{(l)} \\
&Q_j \geq q_j, j \in A_{\text{ER}}^{(l)},
\end{aligned} \tag{9.9}$$

where Γ_i and Q_j are shown in (9.3) and (9.4), respectively. We recall that the γ -parameters imply the SINRs required for achieving certain data rates at the IRs, and that the q -parameters describe the amount of input power needed by ERs to meet an equivalent output DC power requirement. If the found $P_{A^{(l)}}^{\min}$ in (9.9) is within the HAP's power budget P , then the corresponding $A^{(l)}$ is a feasible subset of UEs and equivalently $\mathbf{a}^{(l)} \in \mathcal{A}_F$. Furthermore, the feasible subsets are *downward-closed*, which means that subsets of feasible sets are feasible themselves.

By defining $\mathbf{W}_i = \mathbf{w}_i \mathbf{w}_i^H$, $i \in \mathcal{I}$, and $\mathbf{V}_j = \mathbf{v}_j \mathbf{v}_j^H$, $j \in \mathcal{J}$, we can write the original quadratically-constrained quadratic problem (QCQP) (9.9) in the following format which can be efficiently solved

by SDR techniques.

$$\begin{aligned}
P_{A^{(l)}}^{\min} &= \min_{\substack{\mathbf{W}_i, i \in A_{\text{IR}}^{(l)} \\ \mathbf{V}_j, j \in A_{\text{ER}}^{(l)}}} \sum_{i \in A_{\text{IR}}^{(l)}} \text{tr}(\mathbf{W}_i) + \sum_{j \in A_{\text{ER}}^{(l)}} \text{tr}(\mathbf{V}_j) \\
\text{s.t. : } &\text{tr}(\mathbf{R}_i \mathbf{W}_i) - \gamma_i \left(\sum_{\substack{k \in A_{\text{IR}}^{(l)} \\ k \neq i}} \text{tr}(\mathbf{R}_i \mathbf{W}_k) + \sum_{j \in A_{\text{ER}}^{(l)}} \text{tr}(\mathbf{R}_i \mathbf{V}_j) \right) \geq \gamma_i \sigma_i^2, \quad i \in A_{\text{IR}}^{(l)}, \\
&\sum_{k \in A_{\text{IR}}^{(l)}} \text{tr}(\mathbf{C}_j \mathbf{W}_k) + \sum_{k \in A_{\text{ER}}^{(l)}} \text{tr}(\mathbf{C}_j \mathbf{V}_k) \geq q_j, \quad j \in A_{\text{ER}}^{(l)}, \\
&\mathbf{W}_i \succeq 0, \mathbf{R}_i \succeq 0, \quad i \in A_{\text{IR}}^{(l)}, \\
&\mathbf{V}_j \succeq 0, \mathbf{C}_j \succeq 0, \quad j \in A_{\text{ER}}^{(l)}.
\end{aligned} \tag{9.10}$$

The optimization problem in (9.10) is of conic form, and can be solved using standard tools such as CVX [37]. It can be understood from [62] that the SDR problem in (9.10) is tight meaning that the solutions \mathbf{W}_i^* 's and \mathbf{V}_j^* 's are rank-1 maximum. This will be further explained in subsection 9.4.3.

Next, to further discuss the solution to (9.10), we study two particular models of the network: (i) the WIT scenario, where only IR devices are active, and (ii) the WPT scenario, which correspond to the network with ER devices only. After solving the problem related to either scenario with conventional optimization tools and techniques, we argue the inherent time-greediness feature of these techniques for real-time applications like our network model, which makes such techniques lose their applicability. We propose alternative sub-optimal solutions in subsection 9.6.2 for each scenario.

9.4.1 Wireless Information Transfer Network

Considering IR devices only in the network, i.e. $\mathcal{K} = \mathcal{I}$, the problem (9.9) becomes

$$\begin{aligned}
P_{A^{(l)}}^{\min} &= \min_{\mathbf{w}_i, i \in A^{(l)}} \sum_{i \in A^{(l)}} \|\mathbf{w}_i\|^2 \\
\text{s.t. : } &\Gamma_i \geq \gamma_i, \quad i \in A^{(l)}.
\end{aligned} \tag{9.11}$$

Two well-known methods can be used to solve the sub-problems in (9.11): semidefinite relaxation based technique [53], and uplink-downlink duality based algorithm [50].

SDR-Based Solution

Recalling $\mathbf{W}_i = \mathbf{w}_i \mathbf{w}_i^H$, $i \in \mathcal{K}$, and relaxing the rank-1 constraint $\text{rank}(\mathbf{W}_i) = 1$, $i \in \mathcal{K}$, we can write the second-order cone program (SOCP) shown in (9.11) in the semidefinite relaxed program format shown in (9.12). The resulting problem can be solved by standard tools such as CVX [37].

$$\begin{aligned}
 P_{A^{(l)}}^{\min} &= \min_{\mathbf{W}_i, i \in A^{(l)}} \sum_{i \in A^{(l)}} \text{tr}(\mathbf{W}_i) \\
 \text{s.t. : } &\text{tr}(\mathbf{R}_i \mathbf{W}_i) - \gamma_i \sum_{\substack{k \in A^{(l)} \\ k \neq i}} \text{tr}(\mathbf{R}_i \mathbf{W}_k) \geq \gamma_i \sigma^2, \quad i \in A^{(l)}, \\
 &\mathbf{W}_i \succeq 0, \mathbf{R}_i \succeq 0, \quad i \in A^{(l)},
 \end{aligned} \tag{9.12}$$

Interestingly, it turns out that the SDR form (9.12) and the original problem (9.11) are exactly equivalent [55]. Therefore, the solution to the SDR problem outputs rank-1 matrices. However, it should be noted that, in general, an SDR problem gives a lower-bound on the optimal objective function.

UDD-Based Solution

While the SDR method gives out the optimal solution for the problem in (9.12), a more efficient solver is a fast iterative algorithm based on the uplink-downlink duality [50]. The optimization in the SDR method is performed over the M -by- M \mathbf{W}_i matrices, which have more unknowns than the original M -element beamforming vectors, i.e., the \mathbf{w}_i 's. Hence, the SDR solution comes at the cost of a relatively high computational complexity. To take advantage of the UDD method, we re-write the problem (9.11) by using the normalized beamforming vectors, i.e., $\mathbf{u}_i = \mathbf{w}_i / \|\mathbf{w}_i\|$, and putting them in the matrix $\mathbf{U} = (\mathbf{u}_1, \dots, \mathbf{u}_K)$, while denoting $\rho_i = \|\mathbf{w}_i\|^2$. Accordingly, the problem becomes

$$\begin{aligned}
 P_{A^{(l)}}^{\min} &= \min_{\mathbf{U}, \boldsymbol{\rho}} \|\boldsymbol{\rho}\|_1 \\
 \text{s.t. : } &\Gamma_i(\mathbf{U}, \boldsymbol{\rho}) \geq \gamma_i, \|\mathbf{u}_i\|_1 = 1, \quad i \in A^{(l)},
 \end{aligned} \tag{9.13}$$

where $\boldsymbol{\rho} = (\rho_1, \dots, \rho_K)^T$, and $\Gamma_i(\mathbf{U}, \boldsymbol{\rho})$ is obtained by replacing $\mathbf{w}_i = \sqrt{\rho_i} \mathbf{u}_i$ in (9.3). Then, the minimum powers, ρ_i^* 's, and the normalized beamforming vectors, \mathbf{u}_i^* 's, can be found by applying the algorithm in [50, Table II].

Remark 1

In order for problem (9.11) to always have a solution, the rank of the channel matrix $\mathbf{H} = [\mathbf{h}_1, \dots, \mathbf{h}_K]$ should be greater than or equal to the number of UEs. For well-conditioned channels, the latter condition becomes $M \geq K$. Of course, there may be solutions for cases in which $M < K$, depending on the devices' required SINRs, i.e., the γ_i 's, and their channels, i.e., the \mathbf{h}_i 's.

Here is a brief interpretation for Remark 9.4.1. In order for (9.13) to have a solution $P_{A^{(l)}}^{\min} < \infty$, it depends on the SINR demands as well as the channel coefficients of the users. For example when two users UE₁ and UE₂, are exactly beside each other, they will have same channel coefficients, i.e. $\mathbf{h}_1 = \mathbf{h}_2$. In this case, the problem in (9.13) will not have a solution if and only if $\gamma_1 < 1$ and $\gamma_2 < 1$. Intuitively, in the above example, the power signal to a user produces the same amount of interference for the others. So it is required that the users be spatially separable (i.e., each have its own independent beam) in order for the problem to always have a solution. Since the maximum number of independent beams is equal to the rank of \mathbf{H} ([75]); and the rank of a well-conditioned matrix is equal to $\min\{M, K\}$, the maximum number of independent beams for a well-conditioned matrix is equal to $\min\{M, K\}$. Similar to an $M \times M$ point-to-point link which is capable of multiplexing M independent streams, for $M < K$ the maximum number of independent beams is K and in this case, there might be users with correlated channel coefficients.

With either method, SDR or UDD, the HAP should solve the subproblems in (9.11) for at most $2^K - 1$ times to obtain the optimal allocation vector \mathbf{a}^* . While using the iterative algorithm in [50] is faster than solving with the SDR-based method, the exponential dependence of either of the two solution methods on the number of UEs makes them time-consuming, especially when the number of UEs is large. Sub-optimal solvers can be applied to overcome this issue. In subsection 9.6.2, we propose an iterative suboptimal solution with linear time complexity. Later, in Section 9.7, we propose a DNN-based suboptimal solution which outputs the allocation vector in real time, and is applicable for complex systems where conventional iterative solvers lose their validity.

Remark 2 [*Monotonicity*]

Fixing the beamforming matrix to $\tilde{\mathbf{U}}$, it is clear that by increasing the HAP's maximum power P , the SINR constraints of all devices are better guaranteed. This is an immediate consequence of $\Gamma_i(\tilde{\mathbf{U}}, \alpha P) \geq \Gamma_i(\tilde{\mathbf{U}}, P)$, where $\alpha > 1$ [50].

9.4.2 Wireless Power Transfer Network

In this operating scenario, there are only ER devices, i.e., $\mathcal{K} = \mathcal{J}$. In this case, the optimization problem (9.9) boils down to the following separable QCQP problem:

$$\begin{aligned} P_{A^{(l)}}^{\min} &= \min_{\mathbf{v}_j, j \in A^{(l)}} \sum_{j \in A^{(l)}} \|\mathbf{v}_j\|^2 \\ \text{s.t.} : Q_j &\geq q_j, j \in A^{(l)} \end{aligned} \quad (9.14)$$

which can be converted to the following SDR program after relaxing the rank-1 constraint:

$$\begin{aligned} P_{A^{(l)}}^{\min} &= \min_{\mathbf{V}_j, j \in A^{(l)}} \sum_{j \in A^{(l)}} \text{tr}(\mathbf{V}_j) \\ \text{s.t.} : \text{tr}(\mathbf{C}_j \mathbf{V}_j) &\geq q_j, j \in A^{(l)}, \\ \mathbf{V}_i &\succeq 0, \mathbf{C}_i \succeq 0, j \in A^{(l)}, \end{aligned} \quad (9.15)$$

which can be solved using CVX [37]. Noting that in the separable QCQP problem (9.15), the number of constraints is equal to the number of summation terms of the objective function, the SDR problem is tight, i.e., solving the SDR in (9.15) is equivalent to solving the original QCQP in (9.14). Thus, the solution of the SDR problem results in rank-1 matrices corresponding to the unique optimal beamforming vectors [76]. Furthermore, it is interesting to note that irrespective of the number of energy constraints, all the optimal \mathbf{V}_j^* 's are equal to each other, and recalling that the optimal rank-1 matrix $\mathbf{V}_j^* = \mathbf{v}_j^* \mathbf{v}_j^{*H}$, the optimal beamforming vector would be \mathbf{v}_1^* for all ERs in $A^{(l)}$.

Remark 3 [*Robustness of the Solution*]

Problem (9.15) always has a solution for any M , \mathbf{g}_j 's, q_j 's, and for any number of ER's. This is true, because the interferences from other devices are beneficial leakage resources of energy, in contrast to the IR-only scenario where the interference from other devices has a destructive effect on the SINR of a specific device.

9.4.3 SWIPT Network**Remark 4** [*Number of Required Beams*]

Recall that for the problem in (9.10) to have a solution, the number of HAP antennas should be at least equal to the number of IR devices (cf. Remark 1). The problem would have a solution even if we take $\mathbf{v}_j = \mathbf{0}, j \in \mathcal{J}$. This is due to the monotonicity of the Γ_i 's, $i \in \mathcal{I}$ (cf. Remark 2) and the beneficial type of interference for the ER's (cf. Remark 3). Therefore, if the energy leakage from the information beams to the ERs satisfy their own demands, then the $\mathbf{v}_j, j \in \mathcal{J}$, will be zero, i.e., no dedicated energy beams are needed to fulfill the ERs' demands. Otherwise, only one energy beam will be needed for all ERs, similar to the case of the ER-only network (cf. subsection 9.4.2). Thus, our network always needs to find a maximum of $I + 1$ beamforming vectors instead of $I + J$.

9.5 Revenue-Maximizing Mechanism

In the previous section, we obtained the feasible allocation set \mathcal{A}_F . Now, we aim to find the optimal allocation rule \mathbf{a}^* and the optimal payment rule \mathbf{p}^* , which together constitute the Rmax mechanism. To find the Rmax mechanism, it is initially required that the social-welfare maximization (SWmax) mechanism be obtained because the SWmax solution is applied in obtaining the Rmax mechanism. Thus, in subsection 9.5.1 we obtain the SWmax mechanism, based on which and by applying Myerson's lemma, we will find the Rmax mechanism in subsection 9.5.2.

9.5.1 Social-Welfare Maximization—VCG Auction

Dominant strategy incentive compatible (DSIC) auctions are those desired auctions in which the seller needs no strategy, i.e., need not know the valuation distributions of the UEs to design the auction; and each UE, independent of other agents' bidding strategies, should play truthfully to maximize its own benefit, i.e., $b_k = \nu_k$ for $k \in \mathcal{K}$. For single-parameter environments, the SWmax mechanism, which will be obtained shortly, is DSIC and is often called the Vickrey-Clarke-Groves (VCG) mechanism in the auction literature [56].

Optimal Allocation Rule for the SWmax Mechanism

The optimal allocation vector $\mathbf{a}^* = \operatorname{argmax}_{\mathbf{a} \in \mathcal{A}_F} S(\mathbf{b}, \mathbf{a})$ corresponds to the feasible set of users that results in the largest sum of bid values. In other words, given the bid profile \mathbf{b} , the maximum social welfare $\mathfrak{S}(\mathbf{b})$ which is equal to $S(\mathbf{b}, \mathbf{a}^*)$ is simply found by looking up the table of all social-welfare values corresponding to all allocation vectors in the feasible set \mathcal{A}_F and selecting the maximum.

Optimal Payment rule for the SWmax Mechanism

According to [54, Lemma 3.1], for each UE $_k, k \in \mathcal{K}$, all bid values of other UEs, i.e., \mathbf{b}_{-k} , is a non-decreasing step function in terms of b_k . The critical value of this step function is $\tilde{b}_k = \mathfrak{S}(0, \mathbf{b}_{-k}) - \mathfrak{S}_{-k}(\infty, \mathbf{b}_{-k})$, where $\mathfrak{S}(0, \mathbf{b}_{-k})$ is the optimal social welfare from UEs other than UE $_k$ assuming the latter is *not* served; and $\mathfrak{S}_{-k}(\infty, \mathbf{b}_{-k})$ is the optimal social welfare from UEs other than UE $_k$ assuming that UE $_k$ is served [54]. Consequently, the HAP's SWmax mechanism, based on the bid profile \mathbf{b} from the UEs, is described by [54]

$$\mathbf{a}^* = \operatorname{argmax}_{\mathbf{a} \in \mathcal{A}_F} S(\mathbf{b}, \mathbf{a}), \quad (9.16a)$$

$$p_k^* = \begin{cases} \tilde{b}_k & \text{if } a_k^* = 1 \\ 0 & \text{if } a_k^* = 0 \end{cases}, \quad k \in \mathcal{K}, \quad (9.16b)$$

where (9.16b) is the optimal payment rule.

Here, it is worth noting that social welfare maximization is singular among objectives in that there is a single mechanism that is optimal regardless of the distributional assumptions for the agents' valuations. In fact, the agents' incentives are already aligned with the seller's objective, and one only needs to derive the appropriate payments, i.e., the critical values. For general objectives, e.g., revenue maximization which will be obtained in the next subsection, the optimal mechanism is distribution-dependent.

9.5.2 Revenue Maximization Mechanism—Myerson Mechanism

We place two standard assumptions on our mechanisms: (i) they are individually rational, meaning that no agent has negative expected utility for taking part in the auction; and (ii) agents who do not win, pay nothing, i.e., $a_k = 0 \rightarrow p_k = 0$. A mechanism is DSIC (also called truthful) *in expectation* iff $\mathbb{E}[u_k(\nu_k, \mathbf{b}_{-k})] \geq \mathbb{E}[u_k(b_i, \mathbf{b}_{-k})]$, which for single parameter environments translates into a mechanism having the following conditions [56]: (i) $a_k(b_k, \mathbf{b}_{-k})$ is *monotone non-decreasing* in b_k assuming \mathbf{b}_{-k} is fixed,⁸ and (ii) $p_k(b_k, \mathbf{b}_{-k}) = b_k a_k(b_k, \mathbf{b}_{-k}) - \int_0^{b_k} a_k(z, \mathbf{b}_{-k}) dz$ (a.k.a. Myerson's payment identity). Thus, once the allocation rule is fixed, the payment rule is found by applying the Myerson's payment identity.

As aforementioned, private valuation $\nu_k, k \in \mathcal{K}$, is drawn from the distribution $\mathcal{F}_k(\nu_k)$ with density function $f_k(\nu_k)$. By taking expectation of both sides of the Myerson's payment identity, and summing over all agents, we end up with the following key relation

$$\mathbb{E}_{\boldsymbol{\nu}} \left[\sum_{k \in \mathcal{K}} p_k(\boldsymbol{\nu}) \right] = \mathbb{E}_{\boldsymbol{\nu}} \left[\sum_{k \in \mathcal{K}} \phi_k(\nu_k) a_k(\boldsymbol{\nu}) \right], \quad (9.17)$$

where $\phi_k(\nu_k) = \nu_k - \frac{1 - \mathcal{F}_k(\nu_k)}{f_k(\nu_k)}$ is the *virtual valuation* for every $\text{UE}_k, k \in \mathcal{K}$ [56].

Referring to $\sum_{k \in \mathcal{K}} \phi_k(\nu_k) a_k(\boldsymbol{\nu})$ as the *virtual social welfare* of an auction on the valuation profile $\boldsymbol{\nu}$, (9.17) states that the expected revenue equals the expected virtual social welfare. Thus, the virtual social-welfare-maximizing (VSM) allocation rule is one which chooses the feasible allocation that maximizes the virtual social welfare $\sum_{k \in \mathcal{K}} \phi_k(\nu_k) a_k(\boldsymbol{\nu})$ for each valuation profile $\boldsymbol{\nu}$. In order for

⁸That is, with a non-decreasing monotone allocation rule, bidding less does not cause a bidder to get more of the commodity.

the VSM mechanism to be truthful, the obtained allocation rule has to be monotone non-decreasing, which holds true when the virtual valuations $\phi_k(v_k)$ are monotone non-decreasing.⁹

Therefore, the optimal Rmax mechanism, a.k.a. Mayerson mechanism, can be described as follows:

$$(\mathbf{a}^*, \mathbf{p}') = \text{VCG}'(\mathbf{b}') \quad (9.18a)$$

$$p_k^* = \begin{cases} \phi_k^{-1}(p'_k) & \text{if } a_k^* = 1 \\ 0 & \text{if } a_k^* = 0 \end{cases}, \quad k \in \mathcal{K}, \quad (9.18b)$$

where $b'_k = \phi_k(b_k)$, $k \in \mathcal{K}$, are the elements of the virtual bid profile \mathbf{b}' , and where $\text{VCG}'(\mathbf{b}')$ is the generalized version of the SWmax mechanism function described in (9.16). In fact, since the virtual bids can have negative values, the generalized SWmax mechanism, which takes as input the virtual bid profile \mathbf{b}' and outputs $(\mathbf{a}^*, \mathbf{p}')$, is defined as follows:

$$\mathbf{a}^* = \begin{cases} \underset{\mathbf{a} \in \mathcal{A}_F}{\text{argmax}} S(\mathbf{b}', \mathbf{a}), & \text{if } S(\mathbf{b}', \mathbf{a}^*) > 0, \\ \mathbf{0}, & \text{Otherwise,} \end{cases} \quad (9.19a)$$

$$p'_k = \begin{cases} \mathfrak{S}(-\infty, \mathbf{b}'_{-k}) - S_{-k}^*(\infty, \mathbf{b}'_{-k}), & \text{if } a_k^* = 1 \\ 0, & \text{if } a_k^* = 0 \end{cases}, \quad k \in \mathcal{K}, \quad (9.19b)$$

where $\mathfrak{S}(-\infty, \mathbf{b}'_{-k})$ is the optimal social welfare from UEs other than the UE_k , assuming the latter is *not* served; and $S_{-k}^*(\infty, \mathbf{b}'_{-k})$ is the optimal social welfare from UEs other than UE_k , assuming that UE_k is served. Hence, $p'_k \geq 0$ for $k \in \mathcal{K}$.

The pair $(\mathbf{a}^*, \mathbf{p}^*)$ in (9.18) constitutes the Rmax mechanism which can be described in algorithmic steps as follows: (i) given the bid profile \mathbf{b} and the distributions \mathcal{F}_k , $k \in \mathcal{K}$, compute virtual bids $b'_k = \phi_k(b_k)$, $k \in \mathcal{K}$, (ii) run VCG' described in (9.19), on the virtual bids \mathbf{b}' to get $\mathbf{a}^*, \mathbf{p}'$, (iii) compute p_k by (9.18b), and (iv) output $(\mathbf{a}^*, \mathbf{p}^*)$.

Figure 9.2 is a flow diagram which illustrates the whole process of finding the optimal mechanism.

⁹A sufficient condition for monotone virtual valuations is implied by the monotone hazard rate assumption. If the hazard rate of distribution \mathcal{F}_k , which is defined as $f_k(\nu_k)/(1 - \mathcal{F}_k(\nu_k))$ is monotone non-decreasing, then the virtual valuations are monotone nondecreasing as well.

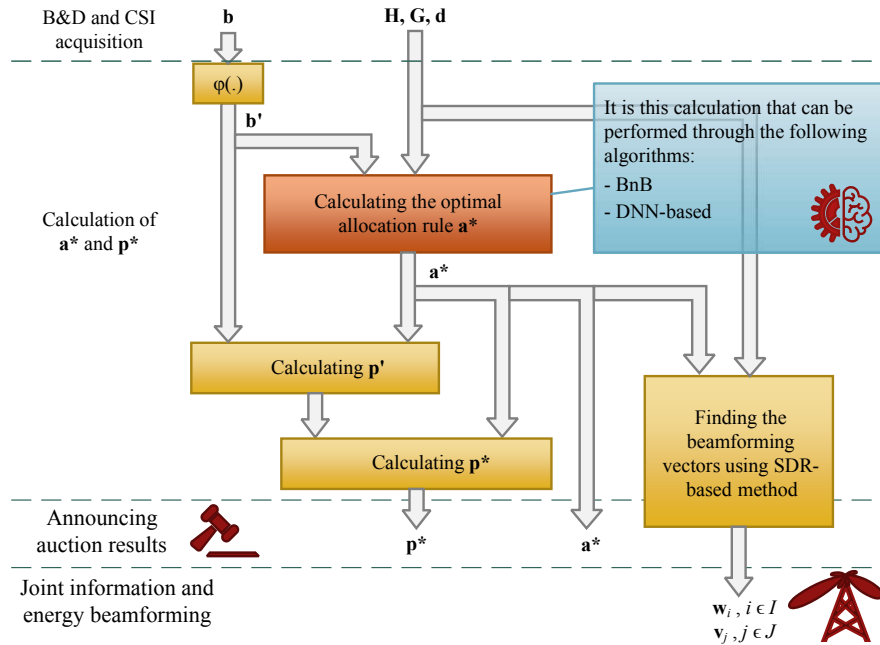


Figure 9.2: The flow diagram of finding the optimal revenue maximization mechanism.

9.6 Iterative Algorithms for Finding the Allocation Rule

9.6.1 Branch-and-Bound Algorithm

Let $\mathcal{L}_k(\mathcal{K})$, $k \in \{0, 1, \dots, |\mathcal{K}|\}$, hold all the k -element subsets of the set \mathcal{K} , where $|\mathcal{K}|$ is the cardinality of \mathcal{K} . Mathematically speaking, we have $\mathcal{L}_k(\mathcal{K}) = \{s | s \subset \mathcal{P}(\mathcal{K}), |s| = k\}$ where $\mathcal{P}(\mathcal{K})$ is the power set of \mathcal{K} , and $|\mathcal{L}_k(\mathcal{K})| = \binom{|\mathcal{K}|}{k}$ is the cardinality of $\mathcal{L}_k(\mathcal{K})$. Considering these notations, the efficient Branch-and-Bound (BnB) algorithm, i.e. Algorithm 2, can be applied to find the optimal allocation rule $\mathbf{a}^* = \begin{pmatrix} \mathbf{a}_{\text{IR}}^* \\ \mathbf{a}_{\text{ER}}^* \end{pmatrix}$. One should note that the first breadth level of the search tree of the proposed BnB algorithm starts with the largest subset of users, i.e. $(\mathcal{L}_{|\mathcal{I}|}(\mathcal{I}), \mathcal{L}_{|\mathcal{J}|}(\mathcal{J}))$. In other words, the branches are formed based on the *exclusion* of a user rather than *inclusion*. This approach is inspired by the fact that all feasible subsets are downward-closed.

9.6.2 Heuristic Sub-Optimal Iterative Solutions

The BnB algorithm to find the feasible set \mathcal{A}_{F} has exponential time complexity in terms of the number of devices, i.e., K . Apart from the very simplistic method of random allocation, next we

Algorithm 2 The efficient Branch-and-Bound algorithm for finding \mathbf{a}^* .

```

1: Initialize:  $A_{\text{IR}} = \{\}, A_{\text{ER}} = \{\}, U = 0, \mathcal{O} = \{(\{\}, \{\})\}$ 
2: Compute  $b'_k, k \in \mathcal{K}$ , using the corresponding valuation functions
3: for  $m = I$  to 0 do
4:   for each subset  $X$  in  $\mathcal{L}_m(\mathcal{I})$  do
5:     for  $n = J$  to 0 do
6:       for each subset  $Y$  in  $\mathcal{L}_n(\mathcal{J})$  do
7:         if  $\{(X, Y)\} \notin \mathcal{O}$  then
8:           Find  $P'$  by solving (9.10) for the subset  $\{(X, Y)\}$  applying CVX [37]
9:            $U' \leftarrow \sum_{i \in X} b'_i + \sum_{j \in Y} b'_j$ 
10:          if  $U' > U$  and  $P' < P$  then
11:             $A_{\text{IR}} \leftarrow X$ 
12:             $A_{\text{ER}} \leftarrow Y$ 
13:             $U \leftarrow U'$ 
14:            UPDATEO( $X, Y$ )
15: Output  $(\mathbf{a}_{\text{ER}}^{\text{air}})$  corresponding to  $\{A_{\text{IR}}, A_{\text{ER}}\}$  as the optimal allocation rule  $\mathbf{a}^*$ 

16: procedure UPDATEO( $X, Y$ )
17:   for  $i = |X|$  to 0 do
18:     for each subset  $X'$  in  $\mathcal{L}_i(X)$  do
19:       for  $j = |Y|$  to 0 do
20:         for each subset  $Y'$  in  $\mathcal{L}_j(Y)$  do
21:           if  $\{(X', Y')\} \notin \mathcal{O}$  then
22:             Add  $(X', Y')$  to  $\mathcal{O}$ 

```

present an iterative heuristic suboptimal solution which has linear-time complexity. Thereafter, we will propose the real-time DNN-based sub-optimal solution.

This allocation strategy is based on the *goodness* factors $\lambda_i = \sigma_{\mathbf{h}_i}^2 b'_i / \gamma_i$ for the IRs, $i \in \mathcal{I}$, and $\mu_j = \sigma_{\mathbf{h}_j}^2 b'_j / q_j$ for the ERs, $j \in \mathcal{J}$. In this method, the HAP starts with the largest subset $\mathcal{L}_K(\mathcal{K})$ and obtains the solution of the optimization problem (9.9). If the subset is found unfeasible, then the HAP would drop the device, either IR or ER, having the least goodness value. Then, the HAP checks the feasibility of the remaining subset. This procedure is repeated until the first feasible set is obtained. This method converges to a suboptimal solution in a maximum of $K - 1$ running time of the iterative optimization method, either SDR-based or UDD-based. The goodness-based algorithm is depicted in Algorithm 3.

The goodness factor is more meaningful when there are only IRs or ERs in the network. For the WIT scenario investigated in subsection 9.4.1, the goodness-based (here called λ -based) algorithm converges in $I - 1$ runs of the problem solver algorithm, e.g. the efficient UDD-based method, in the worst case. In the WPT scenario discussed in subsection 9.4.2, the goodness-based (called μ -based

here) algorithm converges in $J - 1$ runs of the applied problem solver, e.g., SDR-based standard tool CVX, at worst case.

Algorithm 3 The heuristic goodness-based algorithm for finding \mathbf{a}^* .

- 1: *Initialize:* $A = \{\}$; $U = 0$; $\mathbf{a}^* = \mathbf{0}$
 - 2: Compute $b'_k, k \in \mathcal{K}$ using the corresponding valuation functions
 - 3: Make the ordered set \mathcal{K}' sorted increasingly based on $\lambda_i = \sigma_{\mathbf{h}_i}^2 b'_i / \gamma_i$ and $\mu_j = \sigma_{\mathbf{h}_j}^2 b'_j / q_j$
 - 4: **while** $\mathcal{K}' \neq \emptyset$ **do**
 - 5: Find the minimum power P' by solving (9.10) for the set \mathcal{K}' applying CVX [37]
 - 6: $U' \leftarrow \sum_{k \in \mathcal{K}'} b'_k$
 - 7: **if** $U' > U$ **and** $P' < P$ **then**
 - 8: Break
 - 9: **else**
 - 10: Drop the first element of \mathcal{K}' with the least value of goodness factor.
 - 11: Output $\mathbf{a}^* = \begin{pmatrix} \mathbf{a}_{\text{IR}}^* \\ \mathbf{a}_{\text{ER}}^* \end{pmatrix}$ corresponding to \mathcal{K}' as the optimal allocation rule
-

9.7 Deep Learning Based Allocation Rule

As observed in Section 9.4, the time-greedy part of designing the optimal mechanism for the SWIPT network under consideration is due to the many runs of the optimization methods needed to find the allocation rule. In fact, once the optimal allocation rule is found, finding the optimal payment rule is straightforward by applying (9.18) and (9.19). One solution to overcome the complexity of finding the allocation vector is through the use of DNNs.

To solve $\mathbf{a}^* = \operatorname{argmax}_{\mathbf{a} \in \mathcal{A}_F} S(\mathbf{b}', \mathbf{a})$ via deep learning, we observe that it can be regarded as an unknown function mapping from the ensemble of the network parameters of interest, i.e., \mathbf{b}' , \mathbf{d} , and \mathbf{M} , where $\mathbf{M} = [\mathbf{H}, \mathbf{G}]$ with $\mathbf{H} = [\mathbf{h}_1, \dots, \mathbf{h}_J]$ and $\mathbf{G} = [\mathbf{g}_1, \dots, \mathbf{g}_J]$, to the corresponding optimal allocation rule $\mathbf{a}^* = \begin{pmatrix} \mathbf{a}_{\text{IR}}^* \\ \mathbf{a}_{\text{ER}}^* \end{pmatrix}$. Note that the mapping depends on \mathbf{h}_k 's and d_k 's through \mathcal{A}_F . Indeed, DNNs can be viewed as *universal approximators*: if properly trained, they are able to learn the input-output relationship between the parameters and the desired allocation vector. This means that we can optimize a desired performance function for given parameters without explicitly having to solve any optimization problem via SDR, UDD, or any other iterative optimization method, but rather letting the DNN compute the allocation vector.

9.7.1 The Proposed Deep Neural Network Architecture

After trying several core architectures, such as fully-connected neural network (FcNN), convolutional neural network (CNN), and residual neural network (ResNet), the FcNN model showed the best performance in terms of accuracy.

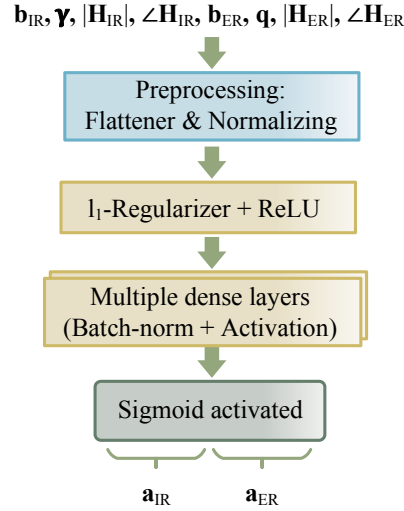


Figure 9.3: The DNN used for finding the allocation vector.

The schematic of the proposed DNN architecture is depicted in Fig. 9.3. The input to the DNN is $[\mathbf{b}'_{\text{IR}}, \boldsymbol{\gamma}, |\mathbf{H}|, \angle \mathbf{H}, \mathbf{b}'_{\text{ER}}, \mathbf{q}, |\mathbf{G}|, \angle \mathbf{G}]$, where $|\mathbf{H}|$ ($|\mathbf{G}|$) and $\angle \mathbf{H}$ ($\angle \mathbf{G}$) denote matrices holding the absolute value and angle of the complex elements of matrix \mathbf{H} (\mathbf{G}). The input data is fed to a preprocessing unit composed of four main operations: *transforming*, *sorting*, *flattening*, and *normalizing*. In transforming, we use the criteria employed in the proposed heuristic method to replace the values of the virtual bids with their corresponding goodness factors. Then, the resulting goodness factors are sorted in ascending (or descending) order. The introduction of these two preprocessing operations makes the training process converge faster and result in a more accurate network at the end of the training. With flattening, the input data are placed in a column vector, and by the normalization operation the flattened data are shifted and scaled according to standard normal distribution. To explain the latter more, for each input data sample x , the normalizing unit, operates $\frac{x - \mu_x}{\sigma_x}$ on x , where μ_x and σ_x^2 are the standard mean and the standard variance functions, both of which are obtained from the training data samples. The output layer has $K = I + J$ nodes, which corresponds to the dimension of the allocation vector $\mathbf{a} = (\mathbf{a}_{\text{IR}}, \mathbf{a}_{\text{ER}})$. The output layer, after being activated by the sigmoid (logistic) function, will take values between 0 and 1. In fact, since

our network is a multi-label multi-class classifier, the activation function of the output layer should be sigmoid function $f(x) = \frac{1}{1+\exp(-x)}$ that maps the summation node value $x \in \mathbb{R}$ to $(0, 1)$.

When using the trained DNN for prediction, we should revert the sorted data back to its original form based on the sorting index set obtained in the sorting operation of the preprocessing unit. Also, we round this output to only take binary values, since the allocation vector is a binary vector.

To train the proposed DNN, we need to populate the training dataset and the corresponding labels. To this end, we solve the corresponding optimization problems for many network realizations using standard semidefinite problem solvers like CVX [37] in the proposed efficient BnB algorithm. We used the *TensorFlow* interface [57] for building and training our DNN model. We tuned the hyper-parameters of the DNN using the recently released hyper-parameter optimization framework *Keras-tuner* [58], which tries a preset number of trials looking for the best possible set of hyper-parameters with built-in search algorithms.

9.7.2 Computational Complexity

SDR-based method

The iterative-based algorithms, SDR- and UDD-based, have exponential time complexity. In Table 9.1, the computational complexity of the proposed goodness-based DNN-based methods and the conventional SDR-based and UDD-based methods are compared with each other. In computing the computational complexity, it is assumed that for the SDR-based the general-purpose interior-point algorithm [60] is used for each branch $k \in \{1, \dots, 2^K - 1\}$ of the proposed BnB algorithm, i.e. Algorithm 2, and for the UDD-based method the iterative algorithm in [50] is used in each branch of the BnB algorithm for the case of the WIT system. As can be seen from the table, in terms of the number of antennas, M , either of the conventional methods as well as the goodness-based method has polynomial time complexity whereas the proposed DNN-based method has linear time complexity. Note that q is a number in the range of $[3, 4]$ depending on the methods used for computing matrix operations, such as computing maximum eigenvalue of a positive semidefinite matrix. Further details are provided in [77]. Importantly, while the conventional algorithms both have exponential time complexity in terms of the number UEs, K , the heuristic method has polynomial time complexity, and the DNN-based method has linear complexity.

Table 9.1: Comparison of the Computational Complexity

SDR	UDD	Goodness	DNN
$\mathcal{O}\left((KM^q + K^2M^2)2^K\right)$	$\mathcal{O}\left(K(M^3 + KM)2^K\right)$	$\mathcal{O}\left(K^2(M^3 + KM)\right)$	$\mathcal{O}(MK)$

9.8 Performance Evaluation and Discussion

Now, we evaluate the accuracy of the proposed DNN architecture in predicting the exact allocation vectors. We instantiate our DNN from the architecture presented in Fig. 9.3 targeted for a system operation where transmissions undergo Rayleigh fading. Specifically, $\mathbf{h}_i \sim \mathcal{CN}(\mathbf{0}, \sigma_{\mathbf{h}_i}^2 \mathbf{I}_M)$ where $\sigma_{\mathbf{h}_i}^2 \sim \mathcal{U}(-80, -60)$ dB, $i \in \mathcal{I}$, and $\mathbf{g}_j \sim \mathcal{CN}(\mathbf{0}, \sigma_{\mathbf{g}_j}^2 \mathbf{I}_M)$ where $\sigma_{\mathbf{g}_j}^2 \sim \mathcal{U}(-60, -40)$ dB, $j \in \mathcal{J}$. Unless otherwise stated, the SWIPT network parameters are as follows: $P_{\max} = 3$ W, $I = 4$, $J = 2$, $M = 8$, $\sigma_i^2 = -50$ dBm, $i \in \mathcal{I}$, $b_k \sim \mathcal{U}(0.1, 1)$ for $k \in \mathcal{K}$, $\gamma_i \sim \mathcal{U}(5, 35)$ dB for $i \in \mathcal{I}$, and $q_j \sim \mathcal{U}(-20, 0)$ dB for $j \in \mathcal{J}$. $\mathcal{U}(a, b)$ denotes the uniform distribution in the interval (a, b) .

Table 9.2: Layout of the proposed DNN architecture (# trainable parameters: 201,454; # non-trainable parameters: 1,376)

Layer	Output dimension
Input (after preprocessing)	108
Dense + Regularizer + tanh	200
Dense + Batch normalization + tanh	296
Dense + Batch normalization + ReLU	392
Dense + sigmoid	6

We first populate the training data by solving the optimization problem (9.8) offline, to find the optimal allocation vectors (as target labels) using the standard semidefinite problem solver tool CVX [37] for 194,000 realizations of the network model with the aforementioned parameters. The proper set of hyper-parameters found are shown in Table 9.2. We dedicated 20% of the data for testing purposes, and split the remaining 80% into 80% for the training and 20% for the validation. While the training and validation sets are used in plotting Fig. 9.4, the testing data is used in plotting Fig. 9.5, Fig. 9.6, and Fig. 9.7.

As depicted in Fig. 9.3, our DNN has three hidden layers, each of which is described in Table 9.2. The regularizer used in the first hidden layer is the $l1$ -activity-regularizer with parameter $l1$ set to 0.001. Activity regularizers allow us to apply penalties on layer activity during optimization. These penalties are incorporated in the binary cross-entropy loss function that the DNN tries to minimize during training. By doing this, we avoid over-fitting of our model. We used the well-known Adam

optimizer [59] with initial learning rate 0.01 and a decay rate of 0.0027. The batch size for training is set to 16. The last layer has a sigmoid activation layer as explained before.

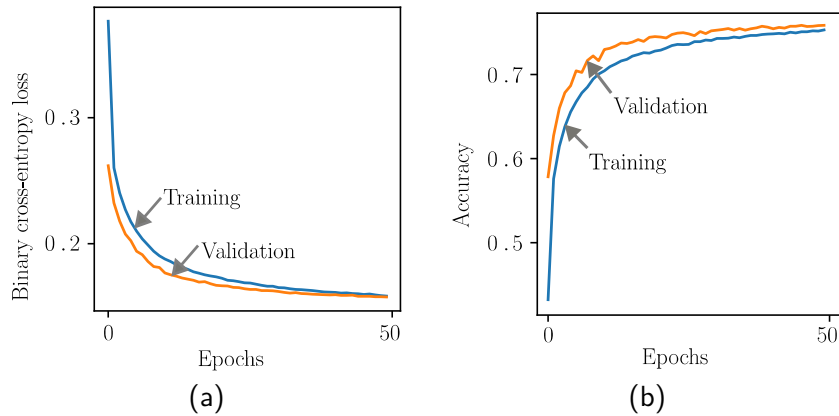


Figure 9.4: (a) The binary cross-entropy metric versus each epoch of training the DNN; (b) The accuracy metric versus each epoch of training the DNN.

Figure 9.4a shows the loss value of the training and validation datasets. As observed, the curves intersect at almost the last epoch, after which over-fitting will occur. Fig. 9.4b shows the accuracy related to the training and validation datasets. The accuracy metric used here differs from the built-in binary accuracy metric in the *Keras* library which counts the fraction of all matches between each element of the predicted allocation vector with its corresponding true allocation vector. This is a customized metric to measure the fraction of *exact* match between the target data and the predicted output data of the DNN. Fig. 9.4b reveals that an accuracy of 76% is reached with the proposed DNN for the SWIPT network. It should be noted that the HAP can get paid even if there is not an exact match between the predicted allocation vector and the true allocation vector. For example, let the true and predicted allocation vectors be $\mathbf{a}_{\text{true}} = (1, 1, 1, 0, 0, 0)^T$ and $\mathbf{a}_{\text{pred}} = (1, 1, 0, 0, 0, 0)^T$, respectively. Then, there happens an error in prediction. However, since the predicted allocation vector is a subset of the true allocation vector, the HAP will get some profit from this fault prediction. It is also interesting to note that even if the predicted is not a subset of the true allocation vector or even if it is not a feasible allocation, the HAP still has the chance to get profit. Recall that a subset $A^{(l)}$ is unfeasible if all the constraints of the subset cannot be covered with the HAP power budget P . However, it is still possible that the beamforming vectors found based on that subset do cover the constraints of a fraction of the devices. Therefore the customized exact accuracy provides a lower-bound on the performance of the HAP. It is interesting to mention

that the achieved 76% exact accuracy is equivalent to the built-in Keras binary accuracy of 95%. For the example mentioned above, the binary accuracy is 83.33% but the exact accuracy is 0%.

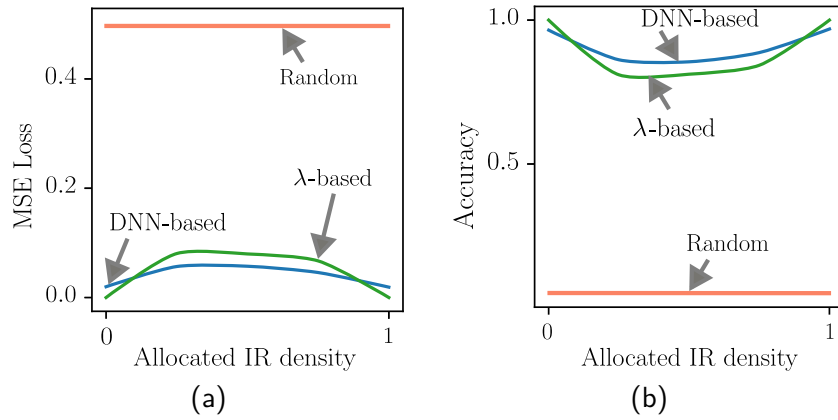


Figure 9.5: Comparison of the DNN-based and λ -based methods: (a) The mean square error (MSE), (b) The exact accuracy.

Figure 9.5 compares the accuracy and the mean square error (MSE) of the DNN-based solver with the proposed iterative λ -based approach for a WIT system with the same default system setting except that here $I = 6$ and $J = 0$. The curves are plotted in terms of the density of 1's in the label test dataset. As Fig. 9.5b shows, the accuracy of the λ -based method is comparable to the DNN-based method while the density of UEs in the system is either very low or very high. The low-density happens when the UEs' constraints cannot be well satisfied with the power budget of the HAP; otherwise a high-density happens. However, in the middle-density range, the DNN-based outperforms the heuristic method.

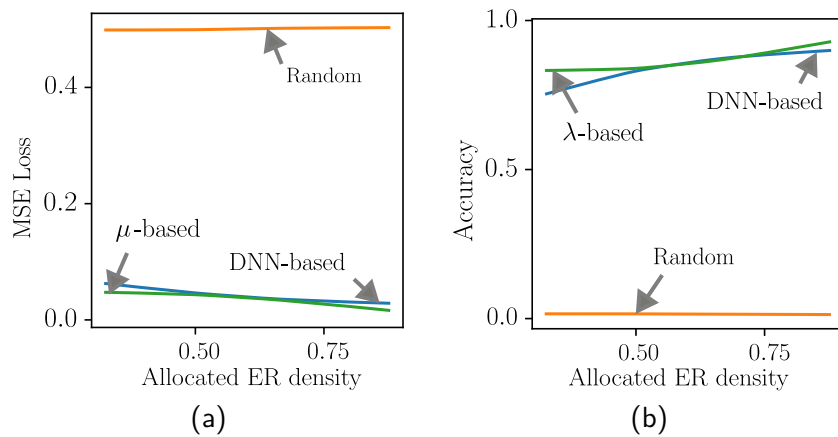


Figure 9.6: Comparison of the DNN-based and μ -based methods: (a) The mean square error (MSE), (b) The exact accuracy.

Similarly, Fig. 9.6 compares the accuracy and the MSE of the DNN-based solver with the proposed iterative μ -based approach for a WPT system with the same default system setting except that here $J = 6$ and $I = 0$. As observed, the accuracy of the heuristic method outperforms the DNN-based method particularly in the extreme densities. Compared to the user density approach,

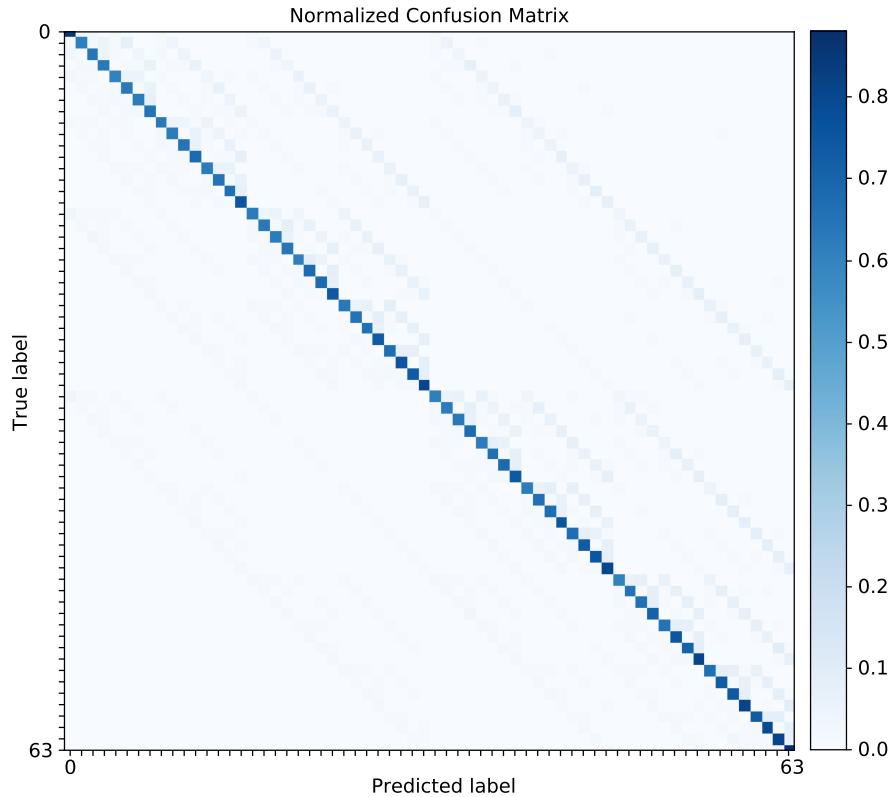


Figure 9.7: The normalized confusion matrix of the trained DNN.

the more exact way of demonstrating the accuracy of a network for a specific target label, is by use of confusion matrices. In fact, these matrices are usable only for multi-class single-label classifications. However, by decoding our model's binary target labels to decimal-valued target labels, we can use the confusion matrix to evaluate the accuracy of the DNN for different classes. In fact, such decoded target labels are the same as subscript l in $\mathbf{a}^{(l)}$. Fig. 9.7 shows the normalized confusion matrix for the same default system setting. Thus, the decoded (One-Hot) targets will have 64 labels. As can be inferred from the colors of the main diagonal of the confusion matrix, the normalized correct predictions range roughly from 70% to 90%.

Table 9.3 reveals the performance of the proposed DNN for three different user configurations with $K = 6$ UEs: 1) the SWIPT system with $I = 4$ and $J = 2$; 2) the WIT system with $I = 6$ IRs and no ERs; and the WPT system with $J = 6$ ERs and no IRs.

Table 9.3: Accuracy of the DNN-Based Method for Different System Models

	Binary accuracy	Exact accuracy
SWIPT	0.95%	0.76%
WIT	0.97%	0.80%
WPT	0.97%	0.79%

9.9 Summary

We tackled the problem of finding the optimal revenue maximizing dominant-strategy incentive-compatible mechanism, namely, the allocation and payment rules, for a SWIPT network wherein a multi-antenna HAP sells its spatially-multiplexed radio links to SINR-constrained information devices, and its power to energy harvesting devices. Having solved the NP-hard revenue maximization problem by applying a proposed efficient Branch-and-Bound algorithm and by leveraging conventional optimization techniques, namely, semidefinite relaxation or uplink-downlink duality methods in each branch, we highlighted the time-greediness of such techniques for finding the optimal allocation rule, especially as the number of network devices increases. We also proposed another iterative, but faster, suboptimal heuristic solution method with linear time complexity. Then, we designed and trained a DNN to find the allocation rule in real time, with an exact accuracy of 76%. While exploring other architectures to increase accuracy is a promising step for future work, considering partial CSI availability at the HAP and then applying machine-learning techniques to jointly estimate the CSI and the optimal allocation rule is also another challenging avenue.

Chapter 10

Summary

10.1 Part I

We achieved a novel tractable formula representing the output DC current of a rectifier to the Fourier series of the input waveform through modified Bessel functions and the Lambert function while considering the nonlinearity of the rectifiers. The formula can be applied in designing more realistic transmit signal shaping and energy beamforming in WPCNs. One of such application is designing optimal scheduling schemes for WPCNs. The findings provide a guideline for deriving similar tractable formulas for different types of rectifier topologies.

10.2 Part II

Through two Theorems, we solidly proved the outperformance of single-beam time sharing scheduling scheme over multi-beam spatial scheduling scheme under max-mean fairness criteria. The results of this part emphasize the importance of considering the nonlinearity of energy harvesters in designing scheduling schemes for WPT-enabled systems.

10.3 Part III

We proposed a distributed algorithm which pushes the UEs as the playing agents toward the NEP of the game while considering the demand traffic of the UEs. We applied both game theory and queuing theory jointly to analyze the WPT model. We enhanced the distributed algorithm by adding the realistic modeling of the playing strategy of the UEs by roll-off factor convention which also gives the agents the right to stay in or leave the game while reinforcing the UEs toward a better NEP which results in higher social welfare. The joint game theory-queuing theory approach shows an interesting analysis approach which had rarely touched by the researchers in the communications area. It is recommended that the results can be applied as an interesting application of reinforcement learning (RL) in designing distributed allocation algorithms under the premise of an auction. It is probably of great interest to researchers working on the hot topic of federated learning in communication networks.

10.4 Part IV

We applied DL to solve MINLP in the SWIPT system model under an auction premise. What highlights our work with most of the recent works on the application of deep learning in the communication networks, is the heterogeneous input data of our network, i.e. *bids, demands, and channel coefficients*. We showed that DL can be viewed as a promising solution to this input data type as well. While analyzing the heterogeneous input data from the viewpoint of information theory to discover the smallest latent space is an interesting research avenue, the results of our work show that multilayer perceptron (MLP) DNN architectures lead to satisfactory results.

Appendix A

Proofs

A.1 Proof of Eq. (2.10)

To solve the equation $p^x = ax + b$ where $p > 0$, $p \neq 1$, and $a > 0$, we use the substitution of $-t = x + b/a$ and write

$$p^x = ax + b \Rightarrow p^{-t} = -a p^{b/a} t \Rightarrow \frac{-\ln(p)}{a p^{b/a}} = t \ln(p) e^{t \ln(p)}. \quad (\text{A.1})$$

Knowing that the solution of equation $y = xe^x$ is $x = W(y)$, where $W(\cdot)$ is the Lambert function, we can write

$$t = \frac{W\left(\frac{-\ln(p)}{a p^{b/a}}\right)}{\ln(p)} \Rightarrow x = -b/a - \frac{W\left(\frac{-\ln(p)}{a p^{b/a}}\right)}{\ln(p)}. \quad (\text{A.2})$$

To find the solution of $i_{\text{out}} = A_0 I_s e^{-\alpha i_{\text{out}}} - I_s$, by comparing it with $p^x = ax + b$ in (A.1), we see that $x = i_{\text{out}}$, $p = e^{-\alpha}$, $a = \frac{1}{A_0 I_s}$, and $b = \frac{I_s}{A_0}$. Therefore, applying (A.2), we obtain

$$i_{\text{out}} = -I_s + \frac{1}{\alpha} W_0\left(A_0 \alpha I_s e^{\alpha I_s}\right), \quad (\text{A.3})$$

where $W_0(\cdot)$ is replaced to refer to the principal-branch Lambert function since the argument of the Lambert function in (A.3) is always positive. ■

A.2 Proof of Theorem 1

With regard to (4.5), the objective here is to prove that $i_{\text{out}}^{\text{UDT}} > i_{\text{out}}^{\text{UDP}}$ for any $K > 1$, $\mu > 0$, $\alpha > 0$, and $I_s > 0$, i.e.,

$$\frac{1}{\mu\sqrt{K}} \left(W_0 \left(\mu I_s I_0(\alpha) e^{\mu I_s} \right) - \mu I_s \right) > \frac{1}{\mu} \left(W_0 \left(\mu I_s I_0(\alpha/\sqrt{K}) e^{\mu I_s} \right) - \mu I_s \right), \quad (\text{A.4})$$

where $\mu = \frac{R_L}{\eta v_T}$ and $\alpha = \frac{\sqrt{2PR_{\text{ant}}}}{\eta v_T} \|\mathbf{h}\|$. Denoting μI_s by γ for simplicity, the inequality in (A.4) can be rewritten as

$$W_0(\gamma e^\gamma I_0(\alpha)) - \gamma > \sqrt{K} \left(W_0(\gamma e^\gamma I_0(\alpha/\sqrt{K})) - \gamma \right), \quad (\text{A.5})$$

where γ and α are positive real numbers; and K , the total number of ERs in the network, is a positive integer. The inequality in (A.5) changes to equality if at least one of the following three conditions holds true: $\gamma = 0$, $\alpha = 0$, $K = 1$. In this case, the performances of the TS and SM schemes are the same. Note that $K = 1$ indicates that there is only one user, $\gamma = 0$ indicates that the diode saturation current I_s and/or the load R_L is zero; and $\alpha = 0$ indicates that P and/or R_{ant} and/or $\|\mathbf{h}\|$ is zero. To prove the inequality, we make use of the following theorem.

Theorem 3. *Let $f(\mathbf{x})$ and $g(\mathbf{x})$ be two differentiable functions of $\mathbf{x} \in \mathbb{R}^n$. Let the domain of these two functions be $\mathcal{D} = \{\mathbf{x} | \mathbf{x} \succeq \mathbf{a}\}$, where $\mathbf{a} = (a_1, a_2, \dots, a_n)^\top$ is an arbitrary real vector and \succeq indicates element-wise inequality. If we have the below two properties, then $f(\mathbf{x}) > g(\mathbf{x}), \forall \mathbf{x} \in \mathcal{D} \setminus \{\mathbf{a}\}$:*

1. $f(\mathbf{a}) = g(\mathbf{a})$,
2. $\frac{\partial f(\mathbf{x})}{\partial x_i} > \frac{\partial g(\mathbf{x})}{\partial x_i}$ for $i \in \{1, 2, \dots, n\}$

Proof. The proof is very simple and can be found in calculus books. ■

Applying Theorem 3, we take $\mathbf{x} = (\gamma, \alpha, K)^\top$ and $\mathbf{a} = (0, 0, 1)^\top$ for our own problem. We denote the left-hand side (LHS) of (A.5) by $f(\mathbf{x}) = f(\gamma, \alpha, K) = W_0(\gamma e^\gamma I_0(\alpha)) - \gamma$ and the right-hand side (RHS) of (A.5) as $g(\mathbf{x}) = g(\gamma, \alpha, K) = \sqrt{K} \left(W_0(\gamma e^\gamma I_0(\alpha/\sqrt{K})) - \gamma \right)$. We see that $f(0, 0, 1) = g(0, 0, 1) = 0$. Now, we should check that a) $\frac{\partial f(\gamma, \alpha, K)}{\partial \gamma} > \frac{\partial g(\gamma, \alpha, K)}{\partial \gamma}$, b) $\frac{\partial f(\gamma, \alpha, K)}{\partial \alpha} > \frac{\partial g(\gamma, \alpha, K)}{\partial \alpha}$, and c) $\frac{\partial f(\gamma, \alpha, K)}{\partial K} > \frac{\partial g(\gamma, \alpha, K)}{\partial K}$. We show these in the following parts.

a) Noting that $\frac{dW_0(x)}{dx} = \frac{W_0(x)}{x(W_0(x)+1)}$, we can write

$$\begin{aligned} \frac{\partial f(\gamma, \alpha, K)}{\partial \gamma} &= \frac{e^\gamma(1+\gamma)I_0(\alpha)W_0(\gamma e^\gamma I_0(\alpha))}{\gamma e^\gamma I_0(\alpha)(1+W_0(\gamma e^\gamma I_0(\alpha)))} - 1 \\ &= -\frac{\gamma+1}{\gamma} \frac{1}{1+W_0(\gamma e^\gamma I_0(\alpha))}. \end{aligned} \quad (\text{A.6})$$

On the other hand, by taking the derivative of the RHS of (A.5), after a bit of simplification, we get

$$\frac{\partial g(\gamma, \alpha, K)}{\partial \gamma} = -\sqrt{K} \frac{\gamma+1}{\gamma} \frac{1}{1+W_0(\gamma e^\gamma I_0(\alpha/\sqrt{K}))}. \quad (\text{A.7})$$

Then, noting that $I_0(x) \geq 1$, $I_0(\alpha) > I_0(\alpha/\sqrt{K})$ for $K > 1$, and that $W_0(x)$ is an increasing function with zero value at $x = 0$, we can write

$$\begin{aligned} 1 + W_0(I_0(\alpha)) &> 1 + W_0(I_0(\alpha/\sqrt{K})) \\ \Rightarrow \frac{\gamma+1}{\gamma} \frac{1}{1+W_0(I_0(\alpha))} &< \frac{\gamma+1}{\gamma} \frac{\sqrt{K}}{1+W_0(I_0(\alpha/\sqrt{K}))} \\ \Rightarrow -\frac{\gamma+1}{\gamma} \frac{1}{1+W_0(I_0(\alpha))} &> -\frac{\gamma+1}{\gamma} \frac{\sqrt{K}}{1+W_0(I_0(\alpha/\sqrt{K}))}. \end{aligned} \quad (\text{A.8})$$

Therefore, $\frac{\partial f(\gamma, \alpha, K)}{\partial \gamma} > \frac{\partial g(\gamma, \alpha, K)}{\partial \gamma}$.

b) Taking the derivative of f and g with respect to α , we obtain

$$\frac{\partial f(\gamma, \alpha, K)}{\partial \alpha} = \frac{I_0'(\alpha)}{I_0(\alpha)} \frac{W_0(\gamma e^\gamma I_0(\alpha))}{1+W_0(\gamma e^\gamma I_0(\alpha))}, \quad (\text{A.9a})$$

$$\frac{\partial g(\gamma, \alpha, K)}{\partial \alpha} = \frac{I_0'(\alpha/\sqrt{K})}{I_0(\alpha/\sqrt{K})} \frac{W_0(\gamma e^\gamma I_0(\alpha/\sqrt{K}))}{1+W_0(\gamma e^\gamma I_0(\alpha/\sqrt{K}))}, \quad (\text{A.9b})$$

¹ Thus, it is needed to prove that the following holds true

$$\frac{I_0'(\alpha)}{I_0(\alpha)} \frac{W_0(\gamma e^\gamma I_0(\alpha))}{1+W_0(\gamma e^\gamma I_0(\alpha))} > \frac{I_0'(\alpha/\sqrt{K})}{I_0(\alpha/\sqrt{K})} \frac{W_0(\gamma e^\gamma I_0(\alpha/\sqrt{K}))}{1+W_0(\gamma e^\gamma I_0(\alpha/\sqrt{K}))}. \quad (\text{A.10})$$

¹Throughout the Appendix section, $f'(x)$, $f''(x)$, denote $\frac{df(x)}{dx}$, $\frac{d^2f(x)}{dx^2}$, respectively. $f(g(x))''$

Noting that $I'_0(x) = I_1(x)$, we can write the inequality in (A.10) as follows:

$$\frac{I_1(\alpha)I_0(\alpha/\sqrt{K})}{I_0(\alpha)I_1(\alpha/\sqrt{K})} \frac{W_0(\gamma e^\gamma I_0(\alpha)) \left(1 + W_0(\gamma e^\gamma I_0(\alpha/\sqrt{K}))\right)}{(1 + W_0(\gamma e^\gamma I_0(\alpha))) W_0(\gamma e^\gamma I_0(\alpha/\sqrt{K}))} > 1. \quad (\text{A.11})$$

Now, it is shown that each of the two fractions in the LHS of (A.11) is greater than 1. Note that the following bounds on $I_{v+1}(x)/I_v(x)$ hold true [78]:

$$\sqrt{1 + \left(\frac{v+1}{x}\right)^2} - \frac{v+1}{x} \leq \frac{I_{v+1}(x)}{I_v(x)} \leq \sqrt{1 + \left(\frac{v+\frac{1}{2}}{x}\right)^2} - \frac{v+\frac{1}{2}}{x} \quad (\text{A.12})$$

Therefore, we have the following inequalities

$$\sqrt{1 + \frac{1}{\alpha^2}} - \frac{1}{\alpha} \leq \frac{I_1(\alpha)}{I_0(\alpha)}, \quad (\text{A.13a})$$

$$\sqrt{1 + \frac{K}{\alpha^2}} - \frac{\sqrt{K}}{\alpha} \leq \frac{I_1(\alpha/\sqrt{K})}{I_0(\alpha/\sqrt{K})}, \quad (\text{A.13b})$$

which leads us to

$$\frac{\sqrt{1 + \frac{1}{\alpha^2}} - \frac{1}{\alpha}}{\sqrt{1 + \frac{K}{\alpha^2}} - \frac{\sqrt{K}}{\alpha}} \leq \frac{I_1(\alpha)I_0(\alpha/\sqrt{K})}{I_0(\alpha)I_1(\alpha/\sqrt{K})}. \quad (\text{A.14})$$

Now, we show that the RHS of (A.14) is smaller than 1. Let us start by assuming that

$$\frac{\sqrt{1 + \frac{1}{\alpha^2}} - \frac{1}{\alpha}}{\sqrt{1 + \frac{K}{\alpha^2}} - \frac{\sqrt{K}}{\alpha}} > 1. \quad (\text{A.15})$$

Since both sides have positive values, we can square them and, after a bit of further manipulation, obtain

$$\sqrt{\alpha^2 + 1} - 1 + K < \sqrt{K(\alpha^2 + K)}. \quad (\text{A.16})$$

By noting that each side of (A.16) is positive, we square each side again and do some manipulation to get

$$2\sqrt{\alpha^2 + 1} < \alpha^2 + 2 \stackrel{(\cdot)^2}{\Rightarrow} 0 < \alpha^4. \quad (\text{A.17})$$

Thus, noting that $\alpha > 0$, one can start from (A.17) and move backward and admit that (A.15) is a true inequality. Then, by considering (A.14), it is confirmed that

$$1 < \frac{I_1(\alpha)I_0(\alpha/\sqrt{K})}{I_0(\alpha)I_1(\alpha/\sqrt{K})}. \quad (\text{A.18})$$

Next, it should be checked that the other fraction in (A.11) is also greater than 1. Define $A = W_0(\gamma e^\gamma I_0(\alpha))$ and $B = W_0(\gamma e^\gamma I_0(\alpha/\sqrt{K}))$. Referring to (A.11), one should check that $\frac{A(1+B)}{B(1+A)} > 1$, which is simplified to $A > B$ since A and B are both positive. It is also clear that $A > B$; because $I_0(\alpha) > I_0(\alpha/\sqrt{K})$ for $K > 1$ and since $W_0(\cdot)$ is an increasing function then $A > B$ is a true inequality. Hence, the proof of part b), i.e. $\frac{\partial f(\gamma, \alpha, K)}{\partial \alpha} > \frac{\partial g(\gamma, \alpha, K)}{\partial \alpha}$, completes here.

c) In this last part, the goal is to prove that $\frac{\partial g(\gamma, \alpha, K)}{\partial K} < 0$. Since f does not depend on K , $\frac{\partial f(\gamma, \alpha, K)}{\partial K} = 0$. Thus, we have

$$\frac{\partial g(\gamma, \alpha, K)}{\partial K} = \frac{W_0(\gamma e^\gamma I_0(\alpha/\sqrt{K})) - \gamma}{2\sqrt{K}} - \frac{\frac{\alpha}{2K} I_0'(\alpha/\sqrt{K}) W_0(\gamma e^\gamma I_0(\alpha/\sqrt{K}))}{I_0(\alpha/\sqrt{K}) (1 + W_0(\gamma e^\gamma I_0(\alpha/\sqrt{K})))}. \quad (\text{A.19})$$

By applying (A.19), the inequality $\frac{\partial g(\gamma, \alpha, K)}{\partial K} < 0$ is equivalent to

$$\frac{\alpha I_1(\alpha/\sqrt{K}) W_0(\gamma e^\gamma I_0(\alpha/\sqrt{K}))}{\sqrt{K} I_0(\alpha/\sqrt{K}) (1 + W_0(\gamma e^\gamma I_0(\alpha/\sqrt{K})))} > W_0(\gamma e^\gamma I_0(\alpha/\sqrt{K})) - \gamma, \quad (\text{A.20})$$

where by first replacing $x = 1/\sqrt{K}$ and then defining $u(x) = \gamma e^\gamma I_0(x\alpha)$ and by recalling that $W_0'(u) = \frac{dW_0(u)}{du} = \frac{W_0(u)}{u(1+W_0(u))}$, it becomes

$$xu'(x)W_0'(u(x)) > W_0(u(x)) - \gamma \quad (\text{A.21})$$

where $u'(x) = \frac{du(x)}{dx}$.

The mean-value theorem states that if $f(x)$ is a continuous function on the closed interval $[p, p+x]$ and differentiable on the open interval $(p, p+x)$, the following holds true for some $t \in (0, 1)$:

$$f(p+x) = f(p) + f'(p+tx)x. \quad (\text{A.22})$$

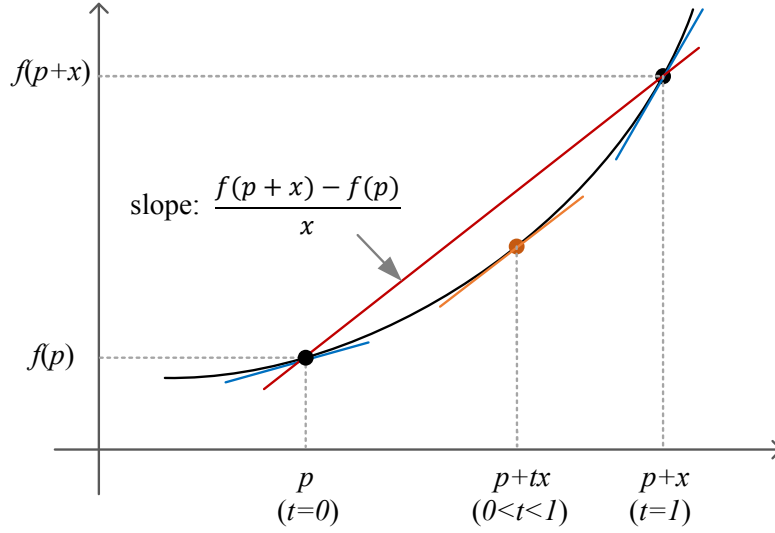


Figure A.1: Illustration for checking validity of (A.23).

If $f(x)$ is a monotonically increasing and convex the following inequality for the endpoint $p+x$ of the interval, which corresponds to $t=1$, holds true.

$$f(p+x) < f(p) + f'(p+x)x. \quad (\text{A.23})$$

The validity of (A.23) is checked illustratively in Fig. A.1. Now since $W_0(u(x)) = W_0(\gamma e^\gamma I_0(x\alpha))$ is a continuous function in $[0, \infty)$ and differentiable in $(0, \infty)$, by setting $p=0$ and for any $x \in (0, \infty)$, given that $W_0(u(x))$ is a monotonically increasing convex function in the interval $(0, x)$, the inequality in (A.23) becomes

$$W_0(u(x)) < W_0(u(0)) + [W_0(u(x))]'x. \quad (\text{A.24})$$

where by noting that $[W_0(u(x))]' = u'(x)W_0'(u(x))$ and $W_0(u(0)) = W_0(\gamma e^\gamma) = \gamma$ the validity of (A.21) is checked. In order to complete the proof, we should prove that $W_0(u(x)) = W_0(\gamma^\gamma I_0(\alpha x))$ is a monotonically increasing convex function. To this end, it should be shown i) $[W_0(u(x))]' > 0$ which is the monotone increasing condition and ii) $[W_0(u(x))]'' > 0$ which is the convexity condition. The former is derived as follows:

$$\begin{aligned} [W_0(u(x))]' &= u'(x)W_0'(u(x)) \\ &= \alpha \gamma e^\gamma I_1(\alpha x) W_0'(\gamma e^\gamma I_0(\alpha x)). \end{aligned} \quad (\text{A.25})$$

Since $I_1(x)$ and $W_0'(x)$ are positive functions, it concludes $[W_0(u(x))]' > 0$. To derive the second-derivative of $WW_0(u(x))$ with respect to x , i.e. $[W_0(u(x))]''$ we write

$$\begin{aligned} [W_0(u(x))]'' &= u''(x)W_0'(x) + [u'(x)]^2 W_0''(u(x)) \\ &= \frac{u''(x)W_0(u(x))}{u(x)[W_0(u(x)) + 1]} - \frac{[u'(x)]^2 [W_0(u(x))]^2 (W_0(u(x)) + 2)}{[u(x)]^2 [1 + W_0(u(x))]^3} \\ &= \frac{W_0(u(x))}{u(x)[W_0(u(x)) + 1]} \left[u''(x) - \frac{[u'(x)]^2 W_0(u(x))(W_0(u(x)) + 2)}{u(x) [1 + W_0(u(x))]^2} \right]. \end{aligned} \quad (\text{A.26})$$

The factor, $\frac{W_0(u(x))}{u(x)[W_0(u(x))+1]}$ in (A.26) which is the same as $W_0'(u(x))$, is clearly positive. Thus, it is required to prove that

$$u''(x) > \frac{[u'(x)]^2 W_0(u(x))(W_0(u(x)) + 2)}{u(x) [1 + W_0(u(x))]^2} \quad (\text{A.27})$$

Since the modified Bessel function $I_0(x)$ is monotone increasing and convex for $x > 0$, we have $u'(x) > 0$ and $u''(x) > 0$. Thus, both sides of the inequality (A.27) are positive. Furthermore, noting that

$$\frac{W_0(u(x))(W_0(u(x)) + 2)}{[1 + W_0(u(x))]^2} = \frac{[1 + W_0(u(x))]^2 - 1}{[1 + W_0(u(x))]^2} < 1,$$

one can prove $u''(x) > \frac{[u'(x)]^2}{u(x)}$ on behalf of proving (A.27), and since $u'(x) > 0$ we should equivalently prove

$$\frac{u''(x)}{u'(x)} > \frac{u'(x)}{u(x)}. \quad (\text{A.28})$$

After simple calculation of derivatives of $u(x)$ and plugging them in (A.28) we have the following inequality for proving:

$$\frac{I_0(x)}{I_1(x)} - \frac{1}{x} > \frac{I_1(x)}{I_0(x)}. \quad (\text{A.29})$$

Using (A.12) we have $\frac{I_1(x)}{I_0(x)} < \sqrt{1 + (\frac{1}{2x})^2} - \frac{1}{2x}$ and $\frac{I_0(x)}{I_1(x)} > \frac{x}{\sqrt{x^2+1}-1}$. Then, instead of (A.29) we can prove the inequality $\frac{\sqrt{4x^2+1}+1}{2x} < \frac{x}{\sqrt{x^2+1}-1}$ whose validity can be easily checked by variable substitution $x = \sinh(y)$ and the identity $\cosh^2(y) - \sinh^2(y) = 1$. ■

A.3 Proof of Theorem 2

With regard to (5.7), the objective here is to prove that $i_{\text{out}}^{\text{UDT}} > i_{\text{out}}^{\text{UDP}}$ for any $K > 1$, $\mu > 0$, $I_s > 0$, and $\alpha_n > 0$, $n \in \{1, \dots, N\}$, i.e.,

$$\frac{1}{\mu\sqrt{K}} \left(W_0 \left(\mu I_s A_0(\boldsymbol{\alpha}) e^{\mu I_s} \right) - \mu I_s \right) > \frac{1}{\mu} \left(W_0 \left(\mu I_s A_0(\boldsymbol{\alpha}/\sqrt{K}) e^{\mu I_s} \right) - \mu I_s \right), \quad (\text{A.30})$$

where we recall that $\mu = \frac{R_L}{\eta v_T}$ and $\alpha_n = \frac{\sqrt{2P\lambda R_{\text{ant}}}}{\eta v_T} \|\mathbf{h}_n\|$. The proof is very similar to the approach used in proving Theorem 1. Again, denoting μI_s by γ for simplicity, the inequality in (A.30) can be rewritten as

$$W_0 \left(\gamma e^\gamma A_0(\boldsymbol{\alpha}) \right) - \gamma > \sqrt{K} \left[W_0 \left(\gamma e^\gamma A_0 \left(\boldsymbol{\alpha}/\sqrt{K} \right) \right) - \gamma \right]. \quad (\text{A.31})$$

Similar to (A.5), the inequality in (A.31) changes to equality if at least one of the following three conditions holds true: $\gamma = 0$, $\boldsymbol{\alpha} = \mathbf{0}$, $K = 1$. To prove the inequality, we make use Theorem 3. This time, we take $\mathbf{x} = (\gamma, \alpha_1, \dots, \alpha_N, K)^\top$ and $\mathbf{a} = (0, 0, \dots, 0, 1)^\top$. We denote the LHS of (A.31) by $f(\mathbf{x}) = f(\gamma, \alpha_1, \dots, \alpha_N, K) = W_0(\gamma e^\gamma \prod_{n=1}^N I_0(\alpha_n)) - \gamma$ and the RHS of (A.31) by $g(\mathbf{x}) = g(\gamma, \alpha_1, \dots, \alpha_N, K) = \sqrt{K} \left[W_0 \left(\gamma e^\gamma \prod_{n=1}^N I_0(\alpha_n/\sqrt{K}) \right) \right] - \gamma$. As observed, we have $f(0, 0, \dots, 0, 1) = g(0, 0, \dots, 0, 1) = 0$. Now, we should verify that a) $\frac{\partial f(\gamma, \boldsymbol{\alpha}, K)}{\partial \gamma} > \frac{\partial g(\gamma, \boldsymbol{\alpha}, K)}{\partial \gamma}$, b) $\frac{\partial f(\gamma, \boldsymbol{\alpha}, K)}{\partial \alpha_n} > \frac{\partial g(\gamma, \boldsymbol{\alpha}, K)}{\partial \alpha_n}$ for $n \in \{1, \dots, N\}$, and c) $\frac{\partial f(\gamma, \boldsymbol{\alpha}, K)}{\partial K} > \frac{\partial g(\gamma, \boldsymbol{\alpha}, K)}{\partial K}$. We show these in the following parts, respectively.

a) Noting that $I_0(\alpha_n) > I_0(\alpha_n/\sqrt{K})$ for $n \in \{1, \dots, N\}$ and $K > 1$, it can be easily confirmed that $\prod_{n=1}^N I_0(\alpha_n) > \prod_{n=1}^N I_0(\alpha_n/\sqrt{K})$. Hence, we have $A_0(\boldsymbol{\alpha}) > A_0(\boldsymbol{\alpha}/\sqrt{K})$, and applying the same reasoning in deriving (A.6)-(A.8), this part is checked true.

b) This part is very similar to the reasoning used in proving part b) in Appendix A.2.

The goal is to prove that $\frac{\partial g(\gamma, \alpha_1, \dots, \alpha_N, K)}{\partial K} < 0$. Trying to obtain this partial derivative and after a bit of simplification, we get the following equivalent inequality:

$$\frac{W_0(\gamma e^\gamma A_0(\boldsymbol{\alpha}/\sqrt{K}))}{1 + W_0(\gamma e^\gamma A_0(\boldsymbol{\alpha}/\sqrt{K}))} \sum_{n=1}^N \frac{\alpha_n}{\sqrt{K}} \frac{I_1(\alpha_n/\sqrt{K})}{I_0(\alpha_n/\sqrt{K})} > W_0(\gamma e^\gamma A_0(\boldsymbol{\alpha}/\sqrt{K})) - \gamma. \quad (\text{A.32})$$

Again we substitute $1/\sqrt{K}$ with x and define $U(x) = \gamma e^\gamma A_0(\boldsymbol{\alpha}x) = \gamma e^\gamma \prod_{n=1}^N I_0(\alpha_n x)$. Then, (A.32) can be written as follows:

$$xU'(x)W_0'(U(x)) > W_0(U(x)) - \gamma, \quad (\text{A.33})$$

which is similar to (A.21) with $u(x)$ replaced with $U(x)$. Similarly, the mean-value theorem can be applied again and the validity of (A.33) can be checked true given that we prove $U(x)$ is a monotonically increasing convex function. Hence, we should prove that $[W_0(U(x))]' > 0$ and $[W_0(U(x))]'' > 0$. The former is derived as follows:

$$[W_0(U(x))]' = U'(x)W_0'(U(x)) \quad (\text{A.34})$$

where again since $W_0'(x) > 0$ and $U'(x) = \gamma e^\gamma (\prod_{n=1}^N I_0(\alpha_n x)) \sum_{n=1}^N \alpha_n \frac{I_1(\alpha_n x)}{I_0(\alpha_n x)} > 0$ it concludes $[W_0(U(x))]' > 0$. For checking $[W_0(U(x))]'' > 0$, the same reasoning used in reaching to (A.28) can be applied here and get the following target inequality

$$\frac{U''(x)}{U'(x)} > \frac{U'(x)}{U(x)}, \quad (\text{A.35})$$

where that $U''(x) > 0$ is true can be easily checked by noting that $\frac{I_1(x)}{I_0(x)}$ is a monotonically increasing function for $x > 0$. Consequently, to prove the inequality (A.35), we start from writing the following true inequality for $\Delta x > 0$

$$\frac{I_1((x + \Delta x)\alpha_n)}{I_0((x + \Delta x)\alpha_n)} > \frac{I_1(x\alpha_n)}{I_0(x\alpha_n)}, \quad n \in \{1, \dots, N\}.$$

Then, we can write

$$\sum_{n=1}^N \frac{I_1((x + \Delta x)\alpha_n)}{I_0((x + \Delta x)\alpha_n)} > \sum_{n=1}^N \frac{I_1(x\alpha_n)}{I_0(x\alpha_n)},$$

and from there we can write

$$\log \left(\frac{\gamma e^\gamma A_0((x + \Delta x)\boldsymbol{\alpha}) \sum_{n=1}^N \frac{I_1((x + \Delta x)\alpha_n)}{I_0((x + \Delta x)\alpha_n)}}{\gamma e^\gamma A_0(x\boldsymbol{\alpha}) \sum_{n=1}^N \frac{I_1(x\alpha_n)}{I_0(x\alpha_n)}} \right) > \log \left(\frac{\gamma e^\gamma A_0((x + \Delta x)\boldsymbol{\alpha})}{\gamma e^\gamma A_0(x\boldsymbol{\alpha})} \right),$$

which can be equivalently written as follows:

$$\log(U'(t)) \Big|_x^{x+\Delta x} > \log(U(t)) \Big|_x^{x+\Delta x} \Rightarrow \int_x^{x+\Delta x} \frac{U''(t)}{U'(t)} dt > \int_x^{x+\Delta x} \frac{U'(t)}{U(t)} dt,$$

Where after operating $\lim_{\Delta x \rightarrow 0}$ on both sides of the inequality and recalling that $U(t)$, $U'(t)$, and $U''(t)$ are all positive for $t > 0$, we have

$$\frac{U''(x)}{U'(x)} \Delta x > \frac{U'(x)}{U(x)} \Delta x, \quad (\text{A.36})$$

which concludes the proof. ■

A.4 Helpful Plots

In this section, plots of the key functions used for proofs in the Appendix section are presented.

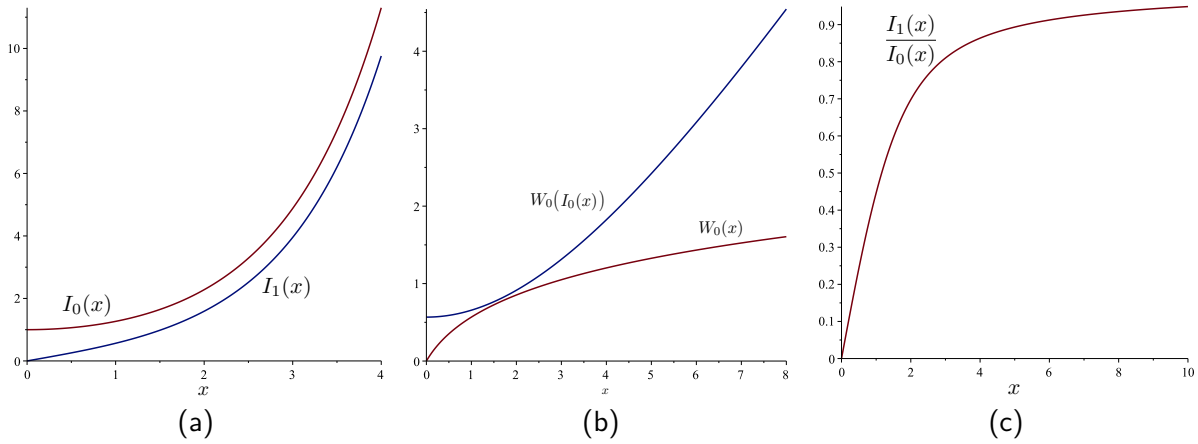


Figure A.2:

Appendix B

Publications

The findings of this thesis have already resulted in several published and submitted transactions and conference papers as listed in the following.

B.1 Journal Papers

- A. Bayat and S. Aïssa, “Fair Scheduling of Wireless Power to Nonlinear Energy Harvesters,” *IEEE Transactions on Green Communications and Networking*, (submitted, 2020).
- A. Bayat and S. Aïssa, “Deep Learning-Based Auction-Driven Beamforming for Wireless Information and Power Transfer,” *IEEE Transactions on Wireless Communications*, (under second round of review).
- A. Bayat and S. Aïssa, “When Bessel Meets Fourier in the Power Representation of Energy Harvesting Rectennas,” in *IEEE Communications Letters*, vol. 24, no. 1, pp. 67–70, Jan. 2020.
- A. Bayat and S. Aïssa, “Auction-Based Design and Analysis of Wireless Power Transfer Network with Critical Users,” in *IEEE Wireless Communications Letters*, vol. 22, no. 11, pp. 2374–2377, Nov. 2018.

B.2 Conference Papers

- A. Bayat and S. Aïssa, “Auction-Driven Multiuser Beamforming with Deep Learning,” in *Proc. IEEE Global Communications Conference (Globecom’20)*, Taipei, Taiwan, Dec. 2020.
- A. Bayat and S. Aïssa, “Shaping Energy Beamforming to the Nonlinearity of Energy Harvesting Devices,” in *Proc. International Conference on Computing, Networking and Communications (ICNC’20)*, Kona, HI, USA, Feb. 2020, pp. 1–5. (**Invited Paper**)
- A. Bayat and S. Aïssa, “Wireless Power Transfer Scheduling: Comparative Study of TDMA and SDMA under Harvesters Nonlinearity,” in *Proc. IEEE Global Communications Conference (Globecom’19)*, Waikoloa, HI, USA, Dec. 2019, pp. 1–6.
- A. Bayat and S. Aïssa, “Admission Control and Power Allocation in Wireless Power Charging Networks,” in *Proc. IEEE International Symposium on Personal, Indoor and Mobile Radio Communications (PIMRC’17)*, Montreal, QC, Oct. 2017, pp. 1–5.

Part V

Résumé Français

Appendix C

Introduction et Objectifs

C.1 Communications Alimenté sans Fil

La durée de vie limitée de la batterie de l'appareil est une préoccupation clé dans la conception des technologies sans fil modernes. La recharge ou le remplacement fréquent des batteries est souvent coûteux en raison du grand nombre d'appareils sans fil utilisés, et même irréalisable dans de nombreuses applications critiques telles que des capteurs intégrés dans des structures, installés dans des environnements difficiles ou des dispositifs médicaux implantés. Les communications alimentées sans fil sont un paradigme pour les systèmes de communication sans fil actuels et futurs (5G et au-delà) qui permet aux appareils sans fil de communiquer tout en obtenant leur énergie de fonctionnement nécessaire à partir d'un émetteur sans fil dédié.

Charger des appareils sans fil n'est pas quelque chose de nouveau et remonte à 1899 lorsque Tesla a mené la première expérience sur WPT[1, 2]. WPT fournit une solution attrayante en alimentant les appareils avec une énergie continue et stable sur l'air. En exploitant les propriétés radiatives en champ lointain des ondes électromagnétiques, les récepteurs sans fil peuvent récolter de l'énergie à distance à partir des signaux RF rayonnés par un émetteur d'énergie (ET). Le WPT bénéficie de nombreux avantages pratiques car il est stable, entièrement contrôlable dans sa puissance d'émission, ses formes d'onde et ses dimensions temps/fréquence occupées pour alimenter les récepteurs d'énergie (ER) — contrairement aux ressources énergétiques intermittentes et incontrôlables comme l'énergie solaire, éolienne ou ambiante Radiations EM. Par conséquent, le WPT

est un candidat idéal pour les applications nécessitant le déploiement de dispositifs à faible consommation, comme dans les réseaux de capteurs sans fil (WSN), les réseaux de surface corporelle sans fil (WBAN) et l'Internet des objets (IoT).

Les communications alimentées sans fil font référence aux réseaux de communication dans lesquels les informations sans fil et le transfert d'énergie (WIPT) ¹ coexistent. Contrairement à la communication sans fil conventionnelle où le canal sans fil vise à transporter des informations entre les nœuds, dans les architectures de réseau WIPT, la puissance (ou l'énergie) sans fil est également transférée via les médias pour charger les ER et leur permettre d'effectuer leurs communications. De cette manière, WIPT peut être considéré comme une application de WPT dans le domaine des communications sans fil. Par WIPT, les appareils utilisent l'énergie RF collectée pour transmettre/décoder des informations vers/depuis d'autres appareils. Sans être interrompu par l'épuisement d'énergie dû à l'utilisation de la communication, WIPT devrait améliorer l'expérience de l'utilisateur et la commodité, avec des performances de débit plus élevées et plus durables que les communications conventionnelles alimentées par batterie [4].

C.2 Les Problèmes de Recherche

Sachant que le WPT est considéré comme un candidat prometteur pour les communications futures [4], l'un des grands défis est le problème proche de la planification équitable de la puissance sans fil des ER. Le canal de bout en bout dans un système WPT est non linéaire et la plupart des recherches dans la littérature supposent un modèle linéaire dans leur analyse et la conception de schémas d'ordonnancement et de formation de faisceaux d'énergie [9, 20, 21]. Des recherches récentes [6, 7] montrent l'importance de considérer la non-linéarité des ER dans la modélisation du dispositif et la conception de signaux de transmission multi-tons plus efficaces. Un problème qui n'a pas été étudié dans ce chemin de recherche est la conception et l'analyse d'algorithmes d'ordonnancement de puissance et de formation de faisceau tout en tenant compte de l'effet de non-linéarité des ER. Ainsi, il est d'abord nécessaire qu'une formule traitable reliant la quantité d'énergie récoltée dans un nœud de sortie ER à la forme d'onde du signal d'entrée soit dérivée.

¹WIPT et WPC indiquent la même signification.

Un autre problème de recherche pertinent, qui peut être considéré comme une continuation du problème déjà mentionné, est la conception d'algorithmes d'allocation pour des informations de forme de faisceau et/ou de puissance en utilisant un cadre d'enchères. La prochaine génération de réseaux de communication sera principalement basée sur des schémas de fourniture de services en ligne centrés sur l'utilisateur, qui donneront à l'utilisateur plus de degrés de liberté pour choisir parmi différents fournisseurs de services pour que ses exigences de QoS soient satisfaites avec le coût minimum. Ainsi, les tâches de marketing et de tarification ne seront plus statiquement réglées à différents niveaux. Au lieu de cela, nous sommes confrontés à un problème d'allocation/planification des ressources inter-couches [22, 23, 24, 25]. Quel que soit le type de technologie WIPT déployé, le nombre d'émetteurs d'informations et de puissance (qui peuvent être colocalisés ou séparés) est limité et les fournisseurs de services doivent desservir plusieurs utilisateurs en même temps. Dans de nombreuses applications, les appareils sans fil sont des entités indépendantes avec un budget monétaire limité qui demandent un service avec un certain niveau de qualité à un fournisseur qui tente indépendamment de maximiser ses propres revenus. Dans de tels réseaux, où toutes les entités se comportent de manière égoïste, les enchères et la conception de mécanismes d'allocation de ressources optimaux basés sur les enchères peuvent rendre chaque entité heureuse et maximiser le bien-être social. Bien que peu nombreux, il existe des travaux de recherche sur l'application des enchères et des techniques de théorie des jeux pour l'allocation des ressources dans les réseaux WPT [26, 27, 28]; et seulement quelques-uns sur WIPT. À notre connaissance, la conception de mécanismes optimaux basés sur les enchères applicables aux réseaux WIPT n'a pas encore été (bien) explorée et c'est ce problème qui est étudié dans cette thèse. Un grand défi dans la conception de mécanismes d'enchères pour les canaux WIPT est l'augmentation de la complexité qui survient en particulier lorsque le nombre d'appareils, c'est-à-dire les IR et les ER, dans le réseau augmente. Avec ce niveau de complexité, les algorithmes itératifs conventionnels sont gourmands en temps et donc plus applicables aux applications temps réel.

C.3 Objectifs de Recherches

Après avoir discuté des principaux problèmes de recherche dans la sous-section précédente, cette sous-section décrit les objectifs de cette thèse. Ces objectifs sont énumérés et expliqués dans les quatre parties suivantes.

C.3.1 Analyse non Linéaire des Redresseurs dans les ER

Cette thèse propose des formules traitables décrivant, avec suffisamment de précision, le courant continu de sortie d'un redresseur typique en fonction des caractéristiques de la forme d'onde d'entrée. Cette formule peut être appliquée pour une analyse précise de l'efficacité de conversion de puissance DC de sortie en entrée RF des ER, une mise en forme efficace du signal d'émission ET dans les systèmes WPT; et la conception de la programmation de la puissance et de la formation de faisceaux d'énergie dans les systèmes WPT.

C.3.2 Analyse des Performances des Schémas de Planification Pour les Systèmes WPT

Compte tenu de l'effet non linéaire des ER qui, à son tour, rend le canal de bout en bout non linéaire, cette deuxième partie de la recherche analyse les schémas d'ordonnancement d'approvisionnement en équité dans un système WPT. En utilisant les formules dérivées dans la partie précédente, l'objectif ici est d'analyser les schémas d'ordonnancement de puissance, à savoir le partage de temps et le multiplexage spatial, et d'évaluer leurs performances pour satisfaire l'équité max-min entre les ER. De telles analyses souligneront l'importance de considérer la non-linéarité des canaux de bout en bout dans la conception d'algorithmes d'ordonnancement de puissance.

C.3.3 Conception et Analyse d'Algorithmes d'Allocation de Ressources Basés sur les Enchères pour les Systèmes WPT

Les enchères sont les bienvenues en tant que cadre de concurrence approprié pour modéliser les agents à comportement égoïste, au problème de l'allocation des ressources dans les systèmes WPT. L'objectif est de rechercher un algorithme d'allocation de ressources distribué efficace géré par les agents jouant des enchères répétées. Ensuite, l'algorithme est analysé pour l'existence des points d'équilibre de Nash et l'efficacité de ces points ainsi que le taux de convergence de l'algorithme sont analysés. Les agents agissant sont les ER. La plupart des algorithmes associés dans la littérature sont conçus pour des réseaux statiques où il existe un nombre fixe d'utilisateurs et/ou les utilisateurs se comportent de manière non adaptative aux offres des autres utilisateurs. Par conséquent, ils ne sont pas optimaux pour les réseaux dynamiques où il y a du *trafic* d'appareils avec des taux d'arrivée

des demandes d'enchères différents et/ou les appareils ont la capacité d'adapter leurs stratégies d'enchères en fonction du comportement d'enchères des autres utilisateurs.

C.3.4 Conception de Mécanismes d'Enchères avec Apprentissage en Profondeur pour les Systèmes SWIPT

Nous explorons des algorithmes traitables pour l'allocation de ressources en temps réel dans les systèmes SWIPT dans un cadre d'enchères. L'objectif est de rechercher des solutions en temps réel pour résoudre les problèmes de gourmandise en temps dans la résolution des problèmes d'allocation de ressources en temps réel, en particulier grâce à la formation de faisceaux d'informations et de puissance pour les systèmes SWIPT, tandis que le bien-être social ou les revenus sont les principaux objectifs. Pour résoudre ce problème, une solution consiste à utiliser l'apprentissage automatique, et en particulier l'apprentissage profond. Récemment, l'intelligence artificielle (IA) a commencé à susciter un intérêt significatif dans le domaine de la recherche sur les réseaux de communication mobiles et sans fil [29]. Après sa victoire claire dans la vision par ordinateur, le traitement du langage naturel, la reconnaissance de la parole et des images, l'IA touche désormais d'autres domaines tels que les communications sans fil et les réseaux mobiles. Cette montée en flèche de la recherche liée à l'IA dans le domaine du sans fil est en effet due à la diversité et à la complexité croissantes des architectures de réseaux mobiles qui ont rendu le traitement, la surveillance et la gestion de ces réseaux insolubles. Ainsi, une solution candidate pour résoudre le problème de la complexité dans la conception de l'allocation en temps réel basée sur les enchères pour les réseaux SWIPT est l'application de l'IA dans le processus de conception.

C.4 Methodologie

Dans cette section, nous décrivons comment les objectifs expliqués dans le chapitre précédent sont atteints. Les contributions associées sont également répertoriées à la fin de chaque section.

C.4.1 Analyse non Linéaire des Redresseurs dans les ER

La théorie des circuits est appliquée pour modéliser les éléments redresseurs, les diodes, dans les circuits ER. La plate-forme de conception de système ADS de KeySight est appliquée pour dessiner les circuits ER et exécuter des simulations pour calculer le courant DC de sortie. Les modèles SPICE du fabricant sont utilisés pour modéliser les diodes utilisées dans les simulations. Les moteurs de simulation *Transitoire* et *Balance harmonique* sont appliqués pour résoudre les circuits associés et obtenir les résultats de la simulation. Les filtres LC correspondants pour l'entrée des ER sont conçus et optimisés dans ADS.

Le théorème des résidus d'analyse complexe est appliqué pour résoudre l'intégrale compliquée qui apparaît lors de la formulation mathématique du courant DC de sortie des ERs. La plateforme Maple permet de vérifier la validité des résultats. Matlab est utilisé pour écrire toutes les formules et à des fins de traçage. Les données de simulation d'ADS sont exportées au format CSV puis importées dans Matlab à des fins de comparaison.

Les processus stochastiques, en tant que composante indissociable des communications sans fil, ici pour cet objectif, sont simplement utilisés pour modéliser les canaux sans fil tout au long de la thèse. En général, *Théorie de l'optimisation* est largement utilisée tout au long de la thèse pour résoudre différentes formes de problèmes d'optimisation. En particulier, le package CVX et les algorithmes de point intérieur de la solution non linéaire intégrée dans Matlab sont utilisés pour résoudre le problème de la formation de faisceaux d'énergie sur des collecteurs d'énergie à antennes multiples.

Contributions

- Une nouvelle formule exacte de forme fermée pour représenter le courant de sortie des ERs en termes de contenu spectral de la forme d'onde incidente est dérivée.
- Une formule de borne inférieure traitable qui peut encore être appliquée à une large gamme de puissance d'entrée des ERs est également dérivée.
- Sur la base de la formule de la borne inférieure, des vecteurs de formation de faisceaux d'énergie pour un système MIMO-WPT point à point sont obtenus. Ensuite, l'importance de considérer

des modèles non linéaires au lieu de modèles linéaires est soulignée par des comparaisons de leur précision dans la description du courant DC de sortie des ERs dans les systèmes WPT.

C.4.2 Analyse des Performances des Schémas de Planification pour les Systèmes WPT

Les processus stochastiques sont utilisés pour modéliser les canaux sans fil. Les algorithmes d'optimisation ainsi que certains algorithmes heuristiques de Matlab pour trouver les vecteurs de formation de faisceau sont appliqués. La plateforme Maple est utilisée pour vérifier la validité des théorèmes proposés. Le réseau est modélisé comme un système WPT multi-utilisateurs à entrées multiples et à sortie unique (MU-MISO).

Contributions

- En utilisant des inégalités complexes de Lambert-Bessel, un théorème de valeur moyenne, un théorème de monotonocité et quelques autres, nous prouvons solidement la supériorité du schéma d'ordonnancement en temps partagé sur le multiplexage spatial sous le critère d'équité max-min tandis que la non-linéarité des ERs est prise en compte . La preuve est d'abord effectuée pour les signaux à une seule dent, puis est étendue aux signaux à plusieurs tons.
- L'analyse des performances est effectuée pour les types de signaux de transmission à une tonalité et à plusieurs tonalités.

C.4.3 Conception et Analyse d'Algorithmes d'Allocation de Ressources Basés sur les Enchères pour les Systèmes WPT

La théorie des jeux est l'outil nécessaire pour analyser les enchères. Nous appliquons la théorie des jeux pour analyser les algorithmes distribués afin de voir s'ils convergent vers les points d'équilibre de Nash (NEPs). Nous utilisons deux mesures du bien-être social et du prix de l'anarchie pour évaluer l'efficacité des algorithmes. Pour que l'ET puisse effectuer le contrôle de puissance et le contrôle d'admission des ERs, le processus de génération des demandes d'offre est modélisé par des chaînes de Markov en temps continu (CTMC), et analysé par des processus stochastiques. La

file d'attente $M/M/N/N$ correspondante, qui est la même que le système de perte d'Erlang, est analysée en utilisant la théorie des files d'attente.

Pour adapter le comportement d'enchères des ERs à la stratégie ET ainsi qu'aux autres comportements d'enchères des ERs, nous utilisons la théorie de l'apprentissage pour renforcer les ERs afin qu'ils adaptent leurs comportements afin de maximiser leurs gains. Nous proposons une stratégie d'enchères auto-stabilisante qui se traduit par des gains plus élevés pour les utilisateurs et une augmentation du bien-être social et une diminution du prix de l'anarchie. L'algorithme de point intérieur de Matlab est appliqué pour calculer ces métriques et comparer la stratégie d'enchères statique avec la stratégie dynamique.

Contributions

- Conception d'un algorithme distribué prenant en compte la dynamique et le comportement d'enchères des ERs.
- Application de la théorie des jeux et de la théorie des files d'attente pour analyser l'algorithme qui est une nouvelle approche.
- Concevoir une stratégie de jeu adaptative basée sur l'apprentissage pour les ERs qui les pousse à un meilleur NEP par rapport à celui où les ERs jouent simultanément sans apprendre de l'historique de jeu passé.

C.4.4 Conception de Mécanismes d'Enchères avec Apprentissage en Profondeur pour les Systèmes SWIPT

Ce dernier objectif de recherche comporte trois éléments clés. Conception de mécanismes d'enchères, apprentissage en profondeur et formation de faisceaux. Pour la partie conception des mécanismes, le lemme de Myerson et les mécanismes de Vickrey-Clarke-Groves (VCG) en économie sont les méthodes de conception les plus candidates. Pour la partie apprentissage en profondeur, le langage de programmation Python avec son énorme collection de bibliothèques d'apprentissage automatique est sans aucun doute la bonne plateforme. Le réseau neuronal profond (DNN) proposé est formé à l'aide de l'interface de programme d'application (API) TensorFlow bien connue. Merci à ComputeCanada pour avoir fourni des ressources informatiques à distance qui ont considérablement

accélére le processus de formation et le processus de génération de la grande quantité d'échantillons de formation. Les données d'entraînement sont manipulées à l'aide de la bibliothèque Pandas. Pour la dernière partie, c'est-à-dire la formation de faisceaux, des techniques de relaxation semi-définie (SDR) pour résoudre des problèmes de cône quadratique du second ordre sont appliquées. La bibliothèque Python CVXPY, similaire à son homologue Matlab CVX, est appliquée pour tirer parti de la formulation des formes standard de problèmes d'optimisation de manière abstraite en Python. En particulier, le solveur de Mosek pour résoudre la programmation semi-définie est utilisé comme méthode de résolution dans CVXPY.

Contributions

- Proposition d'une approche basée sur DNN pour résoudre le problème de la maximisation des revenus qui a traditionnellement une complexité temporelle exponentielle. Cette approche présente une complexité temporelle linéaire en termes de nombre d'UEs dans le réseau et de nombre d'antennes ET. Cette approche met en évidence la façon dont l'apprentissage profond peut être appliqué à des problèmes complexes d'allocation de ressources en tant que solution prometteuse.
- Proposition d'un algorithme itératif heuristique avec une complexité temporelle polynomiale pour résoudre le problème complexe d'allocation de ressources.
- Proposition d'un algorithme BnB (Branch-and-Bound) efficace.

Appendix D

Dérivation de Formules Tractables pour les Récolteuses d'Énergie

Dans RF-WPT, le faible rendement de conversion d'énergie de bout en bout peut être abordé de plusieurs façons, en particulier en i) en augmentant l'efficacité de l'amplificateur de puissance au niveau de l'émetteur d'énergie (ET), ii) en exploitant plusieurs antennes pour former le faisceau de l'énergie vers le récepteurs d'énergie (ERs) [3], iii) la mise en forme du signal d'émission en fonction de la non-linéarité des ERs [7], et iv) l'amélioration des circuits de redressement en employant plusieurs antennes et des redresseurs haute performance [30, 31, 32].

En raison de la non-linéarité du circuit de redressement, le canal RF-WPT de bout en bout n'est plus linéaire. Par conséquent, la puissance DC de sortie dépendrait de la forme de la forme d'onde incidente et de sa puissance. Alors que la plupart des travaux sur RF-WPT considèrent un modèle linéaire reliant le courant DC de sortie du circuit ER au a reçu de la puissance au niveau de son (ses) antenne (antennes) [4, 20], peu ont pris en compte la non-linéarité des redresseurs (cf. [6, 7] et les références y figurant). Dans [6], en écrivant le courant de diode de l'ER sous forme d'expansion en série Taylor, les auteurs ont analysé un circuit redresseur et mis en lumière le fait que l'utilisation de signaux avec un rapport de puissance crête/moyenne élevé, comme les signaux de multiplexage par répartition orthogonale de la fréquence, peut augmenter l'efficacité de la conversion de bout en bout. Dans cette veine de lumière, [7] a proposé une conception de forme

d'onde de transmission multi-sinusoidale qui exploite la non-linéarité pour maximiser le courant DC des dispositifs de collecte.

En exploitant le théorème de résidu, nous proposons une formule de forme fermée qui relie le courant DC de sortie d'un circuit redresseur typique à l'amplitude des coefficients de la série de Fourier de son signal d'entrée multi-tons. Sur cette base, une autre formule facilement traitable est également proposée, appelée formule à limite inférieure.

Les comparaisons basées sur l'analyse et les simulations de circuits montrent que les deux formules sont de bonnes approximations pour la région d'opération de la loi carrée, c'est-à-dire pour une puissance de signal reçu inférieure à -20 dBm [33]. De plus, bien que les deux formules deviennent identiques à l'expression exacte dans le cas d'un signal d'entrée à une seule tonalité, il est démontré qu'elles conservent leur validité pour des niveaux de puissance de signal d'entrée plus importants, par exemple 0 dBm.

D.1 Le Modèle du Système

On considère un RF-WPT point à point entre un ET équipé d'antennes M et un ER mono-antenne. A l'ET, un budget de puissance de P et une bande passante B de N canaux de largeur égale sont utilisés pour envoyer des tonalités sinusoidales pondérées. La fréquence centrale de chaque canal est $f_n = f_1 + (n - 1)\Delta f$ où $\Delta f = B/N$. Considérant le circuit de récolte typique montré dans la

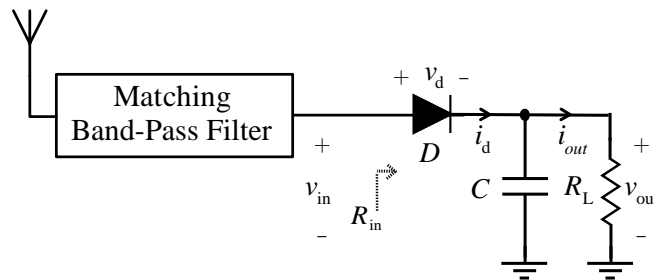


Figure D.1: Schéma fonctionnel simplifié du redresseur.

Fig. D.1 pour l'ER, pour lequel le courant de diode peut être écrit comme $i_d(t) = I_s(e^{\frac{v_d(t)}{\eta v_T}} - 1)$, le

courant DC de sortie i_{out} , en utilisant l'approximation de Taylor peut être écrit comme suit [7]:

$$i_{\text{out}} \approx k_0 + \sum_{\substack{\hat{N} \\ r \text{ even}, r \geq 2}} k_r (\lambda R_{\text{ant}})^{r/2} \mathbb{E} \{y(t)^r\}, \quad (\text{D.1})$$

où λ est le rapport d'impédance du filtre passe-bande, $y(t)$ est le signal incident, R_{ant} est la résistance de l'antenne, \hat{N} est le nombre de la troncature, $k_0 = I_s (e^{\frac{-v_{\text{out}}}{\eta v_T}} - 1)$, et $k_r = \frac{I_s}{(\eta v_T)^{r r!}} e^{\frac{-v_{\text{out}}}{\eta v_T}}$ pour $r \geq 2$. Dans [7], $\hat{N} = 4$ a été supposé dans les simulations. $\mathbb{E} \{y(t)^r\}$ devient plus compliqué en calcul avec l'augmentation de r . Cela nous motive également à adopter une approche différente et à rechercher une formule plus illustrative pour le courant DC de sortie, qui peut être exploitée pour concevoir et analyser des collecteurs d'énergie efficaces et transmettre la forme d'onde.

D.2 Nos Nouvelles Formules

En utilisant le théorème des résidus, nous dérivons la formule représentative suivante pour le courant DC de sortie du redresseur de la Fig. D.1 en termes de magnitudes, c'est-à-dire α_n , de la forme d'onde multi-sinusoidale:

$$i_{\text{out}} = -I_s + \frac{1}{\alpha} W_0 \left(A_0 \alpha I_s e^{\alpha I_s} \right), \quad (\text{D.2})$$

où A_0 est dérivé comme suit

$$A_0 = \sum_{m_3=-\infty}^{\infty} \sum_{m_4=-\infty}^{\infty} \dots \sum_{m_N=-\infty}^{\infty} I_{\sum_{n=3}^N (n-2)m_n}(\alpha_1) I_{\sum_{n=3}^N (n-1)m_n}(\alpha_2) I_{m_3}(\alpha_3) I_{m_4}(\alpha_4) \dots I_{m_N}(\alpha_N). \quad (\text{D.3})$$

où $I_v(\cdot)$ est la fonction de Bessel modifiée de premier type d'ordre v . On peut former \tilde{A}_0 en tronquant chaque sommation dans (D.3) de la limite inférieure de $-\mathcal{M}$ à la limite supérieure de \mathcal{M} . En général, pour tout N , comme $\alpha_n \rightarrow 0 \forall n \in \{1, 2, \dots, N\}$, (D.3) converge vers

$$A_0 = I_0(\alpha_1) I_0(\alpha_2) \dots I_0(\alpha_N). \quad (\text{D.4})$$

Expression (D.4) est une borne inférieure sur A_0 , qui, lors de la substitution dans (D.2), donne une borne inférieure sur i_{out} qui peut être exploitée dans l'analyse et la conception de systèmes RF-WPT.

Appendix E

Planification Équitable et Formation de Faisceaux d'Énergie dans les Systèmes WPT Multi-Bandes

Dans un contexte WPT multi-utilisateurs, un problème de conception important consiste à atteindre l'équité cible dans le service d'énergie sans fil que les appareils reçoivent de l'ET correspondant. En supposant une efficacité de conversion de puissance fixe, quel que soient les niveaux de puissance d'entrée ER, les méthodes d'ordonnement en temps partagé (TS) et en multiplexage spatial (SM) peuvent fonctionner de la même manière en termes d'équité entre les utilisateurs [21]. En pratique, cependant, l'efficacité a une relation non linéaire avec la puissance incidente sur les antennes ER, ce qui soulève la question de savoir comment ces deux schémas d'ordonnement fonctionneraient en termes de satisfaction de l'équité entre les ERs.

En prenant la question ci-dessus comme point de départ, et contrairement à la plupart des travaux dans lesquels un coefficient de conversion linéaire fixe est supposé pour relier la puissance DC de sortie d'un ER à sa puissance d'entrée [20, 21], dans cet article, une relation non linéaire est prise en compte et la supériorité de TS sur SM pour le WPT par blocs sur les canaux à évanouissement plat est démontrée pour les scénarios à bande unique et multi-bande. Les schémas d'ordonnement TS et SM sont étudiés en considérant deux conditions de réseau, *homogène* et *hétérogène*, dans des scénarios de fonctionnement *mono-bande* ou *multi-bandes*. Le cas particulier

du réseau homogène peut être considéré comme le pire des scénarios pour comparer les deux schémas d'ordonnement en termes de fourniture d'équité max-min entre les ERs. Dans le scénario homogène, les schémas optimaux SM et TS sont respectivement la *distribution uniforme de la puissance* (UDP) et la *distribution uniforme du temps* (UDT). Compte tenu du modèle de conversion de puissance non linéaire, il est prouvé que le transfert de la puissance disponible à l'ET vers les ERs de manière circulaire TS, c'est-à-dire UDT, surpasse le partage de la puissance disponible via des faisceaux à gain égal simultanés vers les ERs dans ces Mode SM, c'est à dire UDP. Bien que cela soit prouvé analytiquement pour le cas homogène à la fois dans les opérations à un seul ton et à plusieurs tons, des simulations approfondies sont également effectuées pour confirmer ladite supériorité pour les scénarios homogènes. Les principales contributions sont doubles: premièrement, pour le scénario homogène, nous prouvons analytiquement que lorsque le modèle de non-linéarité des redresseurs dans les circuits de récolte est pris en compte, alors l'ordonnement TS surpasse SM sous les critères d'équité max-min; deuxièmement, en nous inspirant de la manière analytique de raisonnement menée dans le scénario homogène, nous validons la revendication du scénario hétérogène par des séries extensives de simulations pour différents paramètres de réseau. Les résultats fournissent des lignes directrices importantes pour la conception d'une recharge d'énergie sans fil équitable dans les systèmes WPT.

E.1 Réseau Homogène:

Partage de Temps versus Multiplexage Spatial

Nous considérons un réseau électrique sans fil composé d'ERs à antenne unique K dans la couverture d'un ET équipé d'antennes M et ayant accès à B Hz de bande passante qui est divisé en sous-bandes N équi-bande passante tel que $B = N\Delta f$. Le but de l'ET est de maximiser l'énergie récoltée de l'ER avec le plus petit niveau d'énergie récoltée pendant chaque période de transmission de puissance \mathcal{T} en trouvant les vecteurs de formation de faisceau optimaux basés sur les informations côté canal acquises (CSI) de les urgences.

Dans ce cas homogène, les gains de puissance de canal de tous les ERs, qui sont supposés être distribués de manière claire et éloigné les uns des autres en ce qui concerne la largeur de faisceau du réseau d'antennes ET, sont supposés les mêmes dans toutes les sous bandes. Grâce à des théorèmes solides, il est prouvé que TS fonctionne mieux que SM lorsque l'on considère le critère d'équité

max-min. En fait, sous un tel critère, l'énergie récoltée par chaque ER pendant chaque durée de bloc WPT \mathcal{T} , pour les schémas TS et SM, atteindra son maximum si les gains de canal des ERs sont tous égaux au plus grand gain de puissance de canal dans le réseau. Dans le schéma UDT, tout le budget de puissance ET P est dirigé vers l'ER souhaité pour une durée de \mathcal{T}/K . Pour le schéma UDP, l'ET distribue uniformément sa puissance d'émission P dans ses faisceaux de largeur égale de sorte que chaque ER reçoive la même quantité d'énergie tout le temps. Pour les deux schémas d'allocation de puissance, les dispositifs de collecte sont supposés être distribués beaucoup plus loin que la largeur de faisceau du réseau d'antennes ET (cf. Fig. E.1).

E.1.1 Signal de Transmission Mono-Ton

Bientôt dans le Théorème E.1.1, il sera prouvé que lorsque la non-linéarité des redresseurs est prise en compte, alors sous le critère d'équité max-min le schéma UDT est supérieur au schéma UDP.

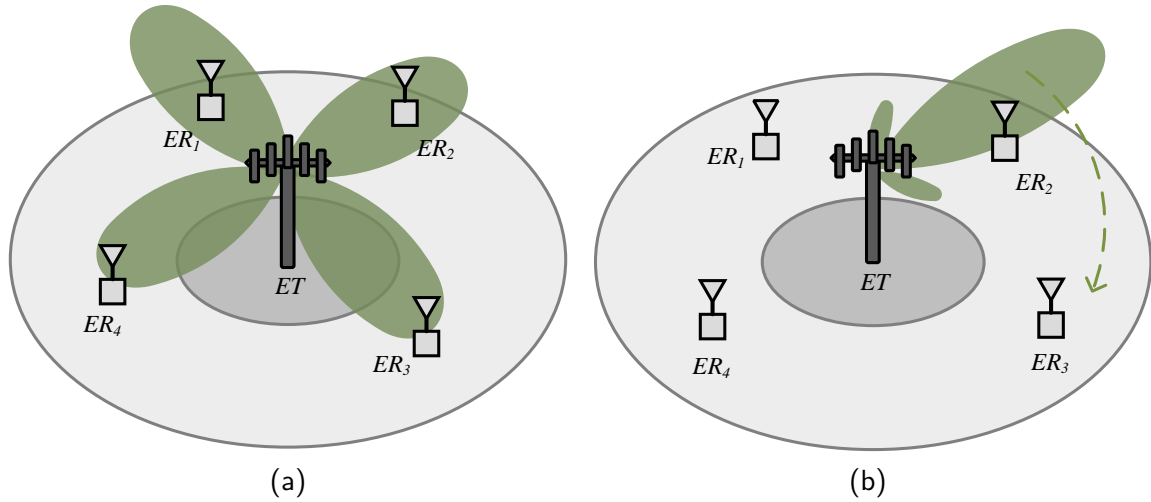


Figure E.1: Illustration des schémas (a) UDP et (b) UDT pour les appareils $K = 4$.

Pour représenter le courant de sortie, nous appliquons la relation suivante qui a été dérivée dans le chapitre précédent:

$$i_{\text{out}} = -I_s + \frac{1}{\mu} W_0 \left(I_0(\alpha) \mu I_s e^{\mu I_s} \right), \quad (\text{E.1})$$

Ensuite, après avoir trouvé les vecteurs de formation de faisceau optimaux pour l'UDT et l'UDP, le courant DC de sortie pour ces deux schémas peut être écrit comme

$$i_{\text{out}}^{\text{UDT}} = \frac{1}{\mu\sqrt{K}} W_0 \left(\mu I_s I_0(\alpha) e^{\mu I_s} \right) - \frac{I_s}{\sqrt{K}}, \quad (\text{E.2a})$$

$$i_{\text{out}}^{\text{UDP}} = \frac{1}{\mu} W_0 \left(\mu I_s I_0(\alpha/\sqrt{K}) e^{\mu I_s} \right) - I_s, \quad (\text{E.2b})$$

où $\alpha = \frac{\sqrt{2P\lambda R_{\text{ant}}}}{\eta v_T} \|\mathbf{h}\|$ avec \mathbf{h} étant le coefficient de canal. Maintenant, nous déclarons ci-dessous notre premier théorème clé pour les signaux de transmission à un seul ton:

Théorème E.1.1. *D'après (E.2), nous avons $i_{\text{out}}^{\text{UDT}} > i_{\text{out}}^{\text{UDP}}$ pour tout $K > 1$, $\mu > 0$, $\alpha > 0$ et $I_s > 0$.*

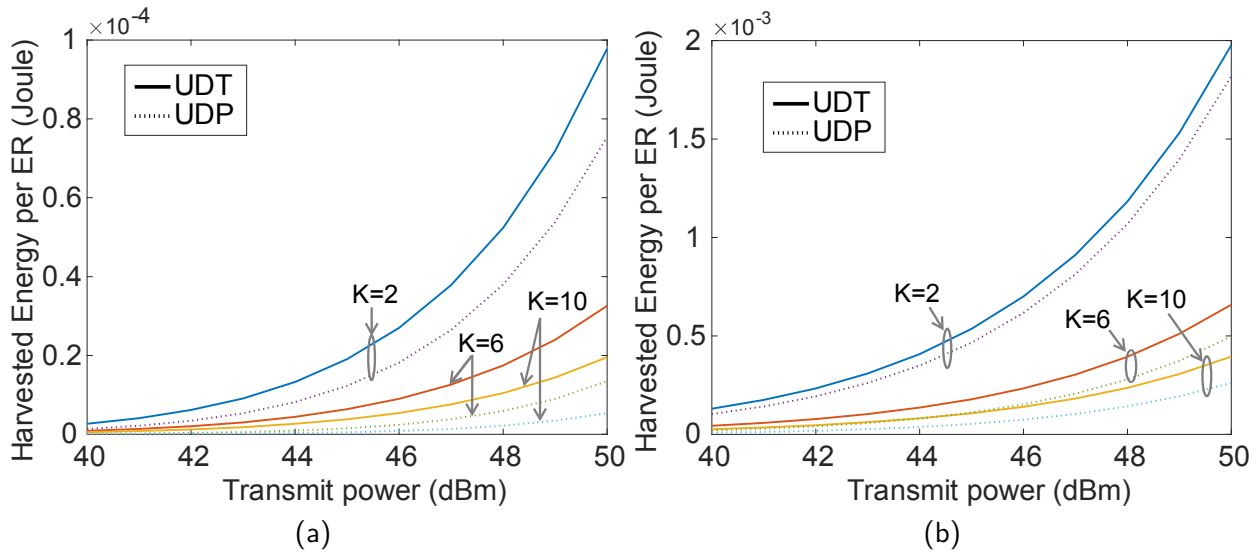


Figure E.2: L'énergie récoltée par ER pendant le bloc de transmission \mathcal{T} pour (a) $M = 4$ et (b) $M = 50$.

Pour illustrer la validation du Théorème E.1.1, la Fig. E.2 compare l'énergie récoltée lors de l'utilisation des techniques UDT et UDP. Les graphiques révèlent la supériorité de UDT sur UDP comme indiqué dans le Théorème E.1.1. Il convient également de noter que l'écart de performance entre ces deux schémas d'allocation se démarque lorsque la puissance d'émission ET P augmente en maintenant fixe le nombre d'ERs dans le réseau. Le même comportement croissant est observé à mesure que le nombre d'ER augmente tandis que la puissance d'émission reste la même. Sur la Fig. E.2b, avec $M = 50$, l'ET a un nombre massif d'antennes. Par rapport à la Fig. E.2, ici l'énergie

récoltée par chaque ER a une augmentation considérable en raison du gain de diversité (puissance) plus important résultant de l'utilisation de réseaux d'antennes massifs à l'ET. En outre, on constate que lorsque M augmente, l'écart de performance entre UDT et UDP devient plus petit.

E.1.2 Signal de Transmission Multi-Tons

Pour le cas homogène, puisque tous les ERs subissent le même coefficient de canal, bien que bien séparés les uns des autres, les poids optimaux de formation de faisceau pour tous les ERs sont les mêmes. Dans ce cas, les courants DC de sortie pour les schémas UDT et UDP deviennent:

$$i_{\text{out}}^{\text{UDT}} = \frac{1}{\mu\sqrt{K}} W_0 \left(\mu I_s \prod_{n=1}^N I_0(\alpha_n) e^{\mu I_s} \right) - \frac{I_s}{\sqrt{K}}, \quad (\text{E.3a})$$

$$i_{\text{out}}^{\text{UDP}} = \frac{1}{\mu} W_0 \left(\mu I_s \prod_{n=1}^N I_0(\alpha_n/\sqrt{K}) e^{\mu I_s} \right) - I_s. \quad (\text{E.3b})$$

La généralisation du résultat du Théorème E.1.1 pour le signal d'émission multi-ton dans le scénario homogène est énoncée dans le théorème suivant.

Théorème E.1.2. *D'après (E.3), nous avons $i_{\text{out}}^{\text{UDT}} > i_{\text{out}}^{\text{UDP}}$ pour tout $K > 1$, $\mu > 0$, $I_s > 0$ et $\alpha_n > 0$, $n \in \{1, \dots, N\}$.*

Comme nous avons fourni des validations pour le Théorème E.1.1 dans la Fig. E.2, de la même manière, nous montrons ici de manière illustrative la validité du Théorème 2 à travers la Fig. 5.1. La configuration du système ici est la même que celle utilisée pour tracer Fig. E.2 sauf le nombre de tonalités, N , qui sur la Fig. E.3 est 2 pour le scénario homogène multi-tons. La figure E.3 compare l'énergie récoltée lors de l'utilisation des techniques UDT et UDP. Comme exemple de validation du Théorème E.1.2, on voit que la figure E.3a et la figure 5.1b révèlent la supériorité de l'UDT sur UDP pour $M = 4$ et $M = 50$, respectivement. Comme observé, l'écart de performance entre ces deux schémas d'allocation se démarque lorsque la puissance d'émission ET P et/ou le nombre d'ERs, K , augmente.

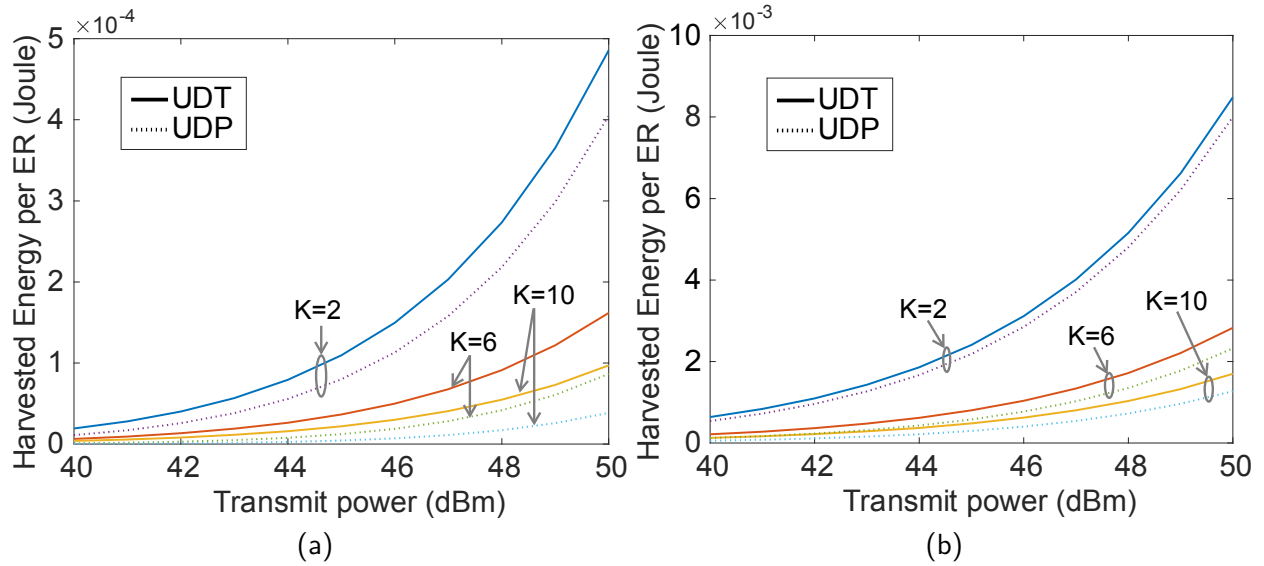


Figure E.3: L'énergie récoltée par ER pendant le bloc de transmission \mathcal{T} pour $N = 4$ sous-bandes: (a) $M = 4$ et (b) $M = 50$.

E.2 Réseau Hétérogène:

Partage de Temps versus Multiplexage Spatial

Pour les réseaux hétérogènes avec des scénarios à un et plusieurs tons, nous montrons à travers des simulations que le schéma d'ordonnancement en temps partagé surpasse toujours le schéma d'ordonnancement à multiplexage spatial. En utilisant des simulations de Monte Carlo, nous comparons les performances supérieures du schéma TS sur le schéma SM pour les scénarios de réseau hétérogènes monotones et multi-tons.

Appendix F

Charge d’Alimentation sans Fil Basée sur les Enchères

Le nombre d’émetteurs de puissance est généralement limité et chaque chargeur d’alimentation sans fil (WPC) doit desservir plusieurs utilisateurs en même temps. Dans [28] et [27], les auteurs ont étudié un WPCN assisté par balise de puissance en utilisant un jeu Stackelberg. Les deux jeux sont des jeux à deux joueurs et il n’y a pas de concurrence entre les utilisateurs. Dans [26], un WPCN est considéré où les utilisateurs envoient leurs offres à un point d’accès pour en recevoir l’énergie. Sous un mécanisme d’enchères et en utilisant la modélisation de Markov, les auteurs analysent la convergence de la stratégie des utilisateurs vers l’équilibre de Nash du jeu. Cependant, la dynamique des utilisateurs, en termes d’arrivée et de trafic par exemple, et l’utilité du WPC n’ont pas été prises en compte. En effet, comment contrôler l’admission des utilisateurs par le WPC et allouer de manière optimale la ressource électrique aux différents utilisateurs reste un problème fondamental d’une importance majeure et nécessite une attention particulière.

En considérant un WPCN, nous prenons en compte le taux d’arrivée des utilisateurs dans la zone de couverture WPC, et proposons un schéma d’admission et d’allocation de puissance qui maximise l’utilitaire WPC tout en gardant les utilitaires des utilisateurs à leur niveau de satisfaction. D’une part, plus il y a d’utilisateurs dans le WPCN, plus le gain du WPC sera élevé. Par conséquent, pour augmenter son taux de profit, le WPC aurait tendance à retarder le service aux utilisateurs en n’allouant pas sa puissance maximale afin de les laisser s’accumuler vers sa capacité d’hébergement

complète, ce qui à son tour pourrait entraîner une diminution considérable des services publics des utilisateurs. En revanche, si le WPC alloue sa puissance maximale indépendamment du nombre d'utilisateurs, son réseau sera vide la plupart du temps lorsque le taux d'arrivée des utilisateurs est faible. Dans ce cas, les utilisateurs seront les plus satisfaits. Ce dilemme nécessite de rechercher un système efficace de contrôle d'admission et d'allocation de puissance dans lequel les utilisateurs et les utilitaires WPC sont pris en compte.

Le chargeur d'alimentation sans fil maintient son taux de service en tirant parti de sa puissance. Du point de vue d'un utilisateur (externe) arrivant, il existe une file d'attente $M/M/N/N$ — la même que le système de perte d'Erlang [45] — que nous modélisons par une chaîne de Markov en temps continu. Du point de vue d'un utilisateur admis (interne), il existe un jeu dans lequel les utilisateurs se font concurrence pour recevoir l'alimentation du chargeur d'alimentation. Nous formulons correctement le problème comme une optimisation contrainte non linéaire, et le résolvons en utilisant un algorithme itératif conçu sur la base de la technique du point intérieur [46].

F.1 La Chaîne de Markov en Temps Continu

L'arrivée des utilisateurs sur le WPCN suit un processus de Poisson de taux λ . Chaque UE i a une demande de puissance d'unités q qu'il souhaite voir remplie par le WPC dans une durée qui est distribuée de manière exponentielle avec le paramètre de taux μ . Le modèle de chaîne de Markov en temps continu (CTMC) du réseau est illustré à la Fig. F.1. Chaque numéro d'état du CTMC représente le nombre d'UE dans le réseau.

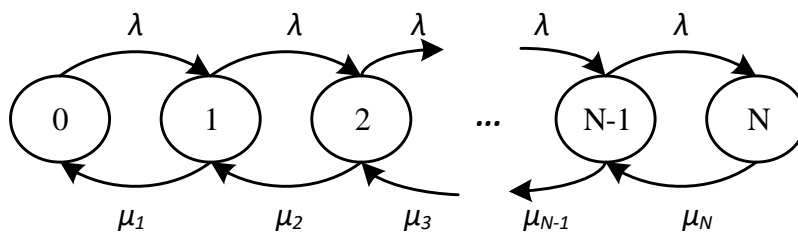


Figure F.1: La chaîne de Markov en temps continu.

Les utilisateurs admis par le chargeur de puissance diffusent leurs offres dans un horaire de plages horaires qui est mis à jour avec la puissance totale allouée chaque fois qu'un nouvel utilisateur est admis. Par conséquent, après chaque période d'enchères, tous les utilisateurs calculent leurs nouvelles stratégies de meilleure réponse (offres) en fonction de la connaissance des offres des autres utilisateurs, et les diffusent sur leurs plages horaires dédiées lors de la prochaine période d'enchères.

Du côté WPC, la capacité de puissance maximale est de P_{\max} unités de puissance, et la capacité d'hébergement maximale est de N UE. Ce dernier est déterminé sur la base de P_{\max} , et de la distance minimale possible aux utilisateurs et de la valeur minimale possible de la puissance récoltée par l'UE. Nous supposons que les coefficients de puissance de canal entre les UE et le WPC ne diffèrent pas de manière significative, et donc notés par h . Avec des stations de charge fixes et des appareils fixes, c'est une hypothèse plausible.

F.2 Trouver l'Équilibre de Nash

Nous formulons le jeu non coopératif et trouvons la stratégie d'équilibre de Nash. On définit l'utilité de l'utilisateur $i \in \{1, 2, \dots, n\}$ dans l'état $n \in \{1, 2, \dots, N\}$ par

$$u_{i,n}(s_{i,n}, s_{-i,n}) = \frac{y_{i,n}}{q} - \frac{\nu w_n s_{i,n}^2}{\sum_{j=1}^n s_{j,n}}, \quad (\text{F.1})$$

où $s_{i,n}$ est la stratégie (enchère) de UE i qui prend des valeurs dans la plage $[s_L, s_U]$ avec s_L étant une petite valeur positive pour éviter les ambiguïtés dans l'analyse, $s_{-i,n}$ désigne les stratégies des autres utilisateurs $n-1$, $y_{i,n}$ est la puissance reçue par l'UE i , toutes liées à l'état n . De plus, ν met à l'échelle la valeur quantitative du coût du service ($w_n s_{i,n}^2 / \sum_{j=1}^n s_{j,n}$) au montant de la satisfaction factor ($y_{i,n}/q$) pour produire un utilitaire significatif pour l'utilisateur, et w_n est la puissance allouée par le WPC à tous les utilisateurs admis dans l'état n . Ensuite, nous pouvons exprimer la fonction de meilleure réponse sous forme fermée, selon

$$F_{i,n}(s_{-i,n}) = \frac{h}{q\nu \left(1 + \sqrt{1 + \frac{h}{q\nu \sum_{\forall j \neq i} s_j}} \right)}. \quad (\text{F.2})$$

L'équation (F.2) implique que lorsque n augmente, la meilleure stratégie de réponse pour chaque utilisateur est d'augmenter son prix d'enchère. Et c'est la raison pour laquelle le WPC souhaite que le réseau soit plein la plupart du temps, afin d'en tirer le meilleur profit.

F.3 Admission des Utilisateurs et Allocation de Puissance

En écrivant les équations d'équilibre, qui disent que la vitesse à laquelle le processus quitte un état est égale à la vitesse à laquelle le processus y entre, nous pouvons trouver la probabilité limite P_n pour chaque état du CTMC. Ainsi, les équations d'équilibre sont

$$\begin{cases} \lambda P_0 = \mu_1 P_1, & n = 0 \\ (\lambda + \mu_n) P_n = \lambda P_{n-1} + \mu_{n+1} P_{n+1}, & 0 < n < N \\ \lambda P_{N-1} = \mu_N P_N, & n = N, \end{cases} \quad (\text{F.3})$$

and can be simplified to

$$\lambda P_n = \mu_{n+1} P_{n+1}, \quad n \in \{0, 1, 2, \dots, N-1\}, \quad (\text{F.4})$$

où $\mu_n, n \in \{1, 2, \dots, N\}$, est le taux de départ de l'état n (cf. Fig. F.1) et est calculé comme suit:

$$\frac{1}{\mu_n} = \frac{q/\mu}{hw_n/n} \Rightarrow \mu_n = \frac{1}{n} \frac{hw_n}{q} \mu, \quad 1 \leq n \leq N. \quad (\text{F.5})$$

A noter que le taux de départ est réciproquement proportionnel au nombre d'utilisateurs dans le réseau. L'équation (F.4) ainsi que l'égalité $\sum_{n=0}^N P_n = 1$ peuvent être écrites sous forme matricielle

$$\begin{bmatrix} \lambda & -\mu_1 & 0 & \dots & 0 & 0 \\ 0 & \lambda & -\mu_2 & \dots & 0 & 0 \\ \vdots & \vdots & \vdots & \ddots & \vdots & \vdots \\ 0 & 0 & 0 & \dots & \lambda & -\mu_N \\ 1 & 1 & 1 & \dots & 1 & 1 \end{bmatrix} \begin{bmatrix} P_0 \\ P_1 \\ \vdots \\ P_{N-1} \\ P_N \end{bmatrix} = \begin{bmatrix} 0 \\ 0 \\ \vdots \\ 0 \\ 1 \end{bmatrix}. \quad (\text{F.6})$$

Après résolution de (F.6), les probabilités limites, P_n , peuvent être trouvées dans la formule de forme fermée

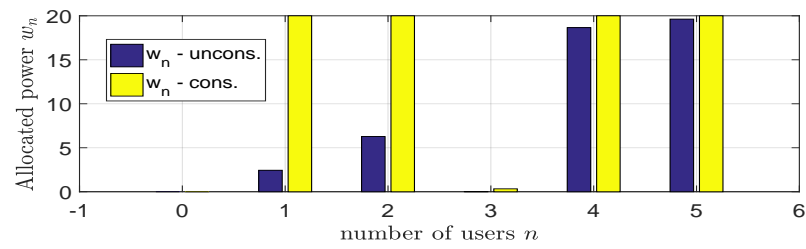
$$P_n = \frac{n! \lambda^n (h\mu/q)^{N-n} w_N w_{N-1} \dots w_{n+1}}{\sum_{n=0}^N n! \lambda^n (h\mu/q)^{N-n} w_N w_{N-1} \dots w_{n+1}}, \quad (\text{F.7})$$

qui est valable pour tout $n \in \{0, 1, 2, \dots, N\}$.

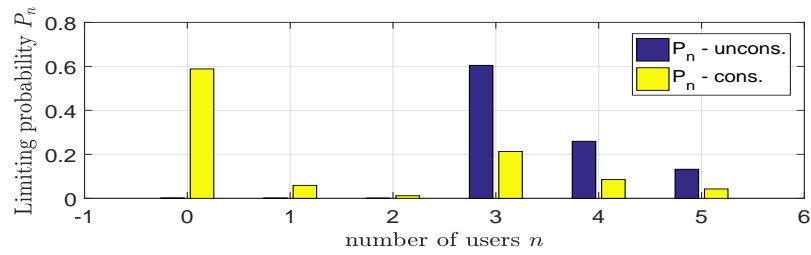
Le WPC trouve le vecteur de puissance avec lequel il maximisera son utilité à long terme tout en respectant la satisfaction des utilisateurs de telle sorte que leur utilité soit supérieure à $1/nu$.

Le nombre moyen d'utilisateurs dans le réseau est égal à $L_a = \sum_{n=1}^N P_n n$, et en appliquant la fameuse formule de Little, le temps d'attente moyen de chaque utilisateur du réseau est donné par $T_a = \frac{L_a}{(1-P_N)\lambda}$.

Maintenant, nous démontrons les performances du schéma de charge de puissance proposé dans la Fig. F.2 pour une configuration réseau typique. La figure montre la puissance allouée w_n et la probabilité limite correspondante P_n dans chaque état n pour deux cas d'optimisation: sans contrainte et contrainte. Dans le cas sans contrainte, le WPC ne se soucie pas des utilitaires et de la satisfaction des utilisateurs, c'est-à-dire comme si $\nu = \infty$, mais veut plutôt avec avidité maximiser sa propre utilité. Comme le montre la Fig. F.2a, le WPC alloue principalement sa puissance lorsqu'il y a plus d'utilisateurs dans le système, ainsi le réseau est presque toujours plein (cf. Fig. F.2b). Dans ce cas, la probabilité d'utilisateurs n dans le système est plus grande pour les états supérieurs que pour les états inférieurs. Inversement, le cas contraint se comporte. Autrement dit, le WPC se soucie des utilitaires des utilisateurs et met une contrainte sur lui-même pour garder les utilisateurs satisfaits jusqu'à leur niveau requis selon le facteur de mise à l'échelle. Comme le montre la Fig. F.2a, le WPC transmet presque dans tous les états avec sa puissance maximale. De cette façon, il peut servir les utilisateurs plus rapidement et garder le réseau plus souvent vide (cf. Fig. F.2b).



(a)



(b)

Figure F.2: (a) La puissance allouée et (b) la probabilité limite dans chaque état, lorsque les utilités des utilisateurs sont prises en compte (cas contraint) et lorsqu'elles ne sont pas prises en compte (cas sans contrainte).

Appendix G

Formation de Faisceaux Axée sur les Enchères Basée sur l'Apprentissage Profond pour SWIPT

Nous considérons un réseau SWIPT hétérogène à bande unique, dans lequel un point d'accès hybride multi-antenne (HAP) tente de maximiser ses revenus en formant le faisceau de l'information et de l'énergie vers les IRs et les ERs à antenne unique, respectivement. Le réseau fonctionne dans un cadre d'enchères. Sur la base des offres, des niveaux de service demandés, des distributions de valorisation apprises et des informations sur l'état du canal (CSI) des utilisateurs, le HAP, en tant que commissaire-priseur et vendeur, vise à trouver l'ensemble optimal d'utilisateurs et la tarification optimale qui maximisent ses revenus, tout en encourageant les utilisateurs à enchérir honnêtement. Nous formulons ce problème de mécanisme comme un problème de programmation non linéaire à nombres entiers mixtes — qui est NP-difficile — et le résolvons en utilisant un algorithme de Branch-and-Bound efficace tout en appliquant la technique de programmation semi-définie (SDP) dans chaque branche. Etant donné que la résolution de ce problème est gourmande en temps, en particulier lorsque le nombre de dispositifs dans le réseau est assez important, ces techniques d'optimisation de programmation dynamique conventionnelles ne sont plus pratiques en raison de leurs délais de calcul excessifs - complexité temporelle exponentielle. Une solution prometteuse à ce problème consiste à appliquer des algorithmes DL, en particulier des réseaux de neurones profonds (DNN), pour produire la solution presque en temps réel. Nous proposons

une architecture basée sur DNN pour résoudre la tâche de classification multi-étiquettes et trouver le sous-ensemble d'utilisateurs souhaité, sur la base duquel les vecteurs de formation de faisceau optimaux peuvent être trouvés en exécutant une fois l'algorithme de relaxation semi-définie (SDR) [62]. Ces architectures basées sur DNN sont des boîtes noires qui doivent être formées, et leurs performances doivent être validées avant de pouvoir être intégrées dans le système pour prédire la solution. Dans cette veine, nous résolvons le problème de programmation non linéaire à nombres entiers mixtes hors ligne pour un très grand nombre de réalisations des données d'entrée dans le HAP, sauvegardons le jeu de données d'apprentissage et les étiquettes d'apprentissage obtenues dans une base de données, puis utilisons ce dernier pour former notre DNN proposé afin d'estimer la règle d'allocation du mécanisme d'enchères proposé pour maximiser les revenus.

G.1 La Modélisation de Réseau

La modélisation du réseau SWIPT comprend la modélisation physique des éléments du réseau, la modélisation comportementale économique (enchère) des appareils et le cadre de l'enchère.

G.1.1 Modélisation Physique

Le réseau SWIPT se compose d'un HAP desservant plusieurs appareils dans une bande de spectre partagée. Le HAP est équipé d'antennes M et a un budget de puissance de P Watts. Un nombre total de $K = I + J$ d'équipements utilisateurs (UEs) coexistent dans le réseau, I désignant le nombre d'IRs et J étant le nombre d'ERs. L'ensemble $\mathcal{I} = \{1, \dots, I\}$ contient les indices des périphériques d'information, et $\mathcal{J} = \{1, \dots, J\}$ est l'index ensemble des dispositifs énergétiques. Tous les appareils sont équipés d'antennes simples et fonctionnent en mode semi-duplex similaire au HAP. Le HAP est de fournir une énergie sans fil aux ERs et d'envoyer des données aux IRs. Sans perte de généralité, nous considérons un précodage linéaire au HAP, de sorte que chaque récepteur ER/IR se voit attribuer un faisceau dédié de transmission d'énergie/d'information.

Le rapport signal sur bruit plus interférence (SINR) du récepteur d'information IR_i , $i \in \mathcal{I}$, peut être écrit comme

$$\begin{aligned} \Gamma_i &= \frac{|\mathbf{h}_i^T \mathbf{w}_i|^2}{\sum_{k \in \mathcal{I}, k \neq i} |\mathbf{h}_i^T \mathbf{w}_k|^2 + \sum_{j \in \mathcal{J}} |\mathbf{h}_i^T \mathbf{v}_j|^2 + \sigma_i^2} \\ &= \frac{\mathbf{w}_i^H \mathbf{R}_i \mathbf{w}_i}{\sum_{k \in \mathcal{I}, k \neq i} \mathbf{w}_k^H \mathbf{R}_i \mathbf{w}_k + \sum_{j \in \mathcal{J}} \mathbf{v}_j^H \mathbf{R}_i \mathbf{v}_j + \sigma_i^2}, \end{aligned} \quad (\text{G.1})$$

où $\mathbf{R}_i = \mathbf{h}_i \mathbf{h}_i^H$ est la matrice de covariance avec $\mathbf{h}_i = (h_{i,1}, \dots, h_{i,M})^T$ comme vecteurs de canal du HAP à IR_i . Le SINR est directement lié aux indicateurs de performance de l'appareil tels que le taux d'erreur sur les bits (BER) et le débit de données. Par exemple, sous un BER fixe et en supposant une modulation d'amplitude en quadrature, un taux réalisable pratique peut être calculé comme $R_i = \log(1 + \Gamma_i/\Upsilon)$ bps/Hz, dans lequel Υ désigne le SNR écart par rapport à la capacité. L'écart SNR est toujours supérieur à 1 (0 dB), et il donne une relation approximative entre le SINR et le débit.

La puissance reçue à ER_j , $j \in \mathcal{J}$, est donnée par

$$\begin{aligned} Q_j &= \sum_{i \in \mathcal{I}} |\mathbf{g}_j^T \mathbf{w}_i|^2 + \sum_{k \in \mathcal{J}} |\mathbf{g}_j^T \mathbf{v}_k|^2 \\ &= \sum_{i \in \mathcal{I}} \mathbf{w}_i^H \mathbf{C}_j \mathbf{w}_i + \sum_{k \in \mathcal{J}} \mathbf{v}_k^H \mathbf{C}_j \mathbf{v}_k. \end{aligned} \quad (\text{G.2})$$

où $\mathbf{C}_j = \mathbf{g}_j \mathbf{g}_j^H$ est la matrice de covariance avec $\mathbf{g}_j = (g_{j,1}, \dots, g_{j,M})^T$ comme vecteurs de canal du HAP à ER_j .

G.1.2 Modélisation des Enchères

Le HAP en tant que vendeur de services joue également le rôle de commissaire-priseur. Les appareils jouent le rôle d'enchérisseurs qui ont des évaluations de service différentes envoyant leurs offres à chaque tour d'enchères pour être servis par le HAP. Le HAP sollicite les offres des appareils de manière scellée, c'est-à-dire que les appareils ne sont pas au courant des offres des autres. On suppose que tous les appareils ont des demandes de service non nulles et jouent dans tous les tours d'enchères. Chaque IR_i , $i \in \mathcal{I}$, envoie sa demande de service sous la forme du SINR minimum, γ_i , requis pour recevoir D_i bits de données pendant la durée de l'enchère τ_a , en enchérissant b_{IR_i} . De même, chaque ER_j , $j \in \mathcal{J}$, demande q_j unités d'énergie pour la durée de l'enchère τ_a en enchérissant b_{ER_j} . Le HAP sait à l'avance que IR_i et ER_j tirent leurs évaluations privées nu_{IR_i} et

ν_{ER_j} des distributions $\mathcal{F}_{\text{IR}_i}$ et $\mathcal{F}_{\text{ER}_j}$ pour chaque tour d'enchère. Ces distributions sont supposées indépendantes, mais pas nécessairement identiques. Sans perte de généralité, nous posons $\tau_a = 1$. Soit également $\boldsymbol{\gamma} = (\gamma_1, \dots, \gamma_I)^T$ et $\mathbf{q} = (q_1, \dots, q_J)^T$ désignent les profils de demande des IR et des ER, respectivement, et désignent $\mathbf{b}_{\text{IR}} = (b_{\text{IR}_1}, \dots, b_{\text{IR}_I})^T$ et $\mathbf{b}_{\text{ER}} = (b_{\text{ER}_1}, \dots, b_{\text{ER}_J})^T$ comme profils de soumission des IR et des RE, respectivement.

G.1.3 Cadre d'Enchères

Nous considérons un environnement d'enchères à paramètre unique (ou unidimensionnel), où les résultats du HAP en tant que concepteur du mécanisme d'enchères sont deux règles: (i) la *règle d'allocation* $\mathbf{a} = \begin{pmatrix} \mathbf{a}_{\text{IR}} \\ \mathbf{a}_{\text{ER}} \end{pmatrix}$, où $\mathbf{a}_{\text{IR}} = (a_{\text{IR}_1}, \dots, a_{\text{IR}_I})^T$ et $\mathbf{a}_{\text{ER}} = (a_{\text{ER}_1}, \dots, a_{\text{ER}_J})^T$, chaque élément du vecteur \mathbf{a}_{IR} (\mathbf{a}_{ER}) étant un indicateur pour savoir si IR_i (ER_j) doit être servi ou non et, par conséquent, $\mathbf{a}_{\text{IR}} \in \{0, 1\}^I$ ($\mathbf{a}_{\text{ER}} \in \{0, 1\}^J$); et (ii) la *règle de paiement* $\mathbf{p} = \begin{pmatrix} \mathbf{p}_{\text{IR}} \\ \mathbf{p}_{\text{ER}} \end{pmatrix}$, où $\mathbf{p}_{\text{IR}} = (p_{\text{IR}_1}, \dots, p_{\text{IR}_I})^T$ et $\mathbf{p}_{\text{ER}} = (p_{\text{ER}_1}, \dots, p_{\text{ER}_J})^T$, avec chaque élément du vecteur \mathbf{p}_{IR} (\mathbf{p}_{ER}) désignant le montant IR_i (ER_j) est requis pour payer le commissaire-priseur, c'est-à-dire le HAP, lors de toute ronde d'enchères. Comme le montre la Fig. G.1, chaque tour d'enchères est composé de quatre

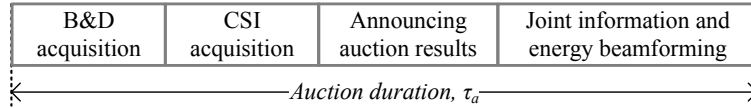


Figure G.1: Répartition de chaque tour d'enchères.

parties: (i) acquisition d'offres et demandes (B & D), (ii) acquisition de CSI, (iii) annonce des résultats des enchères et (iv) formation de faisceaux d'information.

Pour trouver les vecteurs de formation de faisceaux optimaux \mathbf{w}_i^* , $i \in \mathcal{I}$ et \mathbf{v}_j^* , $j \in \mathcal{J}$, l'étape clé est de trouver le vecteur d'allocation optimal \mathbf{a}^* et le vecteur de paiement optimal \mathbf{p}^* qui maximisent les revenus du HAP. Ensuite, le HAP envoie à IR_i et ER_j les paires $(a_{\text{IR}_i}^*, p_{\text{IR}_i}^*)$ et $(a_{\text{ER}_j}^*, p_{\text{ER}_j}^*)$, respectivement, comme résultat de l'enchère faites-leur savoir s'ils ont gagné l'enchère et combien ils devraient payer en cas de victoire.

G.2 La Formulation du Problème

Trouver le mécanisme optimal de maximisation des revenus (Rmax) équivaut à trouver les règles d'allocation et de paiement optimales. Ces règles peuvent être obtenues en résolvant le problème Rmax suivant:

$$\max_{\mathbf{a} \in \mathcal{A}_F} \mathbb{E}_{\nu} [u_{\text{HAP}}] = \mathbb{E}_{\nu} \left[\sum_{k \in \mathcal{K}} p_k(\nu) \right], \quad (\text{G.3})$$

où l'attente est w.r.t. la distribution $\mathcal{F}_{\mathcal{K}} = \prod_{k \in \mathcal{K}} \mathcal{F}_k = \prod_{i \in \mathcal{I}} \mathcal{F}_{\text{IR}_i} \prod_{j \in \mathcal{J}} \mathcal{F}_{\text{ER}_j}$ sur les évaluations des soumissionnaires $\nu_k, k \in \mathcal{K}$. Dans (G.3), \mathcal{A}_F est l'ensemble de tous les vecteurs d'allocation réalisables, qui dépend du CSI des canaux $\mathbf{h}_i, i \in \mathcal{I}$, et $\mathbf{g}_j, j \in \mathcal{J}$, et sur le profil de demande des appareils \mathbf{d} . Un vecteur d'allocation est jugé réalisable si la puissance minimale requise pour satisfaire les contraintes de demande du sous-ensemble de dispositifs représenté par ce vecteur d'allocation est inférieure au bilan de puissance du HAP.

G.3 Trouver l'Ensemble d'Allocation Réalisable \mathcal{A}_F

Pour que le HAP trouve les vecteurs d'allocation possibles parmi toutes les réalisations possibles des vecteurs d'allocation $\mathbf{a}^{(l)} \in \{0, 1\}^K, l \in \{0, 1, \dots, 2^K - 1\}$, une série de problèmes d'optimisation non convexes devrait être résolue. En général, nous sommes confrontés à un programme non linéaire à nombres entiers mixtes. Il y a des problèmes d'optimisation $2^K - 1$ à résoudre, dans le pire des cas, pour obtenir \mathcal{A}_F . Par conséquent, le problème a une complexité temporelle exponentielle. Chaque problème correspondant à $\mathbf{a}^{(l)}$ est un problème de minimisation de puissance, qui consiste à trouver la puissance d'émission minimale requise par le HAP pour répondre aux demandes des UE choisis dans le sous-ensemble $A^{(l)}$. Ces sous-problèmes sont résolus en appliquant les techniques SDR. Si la puissance minimale trouvée était inférieure au budget de puissance d'émission HAP P , alors ce $\mathbf{a}^{(l)}$ particulier est faisable.

G.4 Mécanisme de Maximisation des Revenus

Dans la section précédente, nous avons obtenu l'ensemble d'allocations réalisables \mathcal{A}_F . Nous cherchons maintenant à trouver la règle d'allocation optimale \mathbf{a}^* et la règle de paiement optimal \mathbf{p}^* , qui

constituent ensemble le mécanisme R_{\max} . Pour trouver le mécanisme R_{\max} , il est d'abord nécessaire d'obtenir le mécanisme de maximisation du bien-être social (SW_{\max}) car la solution SW_{\max} est appliquée pour obtenir le mécanisme R_{\max} . Ainsi, dans la sous-section 9.5.1, nous obtenons le mécanisme SW_{\max} , basé sur lequel et en appliquant le lemme de Myerson, nous trouverons le mécanisme R_{\max} dans la sous-section 9.5.2.

G.4.1 Maximisation du Bien-Être Social — Vente aux Enchères VCG

Les enchères compatibles avec une incitation à stratégie dominante (DSIC) sont les enchères souhaitées dans lesquelles le vendeur n'a pas besoin de stratégie, c'est-à-dire qu'il n'a pas besoin de connaître les distributions de valorisation des UE pour concevoir l'enchère; et chaque UE, indépendamment des stratégies d'enchères des autres agents, devrait jouer honnêtement pour maximiser son propre avantage, c'est-à-dire $b_k = \nu_k$ pour $k \in \mathcal{K}$. Pour les environnements à paramètre unique, le mécanisme SW_{\max} , qui sera obtenu sous peu, est DSIC et est souvent appelé mécanisme Vickrey-Clarke-Groves (VCG) dans la littérature des enchères [56].

Règle d'Allocation Optimale pour le Mécanisme SW_{\max}

Le vecteur d'allocation optimal $\mathbf{a}^* = \operatorname{argmax}_{\mathbf{a} \in \mathcal{A}_F} S(\mathbf{b}, \mathbf{a})$ correspond à l'ensemble d'utilisateurs réalisables qui aboutit à la plus grande somme de valeurs d'enchères. En d'autres termes, étant donné le profil d'enchère \mathbf{b} , le bien-être social maximal $\mathfrak{S}(\mathbf{b})$ qui est égal à $S(\mathbf{b}, \mathbf{a}^*)$ se trouve simplement en recherchant le tableau de toutes les valeurs de bien-être social correspondant à tous les vecteurs d'allocation dans l'ensemble des faisables \mathcal{A}_F et en sélectionnant le maximum. Le mécanisme SW_{\max} du HAP, basé sur le profil d'enchère \mathbf{b} des UEs, est décrit par [54]

$$\mathbf{a}^* = \operatorname{argmax}_{\mathbf{a} \in \mathcal{A}_F} S(\mathbf{b}, \mathbf{a}), \quad (\text{G.4a})$$

$$p_k^* = \begin{cases} \tilde{b}_k & \text{if } a_k^* = 1 \\ 0 & \text{if } a_k^* = 0 \end{cases}, \quad k \in \mathcal{K}, \quad (\text{G.4b})$$

où (G.4b) est la règle de paiement optimale.

G.4.2 Mécanisme de Maximisation des Revenus — Mécanisme de Myerson

Comme mentionné ci-dessus, la valorisation privée $\nu_k, k \in \mathcal{K}$, est tirée de la distribution $\mathcal{F}_k(\nu_k)$ avec la fonction de densité $f_k(\nu_k)$. En prenant les attentes des deux côtés de l'identité de paiement du Myerson et en additionnant tous les agents, nous nous retrouvons avec la relation clé suivante

$$\mathbb{E}_{\boldsymbol{\nu}} \left[\sum_{k \in \mathcal{K}} p_k(\boldsymbol{\nu}) \right] = \mathbb{E}_{\boldsymbol{\nu}} \left[\sum_{k \in \mathcal{K}} \phi_k(\nu_k) a_k(\boldsymbol{\nu}) \right], \quad (\text{G.5})$$

où $\phi_k(\nu_k) = \nu_k - \frac{1 - \mathcal{F}_k(\nu_k)}{f_k(\nu_k)}$ est la *valorisation virtuelle* pour chaque UE $_k, k \in \mathcal{K}$ [56].

En se référant à $\sum_{k \in \mathcal{K}} \phi_k(\nu_k) a_k(\boldsymbol{\nu})$ comme le *bien-être social virtuel* d'une enchère sur le profil de valorisation $\boldsymbol{\nu}$, (9.17) déclare que le revenu attendu est égal au bien-être social virtuel attendu. Ainsi, la règle d'allocation virtuelle de maximisation du bien-être social (VSM) est celle qui choisit l'allocation réalisable qui maximise le bien-être social virtuel $\sum_{k \in \mathcal{K}} \phi_k(\nu_k) a_k(\boldsymbol{\nu})$ pour chaque profil de valorisation $\boldsymbol{\nu}$. Pour que le mécanisme VSM soit véridique, la règle d'allocation obtenue doit être monotone non décroissante, ce qui est vrai lorsque les évaluations virtuelles $\phi_k(\nu_k)$ sont monotones non décroissantes. Par conséquent, le mécanisme Rmax optimal, alias le mécanisme de Myerson, peut être décrit comme suit:

$$(\mathbf{a}^*, \mathbf{p}') = \text{VCG}'(\mathbf{b}') \quad (\text{G.6a})$$

$$p_k^* = \begin{cases} \phi_k^{-1}(p'_k) & \text{if } a_k^* = 1 \\ 0 & \text{if } a_k^* = 0 \end{cases}, \quad k \in \mathcal{K}, \quad (\text{G.6b})$$

où $b'_k = \phi_k(b_k), k \in \mathcal{K}$, sont les éléments du profil d'enchère virtuel \mathbf{b}' , et où $\text{VCG}'(\mathbf{b}')$ est la version généralisée de la fonction de mécanisme SWmax décrite dans (G.4). La figure G.2 est un organigramme qui illustre tout le processus de recherche du mécanisme optimal.

G.5 L'Architecture de Réseau Neuronal Profond Proposée

Une solution pour surmonter la complexité de la recherche de la règle d'allocation consiste à utiliser des DNN. Après avoir essayé plusieurs architectures de base, telles que le réseau neuronal entièrement connecté (FcNN), le réseau neuronal convolutif (CNN) et le réseau neuronal résiduel

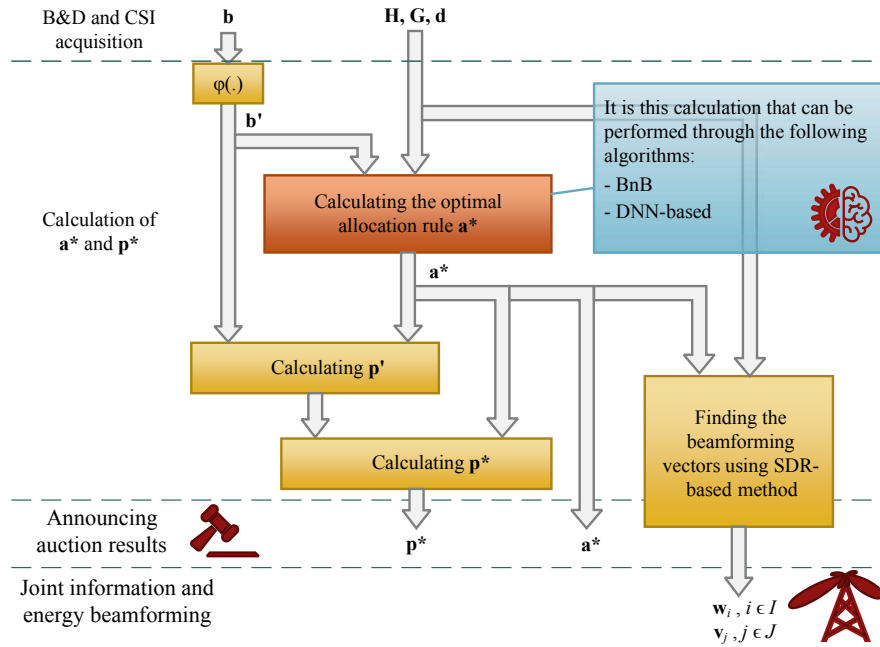


Figure G.2: L'organigramme de recherche du mécanisme optimal de maximisation des revenus.

(ResNet), le modèle FcNN a montré les meilleures performances en termes de précision. Le schéma

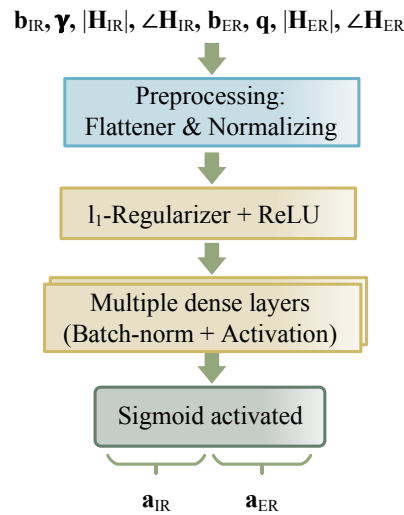


Figure G.3: Le DNN utilisé pour trouver le vecteur d'allocation.

de l'architecture DNN proposée est représenté sur la Fig. G.3.

Pour former le DNN proposé, nous devons renseigner l'ensemble de données de formation et les étiquettes correspondantes. À cette fin, nous résolvons les problèmes d'optimisation correspondants pour de nombreuses réalisations de réseau en utilisant des solveurs de problèmes semi-définis standard comme CVX [37] dans l'algorithme efficace BnB proposé. Nous avons utilisé le 'TensorFlow

interface [57] pour créer et entraîner notre modèle DNN. Nous avons réglé les hyper-paramètres du DNN à l'aide du cadre d'optimisation d'hyper-paramètres récemment publié *Keras-tuner* [58], qui essaie un nombre prédéfini d'essais à la recherche du meilleur ensemble possible d'hyper-paramètres avec -dans les algorithmes de recherche.

G.6 Conclusion

Nous nous sommes attaqués au problème de trouver le mécanisme optimal d'incitation à stratégie dominante maximisant les revenus, à savoir les règles d'allocation et de paiement, pour un réseau SWIPT dans lequel un HAP multi-antenne vend ses liaisons radio multiplexées spatialement à des dispositifs d'information à contraintes SINR, et sa puissance aux dispositifs de récupération d'énergie. Après avoir résolu le problème de maximisation des revenus NP-hard en appliquant un algorithme Branch-and-Bound efficace et en tirant partie de la méthode de relaxation semi-définie dans chaque branche, nous avons mis en évidence la gourmandise en temps de ces techniques pour trouver la règle d'allocation optimale, d'autant plus que le nombre des périphériques réseau augmente. Nous avons conçu et formé un DNN pour trouver la règle d'allocation en temps réel, avec une précision exacte de 76 %. Alors que l'exploration d'autres architectures pour augmenter la précision est une étape prometteuse pour les travaux futurs, la prise en compte de la disponibilité partielle du CSI au HAP, puis l'application de techniques d'apprentissage automatique pour estimer conjointement le CSI et la règle d'allocation optimale est également une autre avenue difficile.

References

- [1] J. J. O'Neill, "Prodigal genius, biography of Nikola Tesla," *Long Island, New York*, 1944.
- [2] M. Cheney, "Tesla: Man out of time, 1981," *Touchstone, New York, NY*, pp. 171–191, 1981.
- [3] Y. Zeng, B. Clerckx, and R. Zhang, "Communications and signals design for wireless power transmission," *IEEE Trans. Commun.*, vol. 65, no. 5, pp. 2264–2290, May 2017.
- [4] S. Bi, C. K. Ho, and R. Zhang, "Wireless powered communication: Opportunities and challenges," *IEEE Commun. Mag.*, vol. 53, no. 4, pp. 117–125, Apr. 2015.
- [5] L. Liu, R. Zhang, and K. Chua, "Secrecy wireless information and power transfer with MISO beamforming," *IEEE Trans. Signal Process.*, vol. 62, no. 7, pp. 1850–1863, Apr. 2014.
- [6] A. Boaventura, A. Collado, N. B. Carvalho, and A. Georgiadis, "Optimum behavior: Wireless power transmission system design through behavioral models and efficient synthesis techniques," *IEEE Microw. Mag.*, vol. 14, no. 2, pp. 26–35, Mar. 2013.
- [7] B. Clerckx and E. Bayguzina, "Waveform design for wireless power transfer," *IEEE Trans. Signal Process.*, vol. 64, no. 23, pp. 6313–6328, Dec. 2016.
- [8] H. Ju and R. Zhang, "Throughput maximization in wireless powered communication networks," *IEEE Trans. Wireless Commun.*, vol. 13, no. 1, pp. 418–428, Jan. 2014.
- [9] Q. Wu, M. Tao, D. W. K. Ng, W. Chen, and R. Schober, "Energy-efficient resource allocation for wireless powered communication networks," *IEEE Trans. Wireless Commun.*, vol. 15, no. 3, pp. 2312–2327, Mar. 2016.
- [10] R. Zhang and C. K. Ho, "MIMO broadcasting for simultaneous wireless information and power transfer," *IEEE Trans. Wireless Commun.*, vol. 12, no. 5, pp. 1989–2001, May 2013.

- [11] I. Krikidis, S. Timotheou, S. Nikolaou, G. Zheng, D. W. K. Ng, and R. Schober, "Simultaneous wireless information and power transfer in modern communication systems," *IEEE Commun. Mag.*, vol. 52, no. 11, pp. 104–110, Nov. 2014.
- [12] B. Clerckx, Z. B. Zawawi, and K. Huang, "Wirelessly powered backscatter communications: Waveform design and SNR-energy tradeoff," *IEEE Commun. Lett.*, vol. 21, no. 10, pp. 2234–2237, Oct. 2017.
- [13] Y. Ma, H. Chen, Z. Lin, Y. Li, and B. Vucetic, "Distributed and optimal resource allocation for power beacon-assisted wireless-powered communications," *IEEE Trans. Commun.*, vol. 63, no. 10, pp. 3569–3583, Oct. 2015.
- [14] R. Morsi, D. S. Michalopoulos, and R. Schober, "Multiuser scheduling schemes for simultaneous wireless information and power transfer over fading channels," *IEEE Trans. Wireless Commun.*, vol. 14, no. 4, pp. 1967–1982, Apr. 2015.
- [15] S. Park, H. Kim, and D. Hong, "Cognitive radio networks with energy harvesting," *IEEE Trans. Wireless Commun.*, vol. 12, no. 3, pp. 1386–1397, Mar. 2013.
- [16] G. Yang, C. K. Ho, and Y. L. Guan, "Dynamic resource allocation for multiple-antenna wireless power transfer," *IEEE Trans. Signal Process.*, vol. 62, no. 14, pp. 3565–3577, Jul. 2014.
- [17] G. Yang, C. K. Ho, R. Zhang, and Y. L. Guan, "Throughput optimization for massive MIMO systems powered by wireless energy transfer," *IEEE J. Sel. Areas Commun.*, vol. 33, no. 8, pp. 1640–1650, Aug. 2015.
- [18] D. W. K. Ng, E. S. Lo, and R. Schober, "Multiobjective resource allocation for secure communication in cognitive radio networks with wireless information and power transfer," *IEEE Trans. Veh. Technol.*, vol. 65, no. 5, pp. 3166–3184, May 2016.
- [19] Y. Zhang, C. Lee, D. Niyato, and P. Wang, "Auction approaches for resource allocation in wireless systems: A survey," *IEEE Commun. Surveys Tuts.*, vol. 15, no. 3, pp. 1020–1041, third quarter 2013.
- [20] M. Xia and S. Aïssa, "On the efficiency of far-field wireless power transfer," *IEEE Trans. Signal Process.*, vol. 63, no. 11, pp. 2835–2847, Jun. 2015.

- [21] J. Xu, S. Bi, and R. Zhang, "Multiuser MIMO wireless energy transfer with coexisting opportunistic communication," *IEEE Wireless Commun. Lett.*, vol. 4, no. 3, pp. 273–276, Jun. 2015.
- [22] D. Niyato, E. Hossain, and Z. Han, "Dynamic spectrum access in IEEE 802.22-based cognitive wireless networks: a game theoretic model for competitive spectrum bidding and pricing," *IEEE Wireless Commun.*, vol. 16, no. 2, pp. 16–23, Apr. 2009.
- [23] Y. Zhang, D. Niyato, P. Wang, and E. Hossain, "Auction-based resource allocation in cognitive radio systems," *IEEE Commun. Mag.*, vol. 50, no. 11, pp. 108–120, Nov. 2012.
- [24] U. Habiba and E. Hossain, "Auction mechanisms for virtualization in 5G cellular networks: Basics, trends, and open challenges," *IEEE Commun. Surveys Tuts.*, vol. 20, no. 3, pp. 2264–2293, third quarter 2018.
- [25] N. Tadayon and S. Aïssa, "Radio resource allocation and pricing: Auction-based design and applications," *IEEE Trans. Signal Process.*, vol. 66, no. 20, pp. 5240–5254, Oct. 2018.
- [26] D. Niyato and P. Wang, "Competitive wireless energy transfer bidding: A game theoretic approach," in *Proc. IEEE International Conference on Communications (ICC)*, Jun. 2014, pp. 1–6.
- [27] S. Sarma, K. Kandhway, and J. Kuri, "Robust energy harvesting based on a Stackelberg game," *IEEE Wireless Commun. Lett.*, vol. 5, no. 3, pp. 336–339, Jun. 2016.
- [28] H. Chen, Y. Li, Z. Han, and B. Vucetic, "A Stackelberg game-based energy trading scheme for power beacon-assisted wireless-powered communication," in *Proc. IEEE International Conference on Acoustics, Speech, and Signal Processing (ICASSP)*, Apr. 2015, pp. 3177–3181.
- [29] C. Zhang, P. Patras, and H. Haddadi, "Deep learning in mobile and wireless networking: A survey," *IEEE Commun. Surveys Tuts.*, vol. 21, no. 3, pp. 2224–2287, third quarter 2019.
- [30] C. R. Valenta and G. D. Durgin, "Harvesting wireless power: Survey of energy-harvester conversion efficiency in far-field, wireless power transfer systems," *IEEE Microw. Mag.*, vol. 15, no. 4, pp. 108–120, Jun. 2014.
- [31] H. J. Visser and R. J. M. Vullers, "RF energy harvesting and transport for wireless sensor network applications: Principles and requirements," *Proc. IEEE*, vol. 101, no. 6, pp. 1410–1423, Jun. 2013.

- [32] M. Foruhandeh and S. Aïssa, “Efficiency of DC combination of rectified waveforms in energy harvesting systems,” in *Proc. IEEE International Conference on Ubiquitous Wireless Broadband (ICUWB’15)*, Montreal, QC, Canada, Oct. 2015, pp. 1–5.
- [33] *Application Note 986: Square Law and Linear Detection*, Hewlett Packard, 1981.
- [34] M. Kreh, “Bessel functions,” *Lecture Notes, Penn State-Göttingen Summer School on Number Theory*, vol. 82, 2012.
- [35] G. De Vita and G. Iannaccone, “Design criteria for the RF section of UHF and microwave passive RFID transponders,” *IEEE Trans. Microw. Theory Techn.*, vol. 53, no. 9, pp. 2978–2990, Sep. 2005.
- [36] “SMS7630 data sheet,” Skyworks.
- [37] M. Grant and S. Boyd, “CVX: Matlab software for disciplined convex programming, version 2.1,” 2014.
- [38] A. Bayat and S. Aïssa, “When Bessel meets Fourier in the power representation of energy harvesting rectennas,” *IEEE Commun. Lett.*, vol. 24, no. 1, pp. 67–70, Jan. 2020.
- [39] —, “Wireless power transfer scheduling: Comparative study of TDMA and SDMA under harvesters nonlinearity,” in *Proc. IEEE Globecom*, Dec. 2019, pp. 1–6.
- [40] B. Clerckx, “Wireless information and power transfer: Nonlinearity, waveform design, and rate-energy tradeoff,” *IEEE Trans. Signal Process.*, vol. 66, no. 4, pp. 847–862, Feb. 2018.
- [41] F. R. Farrokhi, G. J. Foschini, A. Lozano, and R. A. Valenzuela, “Link-optimal space-time processing with multiple transmit and receive antennas,” *IEEE Commun. Lett.*, vol. 5, no. 3, pp. 85–87, Mar. 2001.
- [42] K. Technologies. (2009) Harmonic balance basics. [Online]. Available: <https://edadocs.software.keysight.com/display/ads2009/Harmonic+Balance+Simulation>
- [43] R. M. Corless, G. H. Gonnet, D. E. Hare, D. J. Jeffrey, and D. E. Knuth, “On the Lambert W function,” *Advances in Computational mathematics*, vol. 5, no. 1, pp. 329–359, 1996.
- [44] J. Xu and R. Zhang, “Energy beamforming with one-bit feedback,” *IEEE Trans. Signal Process.*, vol. 62, no. 20, pp. 5370–5381, Oct. 2014.

- [45] S. M. Ross, *Introduction to Probability Models*, 10th ed. Reading, MA: Academic Press, 2010.
- [46] J. Nocedal and S. Wright, *Numerical optimization*. Springer Science & Business Media, 2006.
- [47] Y. Gu and S. Aïssa, “Distributed multi-user wireless charging power allocation,” INRS, Tech. Rep. INRS-EMT-2018-02-14-01, May 2016.
- [48] L. Shi et al., “Wireless power hotspot that charges all of your devices,” in *Proc. ACM MobiCom*, 2015, pp. 2–13.
- [49] A. Zappone, M. Di Renzo, and M. Debbah, “Wireless networks design in the era of deep learning: Model-based, AI-based, or both?” *IEEE Trans. Commun.*, vol. 67, no. 10, pp. 7331–7376, Oct. 2019.
- [50] M. Schubert and H. Boche, “Solution of the multiuser downlink beamforming problem with individual SINR constraints,” *IEEE Trans. Veh. Technol.*, vol. 53, no. 1, pp. 18–28, Jan. 2004.
- [51] A. Bayat and S. Aïssa, “Admission control and power allocation in wireless power charging networks,” in *Proc. IEEE Int. Symp. Pers. Indoor Mobile Radio Commun. (PIMRC)*, Oct. 2017, pp. 1–5.
- [52] —, “Auction-based design and analysis of wireless power transfer network with critical users,” *IEEE Commun. Lett.*, vol. 22, no. 11, pp. 2374–2377, Nov. 2018.
- [53] M. Bengtsson and B. Ottersten, “Optimal downlink beamforming using semidefinite optimization,” in *37th Annual Allerton Conference on Communication, Control, and Computing*, 1999, pp. 987–996.
- [54] J. D. Hartline, “Mechanism design and approximation,” *Book draft. October*, vol. 122, 2013.
- [55] A. B. Gershman, N. D. Sidiropoulos, S. Shahbazpanahi, M. Bengtsson, and B. Ottersten, “Convex optimization-based beamforming,” *IEEE Signal Process. Mag.*, vol. 27, no. 3, pp. 62–75, May 2010.
- [56] N. Nisan et al., “Introduction to mechanism design (for computer scientists),” *Algorithmic game theory*, vol. 9, pp. 209–242, 2007.
- [57] M. Abadi et al., “Tensorflow: Large-scale machine learning on heterogeneous systems,” 2015. [Online]. Available: <https://www.tensorflow.org>

- [58] *Keras Tuner*. [Online]. Available: <https://keras-team.github.io/keras-tuner>
- [59] D. P. Kingma and J. Ba, "Adam: A method for stochastic optimization," *arXiv preprint arXiv:1412.6980*, 2014.
- [60] L. Vandenberghe, V. R. Balakrishnan, R. Wallin, A. Hansson, and T. Roh, "Interior-point algorithms for semidefinite programming problems derived from the KYP lemma," in *Positive polynomials in control*. Springer, 2005, pp. 195–238.
- [61] F. Rashid-Farrokhi, K. J. R. Liu, and L. Tassiulas, "Transmit beamforming and power control for cellular wireless systems," *IEEE J. Sel. Areas Commun.*, vol. 16, no. 8, pp. 1437–1450, Oct. 1998.
- [62] J. Xu, L. Liu, and R. Zhang, "Multiuser MISO beamforming for simultaneous wireless information and power transfer," *IEEE Trans. Signal Process.*, vol. 62, no. 18, pp. 4798–4810, Sep. 2014.
- [63] A. A. Nasir, H. D. Tuan, D. T. Ngo, T. Q. Duong, and H. V. Poor, "Beamforming design for wireless information and power transfer systems: Receive power-splitting versus transmit time-switching," *IEEE Trans. Commun.*, vol. 65, no. 2, pp. 876–889, Feb. 2017.
- [64] Z. Qin, H. Ye, G. Y. Li, and B. F. Juang, "Deep learning in physical layer communications," *IEEE Trans. Wireless Commun.*, vol. 26, no. 2, pp. 93–99, Apr. 2019.
- [65] C. Wen, W. Shih, and S. Jin, "Deep learning for massive MIMO CSI feedback," *IEEE Wireless Commun. Lett.*, vol. 7, no. 5, pp. 748–751, Oct. 2018.
- [66] T. O'Shea and J. Hoydis, "An introduction to deep learning for the physical layer," *IEEE Trans. on Cogn. Commun. Netw.*, vol. 3, no. 4, pp. 563–575, Dec. 2017.
- [67] C. Huang, G. C. Alexandropoulos, A. Zappone, C. Yuen, and M. Debbah, "Deep learning for UL-DL channel calibration in generic massive MIMO systems," in *Proc. IEEE International Conference on Communications (ICC)*, May 2019, pp. 1–6.
- [68] M. Varasteh, J. Hoydis, and B. Clerckx, "Learning modulation design for SWIPT with non-linear energy harvester: Large and small signal power regimes," in *Proc. IEEE International Workshop on Signal Processing Advances in Wireless Communications (SPAWC)*, July 2019, pp. 1–5.

- [69] C. Chun, J. Kang, and I. Kim, “Adaptive rate and energy harvesting interval control based on reinforcement learning for SWIPT,” *IEEE Commun. Lett.*, vol. 22, no. 12, pp. 2571–2574, Dec. 2018.
- [70] Y. Al-Eryani, M. Akrouf, and E. Hossain, “Simultaneous energy harvesting and information transmission in a MIMO full-duplex system: A machine learning-based design,” *arXiv preprint arXiv:2002.06193*, 2020.
- [71] Z. Han, R. Zheng, and H. V. Poor, “Repeated auctions with Bayesian nonparametric learning for spectrum access in cognitive radio networks,” *IEEE Trans. Wireless Commun.*, vol. 10, no. 3, pp. 890–900, Mar. 2011.
- [72] Z. Zheng, L. Song, D. Niyato, and Z. Han, “Resource allocation in wireless powered relay networks: A bargaining game approach,” *IEEE Trans. Veh. Technol.*, vol. 66, no. 7, pp. 6310–6323, July 2017.
- [73] A. Bayat and S. Aissa, “Auction-driven multiuser beamforming with deep learning,” in *2020 IEEE Global Communications Conference: Wireless Communications (GlobeCom2020 WC)*, Taipei, Taiwan, Dec. 2020.
- [74] A. X. Jiang and K. Leyton-Brown, “Estimating bidders’ valuation distributions in online auctions,” in *Proc. IJCAI Workshop on Game Theoretic and Decision Theoretic Agents*, 2005, pp. 98–107.
- [75] D. Tse and P. Viswanath, *Fundamentals of wireless communication*. Cambridge university press, 2005.
- [76] Z. Luo, W. Ma, A. M. So, Y. Ye, and S. Zhang, “Semidefinite relaxation of quadratic optimization problems,” *IEEE Signal Process. Mag.*, vol. 27, no. 3, pp. 20–34, May 2010.
- [77] C. Helmberg, F. Rendl, R. J. Vanderbei, and H. Wolkowicz, “An interior-point method for semidefinite programming,” *SIAM Journal on Optimization*, vol. 6, no. 2, pp. 342–361, 1996.
- [78] P. Balachandran, W. Viles, and E. D. Kolaczyk, “Exponential-type inequalities involving ratios of the modified Bessel function of the first kind and their applications,” *arXiv preprint arXiv:1311.1450*, 2013.